Universität Hamburg

DER FORSCHUNG | DER LEHRE | DER BILDUNG

Thin Films Based on Titania Nanoparticles: Photoactivated Vapor Sensors and Electromechanical Actuators

Dissertation

zur Erlangung des Doktorgrades an der Fakultät für Mathematik, Informatik und Naturwissenschaften

Fachbereich Chemie

Universität Hamburg

vorgelegt von

Finn Dobschall

Hamburg

2025

Dissertation

Titel:	Thin Films Based on Titania Nanoparticles: Photoactivated Vapor Sensors and Electromechanical Actuators
Titel (deutsch):	Dünnschichtfilme basierend auf Titania Nanopartikeln: Photoaktivierte Sensoren für Dämpfe und elektromechanische Aktuatoren
Eingereicht von:	Finn Dobschall
Matrikelnummer:	6948808
E-Mail Adresse:	f.dobschall@web.de
Arbeitsgruppe:	Prof. Dr. Horst Weller / Prof. Dr. Nadja C. Bigall
Insitut:	Institut für Physikalische Chemie
Universität:	Universität Hamburg
Datum der Einreichung:	25. August 2025
Erstgutachter:	PD Dr. Tobias Vossmeyer
Zweitgutachter:	Prof. Dr. Tobias Beck
Druckfreigabe erteilt:	12. Dezember 2025
Datum der Disputation:	26. September 2025
Prüfungskommission:	PD Dr. Tobias Vossmeyer Prof. Dr. Dorota Koziej PD Dr. Tobias Kipp

Diese Arbeit wurde im Zeitraum von Mai 2022 bis August 2025 in der Arbeitsgruppe von Prof. Dr. Horst Weller und nachfolgend Prof. Dr. Nadja C. Bigall, im Forschungsteam von PD Dr. Tobias Vossmeyer, am Institut für Physikalische Chemie im Fachbereich Chemie der Universität Hamburg durchgeführt.

List of Publications

All peer-reviewed research articles that were published within the framework of this thesis are listed below in a chronological order.

1. F. Dobschall, H. Hartmann, S. C. Bittinger, N. Schulz, H. Schlicke, H. K. Trieu, T. Vossmeyer, "Freestanding Membranes of Titania Nanorods, Photocatalytically Reduced Graphene Oxide, and Silk Fibroin: Tunable Properties and Electrostatic Actuation", *Adv. Electron. Mater.* **2025**, 11, 5, 2400602.[1]
2. S. C. Bittinger, J. Struck, F. Dobschall, S. Benthien, H. Hartmann, H. Schlicke, M. Kohantorabi, H. Noei, T. Vossmeyer, "Nanocomposites of Titania/Reduced Graphene Oxide: Flexible Humidity Sensors Tuned via Photocatalytic Reduction", *ACS Appl. Nano Mater.* **2025**, 8, 15, 7428-7439.[2]
3. F. Dobschall, S. C. Bittinger, C. T. Tioka, J. Struck, E. Pariente, MH. Delville, H. Schlicke, T. Vossmeyer, "Photoactivated Detection of Volatile Organic Compounds Using Thin Films of Differently Shaped Titania Nanocrystals", *ACS Appl. Nano Mater.* **2025**, 8, 48, 22955-22964.[3]

Contents

List of Abbreviations

AFM	atomic force microscopy
AG	analyte gas
approx.	approximately
ATR	attenuated total reflectance
BOE	buffered oxide etchant
CB	conduction band
DEG	diethylene glycol
DI	deionized
DRIE	deep reactive ion etching
DUV	deep-ultraviolet
FTIR	Fourier-transform infrared
FWHM	full width at half maximum
GNP	gold nanoparticle
GO	graphene oxide
IDE	interdigitated electrode
IoT	Internet of Things
LbL	layer-by-layer
LED	light-emitting diode
MEMS/NEMS	micro- and nanoelectromechanical systems
MeOH	methanol
MFC	mass flow controller
MIBK	methyl isobutyl ketone
MOX	metal oxide
MPFB	methoxyperfluorobutane
NIR	near-infrared
OC	organic content
ODE	1-octadecene
OLAC	oleic acid
OLAM	oleylamine
PCB	printed circuit board
PDMS	polydimethylsiloxane
PMMA	poly(methyl methacrylate)
ppb	parts-per-billion
ppm	parts-per-million
PTFE	polytetrafluoroethylene

PVA	poly vinyl alcohol
PVD	physical vapor deposition
QCM	quartz crystal microbalance
rGO	reduced graphene oxide
r.h.	relative humidity
RTD	resistance temperature detector
SC	spin-coating
SEM	scanning electron microscopy
SF	silk fibroin
SPION	superparamagnetic iron oxide nanoparticle
TEM	transmission electron microscopy
TEOA	triethanolamine
TGA	thermogravimetric analysis
TNB	titania nanobipyramid
TNC	titania nanocrystal
TND	titania nanodot
TNP	titania nanoplate
TNR	titania nanorod
UV	ultraviolet
VB	valence band
vis	visible
VOC	volatile organic compound
XPS	x-ray photoelelectron spectroscopy
XRD	x-ray diffraction
ZG	zero gas

List of Symbols

a_r	aperture radius
A	area
A_{QCM}	sensitive area of the QCM
a_{e}	cavity edge length
b	instrumental broadening factor
C	capacitance
d	distance
e	elementary charge
E	Young's modulus
E_{gap}	band gap energy
eV_{s}	Schottky barrier height
E_{f}	electric field
ϵ	permittivity
ϵ_0	vacuum permittivity
$\varepsilon_{\mathrm{bi}}$	biaxial strain
$\varepsilon_{\mathrm{ult}}$	ultimate biaxial strain
$f_{0,\mathrm{f}}$	resonant frequency of the coated QCM
Δf_{s}	resonant frequency shift
F	force
G	conductance
G_0	baseline conductance
$\frac{\Delta G}{G_0}$	relative conductance change
$\left(\frac{\Delta G}{G_0}\right)_{\mathrm{max}}$	maximum relative conductance change
h	membrane deflection
I	electrical current
I_{max}	maximum response current
k_{B}	Boltzmann constant
K	shape factor
L	crystallite size
L_{D}	Debye length
λ	wavelength
m_{ads}	sorbed analyte mass
m_{f}	TNC thin film mass
M_{a}	molar mass
μ	shear modulus

n_{ads}	sorbed amount of substance
n_{d}	charge carrier concentration
ν	Poisson ratio
P	pressure
Q	charge
R_{C}	spherical cap radius
ρ	density
s	full arc length
σ_{bi}	biaxial stress
σ_{ult}	ultimate biaxial stress
σ_0	prestress
t_{80}	rise time to reach 80% maximum sensor response signal
t_{m}	membrane thickness
T	temperature
$2\theta_0$	diffraction angle
U_{T}	toughness
V	voltage
Y	biaxial modulus

1 Abstract

In this thesis, functional thin films and membranes consisting of (I) differently shaped TiO_2 nanocrystals (TNCs) and (II) TiO_2 nanorods, graphene oxide, and silk fibroin (TNR/GO/SF) were fabricated and investigated for their application as (I) photoactivated chemiresistors for the detection of volatile organic compounds (VOCs) and (II) electrostatic actuators. While photoactivated chemiresistors offer a promising, low-temperature alternative to conventional thermally activated sensors, the integration of hybrid nanomaterials into micro- and nanoelectromechanical systems (MEMS/NEMS) allows for tunable functional properties beyond those of standard silicon-based devices. Both applications benefit from the incorporation of TNCs due to their unique properties such as high stability and photocatalytic activity.

In the first project presented, the sensing mechanism of photoactivated chemiresistors based on substrate-supported thin films assembled from TNCs was examined, focusing on how their responses to a variety of VOCs are influenced by the structure and morphology of the films as well as the size and shape of the individual TNCs. Established synthesis routes were used to prepare organically-stabilized TiO_2 nanorods (TNRs), TiO_2 nanoplates (TNPs), and TiO_2 nanodots (TNDs). Bare TiO_2 nanobipyramids (TNBs) were provided by the Institut de Chimie de la Matière Condensée de Bordeaux, CNRS, and commercial P25 TNCs were purchased.
Thin films were fabricated by drop-casting the respective suspension on various substrates, followed by deep-ultraviolet (DUV) treatment at 254 nm to remove initial ligands from the TiO_2 surface. While homogeneous thin films with thicknesses of approx. 150 nm were obtained using organically-stabilized TNCs, deposits with an island-like structure of aggregates and cracks with thicknesses of approx. 125 nm were formed using bare TNCs, as demonstrated by atomic force microscopy (AFM) and scanning electron microscopy (SEM). Further, plasma and ozone surface treatments were investigated regarding their ligand removal capabilities.
Next, the ionosorption of oxygen species on the TiO_2 surface was investigated on a TNR thin film by combining charge transport and microgravimetric measurements. Photoactivation of the sensors was achieved using ultraviolet light-emitting diodes (UV LEDs) with a wavelength of 278 nm, resulting in low photocurrents in the single-digit nA range. The ability to adjust the chemiresistive response characteristics was demonstrated by increasing the irradiance of the LEDs, which resulted in shorter response times (measured as the t_{80} time) and increased current signals (measured as I_{max}).
The chemical selectivity of the photoactivated (UV LEDs, 278 nm, ~23 mW/cm^2) TNC-based chemiresistors was tested using various VOCs including ethanol, 1-propanol, 2-

propanol, 1-butanol, toluene, 4-methylpentan-2-one (methyl isobutyl ketone, MIBK), 1-butylamine, and ethyl acetate in the concentration range between 25–200 parts-per-million (ppm). All photoactivated sensors were highly sensitive to alcohols as shown by increasing response currents with increasing concentration. We attribute this selectivity to the selective adsorption of the OH-group and the partial oxidation reaction of the alcohol on the TiO_2 surface, forming the respective aldehyde or ketone. Apart from the effect of the surface-to-volume ratio of the TNCs on the resistive properties, the predominant influencing factor was the structure and morphology of the sensitive layer. The discontinuous, island-like, porous morphology of thin films based on bare TNCs provides high accessibility of the analyte to the surface of the individual TNCs. Thus, their response currents were one order of magnitude higher compared to sensors based on organically-stabilized TNCs, that formed densely packed films. The chemiresistive measurements were correlated with microgravimetric analysis, demonstrating that the adsorption of analyte molecules was not directly translated into the chemiresistive responses for various VOCs. However, for a series of primary alcohols, the maximum response current was related to the vapor pressure of the alcohols, as the amount of sorbed substance increased with decreasing vapor pressure.

The influence of relative humidity (r.h.) on the chemiresistive responses was investigated for 1-propanol as target analyte. It was found that the presence of water disturbed the resistive analyte detection, due to the competitive adsorption of water on the TiO_2 surface that increased with increasing r.h. levels, as shown by microgravimetric measurements.

To address the loss of sensitivity in the presence of humidity, the electrical and chemiresistive properties of a TNR-based sensor were investigated at various r.h. levels and different operating temperatures of up to 72 °C. Charge transport measurements showed that the increase of the photoconductivity of the TNR-based sensor under the influence of different r.h. levels was reduced at increased operating temperatures. Furthermore, it was possible to reliably detect 1-propanol vapor of different concentrations at r.h. levels of up to 50%, although the responses significantly decreased, indicating some limitations.

Finally, the surface modification of TNR-based chemiresistors was investigated using different materials and fabrication methods. While Pt was deposited by sputtering, superparamagnetic iron oxide nanoparticles (SPIONs) and gold nanoparticles (GNPs) were deposited by spin-coating. Further, the formation of GNPs was demonstrated by photocatalytically reducing Au^{3+} on the TNR thin film. The chemiresistive measurements showed impaired sensing characteristics for all surface modifications which could result from changes in the charge carrier concentration of the TNRs.

In the second project presented, a transfer process using contact printing was developed and optimized to prepare freestanding membranes composed of TNRs, GO, and SF, and their direct electrostatic actuation was demonstrated. Initially, a layer-by-layer spin-coating (LbL SC) method using colloidal solutions was employed to fabricate the substrate-supported hybrid thin films with the desired sequence of different materials on various substrates. GO and TNRs were prepared following established synthesis protocols, while SF was purchased commercially. Freestanding membrane sections of up to ~60 000 μm^2 were fabricated by printing the hybrid films onto substrates with cavities or apertures using a polydimethoxysilane (PDMS) stamp. For this transfer process, the hybrid films were sandwiched between a sacrificial layer of polyvinyl alcohol (PVA) and a protective layer of poly (methyl methacrylate) (PMMA). The PVA layer was dissolved in water to detach the hybrid films from the substrate while the PMMA was protecting the hybrid films at the interface with the stamp.

Next, the composition of the hybrid membranes was adjusted by DUV illumination at 254 nm, which photocatalytically converted GO to reduced graphene oxide (rGO). This reduction of the material was mediated by the TNRs and accompanied by an increase in conductivity. In addition to electrical and structural characterization via charge transport measurements and microscopic analysis (AFM and SEM), the mechanical properties were examined using AFM microbulge tests. Here, a significant increase in the Young's modulus from ~22 GPa to ~38 GPa was observed after DUV treatment. We attributed this result to the photo-induced cross-linking of the membrane's organic constituents (GO and SF), as evidenced by the compaction of the hybrid membrane, resulting in a thickness decrease of approx. 30% after the DUV treatment. Furthermore, the ultimate mechanical parameters were assessed via burst experiments on DUV-treated membranes, exhibiting a toughness of ~1.2 MJ/m^3.

Finally, the freestanding membranes were employed as electrostatically driven actuators, leveraging the generated electrical conductivity due to the formation of rGO upon the DUV illumination. A simple electrostatic model is presented that describes the membrane deflection as a function of the applied voltage.

2 Zusammenfassung

In dieser Arbeit wurden funktionale Dünnschichtfilme und Membranen hergestellt, die aus (I) TiO_2-Nanokristallen (TNCs) unterschiedlicher Form und (II) TiO_2-Nanostäbchen, Graphenoxid und Seidenfibroin (TNR/GO/SF) bestehen. Diese Systeme wurden hinsichtlich ihrer Anwendungen als (I) photoaktivierte Chemiresistoren für die Detektion flüchtiger organischer Verbindungen (VOCs) und (II) elektrostatische Aktuatoren untersucht.
Während photoaktivierte Chemiresistoren eine vielversprechende Alternative zu kommerziellen thermisch aktivierten Sensoren darstellen, ermöglicht die Integration hybrider Nanomaterialien in mikro- und nanoelektromechanischen Systemen (MEMS/NEMS) die Veränderung der funktionalen Eigenschaften über Silizium-basierte Geräte hinaus. Für beide Anwendungen kann das Einbringen von TNCs aufgrund ihrer einzigartigen Eigenschaften, wie der hohen Stabilität und photokatalytischen Aktivität, von besonderer Bedeutung sein.

Im zuerst vorgestellten Projekt wurde der Sensormechanismus photoaktivierter Chemiresistoren basierend auf substratgestützten Dünnschichtfilmen aus TNCs untersucht. Der Fokus lag darauf, herauszufinden, wie die sensorischen Eigenschaften gegenüber verschiedenen VOCs durch die Struktur und Morphologie der Filme sowie durch die Größe und Form der einzelnen TNCs beeinflusst werden. Für die Herstellung der organisch-stabilisierten TiO_2-Nanostäbchen (TNRs), TiO_2-Nanoplättchen (TNPs) und sphärischen TiO_2-Nano-partikel (TNDs) wurden etablierte Syntheserouten verwendet. Blanke TiO_2-Nanobipyramiden (TNBs) wurden vom Institut de Chimie de la Matière Condensée de Bordeaux, CNRS, bereitgestellt und kommerzielle P25 TNCs erworben.
Die Dünnschichtfilme wurden durch *Drop-Casting* der jeweiligen Suspension auf verschiedenen Substraten hergestellt. Anschließend wurden die organischen Liganden durch eine tief-ultraviolett (DUV)-Behandlung entfernt. Während homogene Dünnschichten mit einer Dicke von ca. 150 nm unter Verwendung der organisch-stabilisierten TNCs hergestellt wurden, entstanden inselartige Strukturen aus Agglomeraten und Rissen mit einer Dicke von ca. 125 nm bei der Verwendung der blanken TNCs. Außerdem wurden die Einflüsse der Plasma- und Ozon-Oberflächenbehandlung auf das Entfernen der Liganden untersucht.
Die Präsenz von ionosorbierten Sauerstoffspezien auf der Oberfläche des TiO_2 wurde durch die Kombination von Ladungstransport- und mikrogravimetrischen Messungen am Beispiel von TNR Dünnschichtfilmen untersucht. Die Photoaktivierung der Sensoren wurde mithilfe von ultraviolett Leuchtdioden (UV-LEDs), die bei einer Wellenlänge von 278 nm emittierten, realisiert, was zu geringen Photoströmen im Bereich weniger nA

führte. Außerdem wurde die Einstellung der Antwortcharakteristika demonstriert. Hierbei führte die Erhöhung der Bestrahlungsstärke der LED zu kürzeren Antwortzeiten (gemessen als die t_{80} Zeit) sowie einem Anstieg des maximalen Antwortstroms (gemessen als I_{max}).

Die chemische Selektivität der photoaktivierten (UV-LEDs, 278 nm, ~23 mW/cm^2) TNC-basierten Chemiresistoren wurde für verschiedene VOCs, darunter Ethanol, 1-Propanol, 2-Propanol, 1-Butanol, Toluol, 4-Methylpentan-2-on (Methylisobutylketon, MIBK), 1-Butylamin und Ethylacetat, im Konzentrationsbereich zwischen 25–200 Parts per million (ppm) getestet. Alle Sensoren zeigten eine selektive Reaktion gegenüber Alkoholen und wiesen einen zunehmenden Antwortstrom mit steigender Konzentration auf. Es wird angenommen, dass diese Selektivität auf die selektive Adsorption der OH-Gruppe und die partielle Oxidationsreaktion der Alkohole auf der TiO_2 Oberfläche zurückzuführen ist, als deren Produkt das jeweilige Aldehyd oder Keton entsteht. Neben dem Effekt des Oberflächen-zu-Volumen-Verhältnisses der TNCs auf die chemiresistiven Eigenschaften, wurde festgestellt, dass der primäre Einfluss durch die Struktur und Morphologie der sensitiven Schicht entsteht. Die inselartige und poröse Morphologie der Dünnschichtfilme, die aus den blanken TNCs bestehen, ermöglicht eine gute Zugänglichkeit der Oberfläche der einzelnen TNCs für die Analytmoleküle. Daher konnten mit diesen Sensoren Antwortströme gemessen werden, die um eine Größenordnung über den Antworten von organisch-stabilisierten TNC-basierten Sensoren mit einer dichtgepackten Dünnschichtstruktur lagen. Durch die Korrelation von chemiresistiven Messungen mit mikrogravimetrischen Tests konnte gezeigt werden, dass die Adsorption der Analytmoleküle nicht für alle VOCs unmittelbar in die chemiresistive Antwort übersetzt wurde. Für eine Serie von primären Alkoholen war jedoch der maximale Antwortstrom von dem Dampfdruck der Alkohole abhängig, was durch den Anstieg der adsorbierte Stoffmenge mit abnehmendem Dampfdruck gezeigt wurde.

Der Einfluss der relativen Luftfeuchtigkeit (r.h.) auf die chemiresistiven Antworten wurde mit 1-Propanol als Zielanalyt untersucht. Bei diesen Untersuchungen wurde festgestellt, dass die Anwesenheit von Wasser die widerstandsbasierte Analyterkennung störte und die kompetitive Adsorption von Wasser auf der TiO_2 Oberfläche mit steigender r.h. zunahm, wie durch mikrogravimetrische Messungen gezeigt wurde.

Um den Sensitivitätsverlust in der Gegenwart von Feuchtigkeit zu adressieren, wurden die elektrischen und chemiresistiven Eigenschaften eines TNR-basierten Sensors bei verschiedenen r.h. und unterschiedlichen Betriebstemperaturen von bis zu 72 °C untersucht. Ladungstransportmessungen haben gezeigt, dass die Erhöhung des Photostroms des TNR-basierten Sensors unter dem Einfluss verschiedener r.h. bei gesteigerten Betriebstemperaturen verringert wurde. Darüber hinaus war es möglich, 1-Propanol Dampf mit verschiedenen Konzentrationen zuverlässig bei r.h. von bis zu 50% zu detektieren, wobei die

abnehmenden Antworten eine Limitierung aufzeigen.
Abschließend wurde die Oberflächenmodifikation von TNR-basierten Chemiresistoren mithilfe verschiedener Materialien und Herstellungsmethoden untersucht. Während Pt durch Sputtern aufgebracht wurde, wurden superparamagnetische Eisenoxid-Nanopartikel (SPIONs) und Goldnanopartikel (GNPs) durch *Spin-Coating* abgeschieden. Zudem wurde die Bildung von GNPs durch photokatalytische Reduktion von Au^{3+} auf dem TNR Dünnschichtfilm demonstriert. Die chemiresistiven Messungen zeigten die deutliche Beeinträchtigung der sensorischen Antworten für alle Oberflächenmodifikationen, die möglicherweise auf Veränderungen der Ladungsträgerkonzentration der TNRs zurückzuführen sind.

Im zweiten vorgestellten Projekt wurde das *Contact Printing*-Verfahren als Transfermethode für freistehende Membranen aus TNRs, GO und SF optimiert, um anschließend deren direkte elektrostatische Aktuierung zu demonstrieren. Zunächst wurde ein *Layer-by-layer Spin-Coating* (LbL SC)-Verfahren zur Abscheidung der substratgestützten Hybridfilme angewandt. Die kolloidalen Lösungen wurden in gewünschter Reihenfolge der Materialien auf verschiedene Substrate aufgebracht. GO und TNRs wurden nach etablierten Syntheserouten hergestellt, während SF kommerziell bezogen wurde. Die Membranen mit freistehenden Flächen von bis zu ~60 000 μm^2 wurden durch das Übertragen des Hybridfilms mithilfe eines Polydimethylsiloxan (PDMS)-Stempels auf Substrate mit einem Durchgangsloch oder Kavitäten gefertigt. Für diesen Transferprozess wurde der Hybridfilm zwischen einer Opferschicht aus Polyvinylalkohol (PVA) und einer Schutzschicht aus Polymethylmethacrylat (PMMA) geschichtet. Während die PVA Schicht durch Lösen in Wasser das Abtrennen des Films vom Substrat erlaubte, schützte die PMMA Schicht den Hybridfilm an der Grenzfläche zum Stempel.
Anschließend wurde die Zusammensetzung der Hybridmembranen durch die photokatalytische Umwandlung des GOs zu reduziertem Graphenoxid (rGO) angepasst, indem die Proben mit DUV-Licht (254 nm) bestrahlt wurden. Diese Reduktion wurde durch die photokatalytische Aktivität der TNRs begünstigt und ging mit der Erhöhung der elektrischen Leitfähigkeit der hybriden Materialien einher. Zusätzlich zur elektrischen und strukturellen Charakterisierung durch Ladungstransportmessungen und mikroskopischer Analysen (AFM und SEM) wurden die mechanischen Eigenschaften mittels AFM-*Bulge*-Tests untersucht. Hier wurde eine signifikante Erhöhung der Young's Modulen nach der DUV-Behandlung von ~22 GPa auf ~38 GPa gezeigt. Es wird angenommen, dass diese Erhöhung auf die lichtinduzierte Quervernetzung der organischen Bestandteile der Membranen (GO und SF) zurückgeführen ist. Diese Verdichtung der Hybridmembranen führte zu einer Reduzierung der Dicke von ca. 30%. Darüber hinaus wurden die kritischen mechanischen Parameter durch *Burst*-Experimente an den DUV-behandelten Membranen un-

tersucht und es wurde eine Zähigkeit der Membranen von ~1.2 MJ/m^3 bestimmt.
Abschließend wurden die freistehenden Membranen als Aktuatoren eingesetzt, welche, basierend auf der erhöhten elektrischen Leitfähigkeit durch die Bildung von rGO infolge der DUV-Bestrahlung, elektrostatisch angeregt werden konnten. In diesem Zusammenhang wird ein einfaches elektrostatisches Modell vorgestellt, welches die Verformung der Membran in Abgängigkeit der angelegten Spannung beschreibt.

3 Introduction

Sensors play a fundamental role in today's world being implemented in everyday devices such as cars, security systems, fitness gadgets, and smartphones.[4] They provide the interface between physicochemical properties of the environment and electronic systems, facilitating the detection and quantification of a wide array of physical, chemical, and biological parameters. Their ongoing evolution has been driven by the demand for enhanced sensitivity, miniaturization, and energy efficiency, enabling the integration into increasingly complex and compact systems.

Many sensors are based on microelectromechanical systems (MEMS), which combine mechanical structures with electronic circuits via transducers that convert electrical signals into mechanical stimuli and vice versa. Advances in microfabrication and lithography have enabled the precise production of these miniature systems, supporting their widespread use across diverse applications in the automotive technology and consumer electronics.[5] In the course of miniaturization, devices with sizes of functional components in the nanoscale are referred to as nanoelectromechanical systems (NEMS).[6] These technologies not only facilitate the development of integrated sensor systems, but also pave the way for innovative applications in portable and wearable devices. The rapid growth of the Internet of Things (IoT), which seeks to seamlessly connect multiple devices interacting with our environment into a unified smart network, is a major driving force behind the development of advanced technologies of various sensors. This interconnected environment involves the creation of sensors that are highly sensitive, specific, and capable of wireless operation with real-time data transmission.[7]

For the integration of gas sensor into IoT networks, novel approaches are needed, as these applications require small size, low power consumption, and the operation at ambient temperature. The latter in particular remains a driving force behind current research on gas sensors, as the widely used MOX-based gas sensors are operated at high temperatures and their integration into complex circuits on chip is expensive, as it requires thermal decoupling of the heated transducer from the rest of the chip.[8]

Typically, gas sensors consist of a sensitive material and a transducer as functional units. During the sensing process, the sensitive material undergoes a change in a physical property due to chemical or physical interaction with the analyte. This change is translated into an optical or electrical signal by the transducer.[9] Based on this transduction mechanism, gas sensors are categorized into various types such as optical, electromechanical, and electrical sensors.[10–12] Among these, the electrical sensors such as transistors, capacitors, and resistors are frequently used due to their ease of operation.[12,13]

The sensing performance is usually assessed by characteristics, including sensitivity, selectivity, response time, recovery time, and the limit of detection. The incorporation of

nanostructured sensitive and transducing materials can significantly enhance these performance parameters.[14] Nanotechology focuses on structures with dimensions typically between 1 to 100 nanometers, using materials such as metal and metal oxide (MOX) nanoparticles, carbon-based materials like graphene derivatives, and transition metal chalcogenides.[15] Due to their high surface-to-volume ratio, increased reactivity, and tunable electronic properties, nanomaterials enable the development of chemical sensors that are capable of detecting even trace amounts of analytes with high precision.[16,17] Through precise control of the particle size and shape at the nanoscale, tailored materials with optimized physical and chemical properties lead to improved gas adsorption and reaction processes.[10] This nanostructuring not only boosts sensor sensitivity and selectivity but also facilitates low power consumption and device miniaturization, making sensors more portable and efficient.[18]

The detection of volatile organic compounds (VOCs) is of paramount importance due to their high vapor pressure at ambient conditions, widespread source of emission, and dominant share of air pollutants.[10] For example, VOCs can serve as markers for fruit ripening, explosives, and diseases, enabling non-invasive diagnostics. Consequently, the detection and monitoring of VOCs have valuable applications across numerous fields, including healthcare, agriculture, environmental monitoring, and industrial process control.[10]

Not only the detection of hazardous substances, but also their decomposition into harmless components and ultimately their suppressed release through clean energy resource are serious challenges on the global scale. Among many potential materials, TiO_2 or titania is a promising candidate for sustainable technologies resulting from its strong photocatalytic activity allowing for the conversion of solar energy.[19] For instance, the bias voltage for the electrolysis of H_2O can be significantly reduced in the presence of TiO_2 as a photocatalyst.[20] As a result, the energy consumption for the production of hydrogen as a sustainable energy resource is drastically reduced.

This thesis includes two major projects, both focusing on the characterization of functional materials based on nanostructured TiO_2, and the exploration of their potential use in sensing applications. In the first project, thin films of differently shaped titania nanocrystals (TNCs) are investigated as photoactivated, resistive sensors for the detection of VOCs, addressing the need for low temperature gas sensors in IoT networks. The second project covers the demonstration of electrostatic actuation of hybrid freestanding membranes comprising graphene oxide (GO) and TNCs. Here, the tunable functional properties of the hybrid membranes are explored for the fabrication of novel MEMS/NEMS.

The theoretical framework for understanding the work is presented in section 4. Following, section 5 outlines the objectives of the projects, and the results are described and discussed in section 6. Section 7 provides detailed information on the experimental procedures. Further data are summarized in the first section of the Appendix A.1.

4 Films and Membranes from TiO_2 Nanoparticles for Sensing and Actuation

Depositing materials as thin films, typically with a thickness ranging from a few nanometers to several micrometers, offers advantages for various technological applications. This is due to their unique optical, electrical, and mechanical properties, as reported for thin films from different materials such as carbon nanotubes,[21] metal oxide semiconductors,[22] and metal organic frameworks.[23] The ability to precisely control thickness and composition using advanced fabrication methods makes them invaluable in areas such as optics for mirrors[24] and electronics, where they are used in transistors and solar cells.[25,26] Further, many optoelectronic applications require a freestanding membrane section that spans a cavity or through hole, allowing for the actuation of the thin film.[27,28] As a result, the mechanical properties and the resonance behavior of various materials are currently under investigation.

In the present thesis, thin films as well as freestanding membranes comprising TiO_2 are investigated. The theoretical foundation is discussed in the following sections starting with the introduction of nanostructured TiO_2 building blocks in section 4.1. While section 4.2 provides an overview on resistive metal oxide gas sensors including thermal activation and photoactivation, section 4.3 presents the current research development on nanohybrid materials and membranes, focusing on their application in micro- and nanoelectromechanical systems (MEMS/NEMS).

4.1 TiO_2 Nanoparticles

TiO_2 or titania nanoparticles have attracted considerable interest in both scientific research and technological development due to their distinctive physicochemical characteristics, such as their high surface area, chemical stability, and remarkable photocatalytic properties compared to other semiconductor materials. Several studies already reported on the controlled synthesis of differently shaped titania nanocrystals (TNCs) and their distinct fundamental properties on the nanoscale.[29,30] Further, TNCs were investigated for various applications, including photocatalysis, biomedicine, and energy conversion.[19,31,32]

4.1.1 Synthesis

The synthesis of TNCs has evolved over time, beginning with aqueous methods and later expanding to non-aqueous approaches.

In aqueous synthesis methods, TNCs are formed in two steps. First, due to hydrolysis of the titanium precursor, a Ti-water complex is formed including different water species which depend on the reaction conditions.[29] Second, the Ti-water complexes react via condensation and form the Ti-O-Ti bonds constituting the TNCs. Staring off in the 1970s, first synthesis protocols used the sol-gel method to prepare TNCs, resulting in large particles with poor crystallinity. For instance, Matijevic et al. investigated the hydrolysis of $TiCl_4$ in highly acidic solutions, and reported the formation of spherical TNCs with diameters of several hundred nanometers. They found that lowering the pH reduced the rate of hydrolysis, allowing for a more controlled reaction.[33] In order to improve the properties of the particles, a second aqueous method based on the hydrothermal approach was developed, especially improving the crystallinity of the particles. Here, bases are added to generate Ti-hydroxide complexes, which are dehydrated under hydrothermal reaction conditions, resulting in the formation of TiO_2.[34] For example, Zhao et al. reported the large-scale fabrication of brookite TNCs with a spindle shape using titanium oxysulfate as precursor and sodium hydroxide as base. They found that the TNCs preferentially grow along the [001] direction under the employed experimental conditions, and demonstrated the improved crystallinity of the TNCs compared to the sol-gel method.[35] However, controlling the size and shape of the TNCs remains a challenge in aqueous conditions, as the hydrolysis and condensation occur very fast.[36] Further, the dispersibility is poor, which complicates the processing of TNCs and could hinder the thin film fabrication (cf. section 4.1.3).

In non-aqueous approaches, organic molecules replace water as the primary reaction solvent, allowing for a better control over the structural properties, since the reaction rates are slowed down.[37] Using a solvothermal method, Niederberger and co-workers developed a versatile protocol based on $TiCl_4$ as precursor and benzyl alcohol as reaction medium, where the intermediate alkoxide is hydrolyzed to form the final TNCs.[38] By varying the aging time, temperature, and the ratio of benzyl alcohol to $TiCl_4$, the size of the spherical TNCs was tuned between 4–14 nm.[38,39] The addition of surfactants and organic ligands has offered new ways to modulate precursor reactivity, which enabled unprecedented control over the shape, size, and modification of TNCs. As a result, the surfactant-assisted synthesis approach is widely used for the preparation of monodisperse TNCs. In this regard, Gordon et al. reported a surfactant-assisted seeded-growth method to produce shape-controlled TNCs with well-defined faceting.[40] In their approach, brookite titania nanorods (TNRs) and anatase titania nanoplates (TNPs) were synthesized by aminolysis of titanium carboxylate complexes. The latter are formed by dissolving the precursor in oleic acid (OLAC) using oleylamine (OLAM) as co-surfactant. The shape of the resulting nanocrystals was regulated by varying the type of titanium precursor used in the synthesis. Here, $TiCl_4$ led to the formation of nanorods and TiF_4

resulted in the plate-shape, as the fluoride ions act as a shape-directing agent by stabilizing the {001} facets. Further, the exposed crystal facets were adjusted not only by the titanium precursor but also by the co-surfactant, resulting in different proportions of the {101} to {001} facets in anatase TNCs by varying the ratio between OLAM and octadecanol.[40]

In addition to the syntheses reported in literature, several studies focusing on the applications of TNCs are based commercial Titanium(IV)-oxide Aeroxide™ P25 using these TNCs as a standard reference. P25 TNCs are typically obtained in a mixed crystal phase of anatase and rutile with a brought size distribution of approx. 10–40 nm and various shapes.[41]

4.1.2 Properties

As already indicated in the previous paragraph, TNCs exhibit distinct crystal phases, with three naturally occurring structures: rutile, anatase, and brookite. While rutile and anatase both crystallize in the tetragonal crystal system, brookite crystallizes in the orthorhombic system, and all three modifications consist of the same fundamental unit. Each titanium atom is surrounded by oxygen atoms arranged in an octahedral configuration, and the crystal structures differ in the number of shared corners and edges of the (TiO_6)-octahedra, as well as in the bond lengths within these octahedra.[42] Although rutile is the thermodynamically stable phase in the bulk form, TNCs predominantly form in the anatase phase based on its lower surface energy which plays a significant role in the formation of colloidal crystals because of the high surface-to-volume ratio of these materials.[43]

Due to the presence of oxygen vacancies within its crystal lattice, TiO_2 is an intrinsic n-type semiconductor.[44] These defect states can be described as unpaired electrons that originally reside in the O 2p orbitals, which form the valence band (VB). When an oxygen atom is removed, these electrons occupy localized states formed by the Ti 3d orbitals. These states lie in the band gap close to the lower level of the conduction band (CB), with the latter being primarily composed of Ti 3d orbitals.[45] As a result, these electrons can be excited with low energy into the CB and thus influence the electrical properties of the TNCs as the majority charge carriers.[45,46] Since TiO_2 is a wide band gap semiconductor, the thermal activation of charge carriers across the band gap is negligible at room temperature. The band gap energies (E_{gap}) in bulk are 3.02 eV for rutile,[47] 3.20 eV for anatase,[47] and 3.14 eV for brookite.[48] Upon optical excitation with ultraviolet (UV) light of an energy equal to or greater than the band gap energy, electrons are elevated into the CB, creating holes in the VB. The formation of these electron-hole pairs is the basis for

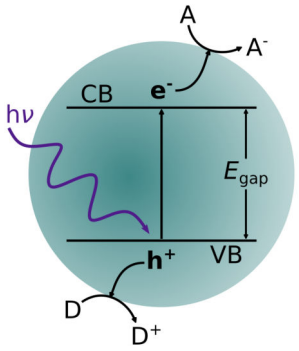

Figure 4.1: Schematic depiction of the photocatalytic processes proposed on a TNC catalyst. When the TNC is illuminated with light of photon energy hν equal to or greater than the band gap energy E_{gap}, an electron is excited from the VB to the CB, resulting in the formation of a hole in the VB. If the photogenerated charge carriers reach the catalyst surface, they can initiate photocatalytic processes - electrons can reduce electron acceptors (A), while holes can oxidize electron donors (D).

the photocatalytic activity of TiO_2 as illustrated in figure 4.1. This photocatalytic activity is fundamentally determined by the electronic band structure and band gap, which influence both the light absorption and the redox capabilities.[49] After the electron-hole pair generation, only those charge carriers that successfully migrate to the surface are available for redox reactions with electron acceptors (A) and donors (D). Typically, reactive radical intermediates participate in the photocatalytic reactions when water and oxygen molecules are adsorbed on the surface of TiO_2.[19] Recombination of electrons and holes or their trapping at defect sites can reduce the photocatalytic activity due to energy loss, emitted as photons or dissipated as lattice vibrations, respectively.[44] For TiO_2, however, the photogenerated holes tend to localize on the material's surface, facilitating the oxidation reaction with donors and also reducing the recombination with the photogenerated electrons.[49] This property, combined with the high oxidation potential and chemical stability of TiO_2, makes it an excellent photocatalyst.[50]

The significant potential of TiO_2 as a photocatalyst has been demonstrated across various critical reactions that support environmental and energy-related applications, such as water splitting for hydrogen production and the degradation of environmental pollutants.[19,51] In this context, the relation between crystal structure and photocatalytic activity has been investigated, e.g., demonstrating higher activity for the anatase compared to rutile crystal phase.[49] DFT calculations reported by Zhang et al. indicated that anatase exhibits the highest mobility and longest lifetime of photoexcited charge carriers among the three phases. These properties are beneficial for enhancing the photocatalytic activity.[52] In contrast, Kandiel and co-workers conducted a comparative study of the photocatalytic performance of brookite, anatase, and their mixed-phase TNCs for methanol (MeOH) oxidation. They reported that brookite TNCs demonstrated the highest photocatalytic MeOH oxidation among the tested materials.[53] Further, Li et al. compared the photocatalytic phenol degradation of phase-pure brookite and anatase nanocrystals in

aqueous solutions as a function of the calcination temperature used in the last step of the nanocrystal formation. For low calcination temperatures, they found higher photocatalytic phenol degradation for brookite compared to anatase, but this trend inverted with increasing temperature.[54] These examples highlight that no crystal phase is universally dominant and further investigations are necessary, taking into account the specifically exposed facets of the crystal phases.
As described in the previous paragraph, numerous studies have demonstrated the synthesis of TNCs with controlled phases and facet exposure, which can be used to analyze their photocatalytic performance. For instance, Gordon et al. reported higher photocatalytic hydrogen production for anatase TNCs with an increasing ratio of {101} to {001} of the exposed facets.[40]

4.1.3 Thin Films

For numerous applications, the fabrication of thin films with controlled properties such as thickness and porosity is of great interest with various physical and chemical preparation techniques being available for this purpose. Using physical vapor deposition, metals such as silver, titanium, or gold can be deposited onto substrates, often serving as electrically conductive layers on printed circuit boards (PCBs).[55] In contrast, chemical vapor deposition relies on gaseous precursors that react and decompose on the surface to form a thin film. This technique is frequently applied for the deposition of graphene films.[56]
Beyond these vapor-based techniques, solution processes are important as they allow for deposition from the liquid phase, which can be applied for a wide range of materials.[57] These coating processes involve dispersing or dissolving the desired material in solvents allowing for the large-area fabrication of the thin film upon solvent evaporation. Dip- and spin-coating (SC) are two plain methods widely used for the thin film fabrication from dispersions. Especially the rotation of the substrate during SC enables the production of very thin films and improves homogeneity and reproducibility.[58]
For the fabrication of nanostructured TiO_2-based thin films, the most common approach involves depositing a liquid precursor containing the titanium source, which is hydrolyzed and condensed on the substrate.[59] To obtain nanostructured films, templates are used to guide the growth of the TiO_2 structure and are subsequently etched away after the TiO_2 deposition. For instance, Xu et al. prepared TiO_2 nanotubes by submerging substrate-supported ZnO nanowires in an acidic solution of $(NH_4)_2TiF_6$, which hydrolyzes and condenses to form TiO_2 while simultaneously dissolving the ZnO.[60] Similarly, Tétreault et al. reported the fabrication of mesoporous single-crystal structures by immersing a silica template in aqueous $TiCl_4$ solution. After heating to form the TiO_2 network, the silica

is selectively etched away in aqueous sodium hydroxide.[61] Another approach is to first synthesize TNCs of defined size and shape, which are then deposited as thin films. For example, Manera et al. fabricated thin films via matrix-assisted pulsed-laser evaporation of brookite nanorods in toluene that were immobilized by freezing on various substrates including silicon wafers and alumina.[62] Watté and co-workers reported the fabrication of crystalline thin films by dip-coating microscopy glasses in suspensions of spherical TNCs with diameters of ~5 nm, followed by calcination at various temperatures.[63] For many applications thin films are fabricated from commercial P25 TNCs by screen printing mixtures of ball-milled P25 and organic solvents, followed by calcination.[64,65] However, due to sintering during the heat treatment, the individual TNCs tend to aggregate, which results in the loss of their shape and increase of their size.

In 1991, an important application of the TNC thin films was demonstrated by O'Regan and Grätzel, who invented the dye-sensitized solar cell.[66] In this device, a thin film of TNCs is coated with a dye consisting of a ruthenium complex to extend the light absorption of the system into the visible (vis) spectrum. Upon illumination with sunlight, excited charge carriers are transferred from the dye into the CB of the TiO_2 and enter the circuit of the cell. The oxidized dye is then reduced by a mediator, which is dissolved in the electrolyte and regenerated at the counter electrode. As a result, a cell voltage can be generated corresponding to the difference between the Fermi level of TiO_2 and the electrochemical potential of the electrolyte.[66]

Our group reported the thin film fabrication of nanocomposites using differently shaped TNCs combined with graphene oxide (GO)[2,67] and dicarboxylic acids as cross-linkers[67] to investigate their mechanical properties[67] and the application in humidity sensors.[2]

In the present thesis, TNCs are considered as fundamental building blocks for thin films, with the latter being examined for their potential use as gas sensors and electrostatic actuators. For both applications, the photocatalytic activity induced by UV illumination is particularly important, as it allows for tuning the composition of the thin films and thus improve their performance for specific functions.

4.2 Metal Oxide-Based Chemiresistors

In the following paragraphs, gas sensors are introduced as one application of thin films that was explored within the framework of this thesis. First, a short timeline of conventional thermally activated metal oxide (MOX)-based sensors is presented, focusing on their sensing mechanism. Next, photoexcitation is introduced as a promising alternative activation method for gas sensors based on the same class of materials, concentrating on thin films fabricated from nanostructured TiO_2.

Gas sensors are devices that convert the presence of a chemical compound in their immediate environment into measurable signals. Typically, the signals are manifested as changes in the electrical properties of the sensitive material. The most common electrically transduced chemical sensors are based on capacitive,[68] potentiometric,[69] and resistive changes,[70] the latter of which is often referred to as a chemiresistor. Figure 4.2 displays the schematic of a conventional thermally activated MOX-based chemiresistor, which consists of four primary components: an inert substrate with a heating meander at the bottom surface, and an interdigitated electrode (IDE) structure on the upper surface. The IDE is coated with the sensitive material, whose resistance is continuously monitored to detect changes upon analyte exposure.

The development of chemiresistive gas sensors dates back to the 1960s, when Seiyama et al. demonstrated the use of ZnO films for detecting various organic molecules.[71] Since then, n-type MOX semiconductors such as SnO_2,[72] ZnO,[73] and WO_3,[74] have been widely employed as chemiresistive sensors. Their responses result from the reaction of analytes on the MOX surface (cf. Section 4.2.1). Despite requiring high operating temperatures, MOX-based chemiresistors are widely used in commercial gas sensing applications due to their high sensitivity, straightforward fabrication, and robust performance.

In contrast, composite resistive sensors - comprising conductive particles like carbon black[75] or metal nanoparticles[14] dispersed within an insulating polymer matrix - are often op-

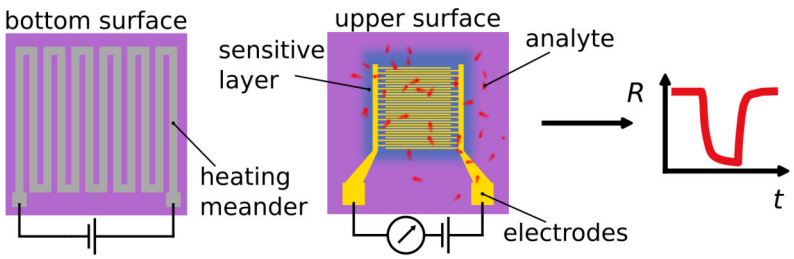

Figure 4.2: Schematic of a thermally activated chemiresistor consisting of the sensitive layer (blue) deposited onto an electrode structure (gold) on the upper surface of an inert substrate (purple). The bottom surface features a metal meander structure as a resistive heater to obtain operating temperatures of 200–450 °C. The resistive response to reducing analyte molecules (red) is depicted in the graph for an n-type MOX-based chemiresistor.

erated at room temperature. Their electrical conductivity heavily depends on the percolation network, where target molecules may induce swelling, which alters the distance between conductive fillers causing changes in the resistance.[76] However, these composites face significant challenges, including higher detection limits, diminished sensitivity at low analyte concentrations, and long-term stability issues arising from network degradation due to particle agglomeration. In comparison, MOX-based chemiresistors are more robust and the investigation on their operation at reduced temperatures will be the focus of this study.

4.2.1 Thermally Activated Vapor Sensing

The detection of a wide variety of analytes, including oxidizing and reducing gases such as NO_x[77] and CO,[78] as well as volatile organic compounds (VOCs)[10] has been reported for thermally activated MOX-based chemiresistors. Typically, these sensors are operated at elevated temperatures between 200–450 °C. At these temperatures, oxygen from the ambient environment reacts on the surface of the MOX, capturing electrons of the n-type semiconductor leading to the formation of dissociated, ionosorbed oxygen species (O^-). This reaction creates an electron-depleted space-charge-layer near the surface, that causes band bending and the formation of a Schottky-type barrier. If granular films are used as the sensitive layer, this barrier impedes the charge transport across the grain boundaries, resulting in a high resistance of the sensor.[79,80] The gas sensing mechanism of thermally activated, n-type, granular MOX-based chemiresistors is schematically depicted in figure 4.3. Upon the exposure of the sensor to gases, the distinct change in the resistance indicates the reducing or oxidizing nature of the analytes. Oxidizing gases can be ionosorbed onto the MOX surface in addition to the ionosorbed oxygen species by cap-

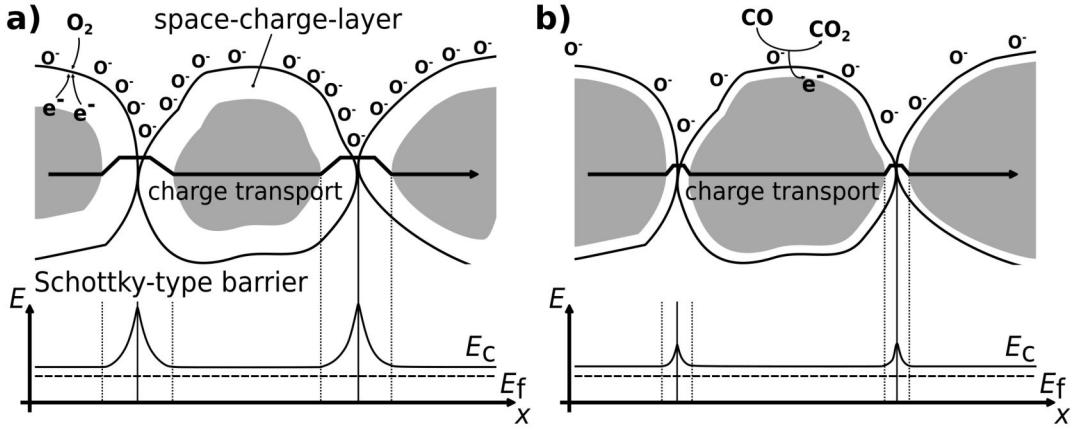

Figure 4.3: Schematic of the vapor sensing mechanism of thermally activated MOX-based chemiresistors, assembling the band diagram and structural model in the a) initial state and b) presence of reducing CO. Inspired by Ref. [79].

turing further electrons from the MOX CB. As a consequence, the Schottky-type barrier height further increases, which causes an increase in resistance. In contrast, reducing gases react with the ionosorbed oxygen species. The oxidation of the reducing analyte releases electrons back into the MOX grains, diminishing the width of the space-charge-layer and lowering the height of the Schottky-type barrier. As a result, the resistance of the sensor decreases (cf. figure 4.3). The conductance G of the sensing material can be described using equation 1,[81]

$$G \propto \exp\left(-\frac{eV_s}{k_B T}\right) \tag{1}$$

in which k_B is the Boltzmann constant, T is the temperature, and eV_s represents the Schottky-type barrier height resulting from the band bending. Consequently, the overall modulation of the electron-depleted space-charge-layer and Schottky-type barrier height governs the sensor's response, making these devices highly sensitive to specific gases via surface chemical reactions and charge transfer processes.[79,80]

As described, both quantities, the height of the Schottky-type barrier and the width of the space-charge-layer, depend on the amount of ionosorbed oxygen, while the latter is further influenced by the Debye length L_D.[82] L_D is a material characteristic, which can be calculated, according to equation 2.[83]

$$L_D = \sqrt{\frac{\epsilon_0 \epsilon k_B T}{e^2 n_d}} \tag{2}$$

Here, ϵ_0 is the vacuum permittivity, k_B is the Boltzmann constant, T is the temperature, e is the elementary charge, and ϵ and n_d denote the material's permittivity and charge carrier concentration, respectively. The charge carrier concentration in n-type MOX semiconductors originates from intrinsic oxygen vacancies that act as donor sites. For these materials, L_D is typically in the range of a few nanometers, e.g., approx. 3 nm for SnO_2 at 250 °C.[83] Since the responses are governed by surface effects, reducing the grain size of MOX materials enhances their sensing performance by increasing the surface-to-volume ratio, as reported for several MOX-based chemiresistors.[82,84] When the grain size decreases to a point where the width of the space-charge layer becomes comparable to the grain radius, the depletion layer extends over the entire grain, resulting in a steep increase in sensor resistance under air. This condition, often called the flat-band regime, occurs when there are no energetic differences between the surface and bulk states.[85] Yamazoe et al. reported a threshold grain size of approx. 10 nm for SnO_2-based chemiresistors exposed to CO and H_2,[82] while Tamaki et al. demonstrated increased sensitivities to NO_2 and NO in WO_3 grains below 25 nm.[84]

The high sensitivity of nanostructured MOX-based chemiresistors enables the detection of analytes at parts-per-million (ppm) and even parts-per-billion (ppb) levels.[86] However,

their requirement for high operating temperatures results in increased power consumption and presents challenges for device miniaturization and integration into compact systems. This high-temperature operation also complicates efforts to tailor chemical selectivity, due to the undifferentiated oxidation of most analyte molecules at the sensor surface, making it difficult to distinguish between target analytes. Moreover, the need for elevated temperatures limits the use of flexible polymer substrates, restricting potential applications in wearable and portable electronics.[87] These drawbacks have motivated ongoing research into alternative approaches using the same class of materials, such as photoactivated MOX-based chemiresistors (cf. section 4.2.2) and the surface sensitization.

Surface sensitization involves modifying the grain surfaces with nanoparticles to enhance the sensor performance, aiming at two distinct mechanisms. Chemical sensitization entails intentionally coating the sensor surface with catalytic materials. For this kind of sensitization, especially small Pt particles or clusters are formed by the reduction of chloroplatinic acids.[88] These catalysts promote selective interactions with target analytes, thereby improving chemical selectivity. Further, the operating temperature required for the detection can be reduced due to the catalytic activation of the analyte molecules and spill-over of analyte species to the MOX surface, where the analyte reacts with the ionosorbed oxygen species.[89] For instance, Saito et al. compared the gas sensing characteristics of porous ZnO ceramics to Pt/ZnO ceramics and found that the oxidation of various hydrocarbons was promoted by the deposition of Pt clusters.[90] These results were interpreted by Kohl, who suggested the adsorption and fragmentation of the hydrocarbons on Pt, followed by the spill-over to the ZnO surface, where the oxidation and consumption of ionosorbed oxygen occurs.[88] Thus, the catalyst does not directly change the sensor's resistance and the chemical sensitization is based on analyte activation.
Electronic sensitization, on the other hand, involves modifying the electronic properties of the MOX-based material by further increasing the electron depleted space-charge-layer. As a result, the change in the resistance of the base material under analyte exposure is even more pronounced.[89] This approach has been demonstrated by modifying SnO_2 sensors with several metals such as Ag, Pd, and Cu.[82] In air, these metals form their respective oxides and cause a highly depleted MOX surface. For example, Yamazoe and co-workers investigated the influence of Pd loading to sensor responses of SnO_2 devices to hydrogen. For decreasing operating temperatures, they found a pronounced increase of the responses.[82] It was suggested, that no mass transfer between the SnO_2 and the PdO occurs and only the electrons are returned to the SnO_2. This return of electrons resulted from the oxidation of hydrogen on the PdO leading to the formation of Pd.[82] Matsushima et al. investigated this electronic interaction between SnO_2 and different metals using x-ray photoelectron spectroscopy (XPS) and reported reversible redox changes of the metal

when exchanging air for hydrogen/air mixtures.[91]

4.2.2 Photoactivated Vapor Sensing

Offering several advantages over conventional thermally activated sensors, photoactivation has emerged as a promising alternative approach for activating MOX-based chemiresistors.[92] Instead of heating the sensitive material to elevated temperatures, light is utilized in these systems to induce electronic excitation within the MOX semiconductor. As a result, reactions of the analyte vapor are triggered on the sensor surface and the power consumption is significantly reduced compared to conventional sensors. With the development of interconnected microdisk light-emitting diodes (μ-LEDs) based on InGaN/GaN quantum wells in 2000 by the research group of Jiang and Lin, a power consumption of 0.2 mW per single μ-LED has been demonstrated,[93] while a commercial thermally activated SnO_2 gas sensor for indoor air quality monitoring (TGS2600, Figaro Engineering Inc.) has a heater power consumption of 210 mW under standard test conditions.[94] Further, the light source-dependent properties of photoactivation allow for improved selectivity.[95] For instance, Liu et al. reported distinct photoactivated sensing behaviors of SnO_2-based sensors toward NO_2 at different light intensities.[96] The development of LEDs that operate in the vis blue and UV wavelength range - needed to overcome the high band gap energies of many MOX semiconductors - has paved the way for technological applications, particularly within Internet of Things (IoT) networks.[97]

As described in section 4.1.2, TiO_2 offers ideal properties for photoactivated gas sensing due to its chemical stability and photocatalytic activity. To increase the sensitive layer's active surface area for analyte sorption, nanostructured materials are preferred.[98] Specifically, the use of monodisperse nanoparticles of well-defined shape allows for the fabrication of thin films with precise control over the morphology and porosity. Thus, the desired sensing properties are enhanced compared to continuous titania layers, as reported for differently shaped TNCs. For instance, Manera et al. fabricated chemiresistors using matrix-assisted pulsed-laser evaporation of brookite nanorods, achieving improved sensitivity to NO_2 under UV illumination.[62] Recently, Wu et al. investigated photoactivated titania nanosheet-based chemiresistors and demonstrated that UV illumination significantly enhanced their sensing performance to 2-propanol vapor compared to measurements in the dark.[99] Šutka and co-workers reported the preparation of titania nanodot-based chemiresistors via a two-step process involving SC and annealing.[100] These sensors showed notably higher responses to various VOCs under UV illumination than in the absence of any light activation. The authors attributed the increased responses to electron accumulation caused by hole scavenging of the VOCs.[100]

Further, commercial P25 TNCs were frequently used for the fabrication of chemiresistors by screen-printing mixtures of ball-milled P25 and organic solvents, followed by calcination. For these systems, enhanced responses under UV illumination to various analytes were demonstrated, including formaldehyde,[64] H_2S,[65] and ethanol.[101] When comparing the responses of photoactivated and thermally activated TiO_2-based chemiresistors, both exhibit similar behavior. For instance, they show a strong decrease in resistance in the presence of different alcohol vapors.[100,102]

Despite these promising features and examples of successful photoactivation of the sensitive material for the detection of various gases, the underlying sensing mechanism of photoactivated MOX-based chemiresistors remains an active area of research. Generally, photons - with energies exceeding the band gap energy of the MOX - that are absorbed by the semiconductor generate electron-hole pairs, which significantly alter its electronic properties. The prevailing explanation for the operating principle of photoactivated MOX-based sensors involves ionosorbed oxygen species which act as reaction centers on the semiconductor's surface. Although ionosorption of oxygen molecules is less probable at room temperature, the presence of ionosorbed oxygen on the surface has been demonstrated under ambient conditions. For instance, Liu et al. reported that SnO_2 films exhibit increased resistance when the atmosphere is changed from nitrogen to oxygen,[96] and Liu et al. showed a similar increase in resistance for TiO_2-based sensors.[103] They attributed this effect to the involvement of O_2^- species.[103] Based on these findings, ionosorbed oxygen species are expected to play a role in photoactivated MOX-based chemiresistors. However, as demonstrated by fading responses to analyte molecules in the dark,[99,100] the mere presence of ionosorbed oxygen species on the sensor's surface is not sufficient to detect analyte molecules. Therefore, the influence of photoactivation and thus the generation and reaction of electrons and holes needs to be considered. It is proposed that photogenerated holes interact with the ionosorbed oxygen, leading to its desorption. As a result, the number of available sorption sites on the surface of the MOX increases while the photogenerated electrons accumulate. This combination of free sorption sites and electron accumulation causes again the ionosorption of oxygen species. This ionosorbed oxygen species are also assumed to be O_2^-, but are expected to bind more weakly to the MOX surface compared to the ionosorbed oxygen species in the dark.[97] Based on this assumption, the ionosorbed oxygen that forms under UV illumination is more reactive compared to ionosorbed oxygen in the dark.[97,104]

Clarifying these mechanisms is essential for the rational design of sensors with enhanced selectivity, reproducibility, and stability. Ongoing research aims to elucidate the interplay between photon energy, surface chemistry, and electronic processes, with the goal to unlock the full potential of photoactivated MOX-based gas sensors.

Based on the understanding of the photoactivated sensing mechanism discussed in literature, the presence of relative humidity (r.h.) may pose a serious challenge for the technological application of photoactivated MOX-based chemiresistors. In contrast to thermally activated sensors, where water molecules tend to be desorbed due to the elevated temperature,[105,106] the operation of photoactivated sensors at room temperature leads to the adsorption of water on the MOX surface. So far, only few studies have examined the influence of r.h. on photoactivated chemiresistive responses. Strikingly, Šutka et al. reported similar responses of titania-based chemiresistors to ethanol with increasing the r.h. in the range of 0–40%.[100] However, MOX-based humidity sensors operated at room temperature exhibit a converse effect as increasing r.h. levels alter the electrical properties by interaction of water on the surface of the sensitive material. For instance, Kannan et al. investigated magnetron sputtered ZnO thin films for humidity sensing, that showed a reversible decrease in resistance to increasing r.h. levels across a r.h. range of 6–84%.[107] Similarly, Faia and co-workers prepared TiO_2 thick films by SC at low speed and reported a decreased resistance with increasing r.h. levels. They further suggested that water desorption occurs with increasing temperature at approx. 60 °C, based on combined resistive and capacitive measurements.[108] It is assumed, that the first layer of water molecules is chemisorbed on the MOX surface while further layers are physisorbed.[107] Gong et al. proposed that the dissociative sorption of water results in an additional n-type doping by the formation of oxygen vacancies,[109] while the physisorbed water can affect the charge transport of the MOX via the Grotthuss mechanism.[108] The latter is assumed to cause a pronounced decrease in resistance with increasing r.h. levels.[107,108,110]

In the context of the present thesis, thin films fabricated from differently shaped TNCs are investigated as photoactivated chemiresistors for the detection of VOCs. To elucidate the underlying sensing mechanism, gas sensing experiments are combined with microgravimetric measurements, and the effect of r.h. is additionally examined.

4.3 Nanomembranes in MEMS/NEMS

In the following paragraphs, the scientific background for the second project will be outlined, in which the application of hybrid nanomembranes as electrostatically driven actuators was investigated. First, the concept of hybrid materials is introduced, focusing on composites based on nanostructured TiO_2 and their mechanical properties. Next, various ways of membrane fabrication are discussed. Finally, the current research development on the electrostatic actuation of freestanding membranes is emphasized.

Conventional MEMS/NEMS are usually fabricated from silicon-based materials using advanced lithography techniques. However, recent research has shifted toward incorporating various nanomaterials to introduce tunable functionalities that extend beyond those of silicon-based devices.[111] In this regard, different approaches include nanoparticle composites of cross-linked noble metal particles[112] or two-dimensional materials such as transition metal dichalcogenides.[111] For example, Jiang et al. described the application of thermo-optical arrays of gold nanoparticle (GNP) composites as infrared (IR) microimagers.[113] These arrays consisted of circular cavities sealed with a polymer/GNP composite nanomembrane with the latter being bulged in response to thermally induced pressure variations. Thus, the IR laser spot position was detected by optically monitoring the deformation of the individual nanomembranes.[113] Many reports also focus on nanomembranes from graphene-based materials as building blocks.[114] For instance, Niklaus and co-workers investigated suspended graphene membranes as piezoresistive accelerometers. In their setup, a silicon proof mass was attached to the movable graphene membrane, which was displaced under acceleration, leading to the generation of a capacitive signal between the electrodes which correlates to the movement.[115]
Several MEMS/NEMS devices require the actuation of their mechanical components and therefore feature a freestanding section of the respective material. In this work, the freestanding layers with typical thicknesses below 100 nm and significantly greater lateral dimensions are referred to as freestanding membranes.

4.3.1 Nanohybrid Materials

Nanohybrid materials, which consist of two or more different components combined at the nanoscale, offer a versatile approach to tailoring material properties for specific applications and overcoming the limitations inherent in individual materials. The strategic integration of various materials can result in enhanced physical strength, improved chemical reactivity, increased catalytic efficiency, and multifunctionality as a result of synergistic interactions between the components.[116] As described in section 4.1.2, TiO_2 is an

excellent candidate for energy-related applications such as photocatalysis, solar energy conversion, and hydrogen production. However, its wide band gap confines light absorption to the UV range. To address this issue the incorporation of dyes,[66] noble metals,[117] or carbon[118] was reported, extending its optical functionalities into the vis spectrum and also promoting charge carrier separation.[118,119] The latter was attributed to increase the responses to various VOCs of thermally activated TiO_2-modified iron oxide nanostructures with rod morphologies compared to those of pure materials.[120]
In addition to the combination of nanostructured TiO_2 with noble metals and other MOX semiconductors, the preparation of nanohybrids combining TiO_2 and graphene-based materials has gained particular attention. Starting with the discovery of graphene in 2004 by Novoselov and co-workers, who prepared the single atom thick layer of sp^2 hybridized carbon arranged in a hexagonal lattice by exfoliation of graphite,[121] its unique properties - such as exceptional mechanical strength and distinctive electronic characteristics - have spurred extensive research. As a result, numerous graphene-based derivatives have been explored.[122] To this end, GO is of particular interest, primarily because it can be produced as colloidal solutions[123] and is therefore suited for liquid based fabrication methods of thin films (cf. section 4.1.3). GO is typically produced by oxidative exfoliation of graphite flakes. The protocol widely used today was initially reported by Hummers and Offeman in 1958.[124] They used potassium permanganate ($KMnO_4$), sulfuric acid (H_2SO_4), and sodium nitrate ($NaNO_3$) to oxidize the graphite, avoiding chlorate oxidants and therefore enhancing the safety. The resulting GO consists of a single atomic layer of carbon atoms arranged in a honeycomb pattern based on the graphitic structure. However, GO contains numerous defects compared to graphene such as oxygen-containing functional groups and vacancies in the carbon lattice that introduce sp^3 hybridization,[125] making GO and its properties fundamentally different from pristine graphene.
The general chemical structure of GO can be described by the Lerf-Klinowski model, comprising aromatic regions, areas of aliphatic carbon rings, and carbon vacancies.[126] This model was established by following the reaction from graphite to GO using ^{13}C nuclear magnetic resonance and Fourier-transform infrared (FTIR) spectroscopy.[126] Figure 4.4 displays the structure of a GO sheet (left side) based on the adapted Lerf-Klinkowski model. The scheme shows hydroxyl and epoxide groups that are attached to the basal plane of the sheet, while the edges are primarily decorated with carboxyl and hydroxyl groups.[127] Due to the presence of oxygen-containing functional groups, the hydrophilic sheets can form stable colloidal solutions in water, facilitating the fabrication of uniform GO thin films.[128] Further, these functional groups offer multiple sorption sites for guest molecules and anchoring groups for the fabrication of hybrid materials.[129] However, as a result of the sp^3 hybridization, the charge carrier transport of the aromatic system is impeded. Thus, GO and its thin films are electrically insulating, which reduces their pos-

sible applications drastically. To restore the electrical conductivity, GO can be reduced by removing polar functional groups and reestablishing the sp^2 hybridized carbon network. The resulting product is commonly referred to as reduced graphene oxide (rGO), that exhibits properties similar to pristine graphene. Various methods such as heat treatment, chemical reduction, or photoreduction can be applied to obtain rGO from GO.[130–132] While chemical reduction is often less feasible due to the lack of control over the spatial location of the reduction,[131] and thermal treatment results in the production of defective sheets,[133] photoreduction displays the most controlled and promising approach for rGO preparation.[134] For photoreduction, the reactions are based on photogenerated charge carriers, that are formed in the semiconducting sp^2 domains upon UV exposure.[132] Koinuma et al. investigated the photoreduction of GO in an oxygen atmosphere, and found that the reduction reactions include surface adsorbed water molecules.[134]
A second approach for the photoreduction uses a composite of GO and a photocatalyst, the latter mediating the reactions by transferring photogenerated charge carriers (cf. section 4.1.2) to the adjacent GO. To this end, the combination of GO with TiO_2 is favorable since the carboxylic acids of the GO strongly bind to the TiO_2 surface, which leads to the formation of robust composites, as demonstrated in recent studies of our group.[2,67] Using DFT calculations, Feldbauer and co-workers reported the strong adsorption of benzoic acid on various anatase crystal facets,[135] and Ayissi et al. found high binding energies for the interaction of titania with carboxylic acid functionalized graphene.[136] A schematic of the TNC-mediated photocatalytic reduction of GO is shown in figure 4.4. The first procedure of reducing GO mediated by a TiO_2 photocatalyst was reported by Williams et al., who dispersed GO into ethanolic colloidal solutions of spherical TNCs (diameters of 2–7 nm). Upon exposing the colloidal mixture to UV light (Xe lamp) a color change from light brown to black indicated the restoration of the aromatic system. They suggest, that

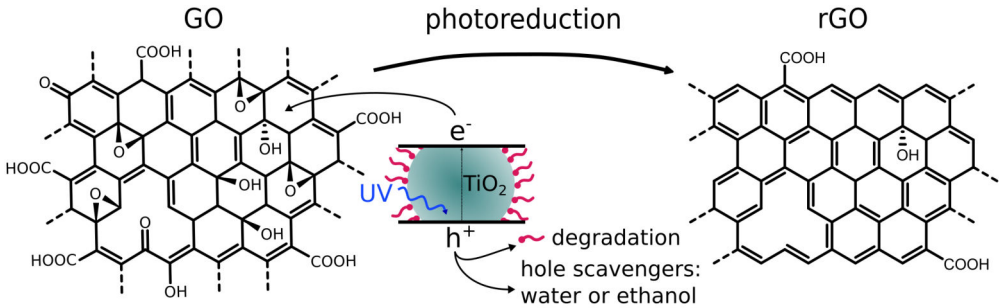

Figure 4.4: Changes in the chemical structure upon the photocatalytic reduction of GO to rGO mediated by a TNC catalyst. The schematic GO structure is based on the adapted Lerf-Klinkowski model, featuring vacancies, epoxide, and hydroxy groups in the basal plane as well as carboxy groups at the edges. Photogenerated electrons cause the reduction of GO and photogenerated holes are scavenged by molecules from the surrounding or cause the degradation of organic ligands. Adapted and reprinted from Bittinger et al., Ref. [2], *Creative Commons CC-BY 4.0* license ©2025 The Authors. ACS Appl. Nano Mater. published by American Chemical Society. (DOI: 10.1021/acsanm.4c06524)

ethanol acts as hole scavenger (cf. figure 4.4), leading to the accumulation of electrons, which are transferred from the TNCs to the GO sheets where they drive the reduction reactions of oxygen-containing functional groups.[137] Further, Bell et al. investigated changes in the chemical structure during the transition from GO to rGO in solution, mediated by a TiO_2 photocatalyst. Using XPS analysis, they reported the removal of oxygen containing functional groups except for the carboxy groups that remain in the rGO.[138] These results are in agreement with a study of our group, in which we also indicated the preferential removal of epoxy and hydroxy groups by XPS and FTIR analysis.[2] Thus, the composites of GO/TiO_2 also remain stable upon the photoreduction due to the presence of carboxylic acids in rGO. Based on the findings in solution, the photocatalytic reduction was extended to hybrid thin films of GO/TiO_2 in ambient conditions. For instance, Li and co-workers reported the large-area reduction of GO/TiO_2 thin films - fabricated from colloidal solutions on various substrates - that was indicated by the increase of the conductivity and darken of the color upon UV illumination.[139] Further, they obtained conductive rGO/TiO_2 patterns with resolutions of 10 μm by illuminating the thin films through photomasks.[139] For thin films in ambient conditions, the photogenerated holes are expected to be scavenged by water molecules (cf. figure 4.4) that are adsorbed on the thin film surface.[139,140]

In our group, the TNC-mediated photocatalytic reduction of GO was studied on GO/TNC hybrid films for the fabrication of humidity sensors.[2] We found increasing conductances for the GO/TNC composites upon the photocatalytic reduction of GO under ambient conditions and suggested the oxidative degradation of the organic ligand of the TNC as a sacrificial hole scavenger (cf. figure 4.4). Further, we demonstrated photocatalytic patterning of the hybrid films and examined how the photocatalytic reduction affected the nanocomposites' resistive humidity sensing performance. For detecting low r.h. levels, rGO-rich hybrid films performed best, while GO-rich hybrid films yielded the best performance at high r.h. levels.[2]

4.3.2 Mechanical Properties of Nanohybrid Films and Membranes

Other important properties that can be adjusted by the composition of hybrid materials are their mechanical characteristics - such as elasticity, strength, and toughness - that are probed under external load. While the toughness is the ability of a material to absorb energy and plastically deform without fracturing, the strength refers to a material's capacity to withstand an applied load without failing or undergoing plastic deformation. The elasticity, characterized by the Young's modulus (E), refers to a material's ability to withstand a deforming force and then recover its original size and shape once the force is no longer

applied. For the adjustment of these properties, the preparation of GO/polymer hybrids is particularly interesting to combine their respective mechanical stability and flexibility. In 2009, Ruoff and co-workers cross-linked GO sheets in colloidal aqueous solution by adding polyallylamine. They fabricated a paper-like material from these components using filtration, and reported an increase in stiffness and strength compared to pure GO films.[141] Further, Tsukruk and co-workers reported the fabrication of robust nanocomposite membranes by incorporating GO sheets in a silk fibroin (SF) matrix by depositing the components alternatingly via SC.[142] They found increasing toughness with increasing GO content, which they attributed to the large number of interactions between the GO and SF, such as the formation of hydrogen bonds and the presence of polar as well as hydrophobic interactions. This synergistic enhancement of the mechanical properties of the composite was based on the amphiphile nature of its components' surface functionalities.[142] In a subsequent study, the same group reported the fabrication of GO/cellulose nanocomposites based on ionic interactions and hydrogen bonding, that exceed the toughness achieved previously for GO/polymer hybrids.[143] Here, they assumed a synergistic effect of the stiff rod shaped cellulose nanocrystals and the flexible GO sheets wrapping the network of cellulose rods.[143]

In general, studying the mechanical properties of nanohybrid thin films, such as elasticity, ultimate tensile strength, maximum elongation, and viscoelastic behavior, are of great interest for potential applications in flexible electronics and MEMS/NEMS. Different analytic procedures have been reported for the mechanical characterization of hybrid thin films, and are schematically shown in figure 4.5. For substrate-supported films, the mechanical characterization is commonly done by using nanoindentation tests.[144] In this technique a nanoindenter or an atomic force microscope is used to record load-displacement curves by pressing a tip of defined geometry into the material and then retracting it (cf. figure 4.5a)). Using suitable models for analyzing these curves allows for the deduction of mechanical properties such as hardness and Young's modulus (E).[145] For instance, Cho et al. prepared GO/SF films with thicknesses of ~520 nm by alternatingly SC the components and reported a Young's modulus of ~22 GPa using nanoindentation tests.[146] However, for precise results, the thickness of the material layer must be substantially greater than the indentation depth to avoid interference from the substrate beneath. Thus, the production of freestanding nanohybrid membranes is beneficial, as it allows for the investigation of material properties without any interference from an underlying substrate. Various fabrication procedures have been applied to obtain freestanding membranes, and will be discussed in the following section 4.3.3. The analytic procedures for mechanical characterization are discussed here.

To this end, microbulge tests are commonly used to non-destructively sample the Young's

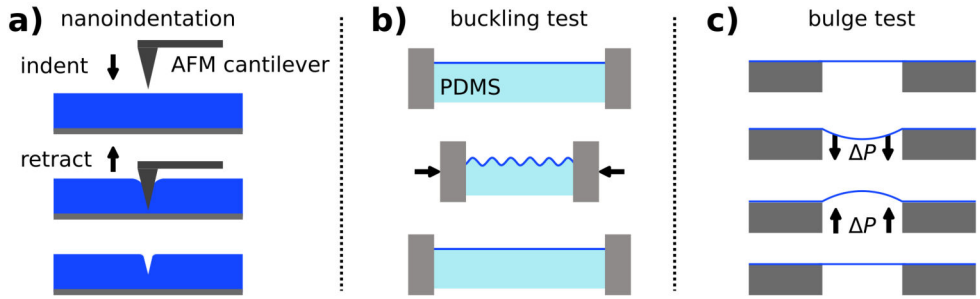

Figure 4.5: Analytic procedures for the mechanical characterization of hybrid film materials. The film to be examined is shown in blue. a) Schematic showing an AFM-based nanoindentation experiment on a substrate-supported thick film. In this setup, the cantilever applies a force to the sample, while both the applied force and the resulting deflection are measured. b) Schematic of a buckling test on a PDMS-supported thin film. Upon the exposure of a compressive strain lateral to the sample, the material stack is buckled. The buckling wavelength is usually measured using optical microscopy or AFM. c) Schematic showing a bulge test on a freestanding membrane. By applying a pressure difference ΔP, the membrane is bulged and the deflection is typically monitored using an AFM, interferometry, or optical microscopy.

modulus, the prestress, or the Poisson ratio - over a large area - of a freestanding membrane deposited onto substrates featuring apertures with circular or square shapes.[147] By applying a pressure on one side of the membrane, the latter is bulged (cf. figure 4.5c)) and the resulting deflection can be determined by different means, e.g., interferometry, optical microscopy, or atomic force microscopy (AFM). In the elastic regime, the Young's modulus can be determined by approximating the bulged membrane as a spherical cap to obtain the biaxial stress and strain (cf. section 6.2.2). For increasing the pressure beyond the elastic regime, the ultimate parameters can be accessed in so-called burst tests. To achieve this burst, the membranes are bulged until they rupture, and from the final set of collected measurement data on intact membranes, the ultimate stress and strain values can be determined. Further, the toughness of the membrane can be calculated at this point, indicating the amount of energy per unit volume which can be absorbed by the material before tearing.

Tsukruk and co-workers conducted bulge tests on GO/SF membranes and reported an increase in the Young's modulus from ~10 GPa to ~145 GPa with increasing fractions of GO, ranging from 0–23.5 vol%.[142] As a further analytic procedure, they employed buckling tests on the GO/SF films deposited onto polydimethylsiloxane (PDMS), a soft substrate with known elastic properties and Poisson ratio.[142] For buckling tests, a compressive strain is applied lateral to the sample, leading to buckled films with a wavelength in the microscale (cf. figure 4.5b)) that can be measured using optical microscopy or AFM. Unlike microbulge tests, this approach does not probe freestanding membranes, however, it investigates a significantly larger area compared to nanoindentation tests. Applying this method, Tsukruk and co-workers reported reduced values of the Young's modulus compared to those obtained from bulge tests for the GO/SF nanocomposites. They attributed

this reduction to local wrinkling of the flexible GO sheets during buckling.[142]

4.3.3 Membrane Fabrication

Graphene is unique in the fabrication of freestanding membranes, as crystalline monolayers can be produced by rubbing graphite directly on thermally oxidized silicon wafers featuring trenches.[148] However, typically the material is first deposited as a substrate-supported thin film and subsequently transferred by various means to substrates featuring cavities or through holes of the desired shape and size. A possible transfer method is based on using sacrificial substrates, as demonstrated by van der Zande at al., who started their process by growing graphene on a copper substrate using chemical vapor deposition.[149] Subsequently, they covered the graphene with a poly(methyl methacrylate) (PMMA) layer, removed the underlying copper substrate via wet etching, exchanged the etchant for deionized (DI) water, and scooped out the graphene/PMMA sample with a structured SiO_2/Si substrate featuring arrays of trenches. Finally, the freestanding graphene membranes were obtained after dissolving the PMMA in dichlorome-thane, followed by critical-point drying.[149] In 2005, Tsukruk and co-workers reported a similar approach by depositing a sacrificial cellulose acetate layer between the silicon substrate and the thin film composed of gold nanoparticles (GNPs) and polyelectrolyte multilayers, that was prepared by SC.[112] The thin films were released from the silicon wafer by dissolving the sacrificial cellulose acetate layer in acetone. Then, these films were transferred to water and lifted with a polished copper holder featuring a central hole of up to 600 μm in diameter.[112] The same group expanded this method to graphene-based hybrid materials including GO/SF[142] and GO/cellulose composites.[143] For the fabrication of the GO/SF hybrid membranes, the sacrificial layer between substrate and film was exchanged for polystyrene which was subsequently dissolved in toluene. The latter was then exchanged for water, and GO/SF membranes were picked from the water air interface.[142] These procedures involve the critical step of scooping the floated membrane from the liquid phase, which limits the level of control due to capillary forces. A promising alternative approach is transfer printing in which viscoelastic stamps are used to detach the substrate-supported thin films from their original substrate and align them on the target substrates. In 2012, Castellanos-Gomez et al. used a PDMS stamp to cleave MoS_2 flakes from a bulk crystal and directly print them onto oxidized silicon substrates with pre-patterned holes.[150] Further, Koppens and co-workers adapted this method and exfoliated graphite to obtain few-layer graphene flakes on a PDMS stamp, transferring the flakes onto arrays of microcavities.[151]

In this thesis, the fabrication of GO-based freestanding membranes was adapted from the transfer process established in our group for membranes of cross-linked GNPs.[152] In this preceding study, the fabrication of electrostatically driven microresonators was demonstrated by transfer printing the membranes onto oxidized silicon wafers featuring an array of microcavities. In addition, the possibility of tuning the prestress of printed GNP membranes was explored by leveraging the pronounced thermal expansion of the PDMS stamp.[152]

4.3.4 Electrostatic Actuation

Actuation is fundamental in MEMS/NEMS devices because it enables the precise control and manipulation of the deflection of freestanding parts such as cantilevers and membranes. This capability is essential for the functionality of various applications, e.g., sensing, switching, or moving parts within a miniaturized platform. Several methods are employed for actuation, including photothermal,[148] magnetic,[153] piezoelectric,[154] and electrostatic approaches.[155] Among these, electrostatic actuation is the most widely used due to its simplicity, low power consumption, and compatibility with microfabrication processes.[155] In the case of a conductive freestanding membrane section that spans the cavity of an oxidized silicon substrate, a capacitor-like arrangement is achieved featuring the membrane and the silicon wafer as the respective electrodes. The application of a voltage between the flexible membrane and fixed electrode generates an attractive force which deflects the membrane toward the bottom of the cavity. While the application of a DC voltage results in a constant deflection of the membrane, AC voltages can induce the oscillation of the membrane. Devices in which the membrane is oscillating are referred to as resonators and can be utilized, e.g., in timing applications.[156] Further, the application of resonators for mass sensing were proposed. Hone and co-workers investigated the resonant responses of monolayer graphene resonators to changes in mass and temperature. They reported that the adsorption of pentacene on the graphene resulted in a decrease of the resonant frequency for high excitation voltages.[157]

In the course of studies on GNPs, our group investigated the applications of composite membranes from cross-linked GNPs in VOC[28,158] and pressure sensing.[159] For graphene-based MEMS with freestanding parts, their application as electrical switches has been particularly demonstrated, e.g., using one-dimensional single-[160] and multi-walled[161] carbon nanotubes that enabled low pull-in potentials. Svensson et al. fabricated a field-effect transistor of suspended graphene gates, that was operated without contacting the surface.[162] As a result, the issue of stiction was mitigated, which can otherwise lead to mechanical failure of electromechanical switches. Further, they demonstrated the appli-

cation of their device geometry for detecting high-frequency motion of the membranes, which is required for mass sensing.[162]

In the present thesis, a nanohybrid material including GO, TNCs, and SF is used to prepare freestanding membranes and the adjustment of their electrical and mechanical properties is demonstrated by tuning their chemical composition. Mediated by the photocatalytic activity of the TNCs, the GO can be reduced introducing electrical conductivity which allows for the electrostatic actuation of the freestanding membranes.

5 Objectives

The goal of this thesis was to investigate functional thin films based on TiO_2 nanocrystals (TNCs) for the application as (I) resistive vapor sensors and (II) electrostatic actuators. For both projects, thin film fabrication, characterization, and the adjustment of the composition were examined. Further, the effect of the composition with regard to the respective application was particularly addressed. Figure 5.1 shows the graphical abstracts for both projects covered in the framework of this thesis. The results will be presented and discussed in the following sections.

(I) The first project focused on the investigation of pure TiO_2 thin films fabricated from differently shaped TNCs and their implementation as chemiresistors for the detection of volatile organic compounds (VOCs). The preparation of TNC-based chemiresistors and their differences in thin film morphology are discussed in section 6.1.2. The main focus of this project, however, was to elucidate the photoactivated sensing mechanism, which is illustrated in section 6.1.3. Herein, chemiresistive measurements were combined with microgravimetric analysis to relate the mass uptake of analyte molecules to changes in the electrical properties of the sensing material. Further, in the experiments summarized in section 6.1.4 the effects of increased operating temperature and relative humidity (r.h.) on the electrical properties of the TNC-based chemiresistors are elaborated. Finally, preliminary results on the surface modification of the sensors by introducing additional nanomaterials and their impact on the chemiresistive properties are discussed in section 6.1.5.

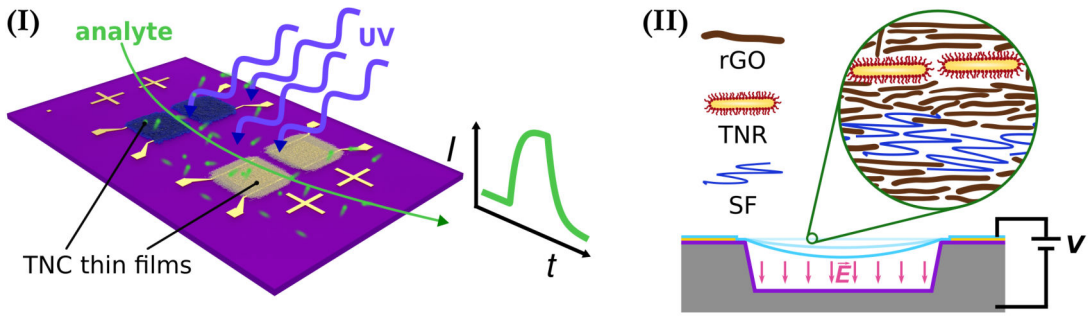

Figure 5.1: Graphical abstract of the two major projects presented in this thesis: (I) photoactivated vapor sensing based on TNC thin films and (II) electrostatic actuation of freestanding hybrid membranes. Subplot (I) was reprinted from Dobschall el al., Ref. [3], *Creative Commons CC-BY 4.0* license ©2025 The Authors. ACS Appl. Nano Mater. published by American Chemical Society. (DOI: 10.1021/acsanm.5c03648) Subplot (II) was adapted and reprinted from Dobschall el al., Ref. [1], *Creative Commons CC-BY 4.0* license ©2025 The Authors. Adv. Electron. Mater. published by Wiley-VCH GmbH. (DOI: 10.1002/aelm.202400602)

(II) In the second project, freestanding membranes of titania nanorods (TNRs), graphene oxide (GO), and silk fibroin (SF) were produced and their use as electrostatically driven actuators was demonstrated. Hybrid thin film design, fabrication, and transfer are discussed in section 6.2.1. Herein, a facile layer-by-layer spin-coating (LbL SC) method is used for film fabrication and the optimization of a stamping process is demonstrated for the transfer of hybrid films onto substrates with apertures or cavities. Further, the influence of the photocatalytic tuning of the membrane composition on structural, electrical, and optical properties is discussed. Mediated by the photocatalytic activity of the TNRs, the reduction of GO to reduced graphene oxide (rGO) as well as a compaction of the membranes is observed. In section 6.2.2, the effect of the photocatalytic tuning on the mechanical properties is studied by AFM microbulge tests. Section 6.2.3 presents the implementation of the tuned hybrid membrane as an electrostatically driven actuator by utilizing its generated conductivity. Finally, section 6.2.4 provides an outlook for the potential application of these hybrid membranes in micro- and nanoelectromechanical systems (MEMS/NEMS).

6 Results and Discussion

6.1 Photoactivated TiO_2 Thin Film Chemiresistors

In this section, key findings are presented that were summarized and published in the journal article: F. Dobschall, S. C. Bittinger, C. T. Tioka, J. Struck, E. Pariente, MH. Delville, H. Schlicke, T. Vossmeyer, "Photoactivated Detection of Volatile Organic Compounds Using Thin Films of Differently Shaped Titania Nanocrystals", *ACS Appl. Nano Mater.* **2025**, 8, 48, 22955-22964.[3]

The application of TiO_2 nanocrystal (TNC) thin films as sensors for the detection of volatile organic compounds (VOCs) is investigated, focusing on how the photoactivation and the shape of the TNCs influences the chemiresistive sensing properties. In the first step thin films were fabricated by depositing dispersions of TNCs of different shapes. Herein, methods to obtain bare TiO_2 surfaces by removing the initial ligands were investigated, and a simple deep-ultraviolet (DUV) treatment based on the photocatalytic activity of the TNCs was established. As a promising alternative to thermal activation, several studies successfully reported photoactivation of titania based chemiresistors and thus reduced the operation temperature while maintaining high sensitivities.[92,95] Even though they showed great potential as a low power alternative to conventional thermally activated MOX-based sensors, the photoactivated sensing mechanism is only vaguely understood. Therefore, this study was set out to examine and analyze the details of the photoactivated sensing mechanism. In this regard, the impact of the excitation wavelength, irradiance, and TNC shape on the electrical and chemiresistive properties of TNC-based sensors was studied. Further, the analyte sorption was assessed by conducting microgravimetric measurements. Since the presence of relative humidity (r.h.) was found to suppress the chemiresistive responses to VOCs, a combination of photoactivation and elevated operating temperatures was explored. Lastly, first attempts on the tunability of the chemiresistive sensing properties by surface modification of the TNC films were carried out.

As part of their respective Master's theses, Christoph Tobias Tioka, M.Sc. (University of Hamburg), collected parts of the results on the surface modification and the influence of the TNC shape,[163] and Tzu-Ying Yu, B.Sc. (University of Hamburg), contributed to the chemiresistive measurements at elevated operating temperatures. The research activities of both students were supervised by the author.

6.1.1 Principle of Vapor Sensing and QCM Measurements

To probe the chemiresistive properties of photoactivated TNC thin films, a commercial gas calibration system (CGM 2000, MCZ Umwelttechnik) equipped with a vapor pressure saturator was used to generate a mixture of VOCs in a carrier gas of defined concentration. A detailed schematic of the flow chart of the commercial gas calibration system is shown in the Experimental section 7.6.
Figure 6.1 provides an overview of the experimental setup including parameters that were varied for gas sensing tests, e.g., the analyte and the excitation wavelength. The set of analytes with a typical concentration range between 25–200 parts-per-million (ppm) consisted of ethanol, 1-propanol, 2-propanol, 1-butanol, toluene, 4-methylpentan-2-one (methyl isobutyl ketone, MIBK), 1-butylamine, and ethyl acetate. Their chemical structures are shown in figure 6.1. The sensors were placed in a test cell with a volume of ~16 mL that featured a quartz window allowing for the illumination of the TNC-based chemiresistors. For this illumination, light-emitting diodes (LEDs) of distinct wavelengths in the ultraviolet (UV), visible (vis) blue, and near-infrared (NIR) were used, that were mounted on an exchangeable aluminum component. Photographs of the test cells are provided in the Experimental section 7.6. By exchanging this aluminum component, the wavelength was set to 278 nm, 401 nm, or 947 nm, and by varying the LEDs' driving current, the irradiance was tuned. A detailed characterization of the LEDs is provided in the Appendix, section A.1.2.
For chemiresistive measurements, the TNC thin films were drop-casted onto interdigitated electrode (IDE) structures. For microgravimetric analysis, quartz crystal microbalances (QCMs) were coated on one side with the TNC thin film via drop-casting. In a typical measurement, the UV LEDs were driven with a current of 150 mA and the chemiresistors were operated at a constant voltage of 10 V. The sensors' current was measured with a sampling frequency of 2 Hz using a Keithley 2601A sourcemeter and the resonant fre-

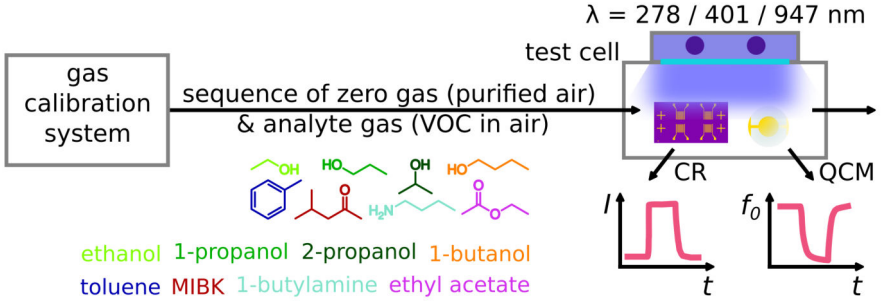

Figure 6.1: Schematic of the experimental setup used for photoactivated chemiresistive and microgravimetric measurements on TNC thin films, which were transiently exposed to different VOCs. Depending on the substrate, the conductivity of the TNC film (CR) or the resonant frequency of the coated QCM were recorded as a function of time. By adjustments of the test cell, the excitation wavelength can be set to 278 nm, 401 nm, and 947 nm.

quency of the QCM was recorded with a sampling frequency of 1 Hz using an Agilent E5100A Network analyzer. The gas calibration system provided purified, dry air as zero gas (ZG) and analyte vapor-enriched air of varying concentration as analyte gas (AG). A constant gas flow of 0.5 L/min through the test cell was generate by a continuous flow controller, and the sensors were exposed transiently to AG followed by ZG, each lasting for 4 min. The measured quantities were the timetraces of the current of the thin film deposited on IDE structures and the timetraces of the resonant frequency of the film-coated QCMs.

The current timetraces were used without a baseline correction and the maximum response current $I_{\max}$ was determined by averaging the current signal during a 10 s interval starting 15 s before the end of each AG exposure.

Further, the chemiresistive sensor signal was expressed as the relative conductance change $\frac{\Delta G}{G_0}$, in which a baseline correction was applied. According to Ohm's law, the conductance G was calculated continuously from the applied voltage V and the measured current I, obtaining a conductance timetrace. This was deployed to calculate the relative conductance change $\frac{\Delta G}{G_0}$, according to equation 3,

$$\frac{\Delta G}{G_0}(t) = \frac{G(t)}{G_0} - 1 \tag{3}$$

where G_0 is the baseline conductance of the sensor during ZG exposure. G_0 was determined for each transient by fitting linear functions to the conductance data for intervals of 30 s before and after the AG exposure. The intervals were taken up to 5 s before the onset of the sensor response to AG exposure, and at the end of the ZG exposure, 5 s before the sensor response to the next AG transient started. Thus, $\frac{\Delta G}{G_0}$ is also referred to as the baseline-corrected relative conductance change of the chemiresistor. The maximum relative conductance change $\left(\frac{\Delta G}{G_0}\right)_{\max}$ was determined by averaging the relative conductance change during a 10 s interval starting 15 s before the end of each AG exposure.

The timetraces of the resonant frequency of the film-coated QCMs were baseline-corrected by fitting linear functions to the frequency data for intervals of 30 s before and after the AG exposure. The intervals were taken up to 5 s before the onset of the sensor response to AG exposure, and at the end of the ZG exposure, 5 s before the sensor response to the next AG transient started. From these baseline-corrected relative resonant frequency timetraces, the frequency shift Δf_s, measured under AG, was analyzed to calculate the change in the mass Δm, using the Sauerbrey equation (cf. equation 4).[164]

$$\Delta m = -\Delta f_s \frac{\sqrt{\mu \rho}}{2 f_{0,f}^2} A_{\mathrm{QCM}} \tag{4}$$

Here, μ is the shear modulus of the quartz (29.47 GPa for the AT-fundamental cut), ρ is the density of the quartz (2.65 g/cm^3), A_{QCM} is the sensitive area of the QCM (0.2827×10^{-4} m^2), and $f_{0,\mathrm{f}}$ is the resonant frequency of the TNC thin film-coated QCM. The latter was determined by averaging the resonant frequency for 100 s while exposing the film-coated QCM to ZG with a constant flow of 0.5 L/min. By averaging the change in the mass Δm during a 10 s interval starting 15 s before the end of each AG exposure, the sorbed analyte mass m_{ads} during the transient AG exposure was calculated. Further, the sorbed amount of substance n_{ads} was calculated by correcting m_{ads} for the molar mass M_{a} of the respective analyte. For comparison, the sorption ability of the blank QCM was investigated in our group for water, 1-propanol, and toluene. While the blank QCM exhibited almost no frequency change to water in the concentration range between 50–10000 ppm, the exposure to toluene and 1-propanol resulted in maximum frequency shifts of approx. 8 Hz at 10000 ppm.[165] Thus, the sorption of analyte molecules on the uncoated side of the QCMs was negligible in the concentration range between 25–200 ppm which was predominantly used in this study.

Further, microgravimetric analysis was used to examine the mass of thin films m_{f} fabricated from differently shaped TNCs. To this end, the resonant frequency of the film-coated QCM was recorded in purified, dry air over a 100 s interval and compared to the resonant frequency of the blank QCM. The TNC thin film mass was then used to calculate the relative mass uptake $\frac{m_{\mathrm{ads}}}{m_{\mathrm{f}}}$ and the relative substance uptake $\frac{n_{\mathrm{ads}}}{m_{\mathrm{f}}}$ under analyte exposure.

For consistency, the chemiresistive properties as well as the mass and substance uptake of TNC thin films were predominantly analyzed by comparing the first 100 ppm transient of the respective measurement of different TNC thin films. The corresponding current timetraces and relative resonant frequency timetraces of all TNC thin films are provided in the Appendix sections A.1.10, A.1.11, A.1.12, A.1.14, A.1.18, and A.1.20.

While all current timetraces were not baseline-corrected, a baseline correction was included for timetraces of the relative conductance change ($\frac{\Delta G}{G_0}$) and the relative resonant frequency (Δf), which is then indicated in the caption of the respective figures as 'baseline-corrected'.

6.1.2 Thin Film Fabrication and Characterization

TiO_2 Nanocrystal Synthesis

For the fabrication of TiO_2 thin films and their application as photoactivated chemiresistors for VOC detection, differently shaped TNCs were either synthesized or purchased. Here, the goal was to understand the photoactivated sensing mechanism, and how shape and size of the particles as well as the structure and morphology of the films affected the chemiresistive properties. Due to the variations in the exposed crystal facets in different TNC shapes,[40,166] that exhibit distinct photocatalytic activity,[53] an impact of the shape on the chemiresistive properties is expected. Further, the distinct surface-to-volume ratios of different sizes and shapes are likely to play a role in the sensing performance.

Titania nanorods (TNRs) and titania nanoplates (TNPs) were synthesized in a non-aqueous, seeded-growth method reported by Gordon et al.[40] with slight modifications.[67] By variation of the chemical environment during the synthesis using different titanium precursors and co-surfactants, the particle shape can be tuned. While oleylamine (OLAM) was chosen as co-surfactant for both shapes, $TiCl_4$ and TiF_4 were used as titanium precursors for obtaining TNRs and TNPs, respectively. Titania nanodots (TNDs) were synthesized following a method developed by the Fraunhofer Center of Applied Nanotechnology, and transferred to the organic phase by exchanging the initial ligand (diethylene glycol, DEG) for OLAM. Details on the syntheses and the phase transfer are provided in the Experimental section 7.1.

Figure 6.2 provides an overview on the characterization of the a) TNRs, b) TNPs, and c) TNDs. Figures 6.2a-c) part i) show representative transmission electron microscopy (TEM) images of the as-synthesized TNCs, that were used for the size determination of the particles. For TNRs, the average length was 41 ± 5 nm and the diameter was 3 ± 1 nm. For TNPs, the average edge length was 22 ± 3 nm with an estimated thickness of ~10 nm. Since the size determination of TNDs was not possible by TEM analysis, the particle diameter was estimated as approx. 7 nm using x-ray diffraction (XRD) analysis. The calculation of the crystallite size using the Scherrer equation is shown in the Appendix, section A.1.3. Figures 6.2a-c) part ii) show the x-ray diffractograms of the respective TNCs, demonstrating differences in the crystal phases. While reflections corresponding to the anatase crystal phase can be observed for the TNPs and TNDs, the TNRs additionally show reflections of the brookite crystal phase. In agreement with previous studies, these additional reflections reveal an anatase/brookite mixed phase.[40,67] Buonsanti et al. investigated the underlying mechanism of the TNR synthesis. They reported the formation of brookite TNRs, which is based on a self-regulated phase transformation of the anatase seeds to brookite upon growth of the rods.[166]

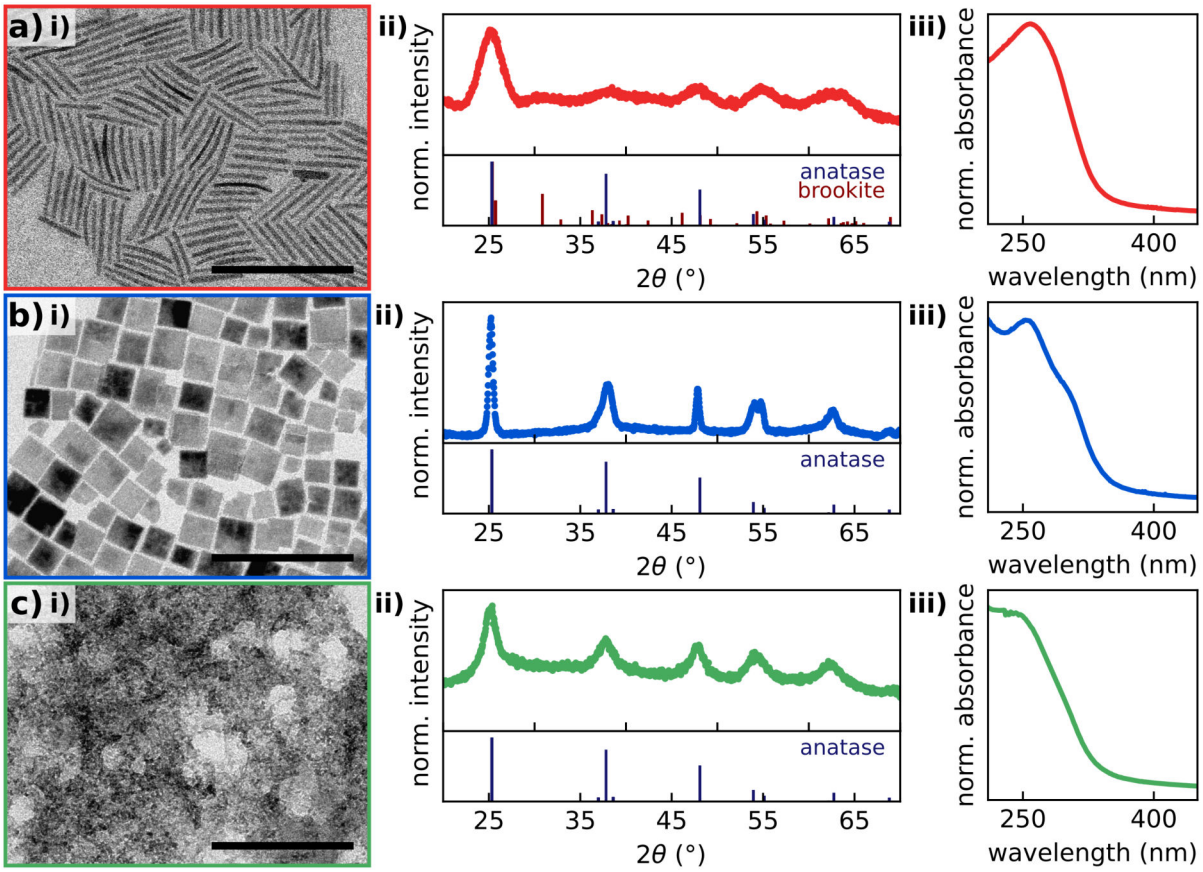

Figure 6.2: Overview of differently shaped TNCs synthesized for thin film fabrication. a) TNRs and b) TNPs were synthesized in organic solution, while c) TNDs were synthesized in aqueous solution and transferred to an organic solution. i) Exemplary TEM images of the TNCs stabilized with OLAM. Scale bars: 100 nm. ii) Normalized x-ray diffractograms with corresponding reference reflections of anatase (TNP and TND) and anatase/brookite (TNR). The XRD reference data were taken from Refs. [167, 168]. iii) Normalized UV-vis absorbance spectra of the respective TNC dispersion in chloroform spin-coated onto quartz glass. Subplots a,b) parts i,ii) were adapted and reprinted from Dobschall el al., Ref. [3], *Creative Commons CC-BY 4.0* license ©2025 The Authors. ACS Appl. Nano Mater. published by American Chemical Society. (DOI: 10.1021/acsanm.5c03648)

The optical properties of thin films spin-coated from dispersions of differently shaped TNCs onto quartz substrates were investigated by UV-vis spectroscopy. Figures 6.2a-c) part iii) display the normalized UV-vis absorbance spectra, showing a pronounced absorbance in the UV region which is related to the band gap energy of the TNCs. For TNRs and TNPs, the maximum absorbance is at ~265 nm, while the TNDs exhibit a shoulder in the same range with a slight increase in absorbance towards smaller wavelengths. Apart from the maximum absorbance, the TNPs show a shoulder at ~305 nm, which originates from the quantized band structure of the TNPs, as reported for organically cross-linked TNP thin films[2,67] and thin films deposited by chemical vapor deposition.[169] The organic content (OC) of the TNRs, TNPs, and TNDs was determined via thermogravimetric analysis (TGA) to be ~39%, ~29%, and ~43%, respectively. Further, TGA was implemented to determine the mass concentration of the TNC stock solutions in chloroform.

Chloroform was also used to dilute the dispersions to the concentrations desired for thin film fabrication. Details on the TGA and corresponding data are provided in the Appendix, section A.1.4.

Titania nanobipyramids (TNBs) were synthesized using a one-step hydrothermal reaction according to the procedure reported by Mino et al.[170] that is based on a method developed by Sugimoto and co-workers.[171] These TNBs were synthesized and provided by Eugénie Pariente and Marie-Hélène Delville (Institut de Chimie de la Matière Condensée de Bordeaux, CNRS). Further, commercial P25 TNCs were purchased from Thermo Fisher Scientific. Figure 6.3 shows an overview on the characterization of bare a) TNBs and b) P25 TNCs. Figures 6.3a,b) part i) show exemplary TEM images of the received TNCs. The TNBs exhibited a square base exposing two pyramids with truncated tips, and had an average height of 44 ± 8 nm with an average edge length of the square base of 30 ± 5 nm. The P25 TNCs did not have a uniform shape. In order to obtain an average size, the projection area of the particles was determined and used to calculate a particle diameter of 25 ± 8 nm, assuming a spherical shape. Figures 6.3a,b) part ii) display the XRD characterization of the TNCs. The diffractogram of TNBs shows the reflections that correspond to the anatase crystal phase. According to the information provided by the manufacturer, the P25 TNCs show additional reflections associated with the rutile crystal

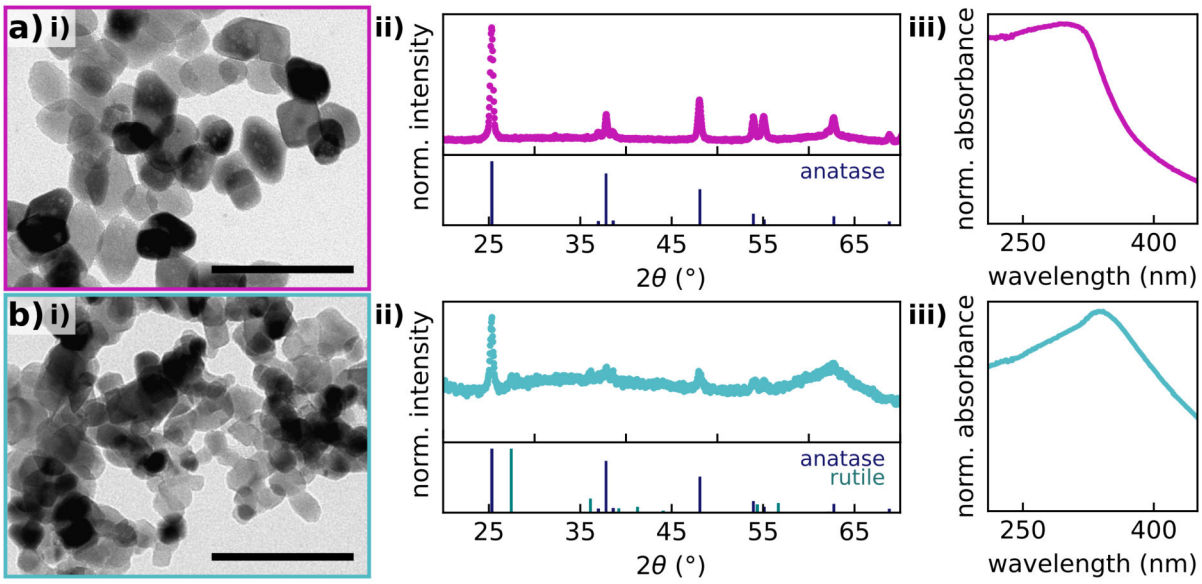

Figure 6.3: Overview of the bare TNCs used for thin film fabrication. a) TNBs were obtained using a hydrothermal synthesis and b) P25 TNCs were purchased. i) Exemplary TEM images of the bare TNCs. Scale bars: 100 nm. ii) Normalized x-ray diffractograms with corresponding reference reflections of anatase (TNB) and anatase/rutile (P25). The XRD reference data were taken from Refs. [167, 172]. iii) Normalized UV-vis absorbance spectra of the respective TNC dispersion in a water/MeOH mixture (1/1, v/v) spin-coated onto quartz glass. Subplot b) parts i,ii) were adapted and reprinted from Dobschall el al., Ref. [3], *Creative Commons CC-BY 4.0* license ©2025 The Authors. ACS Appl. Nano Mater. published by American Chemical Society. (DOI: 10.1021/acsanm.5c03648)

phase, suggesting an anatase/rutile mixed phase. Figures 6.3a,b) part iii) show the normalized UV-vis absorbance spectra of the TNCs deposited onto quartz substrates, exhibiting a maximum absorbance at ~290 nm and ~320 nm for the TNBs and P25 TNCs, respectively. This red-shift compared to the TNRs, TNPs, and TNDs might result from scattering of lager aggregates that form due to the bare nature of the TiO_2 surface for the TNBs and P25 TNCs. The bare surface is demonstrated by TGA of the TNC powders which have a low OC of ~3% for TNBs and ~1% for P25 TNCs (cf. the Appendix, section A.1.4). For thin film fabrication, the particles were dispersed in a water/MeOH mixture (1/1, v/v).

Film Deposition and Surface Treatments

Thin films were deposited by drop-casting the dispersions of OLAM-stabilized TNCs in chloroform or bare TNCs in a water/MeOH mixture on various substrates. For the application as chemiresistors, the accessibility of the TiO_2 surface is crucial, as explained for the thermally activated sensing mechanism of metal oxide (MOX)-based chemiresistors (cf. section 4.2.1).[79] To obtain TNC-based chemiresistors with a large number of sorption sites, various treatments were investigated to remove the organic ligands from the TNC surface. This step was essential especially for the TNRs, TNPs, and TNDs due to the OCs of up to ~43% (w/w). TNR thin films with an OC of ~ 39% were subjected to three different treatments and studied as a model system regarding their changes in the electrical, structural, and chemical properties. The goal was to preserve the shape and size of the individual TNCs within the film to maintain the exposed crystal facets and provide large surfaces without organic ligands. Therefore, treatments implemented under harsh conditions were excluded, e.g., sintering at elevated temperatures, which typically leads to deformation and fusion of particles, often accompanied by phase transition.[173–175]

The first method, a DUV treatment, was based on the exposure of the thin films to DUV illumination. Here, a light source with an emission wavelength of 254 nm was used, that triggers the photocatalytic activity of the TNCs. A detailed description and characterization of the custom-built DUV source is provided in the Appendix, section A.1.1. Photogenerated charge carriers promote the oxidation[176] and degradation of OLAM, as previously reported for TND-based photocatalysts.[177] Plasma treatment was conducted as a second method. Here, the thin films were exposed to air plasma at a slightly reduced pressure of a few mbar. In this context, various studies on films based on metallic nanoparticles[178] and MOX nanoparticles[179] reported effective removal of the stabilizing ligands, while preserving the individual particles inside the films. As a third method, the TNR thin films were purged using an oxygen/ozone mixture at a constant flow rate of approx. 4 L/h. Comparable treatments were reported to remove capping ligands from

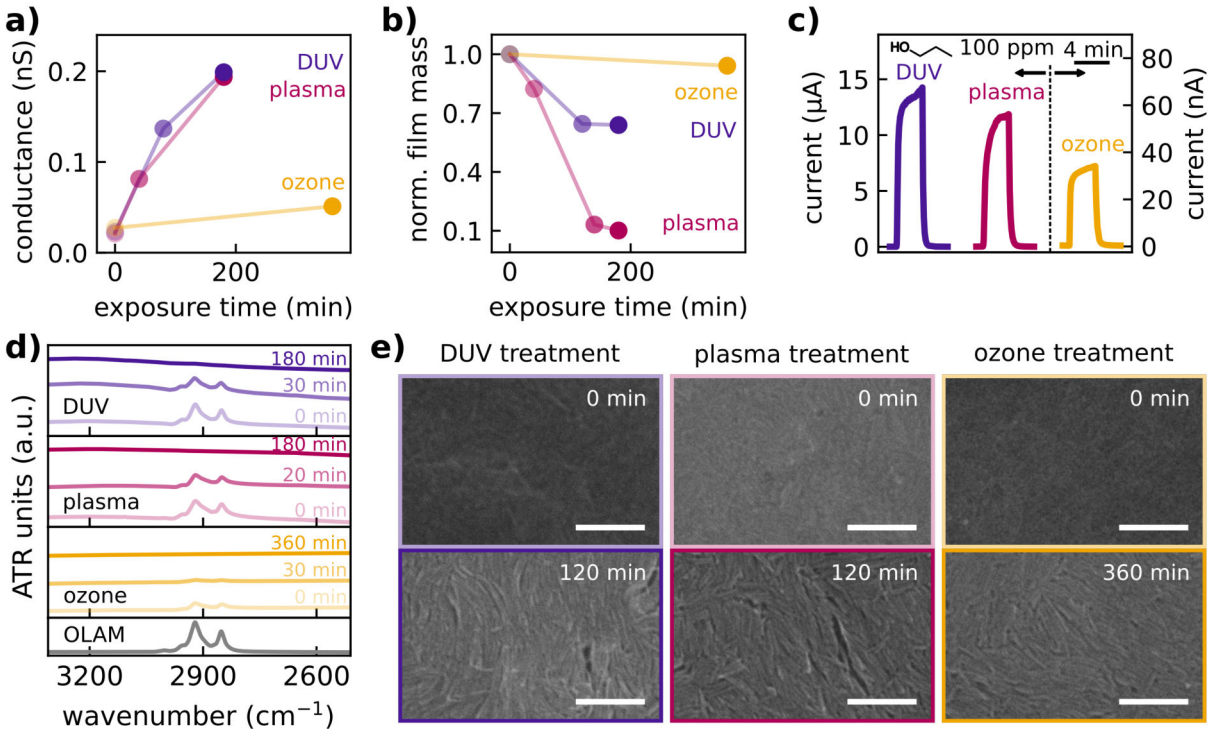

Figure 6.4: Overview of the surface treatments used for the removal of OLAM ligands on TNR thin films. DUV, plasma, and ozone treatments are indicated in purple, red, and yellow color with increasing intensities corresponding to increasing exposure times. a) Evolution of the photoactivated conductances of TNR-based films depending on the surface treatment with increasing exposure times. *IV* curves were recorded in purified, dry air under continuous illumination using UV LEDs (emission wavelength: 278 nm) at an irradiance of ~23 mW/cm^2. b) Evolution of the film mass normalized by the initial mass of TNR-based films with increasing exposure times of different surface treatments. c) Photoactivated current transients of TNR-based sensors treated with DUV illumination, plasma, and ozone for 120 min, 120 min, and 360 min, respectively, to 100 ppm 1-propanol. Purified, dry air was used as carrier gas. During the whole experiment the sensors were continuously illuminated using UV LEDs (emission wavelength: 278 nm) at an irradiance of ~23 mW/cm^2. d) Normalized ATR-FTIR spectra of representative TNR films recorded after increasing exposure times of the surface treatments. The spectrum of OLAM is shown as a reference. e) SEM images of TNR thin films before (top) and after (bottom) surface treatments. Scale bars: 100 nm.

metallic nanoparticles using an oxygen/ozone mixture[180] and by UV-ozone exposure, in which the ozone is generated by DUV illumination in the presence of oxygen.[181]

Figure 6.4 shows the influence of the surface treatments on the electrical, structural, and chemical properties of the TNR thin films. Figure 6.4a) displays the photoactivated conductance evolution for each treatment as a function of the exposure time. The conductance was extracted as the slope of the linear current-voltage (*IV*) curves for voltages swept between ±10 V, while the films were illuminated by UV LEDs (emission wavelength: 278 nm) at an irradiance of ~23 mW/cm^2 (cf. the Appendix, section A.1.2) and kept in an atmosphere of purified, dry air. Initially, the TNR thin films had a poor photoactivated conductance, due to OLAM ligands that separate the individual rods and impede the inter-particle charge transport. As expected, an increase in the conductance of the TNR thin films can be observed with increasing exposure times, suggesting the degradation of

OLAM. While a strong increase of the photoactivated conductance is shown for the DUV and plasma treatment, only a slight increase can be observed for the ozone treatment with even longer exposure times. Based on this reduced increase in conductance for the latter we suggest an incomplete OLAM degradation for the ozone-treated film. Figure 6.4b) shows the evolution of the normalized mass of the TNR films drop-casted on QCM substrates. Here, the low mass reduction of around ~5% after 360 min ozone treatment supports the conductance data and refer to the incomplete removal of organic material of the originally ~39% OC for the TNRs as determined by TGA (cf. the Appendix, section A.1.4). For the DUV treatment, however, the mass reduction of ~36% almost equals the initial OC of ~39%, suggesting a nearly complete OLAM removal after 120 min. Further, the mass remained constant for an additional exposure time of 60 min. The plasma treatment not only caused the highest rate of mass reduction but also exceeded the OC of the TNRs with a mass reduction of ~90%. We assume that besides the OLAM removal, the air plasma detached parts of the TNR thin film from the QCM substrate which led to the degradation of the thin film. This effect is comparable to the cleaning of metal surfaces by plasma treatments.[182,183] For instance, Raiber et al. reported the removal of self-assembled monolayers of alkanethiolates from Au-coated microscopy slides using a hydrogen plasma.[184] In contrast, the increased conductance observed after plasma treatment suggests that the thin film remained intact. This deviation is attributed to the use of different substrates for electrical characterization and microgravimetric analysis.
As an additional characterization method, the chemiresistive responses of the TNR thin films to 1-propanol vapor were studied after exposure times of 120 min DUV, 120 min plasma, and 360 min ozone treatment. Details on the chemiresistive properties and the sensing mechanism of TNC-based chemiresistors will be discussed in section 6.1.3. Briefly, all TNC-based sensors exhibit high selectivity to alcohol vapors presumably based on a partial oxidation reaction. Thus, 1-propanol was chosen as analyte to demonstrate the chemiresistive behavior in preliminary sensing tests. Figure 6.4c) displays the photoactivated current transients of the differently treated TNR films exposed to 100 ppm 1-propanol, that show fast response and recovery times. The recorded timetraces can be found in the Appendix, section A.1.10. Following the trend of the conductance data, pronounced response currents to 1-propanol can be observed for the DUV- and plasma-treated thin films. These response currents are three orders of magnitude higher compared to those of the ozone-treated film. Due to the substantial OLAM degradation during both the DUV and plasma treatment, it is concluded that larger TiO_2 surface areas were unoccupied and thus provided an increased number of available sorption sites for analyte molecules and ionosorbed oxygen species. As a consequence, more analyte molecules can react, leading to higher response currents. For the ozone-treated TNR film, the total number of available sorption sites was reduced, because the OLAM was still attached on the

rods' surface resulting in lower response currents.
To further analyze the chemical composition of the thin films, attenuated total reflectance Fourier-transform infrared (ATR-FTIR) spectroscopy was conducted and the stacked spectra for the treatments with increasing exposure times are shown in figure 6.4d). For these measurements, thicker films were deposited on silicon wafers by repeating the drop-casting to increase the intensity of the signals. Thus, the exposure times cannot be compared to those of single drop-cast thin films used for the other characterization methods. Further, the resolution of ATR-FTIR spectroscopy was low, only allowing for a qualitative analysis of the data. The reference spectrum of OLAM shows pronounced bands around 2900 cm^{-1} corresponding to the CH_2 stretch vibrations of the carbon chain. Initially, these characteristic bands were visible in all TNR films confirming the presence of OLAM as ligand in the deposited material. With increasing exposure times, these bands are reduced and eventually vanish utterly, indicating qualitatively the removal of OLAM upon all treatments. Note, that the characteristic CH_2 bands for the untreated ozone thin film are low in intensity, making it hard to evaluate remaining OLAM after the ozone treatment. Spectra recorded after additional and intermediate exposure times are provided in the Appendix, section A.1.6.
Finally, the structural properties of differently treated thin films were analyzed by scanning electron microscopy (SEM). Therefore, TNRs were deposited on silicon substrates and SEM images of the thin films before and after the respective treatment were compared and are shown in figure 6.4e). Initially, all thin films formed a homogeneous deposit with disordered particles, where individual rods can be distinguished. After the respective treatment, the morphology is preserved. Further, for the DUV and plasma treatment, the contrast of the SEM images increased after the exposure, emphasizing the pronounced OLAM removal compared to the ozone treatment. Additionally, the TNR thin films were analyzed via atomic force microscopy (AFM) after the respective treatment (cf. the Appendix, section A.1.6), showing homogeneous deposits with uniform film thicknesses. The latter were determined at the step edges of intentionally made scratches to be 178 ± 15 nm, 134 ± 13 nm, and 196 ± 20 nm for DUV-, plasma-, and ozone-treated TNR thin films with exposure times of 120 min, 180 min, and 360 min, respectively.
Comparing the influence of the DUV, plasma, and ozone treatment on the electrical, structural, and chemical properties, all treatments show the potential to degrade the OLAM ligand. However, the data on the ozone treatment indicate the incomplete removal, while the plasma treatment not only degraded the OLAM but possibly also damaged the film. Based on these results, we established the DUV treatment with an exposure time of 120 min as the surface cleaning step in the fabrication process of the TNC-based chemiresistors. Here, the degradation of the ligands is mediated by the strong photocat-

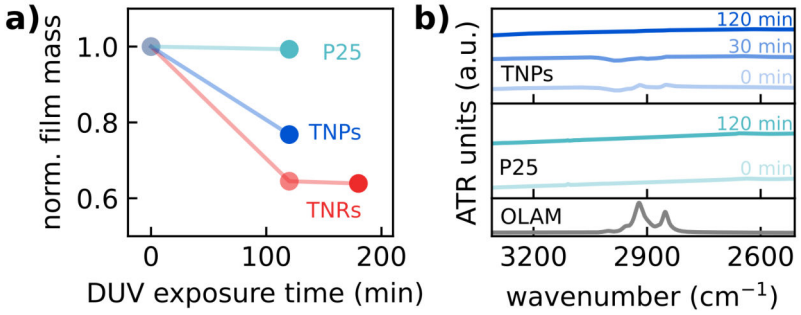

Figure 6.5: Impact of the DUV treatment on the OLAM-stabilized and bare TNCs shown for TNPs (blue) and P25 TNCs (turquoise), respectively. a) Evolution of the film masses (normalized by their initial mass) of TNP and P25 thin films with increasing DUV exposure time. The film mass of the TNR thin film is plotted as a reference. b) Normalized ATR-FTIR spectra of representative TNP and P25 films with increasing DUV exposure time. The spectrum of OLAM is shown as a reference.

alytic activity of the TNCs, which is triggered upon the DUV illumination, as described in section 4.1.2.

Although the hydrothermally synthesized TNBs and commercial P25 TNCs already expose a bare TiO_2 surface, the DUV treatment was applied to all TNC-based chemiresistors to ensure comparability between the different sensors. Figure 6.5a) shows the evolution of the normalized film mass of an OLAM-stabilized TNP and bare P25 thin film, respectively. Further, the TNR thin film data are shown as a reference. Upon the DUV treatment, the mass of the P25 thin film remains almost unaffected (mass reduction below 1%), while the mass of the TNP thin film is reduced by ~23%. These changes are in agreement with the OC of ~29% and ~1%, as obtained by TGA, for TNPs and P25 TNCs, respectively (cf. the Appendix, section A.1.4).

As described in section 4.1.2, the photocatalytic activity of the facets in anatase and brookite TNCs is discussed, without emphasizing the dominance of one of the crystal phases.[40,52–54] Comparing the degradation of OLAM for the thin films based on TNRs and TNPs, it is not possible to provide further information on the differences regarding the photocatalytic activity of the TNPs and TNRs. In a previous study, we investigated the photocatalytic reduction of graphene oxide (GO) in GO/TNR and GO/TNP nanocomposites, in which no clear difference was observed either.[2] For future works, a simplified model system could provide additional insights into the distinct photocatalytic activities of the exposed crystal facets of the respective crystal phase.

Figure 6.5b) displays the stacked ATR-FTIR spectra of the representative films based on TNPs and P25 TNCs with increasing DUV exposure times. As expected, the characteristic CH_2 bands for the OLAM vanish with increasing DUV exposure time for the TNP film, suggesting the OLAM degradation. Further, the untreated P25 film exhibits no characteristic bands due to the bare nature of the P25 TNCs. A detailed ATR-FTIR analysis of all films from differently shaped TNCs exposed to DUV is provided in the Appendix,

section A.1.6. The DUV treatment had no impact on the crystal structure of the TNCs, as verified by XRD analysis on TNRs, TNPs, and P25 TNCs before and after the DUV treatment (cf. the Appendix, section A.1.6). Optical measurements additionally demonstrated no changes in the spectral positions after DUV exposure for times up to 240 min. Here, only a slight reduction in general absorbance after 30 min can be observed, with the latter remaining stable for longer exposure times (cf. the Appendix, section A.1.5).

The impact of the DUV treatment on the structure and morphology of all TNC thin films was studied by SEM analysis of films deposited on silicon wafers. Images before and after the DUV exposure are shown in figure 6.4e) and in the Appendix, section A.1.6. A comparison of the DUV-treated thin films is provided in figure 6.6a), which shows representative SEM images of the thin films based on i) TNRs, ii) TNPs, iii) TNDs, iv) TNBs, and v) P25 TNCs. For all thin films, the individual particles within the film can be distinguished, whereas the morphology varies significantly between the different TNC shapes. For OLAM-stabilized TNCs deposited from dispersions in chloroform (TNRs, TNPs, and TNDs), homogeneous films with disordered particles are formed (cf. figure 6.6a) parts i-iii)). However, the films of bare TNCs deposited from water/MeOH mixtures (TNBs and P25 TNCs) reveal an inhomogeneous morphology featuring larger aggregates and cracks (cf. figure 6.6a) parts iv,v)). Figure 6.6b) shows cross-sectional SEM images of selected TNR, TNP, and P25 thin films in i), ii), and iii), respectively. Confirming the distinct film morphologies, TNR and TNP thin films form a dense layer with a homogeneous thickness, while the P25 deposit is dominated by an island-like structure consisting of aggregates of various sizes.

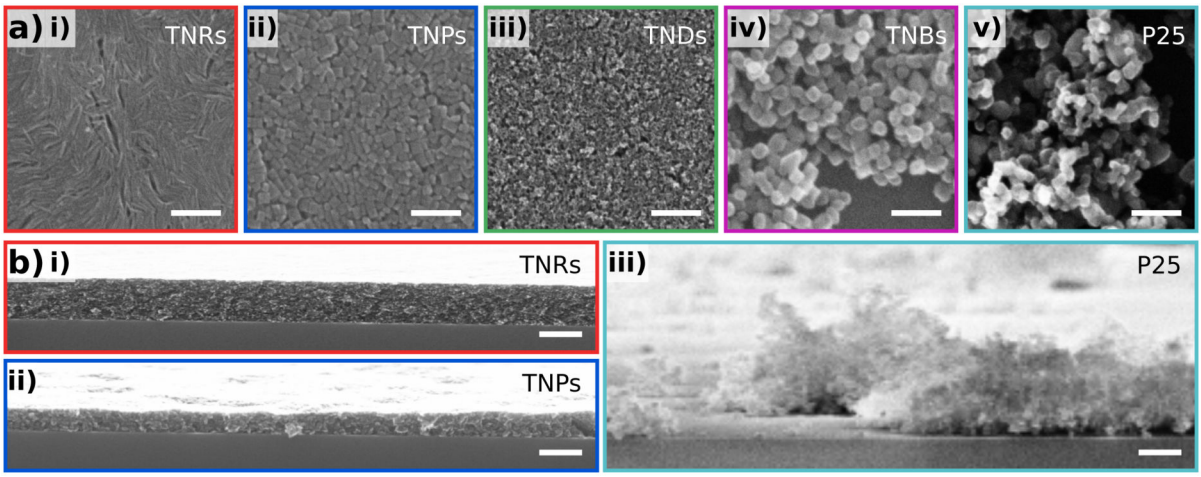

Figure 6.6: a) SEM images of the TNC thin films fabricated from i) TNRs, ii) TNPs, iii) TNDs, iv) TNBs, and v) P25 TNCs after DUV treatment for 120 min. Scale bars: 100 nm. b) Cross-sectional SEM images of i) TNR, ii) TNP, iii) and P25 thin films. Scale bars: 200 nm. Subplot b) was reprinted from Dobschall el al., Ref. [3], *Creative Commons CC-BY 4.0* license ©2025 The Authors. ACS Appl. Nano Mater. published by American Chemical Society. (DOI: 10.1021/acsanm.5c03648)

These findings were further supported by AFM analysis, showing uneven surfaces and aggregate formation for the TNB and P25 thin films compared to TNR, TNP, and TND thin films. Corresponding AFM scans of the TNC-based chemiresistors after 120 min DUV treatment can be found in the Appendix, section A.1.6, demonstrating average film thicknesses of 178 ± 15 nm, 124 ± 13 nm, 158 ± 11 nm, 99 ± 31 nm, and 148 ± 42 nm for TNR, TNP, TND, TNB, and P25 thin films, respectively.

To obtain comparable thicknesses of the films deposited from OLAM-stabilized TNCs and bare TNCs, the P25 thin film fabrication was investigated. By varying the concentration of the P25 dispersion used for thin film fabrication between 2–5 mg/mL, the average thickness of the films was tuned between approx. 130–210 nm. The corresponding AFM data and the influence of the thickness on the chemiresistive characteristics of the chemiresistors to 1-propanol are shown in the Appendix, section A.1.15.

The surface cleaning based on UV illumination was not only investigated using the DUV source, but also for using the UV LEDs of the test cell with an irradiance of ~23 mW/cm^2 at the emission maximum of 278 nm. Detailed data on the microgravimetric analysis of the evolution of the film mass is provided in the Appendix, section A.1.7. Briefly, it was possible to degrade the OLAM using the UV LEDs. The efficiency of the removal using the UV LEDs was significantly reduced compared to the efficiency of the DUV source, which is most likely due to the increased irradiance of ~520 mW/cm^2 and the shorter main emission wavelength of 254 nm of the DUV source. Monitoring the resonant frequency change of the DUV-treated TNR thin film deposited on a QCM substrate, a slight mass reduction upon the UV illumination using the UV LEDs can be observed. This ongoing mass reduction inside the test cell indicated, that the OLAM degradation by the DUV treatment was not complete.

In conclusion, the DUV treatment based on the strong photocatalytic activity of the TNCs was implemented in the fabrication process of all TNC-based chemiresistors and allows for the degradation of the organic ligands without altering the morphology of the thin films and preserving their individual particle character. However, the degradation of OLAM was only shown qualitatively, and the data do not demonstrate the complete removal. For future works, XPS measurements could provide additional insights into the chemical changes on the surface of the TiO_2 with increasing DUV exposure time. Initially, thin films were deposited by drop-casting the particles from dispersions, leading to distinct morphologies of the final TNC-based chemiresistors. For OLAM-stabilized TNC thin films, homogeneous deposits were formed, while samples fabricated from bare TNCs exhibited an island-like structure of larger aggregates and cracks. In order to increase the control over the thickness of resulting TNC films, the deposition via layer-by-layer spin-coating (LbL SC) could be beneficial. First tests on OLAM-stabilized TNCs were

conducted, in which the absorbance of the thin films was measured after each deposition step. In agreement with a previous publication of our group,[67] these data reveal the possibility to establish layered thin films without using further organic cross-linker molecules (cf. the Appendix, section A.1.5).

6.1.3 Sensing Mechanism

To examine the photoactivated sensing mechanism of TNC-based chemiresistors, various parameters were modified, revealing the chemiresistive properties for each condition. Further, the chemiresistive sensing measurements were coupled with microgravimetric analysis to monitor the changes in the mass originating from adsorption of molecules from the surrounding atmosphere. The energy, needed to enable the detection of VOCs, was assessed by tuning the irradiance and wavelength of the photoexcitation. Since ionosorbed oxygen is vital for the sensing mechanism of thermally activated MOX-based chemiresistors, its role in photoactivated chemiresistors was examined. Finally, the particle shape was varied, giving access to the influence of the size of the differently shaped TNCs, including the structure and morphology of the sensitive layer.

Excitation Wavelength

Before focusing on the photoactivated resistive responses to analytes, the charge transport in the TNC thin films and the influence of UV illumination on the latter was investigated. Thin films based on TNRs and TNPs were placed in the test cell (cf. section 7.6). The latter was equipped with two UV LEDs, and continuously purged with purified, dry air. The emission spectrum of the UV LEDs as well as the normalized absorbance spectra of the TNR and TNP thin films are displayed in figure 6.7a). These spectra show the main emission peak at 278 nm and the absorbance maximum of the films at ~265 nm resulting from the band gap of the TNCs. A constant voltage of 10 V was applied to the TNC

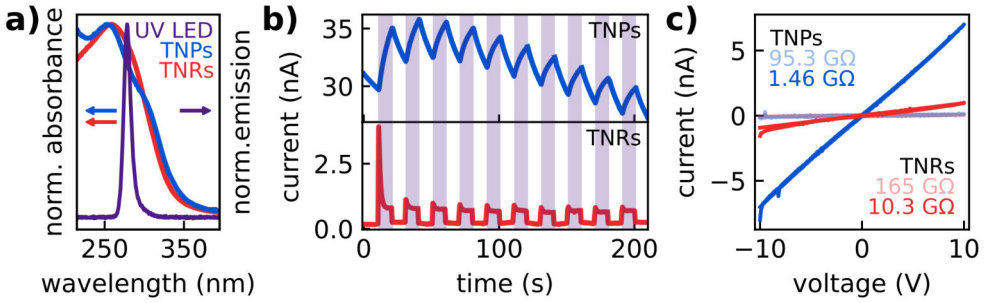

Figure 6.7: Photoactivation of TNP and TNR thin films by illumination using UV LEDs at ~23 mW/cm^2 irradiance. a) Normalized emission spectrum of the UV LEDs with the maximum at 278 nm and normalized UV-vis absorbance spectra of TNP (blue) and TNR (red) thin films, respectively. b) Current timetraces of the TNP and TNR thin films with an applied bias of 10 V recorded while transiently switching the UV LED on and off. White and purple backgrounds indicate the UV LED to be switched off and on, respectively. c) *IV* curves of the TNP and TNR thin films in the dark and under UV illumination. Resistances were obtained from the slopes of linear fits as 95.3 GΩ and 165 GΩ in the dark and 1.46 GΩ and 10.3 GΩ under UV illumination for TNP and TNR thin films, respectively. Subplots a,b) were reprinted from Dobschall el al., Ref. [3], *Creative Commons CC-BY 4.0* license ©2025 The Authors. ACS Appl. Nano Mater. published by American Chemical Society. (DOI: 10.1021/acsanm.5c03648)

thin films and the resulting current was recorded while the UV LEDs were transiently switched between irradiances of 0 mW/cm^2 and ~23 mW/cm^2, each applied for 10 s. The TNC thin films were deposited on IDE structures of 48 finger pairs with a gap distance of 10 μm between the electrodes (cf. the Experimental section 7.3). Figure 6.7b) shows the corresponding current timetraces of the TNP and TNR thin films, demonstrating higher currents when the films were exposed to UV illumination (purple background). In the dark (UV LEDs switched off, white background), the current was low, as expected for a wide band gap semiconductor since the thermal activation of charge carriers at room temperature is negligible. Further, electrons of the intrinsic n-type TiO_2 are bound by the ionosorption of oxygen (O_2^-) species at the TNC's surface, leading to the formation of a Schottky-type potential barrier, which impedes the charge transport between individual particles.[185] The involvement of ionosorbed oxygen in the dark will be discussed in paragraph Operating Atmosphere, and was reported by Manera et al. on brookite TNR thin films.[62] When the UV illumination is switched on, electrons and holes are generated and separated by the electric field resulting from the Schottky-type barrier. While photogenerated holes are dragged to the surface and cause the desorption of oxygen, the electrons accumulate inside the particle causing a sharp increase of the photocurrent, as observed by the spikes for the TNR film in figure 6.7b) when switching on the UV LEDs. However, the combination of free sorption sites and electron excess results again in the ionosorption of oxygen and the reduction of the photocurrent. Eventually, an equilibrium between these two competing reactions is reached, defining the increased, photoactivated conductance.[101] For the TNP thin film, no steady-state was reached within the 10 s interval of illumination, while for the TNR thin film a steady-state was reached after ~5 s exhibiting low photocurrents of ~1 nA. When switching off the UV illumination, the photogenerated charge carriers are consumed by the formation of ionosorbed oxygen and the system returns to its initial state of low conductance.[101,185] For the TNP thin film, this process was again slow, causing a triangular shape of the current timetrace. On the contrary, the recovery for the TNR film was almost instantaneous, leading to a rectangular shape of the current transients. Further, the resistances in the dark and under UV illumination were extracted as the slope of the respective *IV* curve with the latter being displayed in figure 6.7c), showing ohmic behavior for both TNC thin films. The voltage was swept between ±10 V, while the films were kept in an atmosphere of purified, dry air, resulting in photoactivated resistances of 1.46 GΩ and 10.3 GΩ for TNP and TNR thin films, respectively. Considering the geometry of the IDE structure (cf. the Experimental section 7.3) and the respective film thickness, the photoactivated resistivity of the films was calculated as 0.3 GΩ cm for the TNPs and 2.6 GΩ cm for the TNRs.

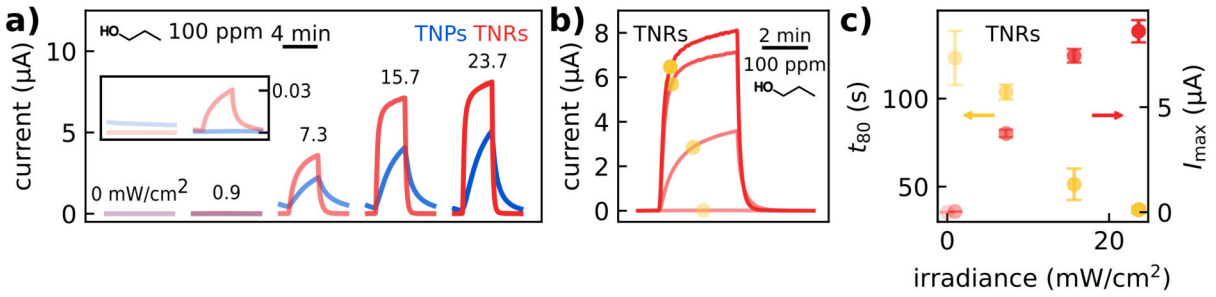

Figure 6.8: Overview of the photoactivated chemiresistive properties of TNR- and TNP-based sensors to 100 ppm 1-propanol. a) Current transients of TNR- (red) and TNP-based (blue) sensors as a function of the irradiance. The color intensity corresponds to the irradiance of the UV LEDs tuned between 0 mW/cm^2 and 23.7 mW/cm^2. b) Stacked current transients of the TNR-based sensor with corresponding response times (t_{80}) indicated as yellow dots. c) Scatter plots of the maximum response currents I_{max} and the response times (t_{80}) vs. the irradiance. The t_{80} time in the dark was excluded in the plot, as there was no response current. The error bars represent the standard deviations of two measurements using the same sensor. Adapted and reprinted from Dobschall el al., Ref. [3], *Creative Commons CC-BY 4.0* license ©2025 The Authors. ACS Appl. Nano Mater. published by American Chemical Society. (DOI: 10.1021/acsanm.5c03648)

To probe the influence of UV illumination on the chemiresistive responses of the TNR- and TNP-based sensors, the thin films were placed in the test cell (~16 mL volume) and exposed transiently to 1-propanol at varying concentrations between 25–200 parts-per-million (ppm) as AG and purified, dry air as ZG. Each transient exposure lasted 4 min, while the chemiresistors were illuminated at distinct irradiances between 0–23.7 mW/cm^2. The latter was tuned by adjusting the driving current of the LEDs (cf. the Apppendix, section A.1.2). Figure 6.8a) shows the current transients of the TNR- and TNP-based chemiresistors exposed to 100 ppm 1-propanol vapor at varying irradiances. All time-traces are provided in the Appendix, section A.1.11. In the dark, no change in the response current to 1-propanol is visible for either chemiresistor. However, the response current can already be switched on with a low irradiance of 0.9 mW/cm^2, and the maximum response current I_{max} increases further with increasing irradiance for both chemiresistors. In comparison, shorter response and recovery times as well as higher response amplitudes can be observed for the TNR-based chemiresistor than for the TNP-based chemiresistor. These distinct transient shapes will be discussed in detail in the paragraph Film Morphology and Particle Shape. Figure 6.8b) shows the stacked current transients of the TNR-based chemiresistor with corresponding response times t_{80}, indicated as yellow dots for the individual transients. The t_{80} response time is defined as the time needed to reach 80% of the maximum response current of the transient signal. To further visualize the improved response characteristics with increasing irradiance, figure 6.8c) displays the scatter plot of the maximum response current I_{max} and the t_{80} time as a function of the irradiance, demonstrating accelerated kinetics and increased current responses with increasing irradiance.

In a previous study, our group demonstrated that adjusting and analyzing the transient response kinetics of chemiresistors can offer additional features to enhance the selective detection of analytes.[186] In that study, the response kinetics of organically cross-linked gold nanoparticle (GNP) films were adjusted by variation of the cross-linker (used to cross-link the GNPs), GNP size, and UV-induced modification of the sensitive layer. These distinct GNP transducers were then used to fabricate a sensor array, that was employed for analyte recognition.[186]

Beyond adjusting the photoactivation solely by varying the irradiance, the impact of tuning the excitation wavelength on the chemiresistive responses was studied. By exchanging the LED holder of the test cell, the excitation was adjusted to UV, vis blue, and NIR light with main emission wavelengths of 278 nm, 401 nm, and 947 nm, respectively. Figure 6.9a) shows the normalized emission spectra of the LEDs as well as UV-vis-NIR absorbance spectra of concentrated TNR and TNP dispersions in chloroform. As mentioned above, the emission wavelength of the UV LED matches the absorbance of the TNC particles, while the wavelength of the blue LED is located at slightly higher wavelengths compared to the maximum absorbance of the TNCs. For the TNPs, an increasing absorbance with increasing wavelength is observed starting at ~600 nm. This feature arises from oxygen vacancies that are formed during the synthesis when using TiF_4 as a precursor due to the presence of fluoride ions on the {001} facets.[40] These vacancies cause an additional n-type doping of the material, resulting in transitions that can be excited by vis red and NIR light.[40] Thus, the absorbance of the TNPs and the emission of the NIR LED overlap, while no low-energy transitions can be observed for the TNRs. Figure 6.9b) shows the current transients of the TNR- and TNP-based chemiresistors photoactivated using the LEDs with distinct emission wavelengths and exposed to 100 ppm 1-propanol vapor. Here, no changes in the photocurrent of the TNR- and TNP-based sensors upon analyte

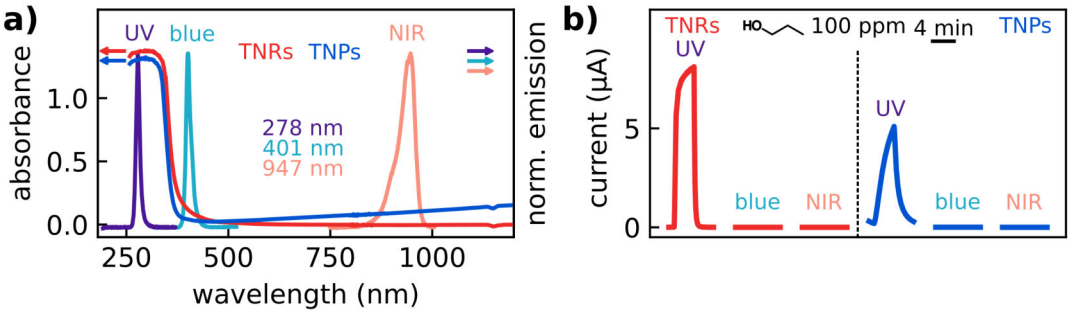

Figure 6.9: a) UV-vis-NIR absorbance spectra of TNPs (blue) and TNRs (red), respectively, and normalized emission spectra of the UV (purple), blue (turquoise), and NIR (coral) LEDs with main emission peaks at wavelengths of 278 nm, 401 nm, and 947 nm, respectively. b) Current transients of TNR- (red) and TNP-based (blue) chemiresistors to 100 ppm 1-propanol under the illumination of the different LEDs. The irradiances were ~23 mW/cm^2, ~195 mW/cm^2, and ~710 mW/cm^2 for UV, vis blue, and NIR LED at their corresponding main emission, respectively.

exposure can be observed for using blue or NIR light for photoactivation. The timetraces are provided in the Appendix, section A.1.11.
These data suggest, that the photoactivated gas sensing in TNC-based chemiresistors is only enabled for UV light with an energy that equals or exceeds the energy of the maximum absorbance of the TNCs, allowing for the excitation of electrons across the band gap. If this condition is met, the irradiance of the UV light can be used to tune the degree of photoactivation and therefore tailor the chemiresistive properties of the TNC-based chemiresistors. Further, if the irradiance-dependent chemiresistive responses depend on the type of analyte, the application in virtual sensor arrays shows a possibility to make use of this feature. Adjusting the irradiance of the illumination of a single TNC-based chemiresistor, could then allow for analyte discrimination. However, further measurements on varying analytes need to be conducted to account for such an application.

Operating Atmosphere

As discussed in section 4.2.1, the adsorption of oxygen molecules and the formation of ionosorbed oxygen species plays a crucial role in the sensing mechanism of thermally activated MOX-based chemiresistors. Based on the reaction of these ionosorbed oxygen species with analyte molecules, the resistance of the material changes, resulting in the sensor response.[79,80] Further, it is assumed that ionosorbed oxygen species are involved in the sensing mechanism of photoactivated MOX-based sensors,[97,104] as described in section 4.2.2.
To examine the impact of ionosorbed oxygen at the TNC's surface on the photoactivated sensing mechanism, the atmosphere inside the test cell was switched between pure nitrogen as ZG and oxygen-enriched nitrogen as AG. Therefore, two commercial gas calibration systems were combined, and one was fed with pure nitrogen, while the other was fed with purified, dry air. By mixing these gases in a 1/1 (v/v) ratio, the AG of oxygen-enriched nitrogen was generated with a concentration of ~10 vol% oxygen. TNR thin films deposited on IDE and QCM substrates were transiently exposed to AG and ZG, each for 4 min, with a constant flow rate of 0.5 L/min. During the exposure, the samples were either kept in the dark or continuously illuminated using the UV LEDs at an irradiance of ~23 mW/cm^2. A commercial sensor (BME680, Bosch Sensortec) was read out in parallel to monitor the operating atmosphere. These data are provided in the Appendix, section A.1.9, whereby the the presence of r.h. during the measurements is excluded.
Figure 6.10a) shows the data of the microgravimetric measurements. Here, figure 6.10a) part i) displays the relative resonant frequency timetraces of the QCM coated with a TNR thin film in the dark and under UV illumination. For both conditions, a fast and repro-

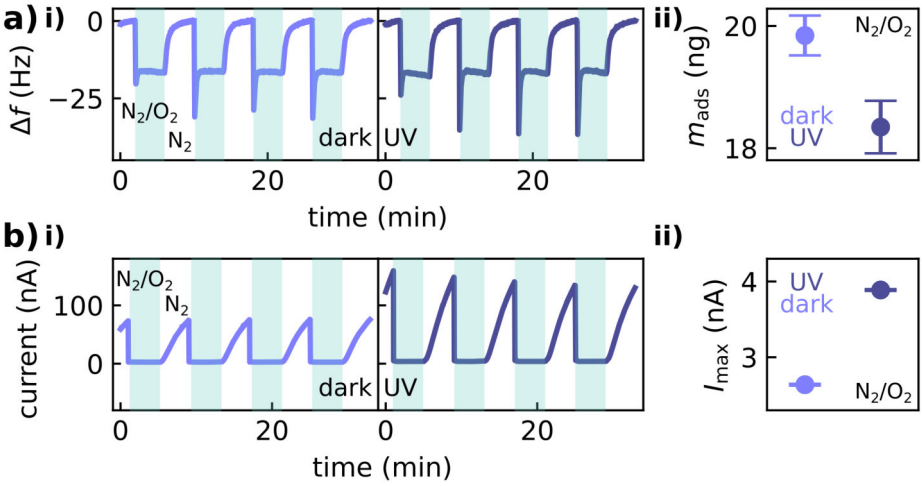

Figure 6.10: Influence of oxygen in the operating atmosphere of the TNC-based chemiresistors shown for TNR thin films in the dark and under UV illumination. Thin films were alternately exposed to nitrogen and a nitrogen/air mixture (1/1, v/v), indicated in the timetrace plot as white and green background, respectively. a) Microgravimetric measurement of a TNR thin film deposited on a QCM substrate. i) Timetraces of the relative resonant frequency recorded in the dark (left) and under UV illumination using the UV LEDs (right). ii) Scatter plot of the mass which was adsorbed in the film (m_{ads}) when exposed to the nitrogen/air mixture and averaged over the transient exposures in the dark and under UV illumination, respectively. b) Chemiresistive measurements of the TNR-based sensor deposited on an IDE structure. i) Current timetraces recorded in the dark (left) and under UV illumination (right). ii) Scatter plot of the maximum response currents (I_{max}) of the TNR-based chemiresistor exposed to the nitrogen/air mixture and averaged over the transients in the dark and under UV illumination, respectively.

ducible decrease of the resonance frequency can be observed when switching the atmosphere to AG (green background). This frequency change demonstrates the increase of the film mass, which is attributed to oxygen adsorption. We assume that the spikes result from pressure fluctuations caused by slightly out-of-phase switching, which arises from the combination of the two gas calibration systems. When switching back to pure nitrogen (ZG, white background), the frequency shift recovers back to zero. Here, the desorption kinetics of oxygen from the TiO_2 surface seem to be slower compared to the adsorption. The mass of ionosorbed oxygen m_{ads} was calculated as described in section 6.1.1, and is shown in figure 6.10a) part ii). Here, the mass of ionosorbed oxygen was averaged over four transients, obtaining values of 19.8 ng in the dark and 18.3 ng under UV illumination. To evaluate the plausibility of these sorbed masses, they were compared to the surface area of the TNRs to assess the surface coverage on the TNRs. First, the number of oxygen molecules per particle was calculated by considering the total mass of the TNR film obtained from QCM measurements (17.5 µg), the volume of a single particle calculated from the TEM data (~230 nm^3), and the density of brookite TiO_2 (4.13 g/cm^3).[187] Next, the projection area of the oxygen molecule in the direction of the O-O axis was assessed, assuming the van der Waals radius of 152 pm for the oxygen atom[188] and the covalent bond radius of 66 pm for the oxygen molecule.[189] Finally, the oxygen surface coverage of an individual TNR was determined by comparing the surface of a rod with the

area required by the accumulated projections of oxygen molecules per rod. In the dark, the surface coverage was 1.8% and 1.6% under UV illumination, revealing only minor differences.

Figure 6.10b) shows the electrical responses of the TNR-based chemiresistors when switching the atmosphere between nitrogen and nitrogen/air mixtures in the dark and under UV illumination. Figure 6.10b) part i) displays the current timetraces with ZG indicated as white background and AG indicated as green background. Here, a significant decrease in current upon the exposure to AG can be observed regardless of the photoactivation. We assume that due to the adsorption of oxygen, as indicated by the microgravimetric measurements, electrons of the n-type TiO_2 are consumed leading to the instant and reproducible decrease of the current. When switching back to pure nitrogen, the current slowly increases again. Under UV illumination, higher currents are reached due to photogenerated charge carriers. Note, that the recovery of the electrical properties is slower compared to the desorption of oxygen as visualized by microgravimetric analysis, suggesting a nonlinear correlation of the response current and the amount of sorbed oxygen. In figure 6.10b) part ii) the maximum response currents I_{max} in oxygen-enriched nitrogen atmosphere in the dark and under UV illumination are compared, revealing lower I_{max} in the dark. These data also align with the ionosorbed oxygen masses, suggesting that the current is inversely proportional to the amount of ionosorbed oxygen at the TNR's surface.

Ultimately, these results indicate the adsorption of oxygen under UV illumination and in the dark. However, the investigations on the influence of the irradiance showed no response current in the dark when the sensor was exposed to 1-propanol vapor (cf. figure 6.8). Thus, the pure presence of ionosorbed oxygen is not sufficient to enable the chemiresistive detection of 1-propanol. These responses were only observed under UV illumination, suggesting higher reactivity due to an activated bond of the ionosorbed oxygen species by photoexcitation. Tian et al. suggested that photoactivated SnO_2-based chemiresistors at room temperature are based on this increased reactivity by UV illumination,[104] which was further discussed in a recent review on light activated gas sensing by Suh et al.[97] Similar to the temperature dependent sorption of oxygen species for thermally activated MOX-based chemiresistors, another explanation could be the influence of UV illumination on the ionosorbed oxygen species. Following this assumption, in the dark mainly O_2^- is formed, whereas under UV illumination the more reactive O^- is formed. To test this assumption, further examination needs to be done, including transients of varying oxygen concentrations to asses if the sorption of oxygen molecules follow a first or second order Langmuir isotherm - the latter indicating the dissociation of oxygen on the surface - and if the sorption behavior varies in the dark and under UV illumination.

Film Morphology and Particle Shape

The chemiresistive responses of the TNC thin films fabricated from differently shaped particles according to the procedure described in section 6.1.2 were investigated and combined with microgravimetric analysis. Here, the selectivity was examined by exposing the TNC-based sensors to a variety of analytes. Further, the influence of the UV illumination on the adsorption of analyte molecules was investigated.

First, the TNC-based sensors fabricated from TNRs and TNPs were compared. These TNCs were synthesized following the procedure reported by Gordon et al.[40] using different precursors to obtain the rod and plate shape (cf. section 6.1.2). Figure 6.11 shows an overview of the sensing properties of the a) TNR- and b) TNP-based chemiresistor, respectively. The sensors were placed into the test cell, in which they were continuously illuminated using the UV LEDs (emission wavelength: 278 nm) at an irradiance of ~23 mW/cm^2 and exposed to transients (4 min) of various analytes. The analytes were

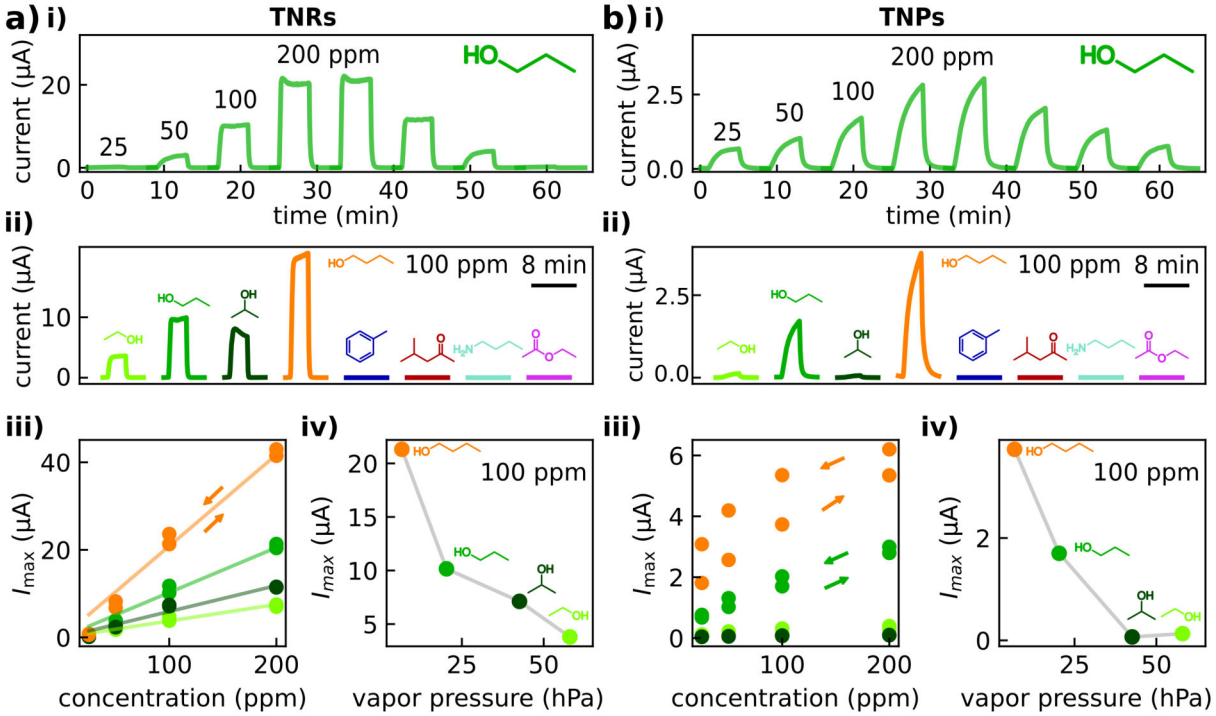

Figure 6.11: Photoactivated chemiresistive responses of a) TNR- and b) TNP-based sensors under UV illumination using UV LEDs (emission wavelength: 278 nm) at an irradiance of ~23 mW/cm^2 to various VOCs. i) Exemplary current timetraces of a typical chemiresistive measurement with vapor concentrations of 25, 50, 100, 200, 200, 100, 50, and 25 ppm, here shown for 1-propanol. ii) Current transients of the TNR- and TNP-based chemiresistors to the first exposure of 100 ppm ethanol, 1-propanol, 2-propanol, 1-butanol, toluene, MIBK, 1-butylamine, and ethyl acetate. iii) Current response isotherms in the concentration range between 25–200 ppm for the tested alcohols. iv) Scatter plot of the maximum response currents (I_{max}) as a function of the alcohols' vapor pressure. Reprinted from Dobschall el al., Ref. [3], *Creative Commons CC-BY 4.0* license ©2025 The Authors. ACS Appl. Nano Mater. published by American Chemical Society. (DOI: 10.1021/acsanm.5c03648)

ethanol, 1-propanol, 2-propanol, 1-butanol, toluene, MIBK, 1-butylamine, and ethyl acetate in the concentration range between 25–200 ppm. Exemplary current timetraces are displayed in figures 6.11a,b) part i), in which the increasing response currents with increasing concentration can be observed for both TNC-based chemiresistors. This increase in conductance is expected, as reported in TiO_2-based sensors for both thermal activation[190] and photoactivation.[100] The current timetraces of both films exposed to all analytes can be found in the Appendix, section A.1.12. As already indicated for the investigation on the irradiance, the distinct transient shapes of the TNR- and TNP-based chemiresistors should be noted. Here, the TNR-based chemiresistor shows short response and recovery times combined with higher maximum response currents compared to those of the TNP-based chemiresistor. The latter exhibits longer response but also short recovery times. We attribute these differences to the size and shape of the particles, as the morphology of both thin films was similar (cf. section 6.1.2). First, the TNRs were only ~3 nm in diameter, exhibiting a significantly higher surface-to-volume ratio compared to the TNPs. Therefore, the electrical properties of the thin film are predominantly determined by the surface states, leading to significant changes in the response currents, as described in literature for thermally activated MOX-based chemiresistors.[79] Regarding the impact of the grain sizes on thermally activated SnO_2-based chemiresistors, Yamazoe et al. demonstrated enhanced sensitivities with decreasing grain size due to the formation of an electron-depleted space charge layer which expands over the entire particle.[82] Further, the slower response dynamics and lower sensitivities of the TNP-based chemiresistor were potentially caused by the chemical composition. During the synthesis, TiF_4 was used as precursor to obtain the plate geometry. In TNCs, the fluoride ions are known to passivate the {001} facets, which present the bottom and top surface of the TNPs.[40] Thus, these {001} facets account for a large share of the TNP surface. Comparable surface passivation effects were reported for TiO_2-based photocatalysts that showed slow and less efficient photodecomposition of dichloracetate[191] and organic dyes[192] in the presence of fluoride ions due to their electron-trapping capacity.

To investigate the impact of fluoride ions on the sensing properties, TNP-based chemiresistors were submerged in NaOH solution to remove the fluoride ions. Typically, the removal is either done by NaOH washing or calcination.[40,193] However, this treatment was not successful, because either the film or the silicon substrate was damaged and the treated TNP-based sensor showed slower response dynamics and reduced maximum response currents under 1-propanol exposure compared to those of the untreated TNP-based sensor. Based on the surface passivation by the fluoride ions, their removal is expected to result in an increase in the response currents to 1-propanol vapor. Detailed information on this NaOH treatment can be found in the Appendix, section A.1.8.

Figures 6.11a,b) part ii) display the current transients that were obtained by exposing

the sensors to different analyte vapors with concentrations of 100 ppm. Both TNC-based sensors showed high selectivity to alcohols as indicated by a significant increase in the current during the exposure to the tested alcohols, and no obvious responses are observed for the other VOCs. We assign this distinct selectivity for alcohols to the selective binding of alcohols to unsaturated titanium ions, followed by its partial oxidation reaction on photoactivated TiO_2, as reported by Mohrhusen and Al-Shamery.[194] In a comprehensive study, they investigated the conversion pathways of methanol (MeOH) on rutile TiO_2 surfaces, considering a variety of influences, e.g., the temperature, light activation, and surface modifications. For all conditions, the reaction starts with the adsorption of MeOH on an unsaturated titanium ion via the hydroxy group. The latter is then dissociated, releasing hydrogen to the surface, where it is consumed by ionosorbed oxygen leading to the formation of water, which is finally desorbed. In the case of the photoactivated rutile surface, oxygen radical species are formed by the UV illumination, that interact and activate the C-H bonds of MeOH. Ultimately, this activation leads to the partial oxidation of MeOH to formaldehyde and the formation of further water molecules.[194,195] As a result, the number of ionosorbed oxygen species is reduced, which results in the increase in electron density of the sensitive material. The response currents of the TNR- and TNP-based sensors are in good agreement with this partial oxidation, as we observed increased currents for alcohol vapors, but no or only negligible responses to MIBK or ethyl acetate. This pattern suggests that the oxidation is completed after the aldehyde or ketone formation. In addition to the study on MeOH, the same group reported the partial oxidation of 2-propanol to acetone under UV illumination,[196,197] and Walenta et al. demonstrated the photochemical oxidation of ethanol to acetaldehyde.[198] In these studies, the photocatalytic reaction of the respective alcohol on the rutile TiO_2 surface was investigated using temperature programmed desorption experiments and Fourier transform infrared reflection absorption spectroscopy. The results align with the mechanism discussed for the photoactivated partial oxidation of MeOH.[194]

As the presented oxidation pathway is based on ionosorbed oxygen species, differences in their amount can be assumed between the TNR- and TNP-based sensors, considering the distinct transient amplitudes. Here, the surface passivation with fluoride ions possibly reduces the amount of ionosorbed oxygen on the TNP-based sensor, leading to overall lower response currents compared to those of the TNR-based chemiresistor. Focusing on the current responses of the TNR- and TNP-based sensors exposed to the tested alcohols, figures 6.11a,b) part iii) show the current response isotherms. For the TNR-based chemiresistor, a linear increase in the maximum response current I_{max} with the increasing vapor concentration (range: 25–200 ppm) can be observed for all alcohols. For the TNP-based chemiresistor however, the isotherms for 1-propanol and especially 1-butanol indicate deviations from linearity, showing hysteresis when first increasing and then de-

creasing the analyte concentration. We assume that the slow response dynamics result in an increased I_{max} for the same vapor concentration with consecutive exposure duration, because the baseline current was not fully recovered after the preceding analyte exposure. Both sensors exhibit the highest response currents when exposed to 1-butanol followed by 1-propanol vapor. To further analyze the differences in the sensitivity between the tested alcohols, figures 6.11a,b) part iv) show the scatter plots of I_{max} at 100 ppm as a function of the vapor pressure of the respective alcohol, demonstrating an inverse relationship. This finding suggests that an increasing amount of analyte molecules is sorbed on the TiO_2 surface with decreasing vapor pressure and subsequently converted to the corresponding aldehyde or ketone. As a result, more molecules can be partially oxidized and the density of electrons in the TNC film increases, resulting in a higher I_{max} for 100 ppm 1-butanol compared to 1-propanol, 2-propanol, and ethanol. This assumption and the slightly increased I_{max} of the TNP-based chemiresistor for ethanol compared to 2-propanol, will be further discussed later, considering the microgravimetric measurements.

To further investigate the influence of the particle shape on the photoactivated sensing mechanism, the chemiresistive responses of sensors fabricated from OLAM-stabilized TNDs, bare TNBs, and bare P25 TNCs were examined. Using the same setup as described in the previous paragraph, the sensors were exposed to a reduced set of analytes, including ethanol, 1-propanol, 2-propanol, 1-butanol, toluene, and MIBK. The recorded current timetraces can be found in the Appendix, section A.1.12.
Figure 6.12 provides an overview of the resistive responses of sensors based on a) TNDs, b) TNBs, and c) P25 TNCs, respectively. Here, figures 6.12a-c) part i) demonstrate the analyte selectivity by comparing the current transients to 100 ppm of the respective analyte vapor. Overall, the TNC-based chemiresistors respond selectively to alcohol vapors, as indicated by the increase in the current during alcohol exposure, and no or only negligible current changes to the other tested VOCs. As discussed above, we attribute this selectivity to the selective adsorption of the OH-group on an unsaturated surface titanium ion.[194–196] The TNB- and P25-based sensors show fast response and recovery dynamics and significantly higher response amplitudes, compared to those of the TNR-, TNP-, and TND-based sensors. However, the surface-to-volume ratio of the TNBs and P25 TNCs was comparable or even lower than that of the TNRs, TNPs, and TNDs. We assume that these superior sensing characteristics of the sensors prepared from bare TNBs and P25 TNCs result from the distinct morphology of the thin films, as described in section 6.1.2. Here, the polydispersity and the bare nature of the particles cause the formation of aggregates, arranging in an island-like structure, which is in contrast to the densely packed thin films of TNRs, TNPs, and TNDs (cf. figure 6.6). Further, using a very different solvent with distinct wetting properties could substantially influence the morphology of the re-

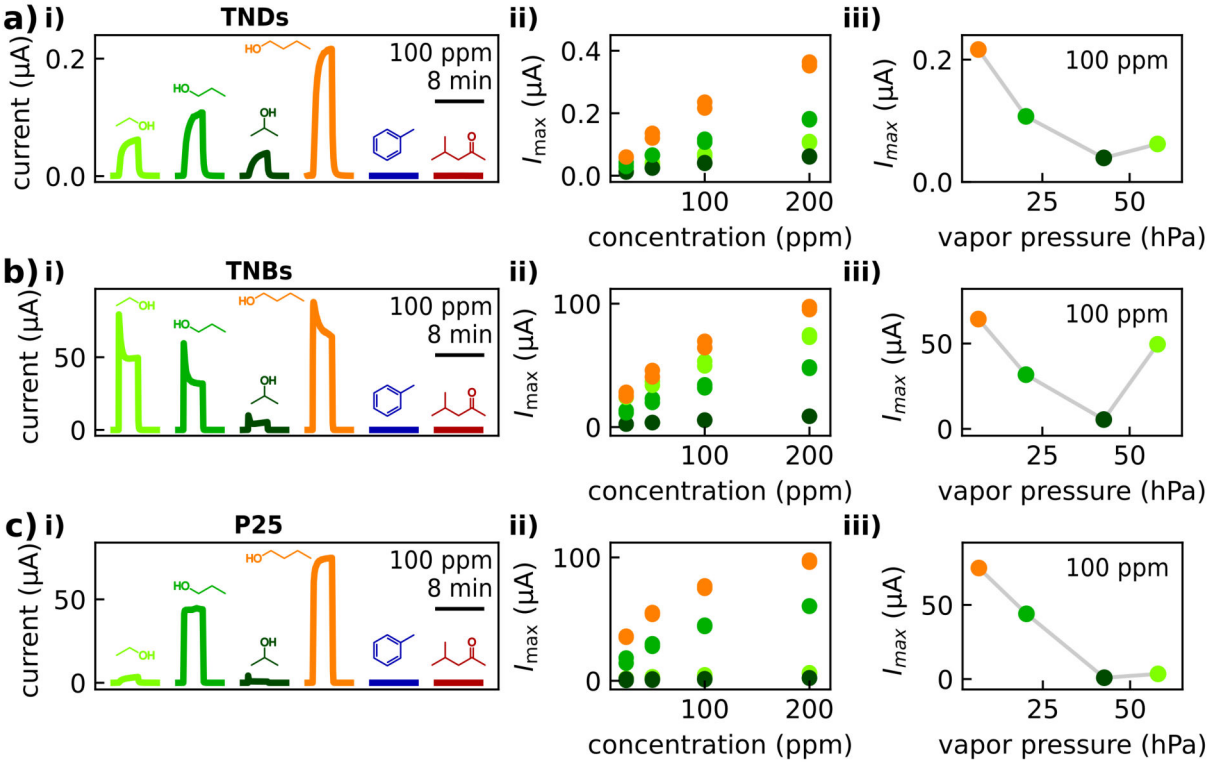

Figure 6.12: Photoactivated chemiresistive responses of a) TND-, b) TNB-, and c) P25-based sensors under UV illumination using UV LEDs (emission wavelength: 278 nm) at an irradiance of ~23 mW/cm^2 to various VOCs. i) Current transients of the TNC-based chemiresistors to the first exposure of 100 ppm ethanol, 1-propanol, 2-propanol, 1-butanol, toluene, and MIBK. ii) Current response isotherms in the concentration range between 25–200 ppm for the tested alcohols. iii) Scatter plot of the maximum response currents (I_{max}) as a function of the alcohols' vapor pressure. Subplot b) was adapted and reprinted from Dobschall el al., Ref. [3], *Creative Commons CC-BY 4.0* license ©2025 The Authors. ACS Appl. Nano Mater. published by American Chemical Society. (DOI: 10.1021/acsanm.5c03648)

sulting films, as chloroform was used for TNRs, TNPs, and TNDs while a water/MeOH mixture was used for TNBs and P25 TNCs. This island-like structure features several cracks and therefore enhances the accessibility of the analyte molecules to the surface of individual TNCs, leading to faster response dynamics and higher sensitivities. Due to the bare nature of the TNBs and P25 TNCs, we further suggest that the pronounced response currents result from the increased number of free sorption sites and ionosorbed oxygen species. As indicated for the TNRs, the OLAM removal was not completely achieved by the DUV treatment (cf. section 6.1.2). As a result, a reduced number of accessible sorption sites are available compared to the bare TNCs and therefore less oxygen is ionosorbed and fewer analyte molecules are oxidized. The influence of remaining ligands on the sensing properties possibly also plays a major role for the TND-based sensors. Here, the response amplitudes are even lower compared to those of the TNR-based sensor, which might be due to the highest OC of ~43%, as shown by TGA (cf. the Appendix, section A.1.4). Further, the TNDs were first synthesized in aqueous medium with DEG as ligand, and then transferred into the organic phase using OLAM as ligand. Thus, the surface is likely to be

stabilized with a mixture of DEG and OLAM, which might cause distinct chemiresistive properties. In this regard, further examination on the impact of the DUV treatment on TND thin films needs to be done, exceeding the qualitative ATR-FTIR analysis, e.g., using XPS surface analysis before and after the DUV treatment.
Analyzing the concentration dependent sensing properties, figures 6.12a-c) part ii) show the current response isotherms of the sensors fabricated from TNDs, TNBs, and P25 TNCs exposed to the tested alcohol vapors. All three chemiresistors show a linear relation between the response current and the concentration with the highest I_{max} for 1-butanol. Figures 6.12a-c) part iii) display the scatter plots of I_{max} at 100 ppm as a function of the alcohols' vapor pressure, showing a deviation from the pure inverse relation with an increased I_{max} for ethanol. This result is observed for all chemiresistors except for the one fabricated from TNRs, where I_{max} is significantly lower for ethanol compared to 2-propanol. These variations in I_{max} could result from the distinct crystal phases of the TNCs, as only the TNRs exhibited brookite in its crystal phase. To review this assumption and further investigate the photoactivated sensing mechanism, microgravimetric measurements were conducted in parallel to the chemiresistive measurements.

By depositing the TNR, TNP, and P25 thin films onto QCM substrates, the sorbed amount of analyte in the thin films was determined and compared to the chemiresistive responses. These tests were conducted using the same setup as described above for the chemiresistive measurements, and the resonant frequency data were analyzed as described in section 6.1.1 by using the Sauerbrey equation (cf. equation 4). Figure 6.13 shows the microgravimetric measurements of the QCMs coated with the a) TNR, b) TNP, and c) P25 thin film, respectively. Here, the reduced analyte set consisted of ethanol, 1-propanol, 2-propanol, 1-butanol, toluene, and MIBK in the concentration range between 25–200 ppm. The TNR thin film was additionally exposed to 1-butylamine in a smaller concentration range between 100–200 ppm. All relative resonant frequency timetraces of the TNC thin films are provided in the Appendix, section A.1.12. The 100 ppm transients of the resonant frequency shifts, displayed in figures 6.13a-c) part i), show that the exposure of all analytes causes a reduction in the resonant frequency. This reduction results from the adsorption of analyte molecules to the TiO_2 surface which leads to an overall increased film mass. The results demonstrate the affinity of the OH-group to the TiO_2 surface, confirmed by strong frequency shifts when the thin films were exposed to alcohol vapors. In addition to the adsorption of alcohols, the TNR and TNP thin films exhibit frequency shifts when exposed to MIBK and toluene, while the P25 thin film only shows frequency shifts under MIBK exposure. This deviation is attributed to the remaining OLAM in the TNR and TNP thin films, which possibly provides sorption sites for the non-polar toluene. Further, the adsorption of MIBK indicates the general affinity of polar functional groups

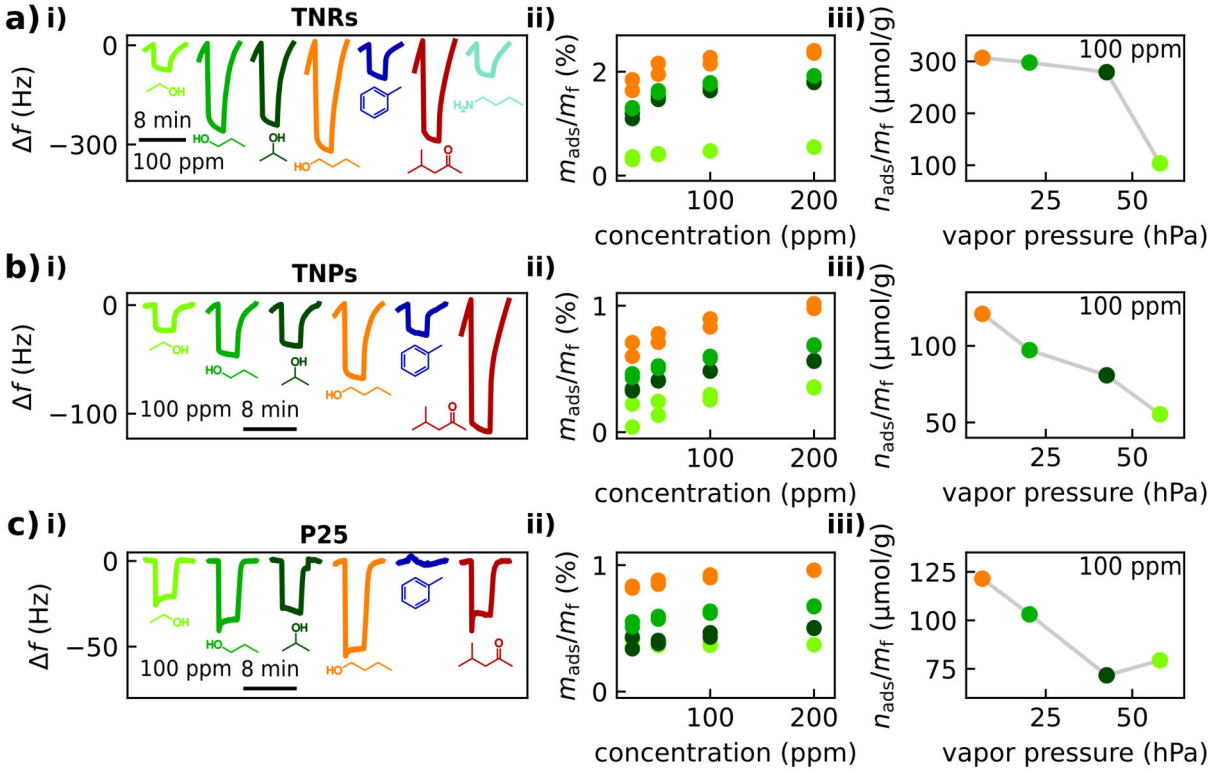

Figure 6.13: Microgravimetric analysis under UV illumination (emission wavelength: 278 nm, irradiance: ~23 mW/cm^2) using QCM substrates coated with a) TNR, b) TNP, and c) P25 thin films. i) Resonant frequency shifts of the QCM coated with the respective TNC thin film to the first exposure of 100 ppm ethanol, 1-propanol, 2-propanol, 1-butanol, toluene, and MIBK. The TNR thin film was additionally exposed to 1-butylamine. ii) Isotherms of the relative mass uptake in the concentration range between 25–200 ppm for the tested alcohols. iii) Scatter plot of the relative substance uptake of the alcohols vs. each alcohol's vapor pressure.

to the TiO_2 surface. Despite the adsorption of MIBK, no obvious current responses were observed, as described in the previous paragraph (cf. figures 6.11 and 6.12), which indicates the absence of the oxidation reaction. These results are in good agreement with the photoactivated partial oxidation pathway reported by Mohrhusen and Al-Shamery, who suppose that the product formation is governed by the C-H dissociation.[194] This assumption was supported by the investigation of the photochemical reactions of 2-propanol and ethanol on rutile TiO_2.[196–198] In the case of MIBK, we further assume that C-H dissociation is inhibited since the carbon of the carbonyl group is completely substituted.

To compare the sorbed analyte mass of the films with each other, the relative mass uptake was calculated by normalizing the mass change with the respective thin film mass. Figures 6.13a-c) part ii) show the isotherms of the relative mass uptake for the tested alcohols. Here, the increased relative mass uptake of the TNR thin film compared to the TNP and P25 thin films indicates the high surface-to-volume ratio of the TNRs. As a result, more analyte molecules can adsorb on the same amount of material for the TNRs compared to the TNPs and P25 TNCs. In contrast to the current response isotherms

(cf. figures 6.11a,b) part iii) and 6.12c) part ii)), the relative mass uptake deviates from a linear relation and follows a saturation function in the concentration range between 25–200 ppm. We assume that this distinct course of the isotherms of the relative mass uptake results from the adsorption of the respective aldehyde or ketone as the product of the alcohols' partial oxidation on the TiO_2 surface. Due to the high affinity of the OH-group to the TiO_2 surface the amount of adsorbed reaction product is possibly reduced at increasing concentrations. Further, the vapor pressure of the reaction product and the steady state surface coverage of the alcohol will contribute to the observed frequency shifts.
Figures 6.13a-c) part iii) show the scatter plots of the relative substance uptake of the alcohol at 100 ppm as a function of the alcohols' vapor pressure. To quantify the amount of sorbed analyte, the latter was not only normalized using the respective TNC film mass but also by using the molar mass of the respective analyte. Generally, the amount of sorbed analyte decreases with increasing vapor pressure, which supports the assumption that I_{max} depends on the sorbed amount of substance (n_{ads}) and thus indirectly on the vapor pressure. This is valid for a series of primary alcohols, as shown for the TNR, TNP, and P25 thin films. However, the sorbed amount of substance significantly differs between the TNC films for 2-propanol compared to the primary alcohols. While n_{ads} of 2-propanol follows the inverse vapor pressure relation for the TNR and TNP thin films, n_{ads} of 2-propanol is smaller compared to ethanol for the P25 thin film. Further, the I_{max} for 2-propanol differs in the sequence of the tested alcohols across the TNC-based chemiresistors. While I_{max} for 2-propanol (cf. figures 6.11a,b) part iv) and 6.12c) part iii)) is smaller compared to ethanol for the TNP- and P25-based sensors, it is higher compared to ethanol for the TNR-based sensor. Thus, further factors, e.g., the exposed facets of the TNCs, the inductive effect of the analytes, and their interconnecting aspects need to be considered. While the +I-effect is comparable among the series of primary alcohols, it is significantly increases for 2-propanol.[199] This could be a reason for the reduced I_{max} to 2-propanol for the TNP-, TND-, TNB-, and P25-based sensors. However, for a comprehensive understanding of the correlation between I_{max}, n_{ads}, the vapor pressure, the crystal facets, and the +I-effect, chemiresistive measurements and microgravimetric analysis on further primary, secondary, and ternary alcohols need to be examined in future studies.

As discussed above, the ionosorption of oxygen on the TiO_2 surface occurs in the dark as well as under UV illumination, while a chemiresistive response is only obtained under UV illumination. To elucidate this effect, the microgravimetric responses of a QCM coated with a TNR thin film were compared in the dark and under UV illumination. The TNR thin film was exposed to a reduced set of VOCs, consisting of 1-propanol, 2-propanol, toluene, and MIBK. Figure 6.14 shows the results of the microgravimetric measurements with additional data on the chemiresistive properties for 1-propanol and 2-propanol. The

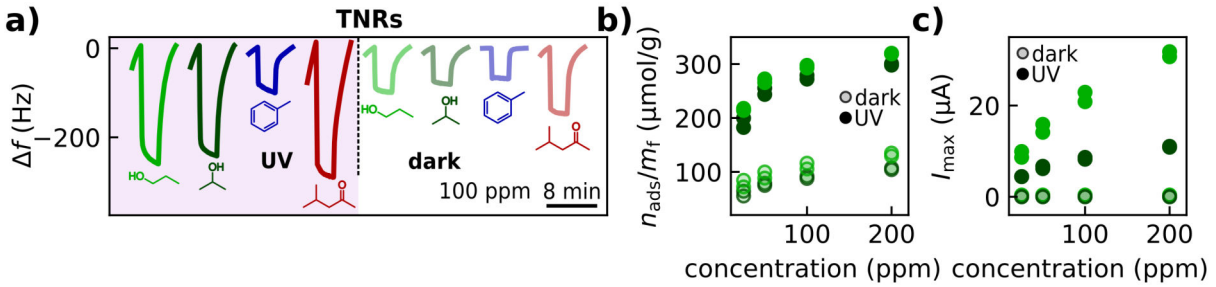

Figure 6.14: a) Resonant frequency shifts of the QCM coated with a TNR thin film to the first exposure of 100 ppm 1-propanol, 2-propanol, toluene, and MIBK under UV illumination using UV LEDs (emission wavelength: 278 nm) at an irradiance of ~23 mW/cm^2 (purple background) and in the dark (white background). b) Isotherms of the relative substance uptake for the tested alcohols in the dark and under UV illumination. c) Current response isotherms of the TNR-based chemiresistor to 1-propanol and 2-propanol in the dark and under UV illumination.

timetraces displaying the current and the relative resonant frequency can be found in the Appendix, section A.1.12. Figure 6.14a) shows the transient resonant frequency shifts of the same TNR thin film in the dark (white background) and under UV illumination (purple background) to analytes with a concentration of 100 ppm, displaying distinct features. First, the frequency shifts are more pronounced for all VOCs under UV illumination, showing that more analyte molecules are adsorbed when the TNR thin film is photoexcited. Second, the shape of the transients is more rectangular in the dark, indicating faster response and recovery dynamics due to faster reaching steady state conditions upon switching from AG to ZG and back. Third, the transients of toluene in the dark and under UV illumination show a minimal difference in the resonant frequency shift, indicating that the adsorption of toluene on the TiO_2 surface is nearly independent of the photoactivation. This result supports the assumption that toluene is adsorbed on the remaining OLAM rather than directly on the TiO_2 surface. Figure 6.14b) shows the isotherms of the relative substance uptake of the TNR thin film which was exposed to 1-propanol and 2-propanol vapor in the dark and under UV illumination. For both analytes, the concentration dependent increase of n_{ads} can be observed with a slightly higher substance uptake for 1-propanol compared to 2-propanol which aligns with the distinct vapor pressures. Again, these isotherms of the relative substance uptake of the TNR thin film level off under UV illumination, while the isotherms in the dark exhibit a more linear shape. This deviation might result from the product of the partial oxidation reaction that remains adsorbed after the reaction for photoactivated TNR thin films. Figure 6.14c) shows the current response isotherms of the TNR-based chemiresistor exposed to 1-propanol and 2-propanol in the dark and under UV illumination. As expected, no response current is measured without photoactivation. Further, the maximum response currents I_{max} under photoactivation increase with increasing concentration for both alcohols. While the photoactivated relative substance uptake n_{ads} for 1-propanol and 2-propanol is almost the

same, the I_{max} for 1-propanol is significantly higher. These results suggest that not only the difference in the vapor pressure but also the enhanced reactivity of 1-propanol needs to be considered. Thus, the pronounced I_{max} is attributed to the combination of lower vapor pressure and higher reactivity of the primary alcohol compared to the secondary alcohol. This result shows that it is not possible to generally relate the chemiresistive sensor response to the sorbed amount of analyte.

The chemiresistive measurements presented above focused on the analyte selectivity and the influence of the particle shape of the TNCs using a rather narrow concentration range between 25–200 ppm. In this range, especially the TNR-based sensors demonstrate a nearly linear increase of I_{max} as a function of increasing concentration (cf. figure 6.14c)). To further analyze the sensor response as a function of concentration, a TNR-based sensor was exposed to 1-propanol with an extended concentration range between 0.5–5000 ppm. Again, the chemiresistive measurements were combined with microgravimetric analysis. For increasing concentrations, these results show the deviation from the linear relation of I_{max} and the concentration. Further, the detection of 1-propanol on the sub-ppm level is demonstrated. Detailed information on this investigation can be found in the Appendix, section A.1.13.

Humidity Influence

To investigate the chemiresistive responses of TNC-based chemiresistors in the presence of r.h., purified air was humidified using the humidification unit of the commercial gas calibration system (cf. section 7.6). Using the same setup as described before, the TNR-, TNP-, and P25-based chemiresistors were transiently exposed to AG and ZG, with distinct r.h. levels of 0%, 10%, and 46%. Again, 1-propanol was used as target analyte and the chemiresistors were operated under UV illumination using UV LEDs (emission wavelength: 278 nm, irradiance: ~23 mW/cm^2). The r.h. level was monitored in parallel to the resistive measurements by using a commercial gas sensor (BME680, Bosch Sensortec). All timetraces are provided in the Appendix, section A.1.14.
Figure 6.15 shows the current transients of the a) TNR-, b) TNP-, and c) P25-based chemiresistor to 100 ppm propanol vapor with varying r.h. levels. In contrast to Šutka et al. who reported stable chemiresistive responses for TND-based sensors to ethanol between 10–40% r.h.,[100] the response currents of all TNC-based chemiresistors to 1-propanol are significantly attenuated already at 10% r.h. compared to those at dry conditions. These results can be explained considering the study of Mohrhusen and Al-Shamery who investigated the reaction pathways of MeOH on a rutile TiO_2 surface for various conditions, including the presence of r.h.[194] They suggested, that due to the adsorption of water molecules to the TiO_2 surface and the formation of surface hydroxyls, the reaction

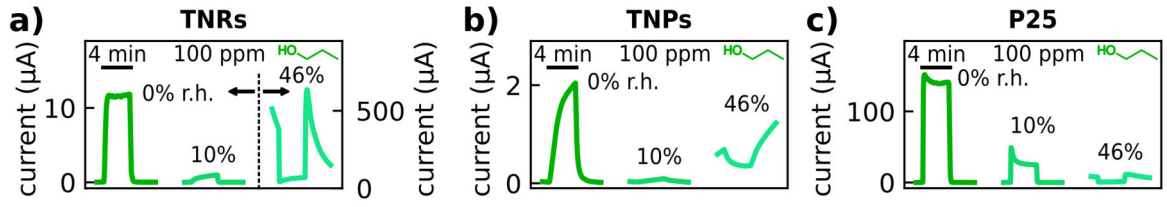

Figure 6.15: Photoactivated current transients of a) TNR-, b) TNP-, and c) P25-based chemiresistors, respectively. The sensors were exposed to 100 ppm 1-propanol with increasing r.h. levels. Both the ZG and the AG line were humidified to the desired level of 0%, 10%, and 46%. Adapted and reprinted from Dobschall el al., Ref. [3], *Creative Commons CC-BY 4.0* license ©2025 The Authors. ACS Appl. Nano Mater. published by American Chemical Society. (DOI: 10.1021/acsanm.5c03648)

rate of MeOH is reduced without affecting its reaction pathway. Again, this was supported by other studies on the photocatalytic partial oxidation of different alcohols on rutile TiO_2 surfaces.[196–198] We assume that this competition between water and analyte sorption and the reduced partial oxidation are the reasons for the decreased response currents for all TNC-based chemiresistors to 1-propanol vapor at r.h. of 10%. Further, the baseline current remains low for 10% r.h., suggesting the adsorption of an incomplete water layer. For increased r.h. levels of 46%, however, the baseline current is significantly higher, suggesting the formation of a complete water layer that enables additional conductivity and governs the charge transport properties via the Grotthuss mechanism.[2,110] When switching to AG at high r.h. of 46%, the TNC-based chemiresistors show a negative current response. Possibly, the current is reduced due to the co-adsorption of 1-propanol within the water layer with the latter impeding the charge transport governed by the Grotthuss mechanism.

To further validate the impact of r.h., microgravimetric measurements using OCMs coated with TNR, TNP, and P25 thin films were conducted. Here, the thin films were transiently exposed - under constant UV illumination using the UV LEDs - to purified, dry air as ZG and humidified air of varying r.h. levels as AG. For the TNR thin film, an additional measurement was conducted in the dark. All relative resonant frequency timetraces are provided in the Appendix, section A.1.14. Figure 6.16 shows the isotherms of the relative substance uptake of water for the a) TNR, b) TNP, and c) P25 thin film. These data demonstrate the affinity of water to the TiO_2 surface, and show the increasing number of sorbed water molecules with increasing r.h. level. Figure 6.16a) also shows that the photoactivation not only increases the adsorption of the target analytes, as described above (cf. figure 6.14), but also increases the water adsorption. For the QCM coated with the P25 thin film, a hysteresis can be observed when decreasing the r.h. level. The increased relative substance uptake for the same r.h. level is attributed to the distinct morphology of the P25 thin film with enhanced accessibility of molecules to the surface of individual

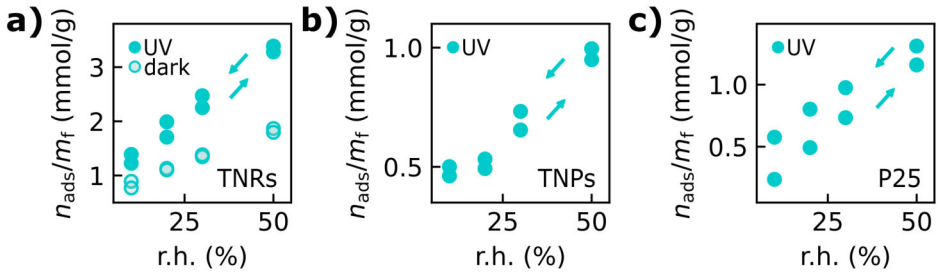

Figure 6.16: Isotherms of the relative substance uptake of photoactivated a) TNR, b) TNP, and c) P25 thin films coated on QCM substrates for r.h. levels between 0–50%. For the TNR thin film in a), the relative substance uptake in the dark is shown additionally.

particles, as described in the preceding paragraphs. This structure possibly promotes the condensation of water and thus delays its desorption.

In conclusion, the systematic variation of different measurement conditions allowed for a comprehensive analysis of the photoactivated sensing mechanism of TNC-based chemiresistors. Equal to thermally activated MOX-based chemiresistors, the sensing mechanism is based on ionosorbed oxygen species acting as a vital reactant in the reactions of analyte molecules on the TiO_2 surface. Further, the photon energy of the photoactivation needs to match the band gap of the TNCs to generate charge carriers and enable the chemiresistive sensor response. If this condition is met, the chemiresistive responses can be tuned by adjusting the irradiance of the illumination. Regardless of the TNC shape, all chemiresistors exhibit selective responses to alcohols, with the latter being partially oxidized, as reported by Morhusen et al.,[194] forming the corresponding aldehydes or ketones. However, the morphology and structure of the chemiresistors significantly influenced the sensing properties, suggesting that an island-like structure is beneficial for vapor sensing due to the increased accessibility of the surface of individual TNCs for analyte sorption. Such island-like structures were formed from bare TNCs, providing a large number of sorption sites for oxygen and analyte molecules. The results also show the affinity of polar molecules to the TiO_2 surface. Thus, increasing levels of r.h. and the adsorption of water are a competing factor to alcohol detection, which poses a major challenge for technological applications of photoactivated TNC-based sensors for the detection of alcohols.

6.1.4 Adjusting the Operating Temperature of Photoactivated VOC Sensors

To further elucidate the photoactivated sensing mechanism and tackle the loss of sensitivity in the presence of humidity, TNR-based chemiresistors were operated at slightly elevated temperatures, aiming for the desorption of water molecules from the TiO_2 surface. However, the chemiresistors were still photoactivated by the UV LEDs, and the temperatures were kept below 80 °C, to mitigate thermal activation. For the fabrication of a heated TNR-based chemiresistor, the TNR dispersion was drop-casted on an alumina substrate, the latter featuring a platinum IDE structure and resistance temperature detector (RTD) on its upper surface as well as a platinum heating meander on the backside. In order to prevent heat dissipation, the substrate was clamped in a custom-designed sample holder, obtaining a freestanding substrate that was contacted using spring-loaded pin connectors. The sample was then placed in the test cell, and was itself contacted using spring-loaded pin connectors (cf. the Experimental section 7.6). Elevated operating temperatures were obtained by increasing the voltage applied to the heating meander. By combining the resistance of the RTD with the temperature measured at the sample surface, the calibration of the temperature was accomplished. The corresponding data are provided in the Appendix, section A.1.16. For the following investigations of the electrical and chemiresistive properties of the TNR-based sensor, the temperature was set to distinct values of 23 °C, 50 °C, and 72 °C, while the r.h. level was varied between 0%, 10%, 30%, and 50%. To test the thermal activation of the sensor in this temperature range, each condition was examined in the dark (UV LED switched off) and under photoactivation using the UV LEDs (emission wavelength: 278 nm) at an irradiance of ~23 mW/cm^2.

Electrical Properties at Varying Humidity Levels

To follow the evolution of the photoactivated conductance and the conductance in the dark with increasing r.h. levels, the sample was placed in the test cell, where it was purged with the desired atmosphere, and *IV* measurements were conducted by sweeping the voltage between ±10 V. For each condition, the respective *IV* curve was fitted with a linear function and the conductance was extracted as the slope of the linear *IV* curve.
Figure 6.17 shows the scatter plots of the extracted conductances (the conductances in the dark are indicated by a dark outline). The corresponding *IV* curves are provided in the Appendix, section A.1.16. Figure 6.17a) shows the conductance as a function of the r.h. at temperatures of i) 23 °C, ii) 50 °C, and iii) 72 °C. At 23 °C, the conductance strongly increases with increasing r.h., demonstrating that the charge transport is governed by the r.h. level and thus depends on the amount of sorbed water on the TiO_2 surface, as shown in figure 6.16. The pronounced increase at higher r.h. levels possibly originates from the

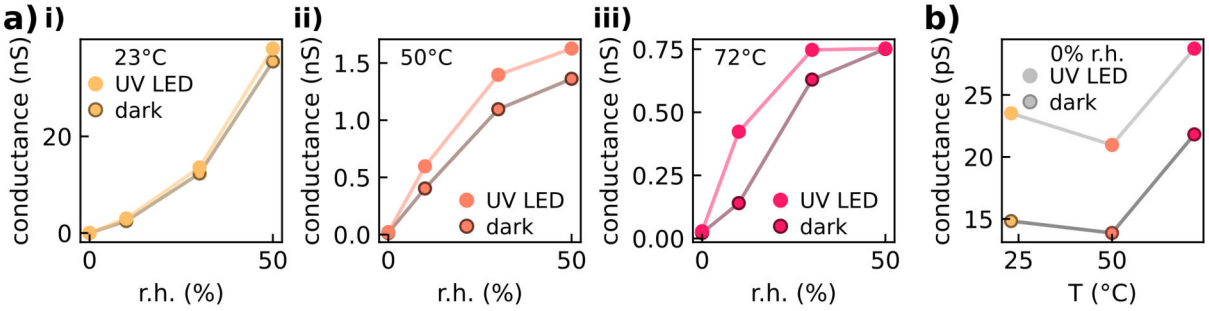

Figure 6.17: a) Scatter plots of the conductance of the TNR-based chemiresistor as a function of the r.h. level at operating temperatures of i) 23 °C, ii) 50 °C, and iii) 72 °C. Darker outlines indicate conductances obtained in the dark. The irradiance of the UV illumination for photoactivated conductances was ~23 mW/cm^2. b) Scatter plot of the conductance of the TNR-based chemiresistor vs. the operating temperature at 0% r.h. in the dark and under UV illumination.

Grotthuss mechanism which takes over the charge transport for the condensation of complete water layers on the surface. For comparison, Yadav et al. investigated the application of ZnO-TiO_2 nanocomposites as humidity sensors in the range between 10–95% r.h. and operated them at room temperature.[110] They reported reduced resistances with increasing r.h. level and attributed large resistance changes at high r.h. to the physisorbed water molecules that allow for the charge transport via the Grotthuss mechanism.[110] For lower r.h. levels, the change in resistance is attributed to chemisorbed water molecules,[107,110] that possibly cause an additional n-type doping of the MOX, as suggested in literature.[109] At 50 °C, the increase in the conductance as a function of the r.h. is significantly attenuated and the scatter plots of the photoactivated conductance and the conductance in the dark indicate saturation behavior. Thus, the increasing r.h. has a reduced influence which is attributed to the reduced amount of sorbed water due to the increased operating temperature. A comparable shape with even higher attenuation of the conductance is shown at 72 °C for increasing r.h. Since all data were received from the same TNR-based chemiresistor, the absolute values indicate the lowest amount of sorbed water at the highest tested temperature of 72 °C. This temperature dependent desorption of water is in agreement with a study of Li et al., who investigated the coverage of water on rutile TiO_2 surfaces using temperature programmed desorption and microgravimetric measurements. They reported that the desorption of water begins at temperatures only slightly above room temperature.[200]

As expected, in the dark, lower conductances were obtained for all temperatures and r.h. levels compared to those under photoactivation, due to the absence of photogenerated charge carriers. Figure 6.17b) shows the conductance as a function of temperature at a constant r.h. of 0%, demonstrating again the increased photoactivated conductance compared to the conductance in the dark. Further, the photoactivated conductances are in the same range and only differ by a few pS for all temperatures. These results suggest

no obvious influence of the elevated operating temperature on the electrical properties, which is expected for a wide band gap semiconductor like TiO_2, since the thermal energy in this temperature range does not exceed ~30 meV, which is insignificant compared to the band gap of 3.14 eV for brookite[48] and 3.20 eV for anatase.[47]

In the experiments described above, we observed that the resistance of the TNR-based sensor on the alumina substrate is higher compared to the TNR-based sensor on the SiO_2/Si substrate under the same conditions (UV LEDs at an irradiance of ~23 mW/cm^2, 23 °C, and 0% r.h.). This deviation is attributed to the differences in the electrode geometry of the IDE structures. Correcting the resistances for the electrode geometries resulted in photoactivated sheet resistances of 150 TΩ/sq for the TNR-based sensor on the SiO_2/Si substrate and 32 TΩ/sq for the TNR-based sensor on the alumina substrate. Based on these values and assuming a comparable resistivity, the thickness of the film on the alumina substrate was approx. five times thicker than the TNR thin film on the SiO_2/Si substrate. However, it was not possible to verify this conclusion by AFM analysis because no suitable thin film step edges on the alumina substrate could be obtained. This circumstance is possibly due to the rough surface of the alumina substrates. Corresponding AFM analysis and SEM images are provided in the Appendix section A.1.16, showing larger aggregates in the size range of a few micrometers on the substrate surface.

Chemiresistive Properties at Varying Humidity Levels

To study the influence of temperature and r.h. on the chemiresistive properties of the TNR-based sensor, the latter was placed in the test cell and transiently exposed to AG followed by ZG, both of which were humidified with the same r.h. level. For AG, the purified and humidified air was enriched with 1-propanol vapor at concentrations between 50–200 ppm, and the sensor was exposed to AG and ZG, each for 4 min. During the chemiresistive measurements, the r.h. level was monitored in parallel via a commercial gas sensor (BME680 Bosch Sensortec) that was read out using a Raspberry Pi. Further, the measurements were conducted under photoactivation using the UV LEDs (emission wavelength: 278 nm) at an irradiance of ~23 mW/cm^2 or in the dark.

Figure 6.18 shows the responses of the TNR-based chemiresistor to 1-propanol at an operating temperature of 23 °C for r.h. levels of 0%, 10%, 30%, and 50% under UV illumination and in the dark. The corresponding current timetraces can be found in the Appendix, section A.1.18. Figure 6.18a) part i) shows the current timetraces of the TNR-based sensor exposed to 1-propanol vapor at 0% r.h. recorded in the dark (top, white background) and under UV illumination (bottom, purple background). In the dark, only very faint current responses can be observed and the baseline current in the range of sev-

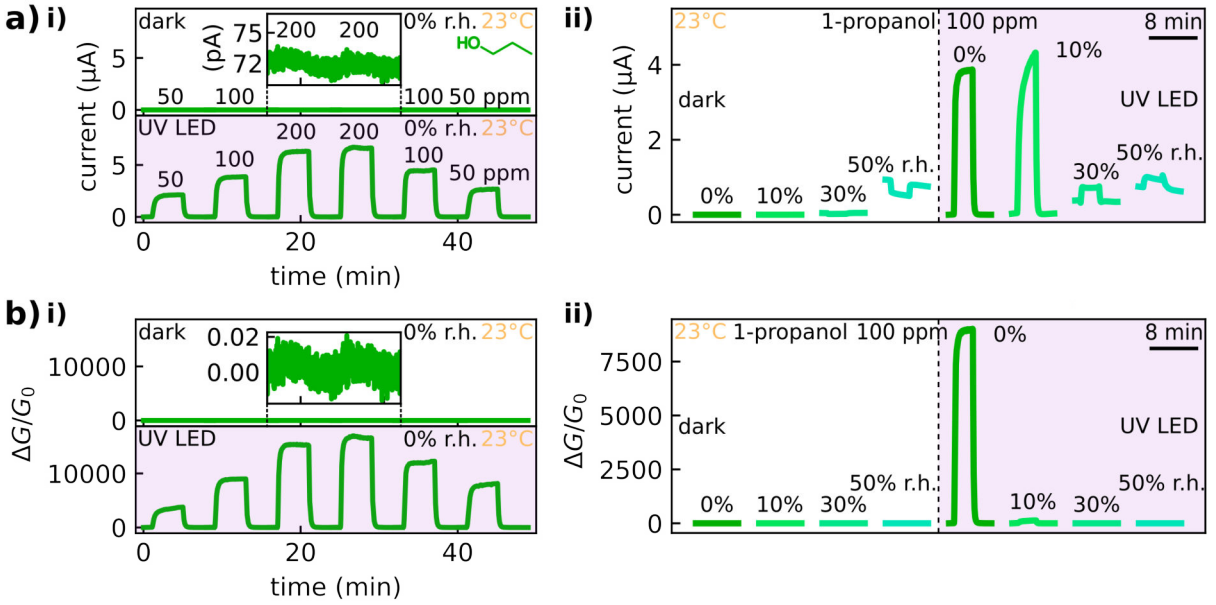

Figure 6.18: a) Response currents and b) baseline-corrected relative conductance changes of the TNR-based chemiresistor to 1-propanol at 23 °C and 0% r.h. in the dark (white background) and under UV illumination (purple background). i) Timetraces of the chemiresistive measurement with vapor concentrations of 50, 100, 200, 200, 100, and 50 ppm. Insets: zoom-in to the a) current and b) relative conductance change of the sensor to both 200 ppm exposures in the dark. ii) Transients of the first 100 ppm exposure of 1-propanol at distinct r.h. levels of 0%, 10%, 30%, and 50%.

eral tens of pA is at the detection limit of the readout device (~1 pA), causing some noise (cf. figure 6.18a) part i) inset). In agreement with the results on the SiO_2/Si substrates, the resistive response is activated under UV illumination which results in fast response and recovery dynamics as well as pronounced current responses upon the 1-propanol exposure. Further, the current response increases with increasing analyte concentration. Figure 6.18a) part ii) displays the current transients to 100 ppm 1-propanol vapor for the tested r.h. levels in the dark (white background) as well as under photoactivation (purple background). In the dark, no current response is visible for low r.h. of 0% and 10%, while an increased baseline current for ZG combined with negative responses to AG are obtained for higher r.h. levels of 30% and 50%. The increased baseline current is in agreement with the electrical responses to humidity described in the previous paragraph. Further, the decrease of the response current observed, when the TNR-based chemiresistor was exposed to 1-propanol vapor, could result from the co-adsorption of 1-propanol within the water layer hampering the charge transport by the Grotthuss mechanism. Under UV illumination, the baseline currents exhibit the same trend as observed for the sensor operated in the dark and are agreement with the electrical responses to humidity described in the previous paragraph. These results confirm, that the current was predominantly governed by the r.h. level when the thin film was exposed to ZG. For all r.h. levels, the current responses to AG remain positive, indicating not only the adsorption of 1-propanol

but also its partial oxidation enabled by the photoactivation. However, this is in contrast to the TNR-based chemiresistors deposited on SiO_2/Si substrates (cf. section 6.1.3) that exhibited negative current responses to AG exposure at the highest r.h. level of 46%. This might be due to the different substrates, featuring different wettability and therefore influence the formation of the water film. Further, the IDE structures on the SiO_2/Si substrates feature smaller gaps between the fingers (10 µm) compared to the gaps of the IDE structures on the alumina substrate (250 µm). These differences are assumed to cause a higher baseline current of the SiO_2/Si substrate compared to the alumina substrate. As a result, the predominant effect for the TNR-based sensor on the SiO_2/Si substrate when switching to AG exposure is given by the co-adsorption of 1-propanol impeding the charge transport by the Grotthuss mechanism, as discussed in section 6.1.3.
To compensate for different baseline currents resulting from distinct r.h. levels, the relative conductance change ($\frac{\Delta G}{G_0}$) was extracted from the recorded current timetraces as described in section 6.1.1 according to equation 3. Note, that this not only included normalizing the conductance using the baseline conductance, but also included a correction for baseline-drifts, which is indicated by the term baseline-corrected. Since all data on varying operating temperatures were obtained using the same TNR-based sensor, we attribute the baseline changes exclusively to the variations in the r.h. level. Figure 6.18b) shows the relative conductance change for the data displayed in figure 6.18a). Figure 6.18b) part i) shows the timetraces of the relative conductance change of the TNR-based sensor exposed to 1-propanol vapor at 0% r.h. recorded in the dark (top, white background) and under UV illumination (bottom, purple background). In the dark, only a very weak and noisy response can be observed, while pronounced responses of up to 15000 are observed under UV illumination. These high values of the response result from the small baseline currents of the TNR-based sensor in the range of several tens of pA as seen from the electrical properties (cf. figure 6.17b)). Figure 6.18b) part ii) displays the transients of the relative conductance change to 100 ppm 1-propanol at different r.h. levels, showing almost no responses for all conditions except for the measurement at 0% r.h. under UV illumination. The corresponding timetraces of the relative conductance change are provided in the Appendix, section A.1.18. Note, that the response at 10% r.h. is strongly reduced compared to the response at 0% due to the baseline current that increased with increasing r.h. level.

Not only the r.h. but also the temperature was varied, and its impact on the chemiresistive responses was evaluated. Figure 6.19 shows the a) current timetraces and b) the timetraces of the relative conductance change of the TNR-based sensor at 0% r.h. and an operating temperature of 72 °C in the dark (white background) and under UV illumination (purple background). In contrast to figure 6.17b) the baseline current shown in

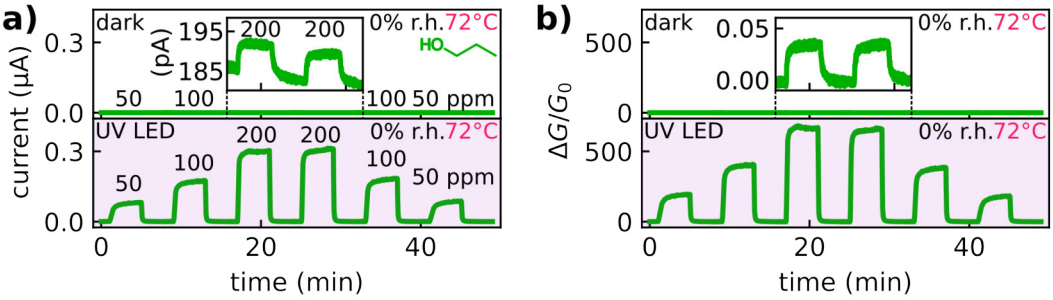

Figure 6.19: Timetraces of the a) current and b) baseline-corrected relative conductance change of the TNR-based chemiresistor to 1-propanol at 72 °C and 0% r.h. in the dark (white background) and under UV illumination (purple background). Insets: zoom-in to the a) current and b) relative conductance change of the sensor to both 200 ppm exposures in the dark.

figure 6.19a) seems to increase due to thermal activation of charge carriers in the dark and under UV illumination. Further, very low response currents to 1-propanol can be detected in the dark that indicate a thermal activation of the chemiresistive response. For comparison, Karunagaran et al. reported imperceptible responses of titania thin films to ammonia below 100 °C, with the maximum response reached at 250 °C.[201] Under UV illumination, the increased temperature leads to lower response currents to 1-propanol compared to those at an operating temperature of 23 °C (cf. figure 6.18) which is possibly due to the reduced amount of sorbed analyte molecules on the TNR's surface, as described in literature. For instance, Kim et al. investigated the molecular desorption of 1-propanol from polycrystalline titania surfaces at 75 °C using temperature programmed desorption and reported the reversible adsorption state at slightly elevated temperatures.[202] Comparing the relative conductance changes in the dark and under UV illumination, which are displayed in figure 6.19b), illustrates that the thermal activation of the chemiresistive response is insignificant compared to the photoactivation, though it needs to be considered at temperatures above 72 °C. Further, the amplitude of the relative conductance change to 1-propanol vapor under UV illumination significantly decreases with increasing temperature by a factor of ~20 from operating temperatures of 23 °C (cf. figure 6.18b) part i)) to 72 °C (cf. figure 6.19b)).

Figure 6.20 provides an overview of the a) current and b) relative conductance change transients of the TNR-based sensor exposed to 100 ppm 1-propanol under UV illumination for varying r.h. levels and operating temperatures. All corresponding timetraces can be found in the Appendix, section A.1.18. The transients for the r.h. levels of 0%, 10%, 30%, and 50% are displayed in figure 6.20 parts i), ii), iii), and iv), respectively. The distinct operating temperature is indicated by the color of the respective transient with yellow, orange, and red corresponding to 23 °C, 50 °C, and 72 °C, respectively. As demonstrated by the electrical properties, the photoactivated conductance was more stable to the influence of r.h. with increasing operating temperature (cf. figure 6.17a) part ii,iii)).

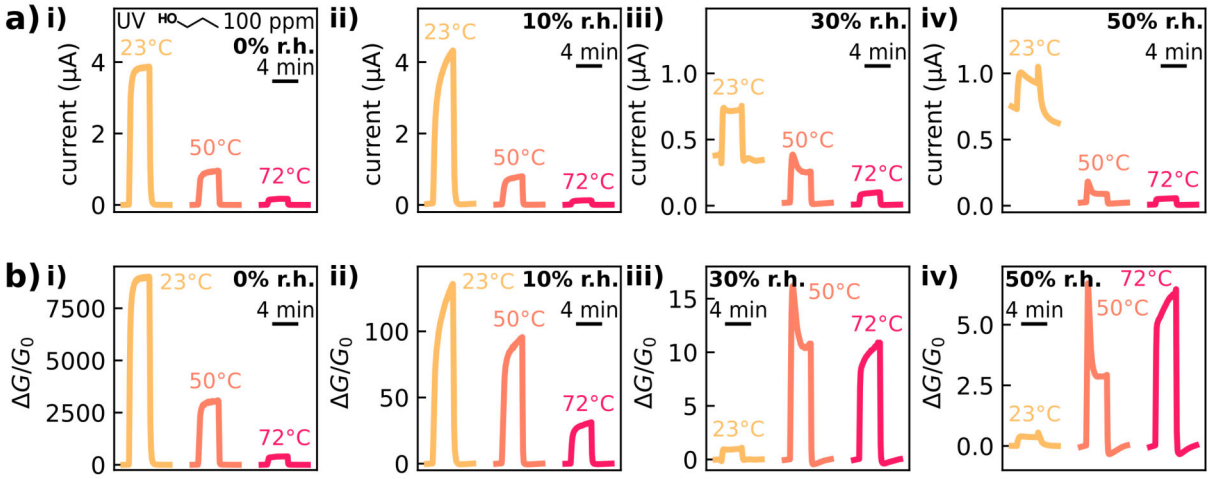

Figure 6.20: Photoactivated transients of the a) current and b) baseline-corrected relative conductance change of the TNR-based chemiresistor to 100 ppm 1-propanol at operating temperatures of 23 °C, 50 °C, and 72 °C. The r.h. levels were set to 0%, 10%, 30%, and 50% and are shown in i), ii), iii), and iv), respectively, increasing from left to right.

Thus, constant baseline currents can be observed at 50 °C and 72 °C for all tested r.h. levels, while the baseline current at 23 °C significantly increases with increasing r.h. (cf. figure 6.20a) parts i-iv)). When exclusively comparing the current responses of the TNR-based sensor, the maximum response current is inversely proportional to the operating temperature for all tested r.h. levels (cf. figure 6.20a) parts i-iv)). This trend changes, however, when the relative conductance change, displayed in figure 6.20b), is considered. Although the responses at all operating temperatures decrease with increasing r.h. level, this effect is more pronounced at room temperature. Due to the increase in the baseline current with increasing r.h. at an operating temperature of 23 °C combined with the decrease in the current response, the relative conductance change significantly drops from ~9000 to ~1. Note, that this still equals a relative conductance change of 100%. With increasing operating temperature, the decrease in the response is attenuated. As a result, the response amplitude obtained at 23 °C interchanges for the response obtained at 72 °C as the highest relative conductance change above r.h. levels of 30% (cf. figure 6.20b) parts i-iv)). It is concluded that the increased operating temperature causes the desorption of water, which results in stable baseline currents, as discussed above. Further, the increased operating temperature causes the desorption of 1-propanol,[202] which results in lower response currents. These results suggest, that this trade off between stabilizing the baseline and decreasing the response current can be accepted to detect the target analytes also at high r.h. levels.

These findings are summarized in figure 6.21 which displays the a) maximum response current I_{max} and b) maximum relative conductance change $\left(\frac{\Delta G}{G_0}\right)_{\mathrm{max}}$ as a function of the r.h. level at the distinct operating temperatures. Figure 6.21a) shows the overall high

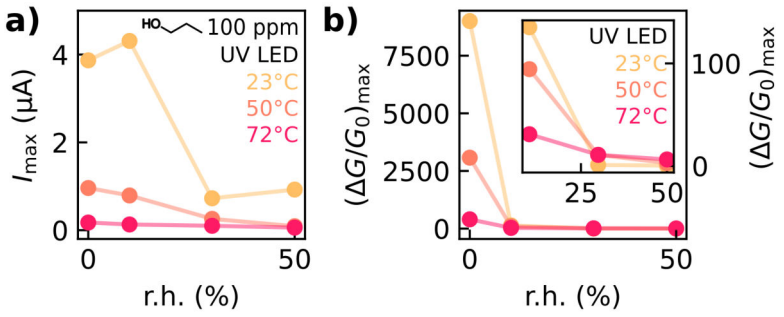

Figure 6.21: Scatter plots of the a) photoactivated maximum response current I_{max} and b) baseline-corrected maximum relative conductance change $\left(\frac{\Delta G}{G_0}\right)_{max}$ of the TNR-based chemiresistor to 100 ppm 1-propanol at 23 °C, 50 °C, and 72 °C operating temperature vs. the r.h. between 0–50%. The inset in b) magnifies the r.h. range between 10–50%, and shows the temperature-dependent crossover of $\left(\frac{\Delta G}{G_0}\right)_{max}$ with increasing r.h. levels.

I_{max} for operating the TNR-based sensor at 23 °C. However, when compensating for the increase in the baseline current, figure 6.21b) shows the crossover of the $\left(\frac{\Delta G}{G_0}\right)_{max}$ at 30% r.h., demonstrating superior sensing properties for increased operating temperatures at elevated r.h. levels.

For comparison, the overview on the current and relative conductance change transients of the TNR-based sensor to 100 ppm propanol at varying r.h. levels and operating temperatures in the dark is provided in the Appendix, section A.1.17.

In summary, increasing the operating temperature causes a reduced increase of the TNR-based sensor conductance with increasing r.h. levels. Thus, it was possible to stabilize the baseline current against the influence of r.h. by increasing the operating temperature. Further, the increase of the operating temperature results in an attenuated sensor response at 0% r.h. possibly due to the desorption of analyte molecules. With increasing r.h. level, however, the sensor responses, expressed as the relative change of conductance, cross over, leading to higher maximum responses at increased operating temperatures. Thus, complementing the photoactivation for thermal activation at temperatures around 70 °C allows for the analyte vapor detection at elevated r.h. levels. However, the baseline-corrected response amplitudes significantly decrease with increasing r.h. even at 72 °C. Hence, the attenuation of the sensitivity with increasing humidity still remains a challenge to be addressed in future works.

This challenge not only remains for the photoactivated MOX-based gas sensors, but was also reported for thermal activation. For instance, Tischner et al. investigated ultrathin SnO_2-based gas sensors for the detection of humidity and CO at operating temperatures between 250 °C to 400 °C. They reported that the prolonged exposure to humidity caused the drift of the sensor signal, which was only recovered by heating the sensor to temperatures above 450 °C for several minutes.[203] Further, Qi et al. investigated the effect of humidity on the electrical response of Sm_2O_3-doped SnO_2 to acetylene and demonstrated

the significant decrease in the sensor response with increasing r.h. level at an operating temperature of 180 °C. They attributed this effect to the adsorption of water on the surface, which led to the decrease in the baseline resistance of the sensor and a reduced number of ionosorbed oxygen species on the MOX surface.[204]

6.1.5 Surface Modification

To tune the chemiresistive properties of MOX-based sensors, surface modification of the sensitive layer with nanostructured materials is a common approach for thermally activated systems. In this study, superparamagnetic iron oxide nanoparticles (SPIONs) and nanostructured noble metals (Pt and Au) were deposited on TNR-based chemiresistors, to achieve electronic and chemical sensitization, respectively. The influence of the material deposition on the structural properties and photoactivated chemiresistive responses of the sensors is discussed in the following paragraphs. These results should be regarded as a preliminary investigation on the possibilities of surface modification of photoactivated TNR-based sensors since no comprehensive analysis was conducted and only the general concept was examined.

Electronic Sensitization

Following the concept of electronic sensitization, the change in the charge carrier concentration of the TiO_2 material by surface modification is a promising approach to tune the sensitivity and selectivity of the sensor.[79] For thermally activated MOX-based sensors, this is usually achieved by the addition of small metal clusters, such as Ag, Pd, or Cu, that form their respective oxide on the MOX surface.[82] For TiO_2, comparable studies were conducted with the objective of improving catalytic properties, but these findings also provide approaches for the field of gas sensors. For instance, Tada et al. investigated the photocatalytic decomposition of 2-naphthol by TiO_2 modified with dispersed iron oxide species. They reported an increased decomposition rate compared to the rate of unmodified TiO_2 and attributed it to improved charge carrier separation.[205] Further, in DFT calculations that aimed at investigating different iron oxide modifications on rutile TiO_2 surfaces, it was demonstrated that the conduction band (CB) edge as well as valence band (VB) edge of all iron oxide modifications are located above the respective CB and VB edge of the TiO_2.[206] When these two materials are in contact, this alignment causes the accumulation of electrons in the CB of TiO_2 and the accumulation of holes in the VB of the iron oxide.

In the present work, spherical SPIONs with a diameter of ~3 nm were deposited by spin-coating 20 µL of the SPION dispersion in toluene on the TNR-based sensor. Subsequently, 20 µL of MeOH were applied to the rotating sample to strip the oleyl phosphate ligands of the SPIONs. The characterization of the SPIONs is provided in the Appendix, section A.1.19. Figure 6.22 provides an overview of the structural and chemiresistive properties of the SPION-modified TNR-based sensor. Figure 6.22a) shows a represen-

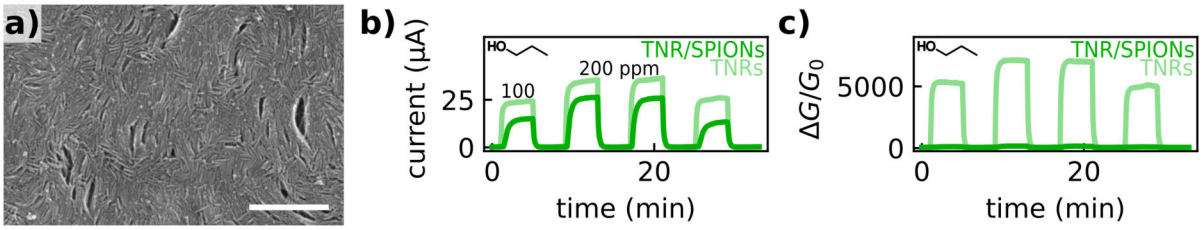

Figure 6.22: Iron oxide modification of the TNR-based chemiresistor by the deposition of SPIONs using spin-coating. a) SEM image of the SPION-modified TNR thin film. Scale bar: 200 nm. Timetraces of the b) current and c) baseline-corrected relative conductance change of the SPION-modified and unmodified TNR-based chemiresistor to 1-propanol with concentrations of 100, 200, 200, and 100 ppm. The sensors were photoactivated using UV LEDs (emission wavelength: 278 nm) at an irradiance of ~23 mW/cm^2.

tative SEM image of the sensitive material. Here, the homogeneous film of disordered TNRs is displayed and few SPIONs, that are randomly distributed over the TNR film are visible. Using the same setup as described in the previous sections of this thesis, the sensors were exposed to transients (4 min) of 1-propanol and MIBK with concentrations of 100 ppm and 200 ppm (AG), followed by transients (4 min) of purified, dry air (ZG). The samples were continuously illuminated using the UV LEDs (emission wavelength: 278 nm) at an irradiance of ~23 mW/cm^2. All current timetraces are provided in the Appendix, section A.1.20. Figures 6.22b,c) show the timetraces of the current and the relative conductance change of the SPION-modified and an unmodified TNR-based sensor to 1-propanol. As described in the preceding sections, the TNR-based chemiresistors exhibit fast response and recovery dynamics combined with high response currents under UV illumination upon the exposure to 1-propanol. In comparison, the SPION-modified TNR-based sensor showed slightly reduced response currents to 1-propanol vapor. The relative conductance changes, however, demonstrate the drastic attenuation of the sensor response of the SPION-modified compared to the unmodified TNR-based sensor. Since the amplitude of the response currents of the modified and unmodified sensors resemble each other, the distinct $\frac{\Delta G}{G_0}$ for the SPION-modified TNR-based sensor results from the increased baseline current. Possibly, due to the energetic positions of the VB edges of TiO_2 and iron oxide,[206] the holes generated by the UV illumination are accumulated in the SPIONs. As a result, the recombination of photogenerated charge carriers in the TNRs is reduced. Thus, electrons accumulate in the TNRs and increase the baseline conductance, as shown in the timetrace for MIBK, where a baseline current above 100 nA is reached (cf. the Appendix, section A.1.20). However, this increased number of electrons seems to have no effect on the amount of ionosorbed oxygen, as the amplitude of the current responses remain almost unaffected.

Since the sensor responses of MOX-based chemiresistors are governed by the space-charge-layer forming at the surface of the individual grains, a combination of iron oxide as base material and nanostructured TiO_2, would be beneficial. In such a system, the effective

transfer of electrons from the iron oxide to the TiO_2 could result in an increase of the width of the space-charge-layer of the iron oxide base material. As a result, the Schottky-type barrier height between iron oxide grains would also increase, leading to high baseline resistances. The reaction of a reducing analyte on the TiO_2 surface will consume ionorbed oxygen species and thus accumulate electrons which can be transferred to the iron oxide. As a result, the change in the resistance of the iron oxide under analyte exposure is even more pronounced. For instance, Wang et al. reported improved thermally activated gas sensing performance for TiO_2-modified iron oxide nanostructures with rod morphologies to various analytes, including 1-butanol, acetone, and ethanol, compared to pure materials.[120] They attributed the high responses to the electron depletion of the iron oxide and the catalytic effect of the TNCs.

Chemical Sensitization

Tuning the chemiresistive properties by chemical sensitization is based on the activation of the target analyte. To this end, noble metals are deposited on the MOX-based chemiresistor, that can activate the analyte by the formation of reactive fragments. These fragments are spilled-over to the adjacent MOX and therefore the noble metal facilitates the chemical reaction on the MOX surface.[82] Kappler et al. reported improved sensor response signals to NO_2, CO, and CH_4 for atomically distributed Pt on SnO_2 films compared to those of unmodified SnO_2 sensors under thermal activation.[207]

In the present work, the deposition of Pt was achieved by sputtering sub-monolayer films on the TNR-based sensors aiming at chemical sensitization. By adjusting the duration of the sputtering, the nominal thickness of the Pt layer was varied between 0.5 nm and 1 nm, which are indicated as TNR/Pt 0.5 and TNR/Pt 1, respectively. These values correspond to sub-monolayers and were estimated by monitoring the Pt deposition on a QCM inside the sputtering instrument. Figure 6.23a) displays a representative SEM image of the TNR/Pt chemiresistor with a nominal thickness of 1 nm (TNR/Pt 1) that only shows

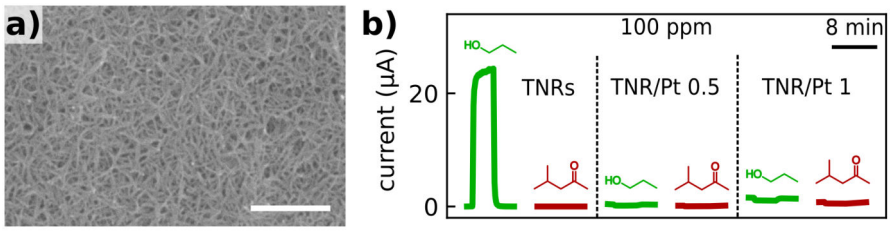

Figure 6.23: Surface modification of TNR-based chemiresistors by Pt sputtering. a) SEM image of the Pt-modified TNR thin film with a nominal Pt thickness of 1 nm (TNR/Pt 1). Scale bar: 200 nm. b) Photoactivated current transients of the unmodified and Pt-modified TNR-based chemiresistors with nominal thicknesses of 0.5 nm (TNR/Pt 0.5) and 1 nm (TNR/Pt 1) to 100 ppm 1-propanol and MIBK.

the TNR thin film structure without any indications of Pt deposit. However, the photoactivated response currents show the alteration of the Pt-modified chemiresistors which suggest a Pt deposition. For the chemiresistive measurements, the same setup was used as described in the previous sections of this thesis. 1-Propanol and MIBK with concentrations of 100 ppm and 200 ppm were used as AG and purified, dry air as ZG. All timetraces are provided in the Appendix, section A.1.20. Figure 6.23b) shows the distinct current transients of an unmodified TNR-based chemiresistor as well as those of the modified TNR/Pt 0.5 and TNR/Pt 1 chemiresistors, revealing no significant current responses except for the unmodified TNR-based sensor to 1-propanol. In addition, a very low response current in the range of tens of nA of the unmodified TNR-based chemiresistor to MIBK can be observed (cf. the Appendix, section A.1.20), indicating an oxidation beyond that of ketones or aldehydes, as described in section 6.1.3. The altered current responses of the Pt-modified TNR-based chemiresistors are attributed to the heterojunction between TiO_2 and Pt. Due to the large offset between the work function of Pt (5.65 eV)[208] and the energy difference from CB edge to vacuum level of TiO_2 (5.1 eV for anatase),[209] the electrons of the intrinsic n-type TiO_2 as well as the electrons generated by UV illumination are possibly dragged into the Pt and leave behind highly depleted TNRs. Further, photogenerated holes may cause the desorption of ionosorbed oxygen from the TiO_2 and, thus, the number of ionosorbed oxygen species significantly reduces. Therefore, the transduction mechanism is interrupted due to missing ionosorbed oxygen regardless of the catalytic property of the Pt. Similarly, Yamazoe proposed, that the chemical sensitization only works in the absence electronic interaction between the modifying material and the underlying MOX.[89]

As a further approach to achieve chemical sensitization, the TNR-based sensors were modified with nanostructured Au either by the deposition of gold nanoparticles (GNPs) on the TNR-based sensors or the formation of GNPs by in situ reduction of the Au precursor on the TNR surface.

For the modification with spherical GNPs (diameter: ~4 nm), 20 µL GNP dispersion in n-hexane was applied to the rotating TNR-based sensor, followed by 20 µL MeOH to strip the dodecylamine ligands of the GNPs. The characterization of the GNPs is provided in the Appendix, section A.1.19. The photoactivated chemiresistive responses to 1-propanol, MIBK, and 1-butylamine were obtained using the same setup as described in the previous sections of this thesis with concentrations of 100 ppm and 200 ppm. The corresponding timetraces are provided in the Appendix, section A.1.20. Figure 6.24a) shows a representative SEM image of the GNP-modified TNR thin film, where the GNPs are visible as small, bright dots distributed randomly yet evenly on the TNR film. Figure 6.24b) shows the current transients of an unmodified and the GNP-modified TNR-based sensor

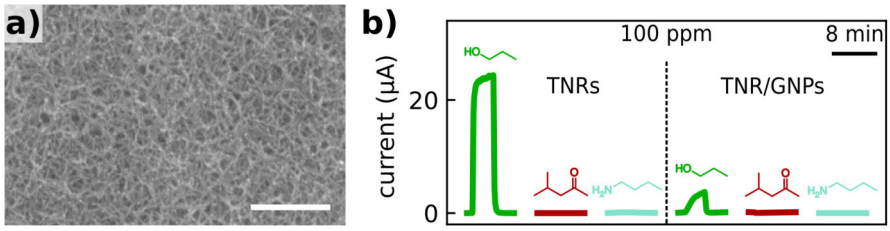

Figure 6.24: Surface modification of a TNR-based chemiresistor by the deposition of GNPs using spin-coating. a) SEM image of the GNP-modified TNR thin film. Scale bar: 200 nm. b) Photoactivated current transients of the GNP-modified and unmodified TNR-based chemiresistor to 100 ppm 1-propanol, MIBK, and 1-butylamine.

to 100 ppm of the respective analyte vapor. Upon the GNP modification, the selectivity is unaffected, showing no significant response currents to MIBK and 1-butylamine. Further, decreased response currents to 1-propanol are detected compared to those of the unmodified TNR-based chemiresistor. Again, we assume, that due to the offset of the work function of Au (5.2 eV)[208] and the energy difference from CB edge to vacuum level of TiO_2, electrons are depleted from the TNRs, causing a reduced amount of ionosorbed oxygen which ultimately leads to lower response currents.

In order to decorate semiconductor nanocrystals with noble metal particles, several protocols have reported the direct reduction of metal precursors on the semiconductor surface, which can be mediated by the photocatalytic activity of the semiconductor.[210,211] As described in section 6.1.2, the photocatalytic activity of the TNRs is also preserved after the deposition of the thin films as indicated by the OLAM decomposition and the chemiresistive sensor responses. This photocatalytic activity of the TNCs was used to reduce Au^{3+} ions directly on the TNR thin film. For this reaction, 25 µL gold(III)-chloride trihydrate in a water/ethanol mixture (1/1, *v*/*v*) were drop-casted on the TNR thin film. The sample was then placed inside the test cell, exposed to UV illumination using UV LEDs (emission wavelength: 278 nm) at an irradiance of ~23 mW/cm^2, and purged with 2000 ppm ethanol vapor in purified, dry air as carrier gas with a flow rate of 500 mL/min for 90 min. Ethanol was continuously supplied during the reaction, acting as a hole scavenger and thus preventing charging effects on the TiO_2.[211] By using two distinct concentrations of the Au precursor solution of 0.1 mol/L and 0.2 mol/L, the ratio of Au/TiO_2 was varied. To calculate the molar ratio of Au/TiO_2, the mass of the TNR thin film was estimated using the volume and the concentration of the dispersion used for drop-casting. Considering the OC determined by TGA, the mass of TiO_2 was calculated and transferred into the amount of substance by considering its molar mass. Comparably, the deposited amount of substance of Au was calculated from the volume and concentration of the precursor solution and the molar mass of Au. Thus, two Au/TiO_2 substance ratios of 1/24 and 1/12 were calculated for the precursor solution of 0.1 mol/L and 0.2 mol/L, respectively. Figure 6.25a) shows representative SEM images of the i) TNR/Au 0.1 and ii) TNR/Au 0.2

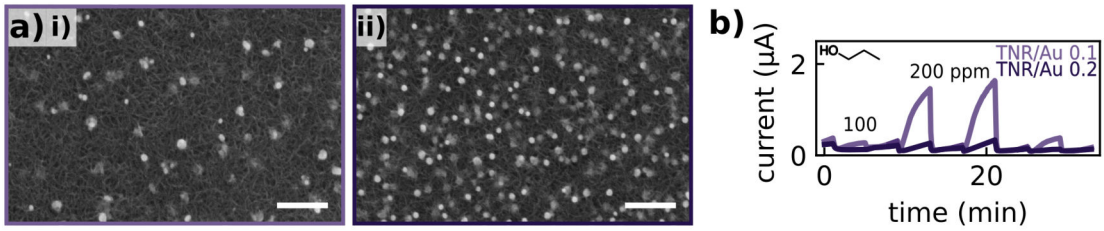

Figure 6.25: Surface modification of TNR-based chemiresistors by the in situ formation of GNPs using photoreduction of Au^{3+} ions. a) SEM images of the gold-modified TNR thin films using distinct precursor concentrations of i) 0.1 mol/L (TNR/Au 0.1) and ii) 0.2 mol/L (TNR/Au 0.2). Scale bars: 200 nm. b) Photoactivated current timetraces of the gold-modified TNR-based chemiresistors TNR/Au 0.1 and TNR/Au 0.2 to 1-propanol with concentrations of 100, 200, 200, and 100 ppm.

samples. For both films, the formation of GNPs of various sizes is visible as bright spots on the underlying TNR thin film. With increasing precursor concentration, the number of GNPs significantly increases and the size of the individual particles slightly decreases from ~25 nm for the TNR/Au 0.1 sample to ~20 nm for the TNR/Au 0.2 sample. This effect can be attributed to the increased concentration, which leads to the formation of more GNPs so that the amount of Au per particle is reduced and thus smaller GNPs are formed on the TNR thin film for the TNR/Au 0.2 sample. Figure 6.25b) shows the current timetraces of the modified TNR/Au 0.1 and TNR/Au 0.2 chemiresistors to 1-propanol vapor at concentrations of 100 ppm and 200 ppm under UV illumination. For the lower Au amount, the TNR/Au 0.1 sensor shows reduced response currents combined with slow response yet fast recovery dynamics compared to those of the unmodified TNR-based chemiresistor (cf. figure 6.24b)). For the increased amount of Au, the response current is further decreased as shown by the TNR/Au 0.2 sensor. Combining the results of GNP modification by photoreduction and spin-coating, the response current decreased with increasing number of deposited GNPs. We attribute this decline to the increased number of removed electrons with increasing total Au amount on the TNR thin film. This effect is assumed to reduce the amount of ionosorbed oxygen on the TiO_2 surface compared to the pure TNR thin film. In agreement with this assumption, the baseline current of the Au- and Pt-modified TNR-based sensors increased to several hundreds of nA, as shown in the timetraces provided in the Appendix, section A.1.20.

Based on the chemiresistive responses of the Au and Pt modification, a chemical sensitization of the TNR-based sensors was not successful possibly due to the removal of ionosorbed oxygen from the TiO_2 surface. However, further investigations on the electronic properties of the heterojunctions under these experimental conditions should be addressed, e.g., by using Kelvin probe force microscopy to spatially resolve the surface potentials, which should indicate charging effects on the surface of the materials.

In conclusion, first attempts on the modification of the TNR-based sensors demonstrated the possibility for depositing various materials after the sensor fabrication, by sputtering, spin-coating of nanocrystals, and the direct formation of GNPs by photocatalytic reduction. However, these modifications attenuated the chemiresistive responses to 1-propanol compared to those of the unmodified TNR-based sensors, especially demonstrating the challenge in chemical sensitization of the TNR-based photoactivated chemiresistors.

6.2 Functional Hybrid Membranes as Actuators

In this section, key findings are presented that were summarized and published in the journal article: F. Dobschall, H. Hartmann, S. C. Bittinger, N. Schulz, H. Schlicke, H. K. Trieu, T. Vossmeyer, "Freestanding Membranes of Titania Nanorods, Photocatalytically Reduced Graphene Oxide, and Silk Fibroin: Tunable Properties and Electrostatic Actuation", *Adv. Electronic. Mater.* **2025**, 11, 5, 2400602.[1]

The transfer process based on polydimethylsiloxane (PDMS) stamps was adjusted to the hybrid material in a preceding study within the framework of the author's Master thesis under the supervision of Hauke Hartmann, former PhD student at the University of Hamburg. In this preliminary study the mechanical properties of freestanding hybrid membranes composed of titania nanorods (TNRs), graphene oxide (GO), and silk fibroin (SF) were explored using atomic force microscopy (AFM) microbulge tests.[212] In the present study, the effect of photocatalytic GO reduction within the hybrid freestanding membrane was additionally investigated, focusing on its influence on the mechanical and electrical properties. Due to the formation of reduced graphene oxide (rGO), electrical conductivity is induced, which enabled the electrostatic actuation of TNR/(GO/rGO)/SF membranes. Further, an electrostatic model is presented that describes the deflection of the membrane as a function of the applied voltage.

6.2.1 Membrane Fabrication and Characterization

Freestanding hybrid membranes of GO, TNRs, and SF were fabricated in a two step process combining procedures established in our group for thin film deposition and thin film transfer, respectively. First, a substrate-supported thin film was deposited by layering the materials in the desired sequence using a layer-by-layer spin-coating (LbL SC) approach. This deposition method was reported for layered TNC thin films with cross-linkers of dicarboxylic acids[67] and GO.[2] Second, the thin film was transferred onto substrates with circular apertures or square cavities using a stamping process. The latter was presented in a preceding publication of our group, in which the prestress adjustment of organically cross-linked gold nanoparticle (GNP) membranes was demonstrated.[152]

Materials

Graphene Oxide

GO was synthesized following the method reported by Hummers et al. in 1958.[124] This procedure is based on the treatment of graphite in a highly oxidizing medium, followed by the exfoliation of individual GO sheets using ultrasonication. Details on the synthesis are provided in the Experimental section 7.2.

Figure 6.26 provides an overview of the GO characterization. A scanning electron microscopy (SEM) image of the freeze-dried GO is displayed in figure 6.26a), showing a porous network of sheet like structures. For film fabrication, GO was used from colloidal

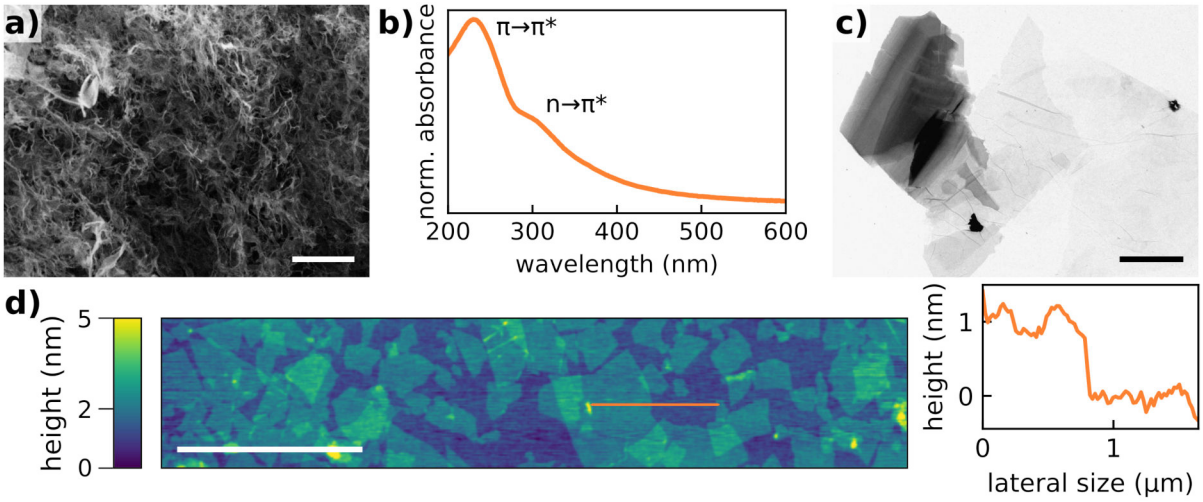

Figure 6.26: Characterization of synthesized GO used for the fabrication of hybrid films. a) SEM image of freeze-dried GO product. Scale bar: 20 μm. b) Normalized UV-vis absorbance spectrum of a diluted GO dispersion in water. c) TEM image of exfoliated GO sheets. Scale bar: 2 μm. d) Topographic AFM image of exfoliated GO sheets spin-coated on a SiO_2/Si wafer. The orange line indicates the location of the height line profile used to extract a sheet thickness of ~1 nm. Scale bar: 2.5 μm.

solutions of monolayered sheets, exhibiting the characteristic optical properties shown in figure 6.26b). The normalized ultraviolet-visible (UV-vis) absorbance spectrum of the diluted dispersion in water features the characteristic bands at ~235 nm and ~300 nm, which correspond to the $\pi - \pi*$ and the $n-\pi*$ transitions, respectively. These bands arise from the combination of graphitic sp^2 hybridized and oxidized sp^3 hybridized areas in GO.[213] Figures 6.26c) and d) show a transmission electron microscopy (TEM) image and the AFM analysis of individual sheets, respectively. To visualize the individual sheets, the solution was deposited on a substrate (either TEM grid or SiO_2/Si wafer), and the spatial dimensions were studied. The lateral dimensions of individual sheets obtained from TEM as well as AFM were up to 4 µm, and the sheet thickness obtained from AFM was ~1 nm. This thickness is in good agreement with values from the literature where an average sheet thickness of ~1.1 nm was reported for an individual atomic layer of GO.[213,214]

TiO_2 Nanorods

TNRs were synthesized according to the seeded growth method reported by Gordon et al.[40] using $TiCl_4$ as precursor (cf. section 6.1.2). In order to obtain TNRs with a higher aspect ratio compared to the ones used for the photoactivated thin film chemiresistors, the amount of added precursor solution was varied.[215] For the seed formation, the amount of added precursor was reduced leading to the formation of a reduced number of seeds. The amount of added precursor solution in the growth step was increased to deposit more material per rod. However, the addition rate was lowered to suppress unwanted seed formation due to accumulation of monomers and high temperatures. Ultimately, oleylamine (OLAM)-stabilized TNRs were obtained and dispersed in chloroform for further use. Detailed data on the adjustments of the protocol for TNR synthesis are described in the Experimental section 7.5.

Figure 6.27a) displays an exemplary TEM image of the TNRs which were used for the

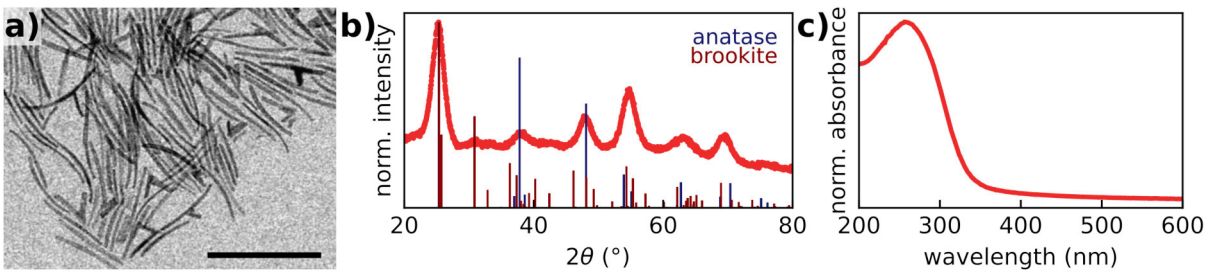

Figure 6.27: Characterization of synthesized TNRs used for the fabrication of hybrid films. a) Exemplary TEM image of the TNRs. Scale bar: 100 nm. b) Normalized x-ray diffractogram of the TNRs deposited on a silicon wafer with corresponding reference reflections for anatase and brookite. Reference cards were taken from Refs. [167, 168] c) Normalized UV-vis absorbance spectrum of the TNRs spin-coated from dispersion in chloroform on a quartz slide.

hybrid film fabrication. The TNRs had an average length of 64 ± 11 nm and a diameter of ~4 nm. Further, figure 6.27b) shows the normalized x-ray diffraction (XRD) pattern of the as-synthesized TNRs. Here, the reflections not only correspond to the anatase crystal phase, but also to the brookite crystal phase, suggesting an anatase/brookite mixed phase of the TNRs, as discussed for the shorter TNRs presented in section 6.1.2 and as reported in previous studies.[40,67] The normalized UV-vis absorbance spectrum is displayed in figure 6.27c) and shows an absorbance maximum at ~265 nm, which is related to the band gap energy of the TNRs. Again, this maximum absorbance in the UV range was used in this study to initiate the photocatalytic activity of the TNRs and thereby tune the composition of the hybrid membranes. The organic content (OC) of the TNRs was determined as ~35% using thermogravimetric analysis (TGA) (cf. the appendix, section A.1.4).

Silk Fibroin

SF was purchased in aqueous solution and is usually extracted from the cocoon of the silk worm by degumming in a boiling sodium carbonate solution. After dissolution in lithium bromide solution, it is dialyzed against ultrapure water, centrifuged, and finally dispersed in ultrapure water.[216] The protein is mainly composed of four amino acids: Ala, Gly, Ser, and Tyr with amounts of ~30%, ~46%, ~12%, and ~5%, respectively. Among these, Ala, Gly, and Ser form the repetitive amino acid sequence Gly-Ser-Gly-Ala-Gly-Ala,[217] which enables the self-assembly of the protein into crystalline antiparallel β-sheets and is stabilized by hydrogen bonds. Tyr is predominantly present in the β-turns, the latter connecting the antiparallel strands.[217,218]
Figure 6.28a) displays a schematic of the primary and secondary structure of the protein focusing on the hydrogen bond stabilized and crystalline β-sheet regions. Figure 6.28b) shows the normalized UV-vis absorbance spectrum of SF in aqueous solution which displays two characteristic features. The absorbance peak at ~280 nm originates from the

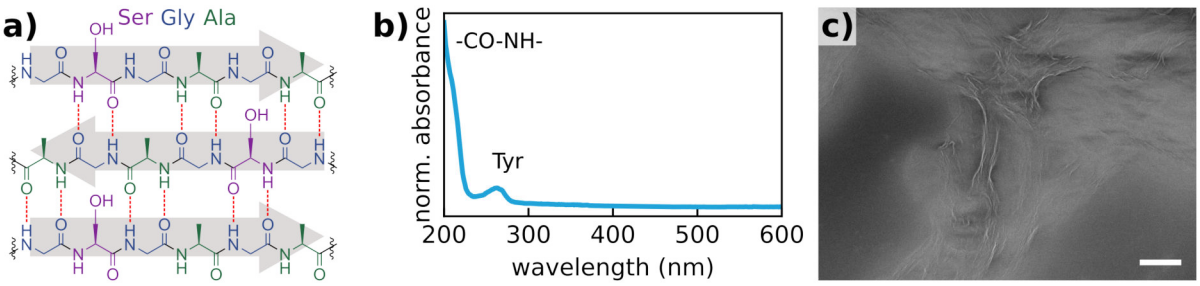

Figure 6.28: Characterization of SF used for the fabrication of hybrid films. a) Schematic of the repeated primary amino acid sequence (Gly-Ser-Gly-Ala-Gly-Ala) self-assembling into an antiparallel β-sheet structure. The antiparallel strands are connected by hydrogen bonds, the latter are indicated as dashed, red lines. b) Normalized UV-vis absorbance spectrum of the diluted SF solution in water. c) SEM image of SF spin-coated from aqueous solution on a silicon wafer. Scale bar: 4 μm.

aromatic system of Tyr. Further, the increasing absorbance towards lower wavelengths arising at ~240 nm is attributed to the peptide bond between the amino acids, which typically absorb in the range between 190–230 nm.[219] Figure 6.28c) shows a representative SEM image of the SF deposited on a silicon substrate reveling a mostly smooth and flat layer with some wrinkles.

Film Deposition via Layer-by-Layer Spin-Coating

The first step in fabricating the freestanding hybrid membranes was the deposition of multilayered thin films of GO, TNRs, and SF using a method that was adapted from the procedure established in our group for layered films of TNCs and molecular cross-linkers.[67] For this purpose, the materials were deposited alternately from solution using LbL SC on various substrates such as quartz slides and SiO_2/Si wafers. Recently, we replaced the dicarboxylic acid for GO[2] that functions as a cross-linker by attaching to the TNRs. As discussed in section 4.3.1 these composites are stable due to the high affinity of carboxy groups to the TiO_2 surface.[135,137] Additionally, this material combination enables the photocatalytic reduction of GO to rGO by consuming the photogenerated charge carriers of the TiO_2, when the latter is exposed to deep-ultraviolet (DUV) illumination. Due to various interactions between GO and SF, such as hydrogen bonds, polar interactions, and $\pi - \pi$ stacking,[142] SF can be incorporated to further support the stability of the hybrid thin films. Figure 6.29a) shows a schematic of the hybrid thin film based on GO as the matrix material, interacting well with the other two materials. Further, the structure was designed to spatially separate the TNRs and SF, to prevent photodegradation of the SF. Accordingly, the TNRs were incorporated in the top layers providing photocatalytic

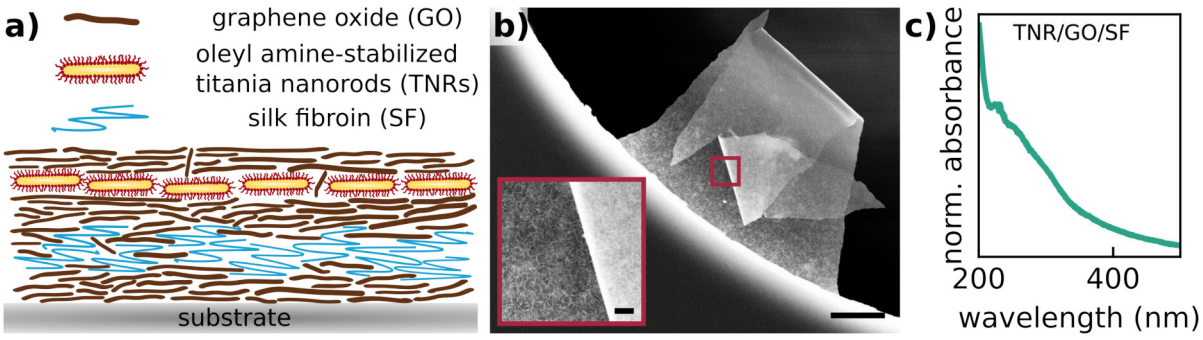

Figure 6.29: a) Schematic depiction of the hybrid thin film consisting of TNRs, GO, and SF. b) Exemplary SEM image of the hybrid membrane M1 after burst test that shows the distinct textures of the top and bottom surface. Scale bar: 4 µm. The inset shows the top surface in the red framed section in higher magnification. Scale bar: 400 nm. c) Normalized UV-vis absorbance spectrum of the hybrid thin film spin-coated on a quartz slide. Subplots a,b) were adapted and reprinted from Dobschall el al., Ref. [1], *Creative Commons CC-BY 4.0* license ©2025 The Authors. Adv. Electron. Mater. published by Wiley-VCH GmbH. (DOI: 10.1002/aelm.202400602)

activity at the surface, while the SF was incorporated in the lower layers. The exact sequence of deposition steps is provided in the Experimental section 7.5. Figure 6.29b) shows an SEM image of the remaining hybrid membrane parts after burst tests (cf. section 6.2.2), demonstrating the distinct structural differences between the top and bottom surface. While the GO/SF dominated bottom surface has a smooth texture, the top surface is governed by the rather homogeneous distribution of TNRs that are mostly covered with GO sheets. On the larger scale, optical micrographs revealed a quite homogeneous morphology, except for some TNR aggregates visible as bright spots (cf. the Appendix, section A.1.21). UV-vis absorbance spectroscopy was conducted on hybrid TNR/GO/SF thin films that were deposited on quartz substrates, and a corresponding spectrum is displayed in figure 6.29c). This spectrum shows a broad shoulder between ~350–230 nm resulting from the absorbance overlap of the features of the individual materials, and the strong absorbance of the SF peptide bonds below ~230 nm.

Transfer Process

The stamping process used for transferring the hybrid TNR/GO/SF thin films onto substrates with apertures or cavities was adapted from the procedure established in our group to tune the prestress of organically cross-linked GNP membranes.[152] Figure 6.30 schematically shows the crucial steps for the transfer, and a detailed schematic of the this process is provided in the Experimental section 7.5. To enable the transfer process, the hybrid thin films were sandwiched between two polymer layers with orthogonal solubility properties. A sacrificial layer of polyvinyl alcohol (PVA) was used underneath the hybrid thin films, and a protective layer of poly(methyl methacrylate) (PMMA) was used on top of the hybrid thin films to stabilize the latter during the transfer process. Further, the transfer was facilitated using GO as the undermost layer of the hybrid thin films. First, the hybrid thin

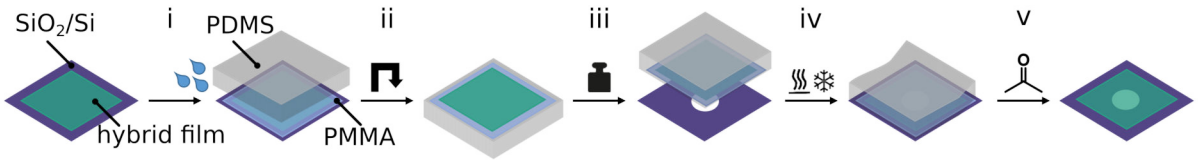

Figure 6.30: Schematic of the fabrication process of freestanding hybrid TNR/GO/SF membranes. i: Detaching the hybrid film (green) from the substrate by dissolving the PVA layer at the film/substrate interface with water. A PDMS stamp (transparent grey) is placed on the PMMA layer (light blue) with the latter protecting the hybrid film. ii: Removing the stamp with the PMMA layer and hybrid film attached to it. iii: Applying controlled pressure to the stamp placed on the target substrate. iv: Detaching the film from the stamp by cycles of heating and cooling, and lifting the stamp. v: Dissolving the protective PMMA layer in acetone to obtain the freestanding hybrid membrane. Rearranged and reprinted from Dobschall el al., Ref. [1], *Creative Commons CC-BY 4.0* license ©2025 The Authors. Adv. Electron. Mater. published by Wiley-VCH GmbH. (DOI: 10.1002/aelm.202400602)

films were divided into four parts and removed along the edges of the substrate to create substrate-supported thin film sections of desired size (~3×3 mm ^{2}). Each thin film section was then transferred individually. A small amount of water was applied to the rim of the film and was dragged into the film/substrate interface where it dissolved the sacrificial PVA layer (figure 6.30, step i). A PDMS stamp was gently pressed against the film, to detach it from the substrate and to transfer it onto the stamp (figure 6.30, steps i, ii). Next, the hybrid film was transferred by pressing the stamp against the target substrate and thus covering the cavity or aperture of the target substrate with the hybrid film (figure 6.30, step iii). By applying three heating and cooling cycles, the thin film was detached from the stamp (figure 6.30, step iv), caused by the different thermal expansion coefficients of the PDMS stamp and the partially substrate-supported hybrid film protected by the PMMA layer.[220] This process allowed for the removal of the stamp, leaving behind the freestanding membrane which was still protected by the PMMA layer. By submerging the substrate in acetone, the PMMA layer was dissolved (figure 6.30, step v). To prevent rupturing of the membranes, the acetone was exchanged for methoxyperfluorobutane (MPFB), which has a lower surface tension and allows for the removal of the substrate from the liquid phase.[221] After drying at ambient conditions, the hybrid membranes with freestanding sections of up to ~6×10^4 μm^2 were exposed to DUV illumination and their mechanical properties were investigated (cf. section 6.2.2). Further, their electrostatic actuation was demonstrated (cf. section 6.2.3). The hybrid film thickness was examined via AFM analysis of height profiles measured at the edges of the film. Exemplary AFM images of the transferred membranes are provided in the Appendix, section A.1.21, showing a typical membrane thickness between 25–30 nm.

TiO_2-Mediated Photocatalytic Tuning of Hybrid Film Composition

After the fabrication of the hybrid TNR/GO/SF membranes, the composition was tuned, mediated by the photocatalytic effect of the TNRs, and the evolution of the optical, electrical, and structural properties of the hybrid membranes was investigated. In order to trigger the generation of photoexcited charge carriers, the samples were exposed to DUV illumination in ambient conditions using a custom-built light source with a main emission wavelength of 254 nm and an irradiance of ~520 mW/cm^2 (cf. the Appendix, section A.1.1). Since the TNRs are sandwiched between layers of GO, the generated electrons are accessible to the adjacent GO, where they can promote the restoration of the aromatic system. This photocatalytic reduction of GO results in the formation of rGO. In earlier works, the formation of rGO in GO/TiO_2 composites was carried out in the presence of ethanol, which scavenges the generated holes and ensures the charge balance in the pho-

toexcited TiO_2.[137,222] Without the presence of an external hole scavenger, the OLAM ligands of the TNRs are oxidized and degraded.[176,177] In a recent study, we explored the tunability of the properties of comparable TNC/GO nanocomposites via photocatalytic reduction of GO and showed the decomposition of the OLAM by using x-ray photoelectron spectroscopy (XPS), among other methods.[2] Further, in section 6.1.2 this photocatalytic decomposition of OLAM is discussed for pure TNC thin films fabricated from dispersions of differently shaped particles using ATR-FTIR spectroscopy. Since the excitation was carried out in ambient conditions in the presence of water, oxygen, and other reactive species, e.g., superoxide- and hydroxy radicals, these are likely to be involved in the photocatalytic processes.[19]

Figure 6.31a) shows the UV-vis absorbance spectra of the hybrid thin film before and after the DUV exposure for 80 min. Not only the general increase in absorbance above a wavelength of ~300 nm, but also the significant red shift of the absorbance shoulder from ~230 nm to ~280 nm, are indicating the formation of rGO.[213] This red shift is caused by the restoration of the sp^2 hybridized aromatic areas.[223] Further, UV-vis spectra of individual components before and after DUV exposure are in agreement with the formation of rGO, since the spectra of the TNRs and SF do not show any absorbance shifts (cf. the Appendix, section A.1.21). The reference absorbance spectra of pure GO also revealed UV-induced changes indicating the photoreduction in the absence of a photocatalyst,[132] as described in section 4.3.1. To demonstrate the significant benefit of incorporating TNRs, the conductance of a TNR/(GO/rGO) film and a pure GO thin film - both fabricated using the same volume of GO - were compared. Figure 6.31b) displays the evolution of the conductance with increasing DUV illumination time. While only a slight increase in the conductance of the pure GO thin film with increasing DUV exposure times can be observed, the conductance of the TNR/(GO/rGO) thin film increases significantly,

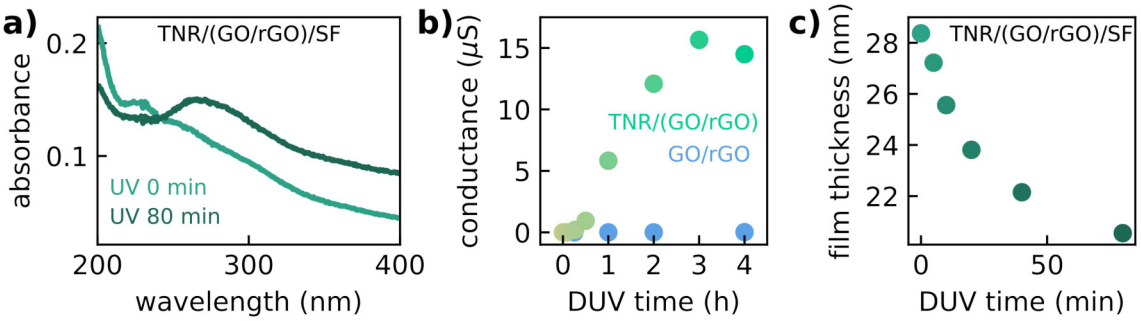

Figure 6.31: Photocatalytic tuning of the hybrid film composition mediated by TNRs under DUV illumination at 254 nm. a) Changes in the UV-vis absorbance spectra of the hybrid thin film spin-coated on a quartz slide upon DUV illumination. b) Evolution of the conductance of thin films with increasing DUV illumination for pure GO (blue) and TNR/GO (green) films, respectively. The conductance data were kindly provided by Dr. Sophia Caroline Bittinger, research associate at the CIC biomaGUNE. c) Evolution of the hybrid film thickness as a function of DUV exposure time.

demonstrating the accelerated formation of rGO in the presence of TNRs as photocatalyst. Exciting the TNRs not only promotes GO reduction, but also triggers radical formation, as demonstrated by Soria et al. using electron spin resonance (ESR).[224] Based on these radicals, various reactions, e.g., radical polymerization and cross-linking in organic materials, can be initiated, as demonstrated for various TiO_2-based nanostructures.[225–227] Figure 6.31c) shows the thickness evolution of a hybrid membrane as a function of the DUV exposure time between 0–80 min. Here, a significant decrease in the thickness with increasing DUV exposure time can be observed, which is attributed to the cross-linking between the different organic membrane components. For increasing exposure times, the compaction slows down, and after 80 min DUV exposure, the membrane thickness was reduced by ~30%. For comparison, Hu et al. attributed the increased mechanical strength of GO/SF biopapers upon electromechanical microstamping to the reduction of GO as well as the cross-linking of SF.[228] In addition to the cross-linking, the reduction of the thickness could also result from the loss of organic material caused by the photocatalytic activity of the TNRs. In this regard, further examination on the impact of the photocatalytic tuning of the hybrid film composition needs to be done using microgravimetric analysis before and after the DUV illumination to assess loss of organic material.

In conclusion, a post-fabrication composition tuning of the hybrid TNR/GO/SF membranes mediated by the photocatalytic properties of the TNRs was presented that can be used to tune the optical, electrical, and structural properties of the membranes. It is concluded that changes in the properties originate from two major effects: the reduction of GO to rGO and, most likely, the cross-linking of the organic materials. The membranes exposed to DUV illumination for at least 60 min are referred to as TNR/(GO/rGO)/SF hybrid membranes in the following sections.

6.2.2 Mechanical Properties

The mechanical properties of the hybrid membranes and especially the influence of the photocatalytic composition tuning were characterized using AFM microbulge tests. For this purpose, the hybrid membranes were transferred onto substrates with a circular aperture. The measurement setup is schematically shown in the Experimental section 7.7, and was used in previous studies to analyze the mechanical properties of various materials such as organically cross-linked TNC and GNP membranes.[67,229,230] To bulge the membrane, the pressure underneath the substrate was reduced, and the deflection was determined using in situ AFM measurements. At each set pressure, ten line scans - which were evenly spaced in the direction orthogonal to the scan direction - were acquired to measure the shape of the bulged membrane. The total scan area was 100×100 μm^2 and each line scan

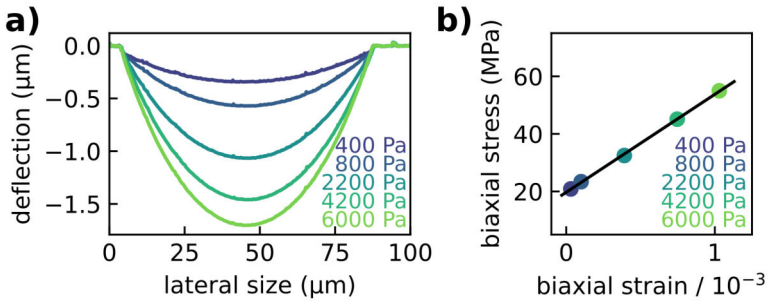

Figure 6.32: a) Baseline-corrected topographic line scans of hybrid TNR/GO/SF membrane M2 recorded at distinct differential pressures. b) Stress-strain curve obtained by fitting a spherical cap to the bulged membrane, with the latter being approximated as part of a thin-walled spherical pressure vessel. The linear curve was fitted to the data and used to extract the biaxial modulus and prestress as slope and intercept of the linear fit, respectively. Subplot a) was reprinted from Dobschall el al., Ref. [1], *Creative Commons CC-BY 4.0* license ©2025 The Authors. Adv. Electron. Mater. published by Wiley-VCH GmbH. (DOI: 10.1002/aelm.202400602)

consisted of 512 pixels. Figure 6.32a) displays exemplary baseline-corrected bulge line profiles traversing the apex of the bulged membrane for increasing differential pressure between 0.4–6 kPa. Deflections were determined with respect to the substrate-supported thin film sections and reached up to ~1.8 µm for the maximum differential pressure of 6 kPa. The topographic data were analyzed using a geometric model, by approximating the bulged membrane as a spherical cap.[147] Based on this approximation, the pressure-dependent radius of the spherical cap R_C was obtained as a fit parameter.[230] A cross-sectional scheme of the bulged membrane including the relevant parameters is provided in the Appendix, section A.1.22. By considering a thin-walled spherical pressure vessel, the biaxial stress σ_{bi} acting on the membrane was computed, according to equation 5:[147]

$$\sigma_{bi} = \frac{\Delta P R_C}{2 t_m} \tag{5}$$

where ΔP is the differential pressure and t_m is the membrane thickness. Approximating the bulged membrane as a thin-walled spherical pressure vessel requires $t_m << R_C$, a condition which is met in all our experiments. The membrane thicknesses were determined by AFM at the step edges prior to the bulge tests, as 26.9 nm and 29.5 nm for membrane M1 and M2, respectively (cf. the Appendix, section A.1.21). Variations in the full arc length s of the bulged membranes were determined geometrically from R_C, according to equation 6:[229]

$$s = 2 R_C \arcsin \frac{a_r}{R_C} \tag{6}$$

in which a_r is the aperture radius. The latter was measured prior to the bulge tests by optical microscopy (cf. the Appendix, section A.1.21). The aperture diameters were ~105 µm and ~84 µm for membrane M1 and M2, respectively. Considering the variations of the

arc length at different pressures, the biaxial strain ε_{bi} was calculated using equation 7.[229]

$$\varepsilon_{bi} = \frac{s}{2a_r} - 1 \tag{7}$$

Here, the initial arc length without differential pressure was approached by the aperture diameter $2a_r$. By plotting the biaxial stress σ_{bi} against the biaxial strain ε_{bi} for every applied differential pressure, stress-strain curves are obtained, as shown in figure 6.32b). In the elastic regime, the biaxial stress and strain show a linear relation, which can be described using equation 8.

$$\sigma_{bi} = Y\varepsilon_{bi} + \sigma_0 \tag{8}$$

Here, the biaxial modulus Y is the constant of proportionality and σ_0 is the membrane's prestress which were extracted from the slope and intersect of the linear fit, respectively. In this regard, tense membranes are assigned a positive, and slack membranes are assigned a negative prestress value. Further, the biaxial modulus Y is related to the Young's modulus E via the Poisson ratio ν,[147,231] according to equation 9.

$$Y = \frac{E}{1-\nu} \tag{9}$$

Figure 6.33 shows an overview on the stress-strain curves obtained for hybrid membranes a) M1 and b) M2, that were made as duplicates to test the reproducibility of membrane fabrication and modification. Small deviations between the stress-strain data for ascending and descending pressure (cf. figures 6.33a,b) part i)) indicate almost purely elastic behavior of the membranes in the pressure range between 0.1–6 kPa. The minor hysteresis is attributed to retarded elastic deformation and pure viscous creep, as described in pre-

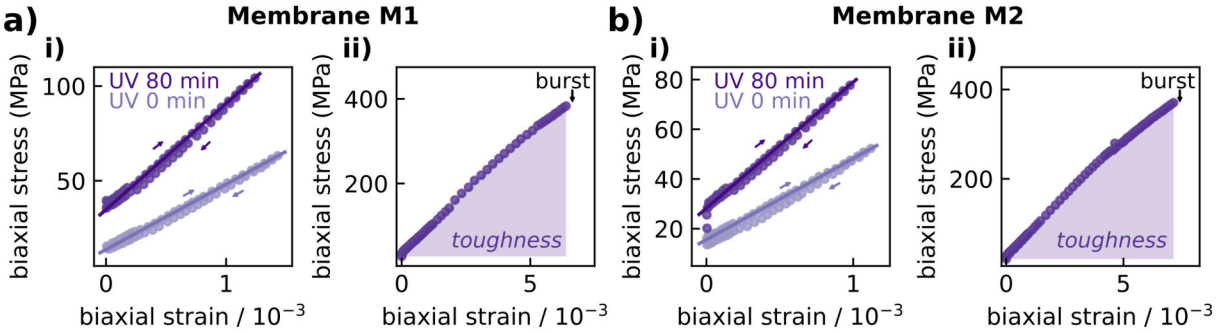

Figure 6.33: Mechanical properties of hybrid membranes a) M1 and b) M2 probed by microbulge tests with in situ AFM measurements. i) Stress-strain curves of the hybrid membranes before (light purple) and after 80 min DUV exposure (dark purple). Linear curves were fitted to the data recorded in the direction of ascending pressure. ii) Stress-strain curve of the burst test with the toughness of the membrane calculated from the area underneath the graph. Rearranged and reprinted from Dobschall el al., Ref. [1], *Creative Commons CC-BY 4.0* license ©2025 The Authors. Adv. Electron. Mater. published by Wiley-VCH GmbH. (DOI: 10.1002/aelm.202400602)

vious studies on organically cross-linked GNP membranes,[230] carbon nanomembranes from cross-linked aromatic self-assembled monolayers,[232] and organically cross-linked TNC membranes.[67] For consistency, the biaxial modulus and the prestress were always extracted from the linear fit in the direction of ascending pressure (cf. figures 6.33a,b) part i)). An overview on the mechanical data of both membranes is provided in table 6.1. These results show that membranes M1 and M2 had very similar elastic properties with an averaged biaxial modulus and prestress of ~33 GPa and ~14 MPa, respectively. By applying equation 9, the biaxial modulus was translated into the Young's modulus of ~22 GPa, using a Poisson ratio of $\nu = 0.33$, as reported for disordered dense films of various nanomaterials.[233,234] For comparison, Cho et al. reported a Young's modulus of 22 GPa for similar GO/SF composite films by applying a nanoindentation method.[146] Conducting bulge and buckling tests on GO/SF membranes, Hu et al. reported increasing Young's moduli between ~10 GPa to ~145 GPa with increasing fraction of GO incorporated from 0–23.5 vol%. For a GO volume fraction of ~3%, they measured a modulus of ~25 GPa.[142] Young's moduli of the individual components were reported to reach values up to ~207 GPa for pure GO monolayers[235] and between 4–22 GPa for SF films. For the latter, the Young's modulus increases with increasing amount of crystalline β-sheet regions.[236,237] Further, membranes of TNRs cross-linked by 1,12-dodecanedioc acid had a Young's modulus of ~5 GPa, as previously reported in our group.[67]

As discussed in section 6.2.1, the membrane composition was tuned by photocatalytic GO reduction and cross-linking of the organic material, both mediated by the TNRs upon DUV exposure. To examine the possibility of adjusting the membranes mechanical properties by tuning the membrane composition, microbulge tests were repeated after 80 min of DUV exposure on the TNR/(GO/rGO)/SF membranes. These stress-strain data are also displayed in figures 6.33a,b) part i) (dark purple), and reveal enhanced mechanical properties with an averaged Young's modulus of ~35 GPa and an averaged prestress of ~32 MPa for both membranes (M1 and M2). Again, a reduction in the membrane thickness upon DUV illumination of ~30% was determined for M1 and M2 (cf. table 6.1), which is attributed to the compaction of the membranes by cross-linking of the organic materials. We assume that this cross-linking between the different components resulted in the increased stiffness of DUV-exposed hybrid membranes. Comparable to our findings, Hu et al. reported an increase in the mechanical strength of GO/SF biopapers upon electromechanical microstamping, and attributed the changes to the cross-linking of SF and reduction of GO.[228] As a supportive effect, the formation of rGO might also increase the mechanical properties. For instance, Turchanin et al. reported an increase in the Young's modulus from ~12 GPa to ~48 GPa for carbon nanosheets by increasing the degree of order in the carbon network using thermal annealing.[238] They attributed the

Table 6.1: Properties of the hybrid membranes M1 and M2 before and after the composition tuning by DUV exposure for 80 min. The quantities listed are the: membrane thickness t_m, biaxial modulus Y, Young's modulus E, prestress σ_0, biaxial ultimate stress σ_{ult}, biaxial ultimate strain ε_{ult}, and toughness U_T.

Sample	t_m / nm	Y / GPa	E / GPa	σ_0 / MPa	σ_{ult} / MPa	ε_{ult} / %	U_T / MJ/m^3
M1	26.9	34.5	23.1	13.7	-	-	-
M2	29.5	32.6	21.8	15.6	-	-	-
M1UV	17.3	56.3	37.5	34.9	383.2	0.64	1.13
M2UV	21.0	50.9	33.9	28.3	370.4	0.71	1.25

degree of order to the size of sp^2 hybridized aromatic areas, which also increases upon the photocatalytic reduction.[223]

In addition to the elastic mechanical properties, the ultimate mechanical properties of the DUV-exposed TNR/(GO/rGO)/SF membranes were determined by burst experiments. For these investigations, the pressure was increased until the membranes ruptured. The corresponding stress and strain of the final set of collected measurement data prior to this point are defined as the ultimate biaxial stress σ_{ult} and the ultimate biaxial strain ε_{ult}. Figures 6.33a,b) part ii) show the corresponding stress-strain curve, from which the toughness U_T was calculated by integrating the curve up to the point of burst. This area underneath the graph indicates the maximum energy that can be stored in the membrane. Only few remains of the freestanding membrane sections can be observed in optical micrographs of the substrates after the burst experiments. These images are provided in the Appendix, section A.1.21. The ultimate parameters are presented in table 6.1, and are again very similar for membranes M1 and M2 with averaged values of ~377 MPa, 0.68%, and ~1.2 MJ/m^3 for the ultimate biaxaial stress, ultimate biaxial strain, and toughness, respectively. Comparable results with a toughness of ~1.5 MJ/m^3 were reported by Hu et al. for GO/SF membranes with a GO fraction of ~11.5 vol%.[142] Note, that the effect of GO reduction was not investigated in their study.

In conclusion, tuning of the composition mediated by the photocatalytic activity of the TNRs affected the mechanical properties of the hybrid membranes significantly, leading to an increase in the Young's modulus and the prestress. We assume that this increase in the Young's modulus upon DUV exposure was predominantly due to the cross-linking between the organic membrane components.

6.2.3 Electrostatic Actuation

For the fabrication of electrostatically driven membrane actuators, the presented photocatalytic tuning of the hybrid film composition was implemented to induce electrical

conductivity due to the formation of rGO. The actuators were fabricated by stamping the hybrid TNR/GO/SF thin film onto a silicon substrate, with the latter featuring an array of square cavities. A cross-sectional SEM image of a substrate is provided in the Appendix, section A.1.23, and shows the cavity's depth of ~21.5 µm and edge lengths of ~245 µm, resulting in freestanding membrane sections of ~6×10^4 µm^2. By exposing the insulating TNR/GO/SF membrane to DUV illumination for 120 min, it was turned into a conductive TNR/(GO/rGO)/SF membrane. This adjustment is based on the reduction of GO, as described in section 6.2.1. The thickness of hybrid membrane M3, used for the electrostatic actuation, after DUV exposure was ~10 nm after DUV exposure (cf. the Appendix, section A.1.21). The sample consisted of two separate conductive planes: the membrane serving as top electrode and the p-doped silicon substrate as bottom electrode. Separation of the electrodes was achieved by a thermally grown layer of silicon oxide and the membrane was contacted by gold electrodes deposited on top of the silicon oxide layer. A schematic of the setup is provided in the Appendix, section A.1.23, that illustrates the actuation of the membrane by applying voltage signals, and measuring the resulting deflection of the membrane in parallel using AFM analysis.
Figure 6.34a) shows the applied bias voltage with rectangular signals ranging from -40 V

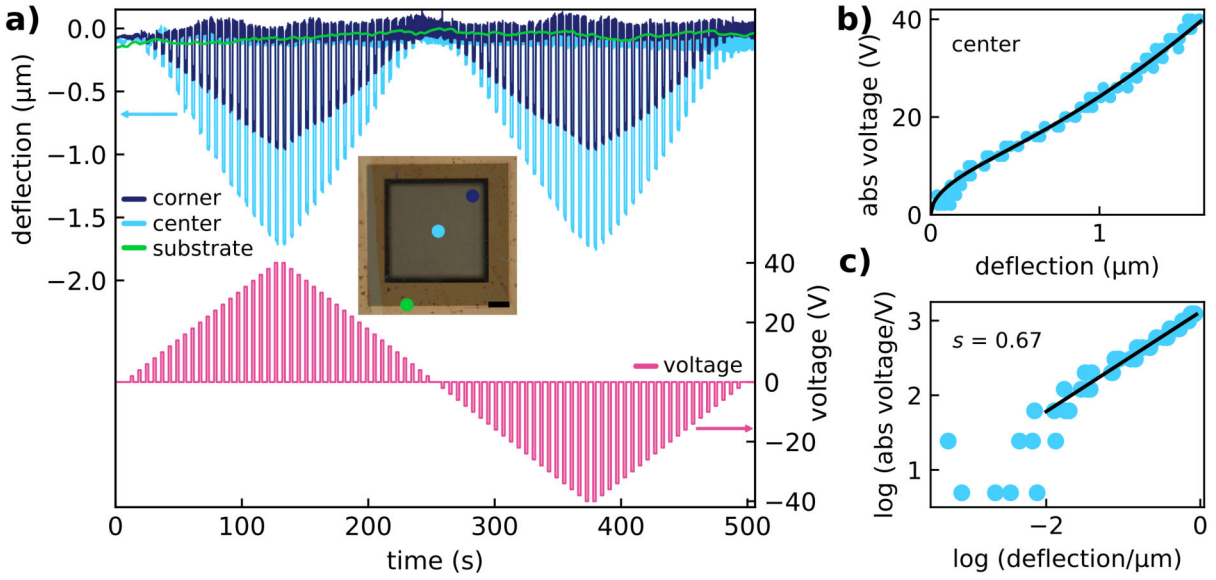

Figure 6.34: Electrostatic actuation of the TNR/(GO/rGO)/SF membrane M3. a) Baseline-corrected deflection timetraces at different positions on the freestanding membrane (blue traces) and the substrate-supported section (green trace) in response to the applied voltage (red trace). The inset shows an optical micrograph of the membrane spanning the square cavity (edge length: ~245 µm, depth: ~21.5 µm) with colored dots marking the different positions of deflection measurements. Scale bar: 50 µm. b) Voltage-deflection correlation obtained at the center of membrane M3. The fit of equation 10 to the data within the deflection range of 0.1–1.7 µm is indicated as the solid line. c) log/log plot of the voltage-deflection correlation in the deflection range between 0–1 µm. The deflection was measured at the center of the membrane. The solid line represents a linear fit to the data within the range of 0.1–1 µm with a slope of 0.67. Rearranged and reprinted from Dobschall el al., Ref. [1], *Creative Commons CC-BY 4.0* license ©2025 The Authors. Adv. Electron. Mater. published by Wiley-VCH GmbH. (DOI: 10.1002/aelm.202400602)

to +40 V and the corresponding baseline-corrected deflections obtained at different positions on the membrane using the AFM. The latter was operated in intermittent contact mode without scanning the sample. As expected, the membrane was always deflected toward the bottom electrode regardless of the bias polarity, since the force acting on the membrane only depends on the absolute value of the voltage.[158] For increasing absolute voltages, the deflection also increased, with the latter reaching up to ~1.7 µm at ±40 V measured at the center of the membrane. Further, the deflection was also measured closer to the edge of the freestanding membrane section where smaller deflections were obtained. The deflection timetraces for both positions on the freestanding membrane section were fully reversible and thus showed the elastic behavior of the membrane in this potential range (cf. figure 6.34a) blue traces). In order to exclude a direct response of the AFM tip to the applied voltage, the AFM tip was positioned on a substrate-supported section of the membrane. When applying the same rectangular voltage signals, the AFM tip remains undisturbed, as shown by the green trace in figure 6.34a).
To describe the correlation between the applied bias voltage V and the membranes' center point deflection h, a simple parallel-plate capacitor was assumed. This capacitor is assembled from the hybrid membrane and the silicon wafer as the respective electrodes.[230,239] Further, this approximation implies a homogeneous electric field and therefore neglects field changes due to the membrane deformation during actuation. Following these conditions, the voltage-deflection correlation can be described, according to equation 10.[158]

$$\frac{\epsilon V^2}{2d^2} = \frac{8Yt_\mathrm{m}}{6(1+\nu)a_\mathrm{e}^4}h^3 + \frac{3.393\sigma_0 t_\mathrm{m}}{a_\mathrm{e}^2}h \tag{10}$$

Here, d is the distance between the electrodes (21.5 µm), a_e is half the edge length of the cavity (122.5 µm), Y is the membrane's biaxial modulus, σ_0 is the prestress, t_m is the membrane's thickness (~10 nm), ν is the Poisson ratio (0.33),[233,234] and ϵ is the permittivity approximated by ϵ_0 for vacuum. According to our previous study, in the range of small deflections ($h << d$), the model provides a useful description of the deflection-voltage correlation, as long as the conditions $h << a_\mathrm{e}$ and $t_\mathrm{m} << h$ are fulfilled.[230] A detailed derivation of equation 10 is provided in the Appendix, section A.1.23. Figure 6.34b) displays the applied absolute voltage as a function of the membrane's center point deflection with the solid line representing the fit of the data according to equation 10. Fulfilling the aforementioned conditions, the fit was applied to the data points in the deflection range between 0.1–1.7 µm and shows good conformity with the data. Besides the biaxial modulus Y and the prestress σ_0, all parameters were measured or are known from literature.[147] Microbulge tests revealed a biaxial modulus of ~54 GPa for DUV-exposed TNR/(GO/rGO)/SF membranes M1 and M2. This value was presumed for the membrane M3 to extract σ_0 as the only fit parameter to be ~1.4 MPa. We assume that this reduced

value compared to the prestress of M1 and M2 (~32 MPa) results from the different geometry and size of the substrates. The substrates for bulge tests feature circular apertures with a maximum diameter of ~105 µm, whereas the substrates for the electrostatic actuation feature square cavities with an edge length of ~245 µm. Further, the shape of the fit allows for assigning the individual terms of equation 10 to the deflection ranges. For small deflections up to ~1 µm, the square-root-like characteristic indicates that the membrane behavior was governed by the second term of equation 10, which is defined by the residual stress. As verification, figure 6.34c) displays the voltage-dependent deflection data on a log/log scale. Here, the slope of 0.67 confirms the prestress dominated behavior for small deflections. Note, that deflections below 0.1 µm were excluded from the fit to fulfill the condition $t_m << h$. For deflections exceeding ~1 µm, the first term of equation 10, governed by the elasticity, becomes more dominant, as indicated by the positive curvature of the fit and the data.

In conclusion, the facile tunability of the electrical properties by DUV exposure allowed for the electrostatic actuation of the conductive TNR/(GO/rGO)/SF membranes and showed their purely elastic behavior in the applied potential range. Further, the voltage-dependent deflection of the membrane was described well using a simple electrostatic model.

6.2.4 Outlook: MEMS/NEMS

Due to the tunability of the mechanical and electrical properties, the freestanding hybrid membranes of TNR/GO/SF and TNR/(GO/rGO)/SF are interesting candidates for the application in micro- and nanoelectromechanical systems (MEMS/NEMS) as optical devices or sensors. Whereas several studies already showed the possibility of fabricating MEMS from freestanding nanomaterials, e.g., single/multi-walled carbon nanotubes,[160,161] graphene sheets,[155,162] and gold films,[27] these systems lack the possibility to adjust the properties after device fabrication. However, it was shown that these freestanding nanomaterials can be used for many devices, such as electrical switches,[160] electrostatic resonators,[155] and field-effect transistors,[162] being able to replace silicon based systems.

Further, our group studied the application of membranes from cross-linked GNPs as devices for the detection of volatile organic compounds (VOCs)[28,158] and pressure sensing.[159] Note, that under ambient conditions the dithiol cross-linkers are prone to oxidation, which limits their operation lifetime. Further, the Young's modulus of these cross-linked GNP membranes (~3 GPa)[230] was significantly smaller compared to those of the TNR/(GO/rGO)/SF membranes.

Since the hybrid membranes presented in this study are mechanically more robust, they show great potential for implementation in MEMS/NEMS devices. Due to their numerous sorption sites, these hybrid materials are also interesting for the detection of gases and vapors. Several studies demonstrated the use of GO/rGO-based materials for the detection of analytes such as CO, NH_3, H_2O, NO_2, acetone, and alcohol vapors.[240–242] In these materials, the proposed mechanism is based on charge transfer interactions between the analyte and the GO/rGO network.[240,241] Especially, the possibility to tune the ratio between insulating GO and conductive rGO within the hybrid material is a valuable tool to transition from an n-type (GO) to a p-type (rGO) sensing behavior.[242]

Recently, we reported the fabrication of (GO/rGO)/TNC nanocomposites with adjustable GO/rGO ratios for the application as humidity sensors. The composition was tuned by the reduction of GO to rGO, which was mediated by the photocatalytic activity of the TNCs. These sensors exhibited either positive or negative resistive responses to increasing humidity, depending on their composition and the r.h. level. As a result, rGO-rich hybrid films showed the best performance for detecting low r.h. levels, while GO-rich hybrid films yielded the best performance at high r.h. levels.[2]

Further studies, will include additional functionalization by incorporating different nanomaterials during the LbL SC process of thin film deposition, advancing the hybrid membrane for the specific application.

7 Experimental Section

All experimental procedures including syntheses and characterization of nanomaterials, thin film fabrication and characterization, as well as the measurement procedures will be described in detail in the following sections.

7.1 Synthesis of TiO_2 Nanocrystals

Titania nanocrystals (TNCs) of different shapes were used in both presented studies. Titania nanorods (TNRs) and titania nanoplates (TNPs) were synthesized according to the seeded-growth approach reported by Gordon et al.[40] with slight modifications.[67] Titania nanodots (TNDs) were synthesized by a method established at the Fraunhofer Center of Applied Nanotechnology. All reactions were carried out in a nitrogen atmosphere using standard Schlenk technique. Titania nanobipyramids (TNBs) were synthesized using a one-step hydrothermal reaction based on a method by Sugimoto et al.[171] with modifications reported by Mino et al.[170] The TNBs were synthesized and kindly provided by Dr. Marie-Hélène Delville, head of research, and Eugénie Pariente, research associate and PhD student at the Institut de Chimie de la Matière Condensée de Bordeaux, CNRS.

Materials and Apparatus. (*Chemicals*) Titanium(IV) fluoride (99%) was purchased from Alfa Aesar. 1-Octadecene (ODE, 90%), oleic acid (OLAC, 90%), oleylamine (OLAM, 98%), diethylene glycol (DEG, 99%), and titanium(IV) chloride (99%) were purchased from Merck. Acetone (99.8%), Chloroform (99%), 2-propanol (99.7%), methanol (MeOH, 99.8%), and toluene (99.5%) were purchased from VWR Chemicals. Deionized (DI) water (resistivity: 18.2 MΩ cm) was purified using an ELGA LabWater purification system. (*Apparatus*) Syringe pump (KDS Legacy 100, KD Scientific), centrifuge (Sigma 3-18K), and ultrasonic bath (Bandelin Sonorex RK 255H).

TNR Synthesis. For the synthesis of TNRs with an average length of ~40 nm, a precursor solution of 20 mL ODE and 6.8 mL OLAC as well as a reaction solution of 60 mL ODE, 60 mL OLAM, and 3.6 mL OLAC were prepared. Both solutions were degassed in vacuum at 120 °C for 15 min and cooled down to 60 °C. Under vigorous stirring, 0.5 mL $TiCl_4$ were added to the precursor solution, which was stirred for 10 min to complete the formation of the brown titanium oleate complex. Next, 2.5 mL of the precursor solution were added to the reaction solution and the mixture was heated to 290 °C under reflux and vigorous stirring. The reaction solution was stirred for 10 min to achieve seed formation. Following, 10 mL of the precursor solution were continuously added to the reaction solution at a constant rate of 9 mL/h using a syringe pump. During the reaction,

the temperature was kept constant at 290 °C. A gradual change in color of the solution from brown to yellow indicated the formation of TNRs. After the addition of precursor was completed, the mixture was stirred for 10 min, and was then cooled down to ambient temperature. The suspension was precipitated with 2-propanol (1/1, v/v) and centrifuged for 15 min (4000 g, 15 °C). Redispersed precipitate in toluene was precipitated again in a mixture of 2-propanol/acetone (6/1/1, $v/v/v$), and centrifuged again as described above. Finally, the resulting solid was redispersed in 15 mL chloroform, yielding a clear-yellow solution.

TNP Synthesis. TNPs with an edge length of ~22 nm were synthesized with the following modifications. Instead of $TiCl_4$, 0.45 g TiF_4 were dissolved in the precursor solution containing 16 mL ODE and 5.4 mL OLAC. To achieve complete dissolution of the precursor, the solution was heated to 100 °C. Seeds were formed by adding 1 mL of the precursor solution to the reaction solution. For the growth, 18 mL of the precursor solution were continuously added at a constant rate of 9 mL/h using a syringe pump. In this reaction the gradual change in color from light brown over pale-green to deep-blue indicated the formation of TNPs. For purification, the suspension was precipitated with 2-propanol (1/1, v/v) and centrifuged for 15 min (6000 g, 15 °C). Redispersed precipitate in toluene was washed and precipitated again, and the resulting solid was redispersed in 15 mL chloroform. After the redispersion, a colorless precipitate formed, that was removed using a syringe filter (PTFE, 200 µm), yielding a dark-blue, clear solution.

TND Synthesis. TNDs with an estimated diameter of 5–10 nm were synthesized with DEG acting as solvent and ligand. 120 mL DEG were degassed in vacuum at 60 °C for 60 min. Under vigorous stirring, 8 mL $TiCl_4$ were added to the DEG, and the stirring was continued for 10 min. Then, 4 mL DI water were added to the reaction solution, and the mixture was heated to 160 °C, keeping the temperature constant for 240 min. Next, the mixture was cooled down to ambient temperature. A colorless precipitate was formed by adding the reaction solution to 500 mL acetone. Approx. 350 mL of the colorless supernatant were removed, and the remaining precipitate was centrifuged for 15 min (8000 g, 15 °C). Next, the precipitate was washed with acetone and centrifuged again for 15 min (8000 g, 15 °C). Lastly, the solid was dried under vacuum, yielding a light yellow crystalline powder.

Surface Modification and Phase Transfer. In order to obtain the TNDs in organic dispersions, the DEG ligand was exchanged for OLAM. The procedure was based on the method reported by Hensel et al.[67] 1 g of dried TNDs was dispersed in 5 mL OLAM,

followed by the addition of 15 mL toluene and 5 mL 2-propanol. The yellow solution was stirred for approx. 21 h. Next, the solution was washed and precipitated with acetone (2/3, v/v) to remove free ligand molecules. After centrifugation for 15 min (8000 g, 15 °C), the precipitate was redispersed in 30 mL chloroform, yielding a slightly turbid, yellowish solution. Finally, the solution was filtrated using a syringe filter (PTFE, 1 µm), yielding a clear, yellowish solution.

TNB Synthesis. TNBs with an average height of ~44 nm and an average edge length of ~30 nm were synthesized using a one-step hydrothermal reaction. The hydrolysis of the $Ti(TEOA)_2$ complex in aqueous solution (TEOA stands for triethanolamine) with a complex concentration of 40 mM was forced at a pH of 10 and a temperature of 180 °C for 96 h. Upon completion of the hydrothermal step, the sample was calcined at 400 °C for 120 min, resulting in a colorless powder which was dispersed in 25 mL DI water, yielding a turbid, colorless dispersion.
For film fabrication and characterization, the TNB stock solution was diluted in MeOH (1/1, v/v) and sonicated for 30 min.

P25 Preparation. Titanium(IV)-oxide Aeroxide™ P25 was purchased from Thermo Fisher Scientific.
For film fabrication and characterization, the colorless powder was dispersed in a water/MeOH mixture (1/1, v/v) and sonicated for 30 min, yielding a turbid, colorless dispersion.

TEM Analysis. Transmission electron microscopy (TEM) analysis was performed to determine the size and shape of the as-synthesized and as-prepared TNCs. The measurements were conducted in the Department for Electron Microscopy of the Institute of Physical Chemistry by Stefan Werner using a JEOL JEM-1011 microscope (LaB_6, 100 kV). For sample preparation of TNRs, TNPs, and TNDs in organic solution, 7 µL stock solution were dissolved in 1 mL toluene. For sample preparation of TNBs and P25 TNCs in a water/MeOH mixture (1/1, v/v), 10 µL of the latter were diluted in 0.5 mL water. 10 µL of the respective dilution were drop-casted onto a carbon-coated copper grid. The particle size statistics for the TNR, TNP, TNB, and P25 samples were evaluated using the software *ImageJ*.

TG Analysis. The organic content (OC) and the mass concentration of the TNC stock solutions were determined by thermogravimetric analysis (TGA) using a thermomicrobalance (NETZSCH TG209 F1 Iris System). 400–500 µL of the respective stock solution

were dried in an alumina crucible by evaporating the solvent at ~60 °C. In a nitrogen atmosphere, the temperature was increased in two steps. First, the temperature was increased to 120 °C (10 K/min), and kept constant for 20 min. Second, the sample was heated to 800 °C (10 K/min) for 20 min. In a final step, the atmosphere was exchanged for dried air while the temperature was maintained at 800 °C for 20 min.

UV-vis Spectroscopy. For ultraviolet-visible (UV-vis) spectroscopy measurements, 5 µL of the respective TNC stock solution in chloroform were diluted in 1 mL chloroform. Spectra were recorded in a quartz cuvette (optical path: 10.00 mm) using a Varian Cary50 spectrophotometer. The wavelength range was set between 200–600 nm and all data were corrected for the absorbance of chloroform.

UV-vis-NIR Spectroscopy. For UV-vis-near-infrared (UV-vis-NIR) spectroscopy measurements, dispersions of TNRs and TNPs in chloroform were prepared with concentrations of ~1.33 and ~0.33 mg/mL, respectively. The spectra were recorded in a quartz cuvette (optical path: 10.00 mm) in the wavelength range between 200–1500 nm using an Agilent Cary5000 spectrophotometer. All spectra were corrected for the absorbance of chloroform.

XRD Analysis. X-ray diffraction (XRD) measurements were conducted to characterize the crystal structure of the TNCs. The measurements were performed by Nina Schober, Stefan Werner, and Charis Rabea Schlundt in the 2θ range from 20-90° using a Philips X'Pert PRO MPD powder diffractometer with a Cu-K_α source (1.54 nm). For sample preparation, 70–120 µL of the respective TNC stock solution were drop-casted on XRD Si wafers and dried under ambient conditions. Crystal structure analysis was determined by comparing the obtained diffractograms with reference data from the ICSD database Refs. [167, 168, 172].

7.2 Synthesis of Graphene Oxide

Graphene oxide (GO) was synthesized according to the procedure reported by Hummers and Offeman[124] with slight modifications and additional purification via dialysis. The synthesis was carried out and the material was kindly provided by Julia Angelica Voss, research associate and PhD student at University of Hamburg. Details on the synthesis and further characterization can be found in her Bachelor's thesis.[243]

Materials and Apparatus. (*Chemicals*) Graphite (-325 mesh, 99.8%) and potassium permanganate (99%) were purchased from Alfa Aesar. Sulfuric acid (95%) was purchased from Chemsolute. Hydrogen peroxide (30%) was purchased from Merck. Hydrochloric acid (37%) and methanol (MeOH, 99.8%) were purchased from VWR Chemicals. DI water (resistivity: 18.2 MΩ cm) was purified using an ELGA LabWater purification system. (*Apparatus*) Centrifuge (Sigma 3-18K), dialysis tubing (Spectra/Por©MWCO 3500 standard RC), ultrasonic bath (Bandelin Sonorex RK106), freeze dryer (Christ Alpha 1-4 LDplus), plasma cleaner (Harrick Plasma PDC-002), and spin-coater (Suss MicroTec Lab-Spin 6 TT).

Synthesis. First, 2.0 g graphite flakes and 1.0 g sodium nitrate were suspended in 47 mL sulfuric acid while cooling the mixture using an ice bath. While stirring, 6.0 g potassium permanganate were added slowly and portion-wise. Next, the dark-brown mixture was stirred for 15 min and then heated to 40 °C. The mixture thickened and after 20 min, 400 mL DI water were added slowly, followed by the stepwise addition of 2 mL hydrogen peroxide solution (30%), resulting in a change of the color from almost black to light-brown. After cooling down, the mixture was centrifuged for 20 min (5000 g, 10 °C) and the supernatant was discarded. In a first washing step, the precipitate was suspended in 180 mL DI water, followed by centrifugation for 5 min (3500 g, 10 °C). In the second washing step, the precipitate was suspended in 180 mL hydrochloric acid and centrifuged as described before. The final precipitant was suspended in 200 mL DI water and purified using dialysis tubing (molecular cut-off: 3.5 kDa) for two weeks. Afterwards, 140 mL DI water were added to the suspension and it was sonicated for 90 min. In order to obtain exfoliated GO flakes, the suspension was repeatedly centrifuged for 40 min (9000 g, 15 °C). Here, the black precipitate was discarded and the dispersion was sonicated for 30 min. The product was freeze-dried, resulting in a brown aerogel which was used for the characterization. The freeze-dried GO was redispersed in DI water (1 mg/mL) and sonicated for 15 min.

AFM Analysis. Atomic force microscopy (AFM) analysis was used to analyze the thickness and lateral size of single GO sheets. For sample preparation, 20 µL GO (0.4 mg/mL) in a water/MeOH mixture (1/1, *v*/*v*) were deposited via spin-coating (3000 rpm, 60 s) on SiO_2/Si substrates. Before deposition, the wafer was treated in an air plasma for 3 min, yielding a hydrophilic surface. Topographic maps at different areas of the substrate were obtained using a JPK NanoWizard 3 AFM with NSG01 cantilever in tapping mode. Height profiles were extracted from AFM images using the software *Gwyddion 2.56*.

Scanning Electron Microscopy. The morphology of the freeze-dried material was investigated via scanning electron microscopy (SEM). The measurements were performed in the Department for Electron Microscopy of the Institute of Physical Chemistry by Robert Schön using a Zeiss LEO 155 Gemini microscope (acceleration voltage of 5 kV). For sample preparation, the material was directly deposited on a SEM sample holder using double sided adhesive carbon tabs.

TEM Analysis. TEM analysis was performed to determine the lateral dimensions of the as-synthesized GO. The measurements were conducted in the Department for Electron Microscopy of the Institute of Physical Chemistry by Stefan Werner using a JEOL JEM-1011 microscope (LaB_6, 100 kV). For sample preparation, 10 µL GO stock solution were diluted in 1 mL water, and 10 µL of the dilution were drop-casted onto a carbon-coated copper grid. Lateral dimensions were evaluated using the software *ImageJ*.

UV-vis Spectroscopy. For UV-vis spectroscopy measurements, 20 µL GO (0.4 mg/mL) in a water/MeOH mixture (1/1, *v*/*v*) were deposited via spin-coating (3000 rpm, 60 s) on quartz substrates. This deposition step was repeated five times with a delay time of 25 s after every step. Before deposition, the quartz slide was treated in an air plasma for 3 min, yielding a hydrophilic surface. The substrates were placed in a home-built sample holder and four spectra in the range between 200–600 nm were recorded using a Varian Cary50 spectrophotometer at different positions. The absorbance spectrum was obtained by averaging the four spectra, which were corrected for the absorbance of the quartz substrate.

7.3 Lithographic Fabrication of Photomasks and Microstructured Substrates

Microstructured substrates for both projects were fabricated using standard photolithography. For conductivity and vapor sensing measurements, custom-designed electrode structures were fabricated on SiO_2/Si wafers using chromium-coated photomasks. For microbulge tests, substrates with a circular aperture were fabricated using deep reactive ion etching (DRIE) on photolithographically patterned silicon wafers. The substrates with an aperture were produced and kindly provided by Prof. Dr.-Ing. Hoc Khiem Trieu and Dr. Norbert Schulz, former research associate at Hamburg University of Technology. For actuator measurements, square cavities were etched into thermally oxidized silicon wafers, and top electrodes were deposited using physical vapor deposition (PVD).[152] Cavity arrays were produced and kindly provided by Hauke Hartmann, former research associate at University of Hamburg.

Materials and Apparatus. *(Chemicals and Materials)* Titanium (99.99%) was purchased from Alfa Aesar. Gold granules (99.99%) was purchased from ESG Edelmetall-Service GmbH & Co. KG. Iodine (99.5%) was purchased from Grüssing GmbH. Potassium iodide (99.5%) and triammonium citrate (97%) were purchased from Merck. Hydrogen peroxide (30%) was purchased from VWR Chemicals. DI water (resistivity: 18.2 MΩ cm) was purified using an ELGA LabWater purification system. Chromium-coated glass blanks (Nanofilm, 2.5×2.5×0.06 in^3, SL LRC 10M) were purchased from MB Whitaker. SiO_2/Si wafers (orientation <100>, 500 nm SiO_2, diameter: 200 mm, thickness: 725±10 µm, 8-25 Ω cm, p-doped) were purchased from Si-Mat Wafer. *(Apparatus)* Thermal vacuum evaporation system (œrlikon Leybold Vacuum, UNIVEX 350G), hot plate (Chemat Technology, INC., Model KW-4AH), micro writer (Durham Magneto Optics Ltd. MicroWriter ML-3), mask aligner (Karl Suss MJB-3 Mask Aligner, equipped with an Osram HBO 200W/DC, Hg lamp, multiline spectrum), spin-coater (Suss MicroTec, LabSpin 6 TT), and muffle furnace (Nabertherm L9/SKM).

Fabrication of Photomask

For the preparation of interdigitated electrode (IDE) structures, a chromium-coated glass blank was patterned. Patterns were designed using the software *Klayout 0.27.9*. The chromium-coated glass blank was coated with positive photoresist AZ ECI 3012 via spin-coating (3000 rpm, 60 s). After soft-bake at 90 °C for 90 s, the resist was patterned by selective irradiation according to the structure shown in figure 7.1 using a micro writer (50 mJ/cm^2 λ = 385 nm, with a resolution of 0.6 µm), followed by post-exposure bake at

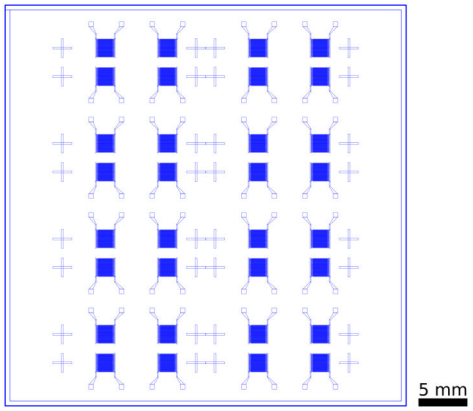

Figure 7.1: Design of the photomask used for the fabrication of 8 sensor substrates (~16×10 mm^2) on oxidized silicon wafers. Each substrate includes 4 IDE structures consisting of 96 fingers of 10 µm width, spaced by 10 µm, with an overlap of 1500 µm.

110 °C for 60 s. The photoresist was developed in a mixture of DI water and AZ 326 MIF developer solution (4/1, v/v) under gentle whirling for 60 s. Next, exposed chromium areas were removed in a commercial chromium etchant solution (TechniEtch Cr01) for 60 s. Each step was followed by immersion in and rinsing with DI water. Next, the photoresist was removed with acetone. Finally, the photomask was cleaned in 2-propanol and water and then dried in a nitrogen stream.

Fabrication of IDE Substrates

IDE arrays were fabricated on SiO_2/Si wafers. First, SiO_2/Si wafers (~41×41 mm^2) were coated with Ti/Au (thickness: 10 nm/40 nm) via thermal evaporation, and covered with negative photoresist AZ nLOF 2020 using spin-coating (3000 rpm, 60 s). Next, the photoresist was soft-baked at 110 °C for 60 s, and exposed through the custom-designed photomask using a mask aligner for 12 s. The substrates were baked at 110 °C for 60 s, and the resist was developed in an AZ 726 MIF developer for 60 s. Development was stopped by immersion in and rinsing with DI water. Next, the exposed gold areas were removed by immersion in a gold etchant solution ($KI/I_2/H_2O$, 4/1/200, $m/m/m$) under gentle whirling for approx. 2 min. Exposed titanium areas were removed by immersion in a solution of 5% triammonium citrate in 30% H_2O_2 at 35 °C for approx. 4 min. In both steps, the etching was stopped by immersion in and rinsing with DI water. Then, the photoresist was removed by immersion in TechniStrip NI555 at 60 °C for 35 min. Finally, the substrates were cleaned in acetone, 2-propanol, and water and were dried in a nitrogen stream.

Fabrication of Substrates with an Aperture

Substrates with a defined circular aperture (diameter: 80–120 μm) were patterned on silicon wafers by photolithography, and generated by DRIE. Alternating steps of etching and surface passivation allowed for anisotropic etching perpendicular to the wafer surface. The etching step was based on energetic high-frequency electric field that produced the combination of chemical dry etching with highly reactive SF_6-plasma and physical sputtering with Ar-plasma. While the SF_6-plasma caused isotropic etching, the Ar-plasma removed the material along the direction of the applied electric field. For passivation, the surface was covered with a fluoropolymer layer, which is resistant to the isotropic SF_6-etchant. By controlling the duration of the steps, the aperture was formed with high precision. Lastly, the substrates were heated in a muffle furnace under air at 1000 °C for 6 h, to form a homogeneous SiO_2 layer with a thickness of ~250 μm.

Fabrication of Cavity Substrates

Square cavity arrays (egde length: ~245 μm, depth: ~21 μm) were fabricated on SiO_2/Si wafers following a two step process. First, the wafers were patterned using standard photolithography. Exposed SiO_2 surfaces were then etched with buffered oxide etchant (BOE), followed by anisotropic depth etching using potassium hydroxide solution. After stripping the photoresist, the remaining SiO_2 was removed by BOE treatment, and a homogeneous layer of SiO_2 was grown thermally using the muffle furnace. Second, electrodes were fabricated by depositing Ti/Au (thickness: 10 nm/40 nm) layers via thermal evaporation. The electrodes were structured using standard photolithography as described in the previous paragraph for IDE fabrication. Detailed instructions are provided in a recent publication of our group.[152]

7.4 Fabrication and Characterization of TiO_2 Thin Film Chemiresistors

Depending on the targeted measurement, TiO_2 thin films were directly drop-casted on SiO_2/Si wafers (~16×10 mm^2) and alumina substrates (~15×13 mm^2) (both featuring IDE structures), silicon wafers, and quartz crystal microbalances (QCMs) or spin-coated on quartz slides (~20×20 mm^2). Differently shaped TNCs were used, and organic ligands were removed by a deep-ultraviolet (DUV) treatment.

Materials and Apparatus. (*Chemicals and Materials*) TNRs in chloroform (~4 mg/mL), TNPs in chloroform (~2 mg/mL), TNDs in chloroform (~4 mg/mL), TNBs in water/MeOH (~2 mg/mL, 1/1, *v*/*v*), P25 TNCs in water/MeOH (~3 mg/mL, 1/1, *v*/*v*), GNPs in heptane (~20 μM), and SPIONs in toluene (~0.4 mg/mL). Sodium hydroxide (97%) was purchased from Grüssing GmbH. Tetrachloroauric(III)acid trihydrate (99.99%) and oleylamine (OLAM, 98%) were purchased from Merck. 2-Propanol (99.5%), ethanol (99.8%), and methanol (MeOH, 99.8%) were purchased from VWR Chemicals. Oxygen 4.5 (compressed UN 1072) was purchased from Westfalen AG. DI water (resistivity: 18.2 MΩ cm) was purified using an ELGA LabWater purification system. IDE with heater and temperature detector on alumina (15×13 mm^2, platinum heater, RTD, and IDE 16 fingers 250 μm width and spacing) were purchased from the Electronics Design Center at Case School of Engineering at Case Western Reserve University. QCMs (resonant frequency: 10.00 MHz, diameter: 13.9 mm, Ti/Au ~10 nm/~200 nm electrodes with 6 mm diameter) were purchased from openQCM. SiO_2/Si wafers (<100> orientation, 500 nm SiO_2, diameter: 200 mm, thickness: 725±10 μm, 8-25 Ω cm, p-doped) and Si wafers (<100> orientation, diameter: 76.2 mm, thickness: 380±20 μm, 8-25 Ω cm) were purchased from Si-Mat. Quartz slides (20×20×0.5 mm^3) were purchased from Won Ik Quartz Europe. (*Apparatus*) Plasma cleaner (Harrick Plasma PDC-002), spin-coater (Suss MicroTec, LabSpin 6 TT), ultrasonic bath (Bandelin Sonorex RK 255H), ozonizer (Erwin Sander, Laborozonisator 301.7), and sputtering instrument (Gatan PECSTMModel 682 Ar ion beam system).

Preparation of Substrates. Prior to film deposition, the particular substrate (alumina, silicon, oxidized silicon, quartz slides, and QCMs) was treated in an air plasma under reduced pressure for 3 min.

TiO_2 Thin Film Deposition. Predominantly, thin films were fabricated by drop-casting 10 μL of the TNC dispersion onto the desired substrate, followed by drying under ambient conditions. For alumina substrates, a second step of drop-casting was added to fully cover

the IDE structure. Immediately prior to deposition, the TNC dispersions in water/MeOH mixture were sonicated for 5 min to disintegrate particle clusters.
For UV-vis spectroscopy measurements, quartz slides were placed on the spin-coater and constantly rotated at 3000 rpm. 25 µL of the particular TNC dispersion were applied to the rotating substrate. After a delay time of 25 s, the deposition was repeated up to six times. For TNC dispersions in chloroform, a washing step with 25 µL 2-propanol was added after every TNC deposition, which was also spaced by a delay time of 25 s.

Surface Treatments

Using three different treatments, organic ligands were removed from the surface of the substrate-supported TNC thin films. The DUV treatment was based on the photocatalytic activity of TiO_2, the ozone treatment was based on the exposure to an oxygen/ozone mixture, and the plasma treatment was based on exposing the thin films to air plasma.

DUV Treatment. For the photocatalytic decomposition of organic ligands, a DUV treatment was implemented using a custom-built DUV light source (main emission: 254 nm). Characterization of the light source is provided in the Appendix, section A.1.1. After film deposition, the substrate-supported TNC thin films were treated for varying exposure times between 30–240 min under ambient conditions. Heating of the samples was prevented by continuously ventilating the setup using two fans. The exposure time of thin films for vapor sensing measurements was set to 120 min.

Ozone Treatment. For the oxidative decomposition of organic ligands in an oxygen/ozone atmosphere, the substrate-supported TNC thin films were placed in a 100 mL single neck round bottom flask. The ozonizer was fed with an oxygen pressure of 0.05 bar which resulted in a flow rate of approx. 4 L/h. The atmosphere in the flask was continuously replaced, and the gas outlet was neutralized by bubbling into a saturated sodium thiosulfate solution. Treatment times were varied between 5–360 min, while the treatment time of thin films for vapor sensing measurements was set to 360 min.

Plasma Treatment. The plasma treatment was executed on the deposited TNC thin films under reduced pressure of ~1.3 mbar. The exposure time was varied between 2–180 min, while it was set to 180 min for thin films fabricated for vapor sensing measurements.

NaOH Treatment. Apart from the OLAM as stabilizing ligand, the surface of TNPs was also partially functionalized with fluoride ions. In order to remove these fluoride ions, the substrate-supported TNP thin films were submerged in 15 mL 0.1 M aqueous NaOH solution. After 20–40 min, the NaOH was slowly removed using a syringe and the samples were washed with water and 2-propanol and dried in a nitrogen stream.

Surface Modification

In order to modify the composition of the TNC thin films after the fabrication, additional deposition steps of various materials were carried out. Nanostructured functionalization was achieved by depositing gold nanoparticles (GNPs) or superparamagnetic iron oxide nanoparticles (SPIONs), and by sputtering small amounts of platinum on the DUV-treated TNR thin films. Spherical, dodecylamine-stabilized GNPs (diameter: ~4 nm) were synthesized following the procedure reported by Leff et al.,[244] and kindly provided by Ahir Bose, research associate and PhD student at University of Hamburg. Spherical, oleyl phosphate-stabilized SPIONs (diameter: ~3 nm) were synthesized in a flow reactor,[245] and kindly provided by Dr. Sebastian Willruth, former research associate at University of Hamburg.

SPION Deposition. Substrate-supported TNR thin films were placed on the spin-coater. Under constant rotation at 3000 rpm, 20 µL of the SPIONs in toluene were applied, followed by 20 µL of MeOH. The steps were spaced by a delay time of 30 s.

Platinum Deposition. Nanostructured platinum was deposited by sputtering Pt onto TNR thin films. In order to achieve a sub-monolayer, the nominal film thickness was set to 0.5 nm and 1 nm resulting in deposition times of 4 s and 11 s, respectively.

Gold Deposition. The deposition of nanostructured gold on the TNR thin film was implemented using two methods. For the first method, substrate-supported TNR thin films were placed on the spin-coater. 20 µL of the GNPs in heptane were applied, followed by 20 µL of MeOH. The steps were spaced by a delay time of 30 s. The substrate was constantly rotated at 3000 rpm.
The second method was based on the photocatalytic reduction of Au^{3+} ions on the TNR thin film. For the precursor, tetrachloroauric(III) acid trihydrate was dissolved in a water/ethanol mixture (1/1, v/v). Two concentrations of 0.1 mg/mL (~0.51 mM) and 0.2 mg/mL (~1.02 mM) were prepared and 25 µL of the respective solution were drop-casted each onto a substrate-supported TNR thin film. Next, the samples were placed in a custom-

built test cell and simultaneously exposed to UV light and ethanol vapor with a concentration of 2000 parts-per-million (ppm) for 90 min. The gas flow through the test cell was set to 0.5 L/min. Detailed information on the test cells and the commercial gas calibration system can be found in the Experimental Section 7.6.

Characterization of TiO_2 Thin Films

The characterization methods described in the following section were applied to the titania thin films for all previously described surface treatments and surface modifications. Additionally, certain experimental methods were deployed after various exposure times to investigate the effects of the particular treatments.

Charge Transport Measurements. For charge transport measurements, TNC thin films were deposited on IDE structures on SiO_2/Si substrates. The influence of photoactivation and varying levels of relative humidity (r.h.) on the charge transport was investigated by placing the samples in custom-built test cells (cell volume: ~16 mL), which allow for the adjustment of the atmosphere and the illumination. Detailed information on the gas calibration system can be found in the Experimental section 7.6. Prior to every measurement, the samples were purged with purified air of the particular r.h. level (between 0–50%) for 5 min to equilibrate to the atmosphere. Spring-loaded pin connectors were used to contact the chemiresistors to a Keithley 2601A sourcemeter. Current-voltage (*IV*) curves were obtained by sweeping the voltage between ±10 V (in steps of 0.1 V) and recording the resulting current.

Film Mass Analysis. To analyze the mass reduction upon the removal of organic ligands, the TNC films were deposited onto one side of the QCMs. The QCMs were clamped in sample holders (openQCM), which were placed inside the test cell and contacted to an Agilent E5100A Network analyzer using spring-loaded pin connectors. The resonance frequency was recorded over a span of 100 s in purified, dry air with a constant gas flow of 0.5 L/min before and after film deposition as well as after distinct exposure times.

Film Thickness Analysis. The TNC film thickness was examined using AFM analysis. To this end, films deposited on SiO_2/Si substrates were scratched using a scalpel to generate step edges. Across the step edges, height maps of 20×2 μm^2 or 10×2 μm^2 covering equal parts of the film and underlying substrate were recorded using a JPK NanoWizard 3 AFM with NSG01 cantilever in tapping mode. For every film, height maps at three different positions on the sample were recorded and analyzed using the software *Gwyddion 2.56*.

The film thickness was calculated by averaging nine height profiles.

FTIR Spectroscopy. To analyze the removal of organic ligands, TNC films of increased thickness were deposited onto silicon substrates by repeating the drop-casting described in the previous section four times. The spectra were recorded using a Bruker Invenio R spectrometer in combination with a Specac Golden Gate ATR unit (ATR stands for attenuated total reflectance). Reference spectra were recorded by directly drop-casting 5 µL OLAM onto the ATR unit. For recording the Fourier-transform infrared (FTIR) spectra of the ozone-treated films, a Bruker Vertex70 spectrometer was used. All spectra were recorded in the range of 4000–400 cm^{-1} with a scan rate of 128, and the baseline was recorded from ambient surrounding.

Scanning Electron Microscopy. The changes in the morphology of the thin films after surface treatments and surface modifications were investigated via SEM analysis. For sample preparation, the TNC films were deposited onto silicon wafers. The measurements were performed in the Department for Electron Microscopy of the Institute of Physical Chemistry by Robert Schön using a Zeiss LEO 155 Gemini microscope (acceleration voltage of 10–20 kV).

UV-vis Spectroscopy. For UV-vis spectroscopy measurements, TNC thin films were deposited via spin-coating (3000 rpm, 60 s) on quartz substrates. 25 µL of the respective TNC solution were applied to the rotating substrate and the deposition was repeated for up to six times. Each deposition step was spaced by 25 s delay time. The substrates were placed in a home-built sample holder and four spectra were recorded at four different film positions using a Varian Cary50 spectrophotometer. The spectra were recorded in the wavelength range between 200–600 nm and corrected for the absorbance of the quartz substrate. The absorbance spectrum of the film was obtained by averaging the four spectra.

XRD Analysis. The influence of the DUV, plasma, and NaOH treatments on the crystal structure of TNC films were analyzed using XRD measurements. For sample preparation, 70–120 µL of the respective TNC stock solution were drop-casted on XRD Si wafers and dried at ambient conditions, followed by the specific treatment. The measurements were performed by Nina Schober, Stefan Werner, and Charis Rabea Schlundt in the 2θ range from 20-90° using a Philips X'Pert PRO MPD powder diffractometer with a Cu-K_α source (1.54 nm). Crystal structure analysis was performed by comparing the obtained diffractograms with reference data from the ICSD database Ref. [167, 168, 172].

7.5 Fabrication and Characterization of TNR/(GO/rGO)/SF Membranes

Hybrid films of TNRs, GO, and SF were prepared on thermally oxidized silicon wafers and quartz slides by using a layer-by-layer spin-coating (LbL SC) process. The procedure was inspired by a method that was established in our group.[2,67] Freestanding membrane sections on square cavities and circular apertures were obtained using a transfer procedure based on polydimethylsiloxane (PDMS) stamps. This transfer printing has been adapted based on the process established in our group.[152] TNRs used in this project were kindly provided by Dr. Sophia Caroline Bittinger, research associate at the CIC biomaGUNE, former PhD student at University of Hamburg. The synthesis was carried out as described in section 7.1 with modified reaction parameters to achieve TNRs with a high aspect ratio. A precursor solution of 100 mL ODE, 6.25 mL OLAC, and 2.2 mL $TiCl_4$ was prepared. For seed formation, 0.5 mL of precursor solution were injected into the reaction solution of 60 mL ODE, 60 mL OLAM, and 3.6 mL OLAC. In the growth step additional 30 mL of precursor solution were continuously added to the reaction solution with a reduced rate of 0.3 mL/min compared to the synthesis described in section 7.1.[215]

Materials and Apparatus. (*Chemicals and Materials*) TNRs in chloroform (~0.5 mg/mL), GO in water/methanol (~0.4 mg/mL, 1/1, *v*/*v*). Chlorobenzene (99%) was purchased from Burdick Johnson. Polydimethylsiloxane (PDMS, Sylgard 184) was purchased from Dow Corning Inc. Polyvinyl alcohol (PVA, 2.2 kDa) was purchased from Fluka. Methoxyperflourobutane (MPFB, 99%), poly (methyl methacrylate) (PMMA, average molecular weight: ~120 kDa), and silk fibroin solution (SF, 50 mg/mL, average molecular weight ~100 kDa) were purchased from Merck. Acetone (99.8%), methanol (MeOH, 99.8%), and chloroform (99%) were purchased from VWR Chemicals. DI water (resistivity: 18.2 MΩ cm) was purified using an ELGA LabWater purification system. Quartz slides (10×10×0.5 mm^3) were purchased from Won Ik Quartz Europe. SiO_2/Si wafers (<100> orientation, 500 nm SiO_2, diameter: 200 mm, thickness: 725±10 μm, 8-25 Ω cm, p-doped) and Si wafers (<100> orientation, diameter: 76.2 mm, thickness: 380±20 μm, 8-25 Ω cm) were purchased from Si-Mat. (*Apparatus*) Hot plate (Harry Gestigkeit Präzitherm 2860SR), plasma cleaner (Harrick Plasma PDC-002), spin-coater (Suss MicroTec LabSpin 6 TT), and vacuum pump (Schmalz EVE-TR 4 AC3).

Preparation of Substrates. Before film deposition and film transfer, the SiO_2/Si substrates were treated in an air plasma for 3 min, yielding hydrophilic surfaces.

Preparation of SF. Frozen SF solution 50 mg/mL was thawed, diluted with DI water, and frozen in smaller volumes of 2 mL with a concentration of 25 mg/mL. Samples were kept under dry ice and fresh solutions with a concentration of 2 mg/mL were prepared every two weeks. These solutions were used for the hybrid film fabrication without further purification.

TNR/GO/SF Film Deposition. The desired substrate was placed on the spin-coater and constantly rotated at 3000 rpm. For the deposition, GO in water/MeOH (1/1, *v*/*v*), TNRs in chloroform, and SF in water were used following the sequence shown in table 7.1. The volume for each step was 25 µL and the steps were spaced by a delay time of 25 s. Each SF deposition was followed by the deposition of 25 µL DI water.

Table 7.1: Overview of the deposition steps for the fabrication of TNR/GO/SF thin films.

Substance	Dispersant	Iterations
GO	H_2O/MeOH	2
SF	H_2O	3
GO	H_2O/MeOH	1
SF	H_2O	1
GO	H_2O/MeOH	3
TNRs	$CHCl_3$	1
GO	H_2O/MeOH	2

TNR/GO/SF Film Transfer. For the GO/TNR/SF film transfer, two additional polymer layers were added to the deposition described in the previous paragraph. A schematic depiction of the transfer process by contact printing is provided in figure 7.2. Squared pieces (~10×10 mm^2) of oxidized silicon were placed on the spin-coater and covered with 100 µL ~25 mg/mL PVA solution in water. Next, the rotation with 3000 rpm was started. After a delay time of 100 s, the TNR/GO/SF film was deposited as described in the previous paragraph. The film was mechanically divided into four evenly sized sections (~3×3 mm^2) by removing the film edges and carving a cross shape in the center using a scalpel. Subsequently, the substrate was purged with a strong stream of nitrogen to remove any residues from scratching. The substrate was placed back on the spin-coater and 70 µL ~50 mg/mL PMMA solution in chlorobenzene were applied to the rotating (3000 rpm) substrate. After a delay time of 100 s, the substrate was baked at 60 °C for 10 min. Again, the PMMA layer was mechanically removed along the edges of the sections followed by purging in

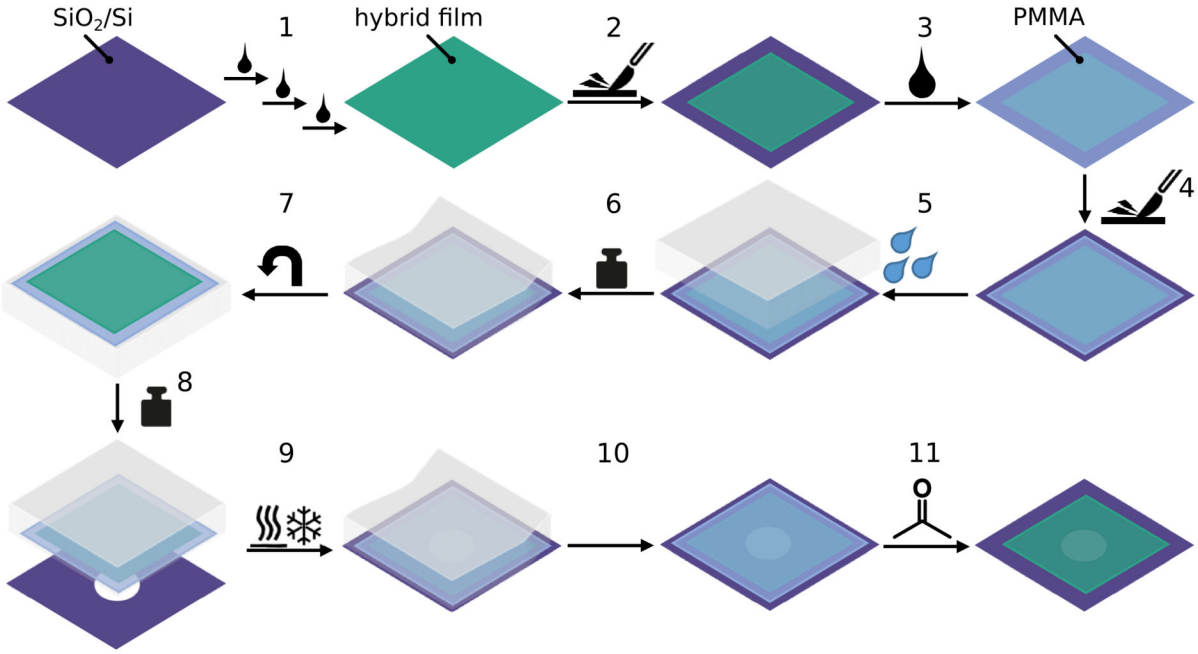

Figure 7.2: Schematic of the fabrication process of freestanding membranes. Reprinted from Dobschall el al., Ref. [1] *Creative Commons CC-BY 4.0* license ©2025 The Authors. Adv. Electron. Mater. published by Wiley-VCH GmbH. (DOI: 10.1002/aelm.202400602)

a strong stream of nitrogen. For detaching the films from the oxidized silicon substrate, one section was covered with 10–15 µL DI water with the latter dissolving the undermost PVA layer. Then, a rectangular PDMS stamp (~6×5×1.6 mm^3) was pressed against the particular section at a pressure of ~0.26 bar for 5 s, picking up the hybrid film. The stamp with the hybrid film was pressed against the target substrate with a pressure of 1.8 bar using a custom-built pressing device. By three cycles of heating the structure to 70 °C and cooling it down to −3 °C using thermoelectric cooling under nitrogen flow, the hybrid film was detached from the stamp and transferred onto the target substrate. The stamp was slowly lifted using a custom-built lifting device at a speed of ~120 µm/min, while the target substrate was adhered using reduced pressure. Details on the pressing and lifting device were reported by Hartmann et al.[152] For the removal of the PMMA layer, the substrate was placed upright in a custom-built PTFE container (volume: ~8 mL), which was slowly filled with ~15 mL acetone through the lower inlet. Dissolved PMMA in acetone was pushed out through the upper outlet that was opposing the inlet. Remaining acetone was exchanged for methoxyperfluorobutane (MPFB). To this end, ~15 mL MPFB were introduced through the lower inlet pushing the remaining acetone through the upper outlet. Finally, the MPFB was removed and the substrate was dried under ambient conditions.

Photocatalytic Composition Tuning of TNR/GO/SF Membranes

Photocatalytic Reduction. The photocatalytic reduction of GO to reduced graphene oxide (rGO) was implemented by exposing the freestanding TNR/GO/SF membranes to DUV radiation using a custom-built DUV light source (main emission: 254 nm) for various exposure times up to 120 min. Characterization of the light source is provided in the Appendix, section A.1.1. Two fans were continuously ventilating the setup to prevent the samples from heating up.

Characterization of TNR/(GO/rGO)/SF Film

The experimental methods described in the following section were applied to the substrate-supported hybrid films as well as freestanding hybrid membranes. Further, the effects of photocatalytic reduction were investigated.

Film Thickness Analysis. The influence of the DUV treatment on the hybrid film thickness was examined using AFM analysis. To this end, the same freestanding membranes used for both microbulge and actuator measurements, were investigated using a JPK NanoWizard 3 AFM with NSG01 cantilever in tapping mode. Height maps with sizes of 10×2 μm^2 were recorded at the edges of hybrid films, which feature the step edges generated in the film transfer step. For every film, height maps at three different positions on the sample were recorded and analyzed using the software *Gwyddion 2.56*. The film thickness was calculated by averaging nine height profiles.

UV-vis Spectroscopy. For UV-vis spectroscopy measurements, hybrid films were deposited on quartz substrates and placed in a home-built sample holder. Four spectra at different positions on the film were recorded in the wavelength range between 200–600 nm using a Varian Cary50 spectrophotometer. The absorbance spectrum of the film was obtained by averaging the four spectra, each corrected for the absorbance of the quartz substrate. Spectra were recorded for various DUV exposure times.

Scanning Electron Microscopy. SEM analysis was applied to investigate the morphology of the freestanding hybrid membranes. To this end, hybrid membranes were examined after burst experiments (cf. section 7.7). The measurements were conducted in the Department of Electron Microscopy of the Institute of Physical Chemistry at University of Hamburg by Robert Schön, using a Zeiss LEO 155 Gemini microscope (acceleration volt-

age: 20 kV).

Optical Microscopy. The film morphology and the exact diameter of the aperture were characterized by optical microscopy using an Olympus BX51 equipped with UC30 CCD camera. Further, remaining membrane parts were investigated after burst experiments.

7.6 Vapor Sensing Experiments

General Setup

Vapor sensing experiments were based on the sequential exposure of samples to zero gas (ZG) and analyte gas (AG). Vapors with defined concentrations were provided using a commercial gas calibration system (CGM2000, MCZ Umwelttechnik) composed of several modules. The flow chart of all modules - air purification unit (yellow frame), vapor saturation system (green frame), 2nd dilution unit (red frame), and humidification unit (blue frame) - is shown in figure 7.3. For all experiments, purified, dry air was used as ZG that was generated from ambient air using a commercial zero gas generator and catalytic gas purifier (NGA 600-25 MD and K15, MCZ Umwelttechnik). In a first step, the ambient air is pressurized, dried over an adsorption dryer, and collected in a pressure tank. Following, the dried air is filtered using several materials in four filter cartridges: silica gel with indicator (orange gel) for further removal and indication of humidity, $KMnO_4/Al_2O_3$ for the removal of H_2S, NH_3, NO_x, SO_2, and SO_3, activated carbon for the removal of high boiling carbons, NO_2, and O_3, and molecular sieve (10 Å) for the adsorption of CO, CO_2, H_2O, and H_2S. In a last step, the air is passed through a catalytic purification unit consisting of a Pt catalyst, which is heated to 485 °C, to remove methane and CO. After passing through a cooling coil and a dust filter, the purified, dry air is continuously fed to the vapor saturation system (cf. figure 7.3, green frame).
There, the ZG is split into two lines and the first line provides pure ZG with a defined flow rate. Within the vapor saturation system, all gas flows are regulated using mass flow controllers (MFCs). The second line provides the AG with a defined analyte concentration. To this end, ZG is guided at a certain flow rate through a saturator vessel containing the liquid analyte compound which is typically heated to 30 °C. Next, the mixture is guided to a condenser where the temperature is set to 15 °C and analyte-saturated vapor is produced. Finally, the desired concentration is obtained by guiding the saturated vapor into a mixing chamber and diluting it with ZG adding up to the total flow rate. The flow rate for both lines is typically set to 2 L/min. To obtain vapor concentrations of volatile organic compounds (VOCs) with a high vapor pressure in the low ppm range, the 2nd dilution unit was used, in which the AG is further diluted with ZG (cf. figure 7.3, red frame).
For vapor sensing experiments, the exposure of the samples to ZG and AG is obtained by switching between both lines using an externally controlled valve. For all experiments, the flow through the test cell was set to 0.5 L/min using a flow controller. For vapor sensing experiments at increased r.h. levels, the humidification unit (cf. figure 7.3, blue frame) was additionally operated, humidifying both lines individually. For this purpose, water-saturated vapor at a desired flow is generated by passing ZG through water baths,

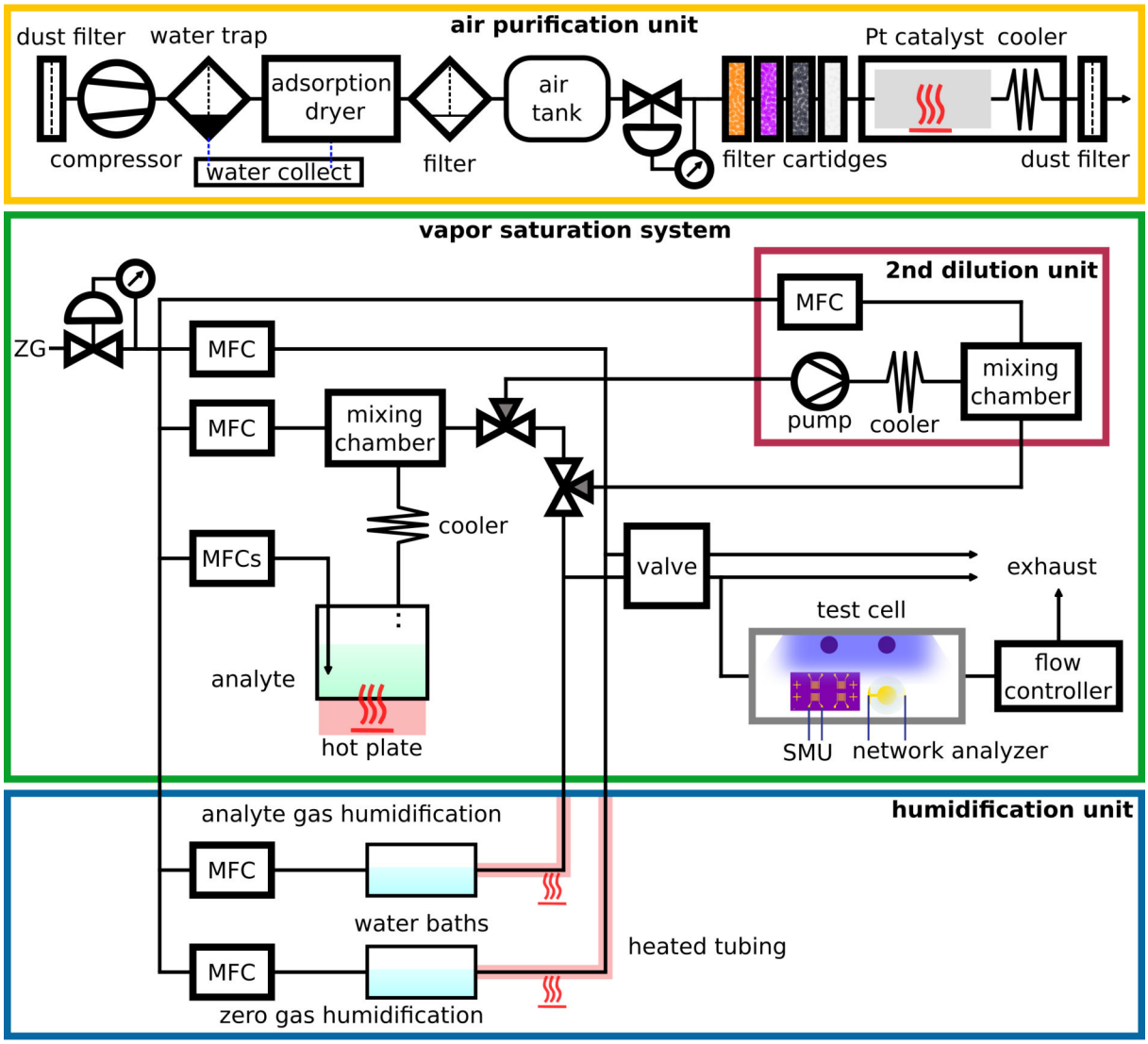

Figure 7.3: Schematic depiction of the flow chart of the vapor sensing set up. For all measurements, the ZG is provided using the air purification unit (yellow frame). This purified, dry air is fed to the vapor saturation system (green frame) to provide AG with defined analyte concentrations. For VOCs with a high vapor pressure, the 2nd dilution unit (red frame) is connected to obtain low analyte concentrations. For vapor sensing experiments at increased r.h. levels, the humidification unit (blue frame) is connected.

with the latter being heated to 28 °C. The water-saturated vapor is passed into the vapor saturation system through heated tubing (60 °C), where it is mixed at a T-piece with the ZG or AG. Using this humidification unit, purified air and analyte vapor with a desired r.h. level and a total flow rate of 2 L/min are provided as ZG and AG, respectively.

Testcell Design

Two custom-built aluminum test cells with a testing volume of ~16 mL were used for the sensing measurements. Figures 7.4a-c) show photographs of the test cells, in which the

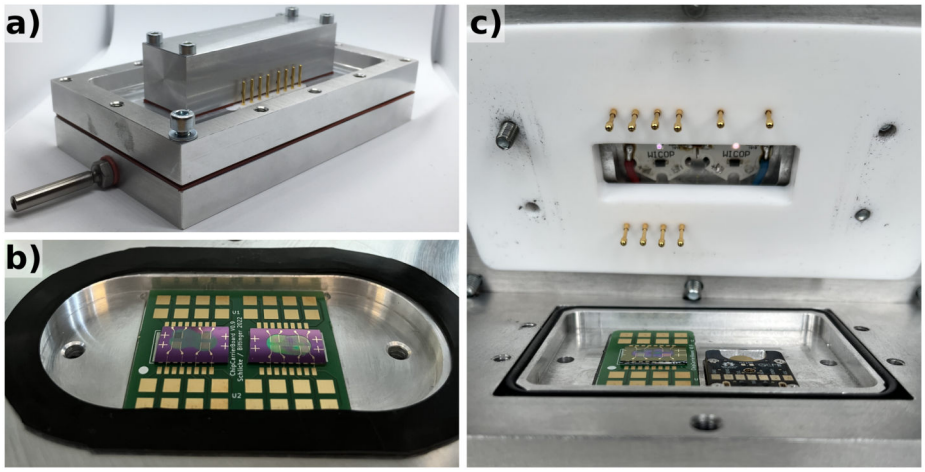

Figure 7.4: Photographs of aluminum test cells used for vapor sensing measurements. a) Picture outlining the three major parts of the test cells: Bottom part with gas inlet and outlet. Center part for connection to the readout. Top part holding the LEDs. b) Test cell used for resistive vapor sensing measurements. Exemplary PCB carrying two TiO_2 thin films on IDE structures. Cell volume: ~16 mL. c) Test cell for simultaneous chemiresistive and microgravimetric measurements showing the UV illumination through the quartz glass. PCB carrying TiO_2 chemiresistor on IDE on the left and TiO_2 film-coated QCM on the right. Cell volume: ~16 mL.

thin films were exposed to analyte vapor and illumination at specific wavelengths in parallel. Both cells are assembled from three major parts, shown in figure 7.4a): The bottom part carries the desired substrate and provides the gas inlet and outlet. Electrical contact to the readout is provided by spring-loaded pin connectors that are embedded in PTFE bits in the center part. The top part holds two light-emitting diodes (LEDs) that are illuminating the testing volume through a quartz slide (75×25×2 mm^3, Won Ik Europe). This top part can be exchanged easily to set the illumination wavelength to 278 nm (CUD7MN1A, Sensor Electronic Technology Inc.), 401 nm (TCN0MF1A, Sensor Electronic Technology Inc.), or 947 nm (LST1-01G01-IR03-00, NewEnergy LLC). The testing volume is sealed by two O-rings at the bottom/center and the center/quartz interface.

7.6.1 TiO_2 Thin Film Chemiresistors

The resistive responses of the TiO_2-based chemiresistors to various analyte vapors were investigated and combined with microgravimetric measurements. Further, the photoactivated chemiresistive sensing properties were investigated at increased operating temperatures with special emphasis on the influence of the r.h. level.

Materials and Apparatus. (*Chemicals and Materials*) 1-Propanol (99.5%) and toluene (99.5%) were purchased from Grüssing GmbH. 1-Butylamine (99.8%), 1-butanol (99.8%), and 4-methylpentan-2-one (methyl isobutyl ketone, MIBK, 98.5%) were purchased from

Merck. 2-Propanol (99.5%), ethanol (99.9%), and ethyl acetate (99.8%) were purchased from VWR Chemicals. DI water (resistivity: 18.2 MΩ cm) was provided using an ELGA LabWater purification system.

Resistive Vapor Sensing

For vapor sensing experiments, the substrate-supported TiO_2 thin films on IDE structures were glued onto custom-designed printed circuit boards (PCBs, manufactured by AISLER Germany GmbH) and contacted via wire-bonding. Sensors were placed in the test cells (cf. figures 7.4b-c)) and contacted by spring-loaded pin connectors to a Keithley 2601A sourcemeter. The latter provided a constant voltage of 10 V and measured the resulting current with a sampling frequency of 2 Hz. Another Keithley 2601A sourcemeter provided a constant current to the LEDs. By adjusting the current the desired irradiance was employed. The characterization of the LEDs is provided in the Appendix section A.1.2. The sensors were exposed to various analytes (ethanol, 1-propanol, 2-propanol, 1-butanol, 1-butylamine, MIBK, toluene, and ethyl acetate). Typically, the concentration ranged between 25-200 ppm, but was increased to 0.5–5000 ppm for the determination of the response isotherm to 1-propanol. The sensors were alternately dosed with AG and ZG, each for 4 min. The influence of increasing r.h. on the photoactivated resistive vapor sensing was investigated by humidifying the AG and ZG with r.h. up to 50% using the humidification unit. Actual r.h. levels were monitored using a commercial gas sensor (BME680, Bosch SensorTec) which was read out using a Raspberry Pi.

QCM Measurements

To determine the amount of analyte molecules adsorbing on the TiO_2 thin films, microgravimetric measurements on QCMs were combined with vapor sensing measurements. For this purpose, the QCMs coated on one side were clamped in sample holders (open-QCM) with the TNC film facing up. Inside the test cell (cf. figure 7.4c)) the holder was connected to an Agilent E5100A Network analyzer using spring-loaded pin connectors. The baseline resonance frequency was recorded in ZG atmosphere with a constant flow of 0.5 L/min for 100 s prior to every analyte exposure. During the vapor sensing measurements, the resonance frequency was continuously recorded with a sampling frequency of 1 Hz using the Network analyzer.

Resistive Vapor Sensing at Elevated Operating Temperatures

For vapor sensing measurements at elevated operating temperatures, the TiO_2 thin films were deposited onto alumina substrates with the latter including a platinum IDE and resistive temperature detector (RTD) on the front of the substrate as well as a heating meander on the backside of the substrate (cf. figures 7.5a,b)). Substrates were clamped in custom-designed sample holders composed of two PCBs (cf. figure 7.5c)), placed inside the test cell, and contacted using spring-loaded pin connectors. The PCBs were manufactured by AISLER Germany GmbH. Constant voltages were applied to the RTD, IDE structure, and the heater using Keithley 2601A sourcemeter units. The voltages were 0.1 V for the RTD and 0 V, 5 V, or 8 V for the heating meander depending on the desired temperature. The IDE was provided with a constant voltage of 10 V and the resulting current was measured with a sampling frequency of 2 Hz. Simultaneously, a Keithley 2601A sourcemeter provided a constant current to the UV LEDs, which was adjusted regarding the desired irradiance. As ZG, purified air with various r.h. levels of 0%, 10%, 30%, and 50% was used. The sensors were dosed with 1-propanol vapor in the concentration range between 50–200 ppm with various r.h. levels of 0%, 10%, 30%, and 50% for 4 min spaced by 4 min of ZG. Actual r.h. levels were monitored using a commercial gas sensor (BME680, Bosch SensorTec) which was read out using a Raspberry Pi.

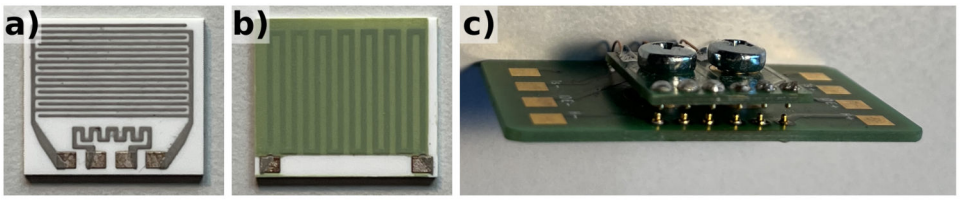

Figure 7.5: Photographs of the alumina substrate and sample holder used for resistive vapor sensing measurements at elevated operating temperatures. a) Upper side of the alumina substrate exposing the platinum RTD and IDE structure consisting of 16 fingers of 250 µm width, spaced by 250 µm, with an overlap of 12500 µm. b) Bottom side exposing the platinum heating meander covered with a glassy insulation layer. c) Custom-built sample holder with 12 spring-loaded pin connectors to clamp and contact the substrate.

7.7 Mechanical Properties and Electrostatic Actuation

The mechanical properties of TNR/GO/SF and TNR/(GO/rGO)/SF freestanding membranes and the electrostatic actuation of TNR/(GO/rGO)/SF freestanding membranes were probed using microbulge tests and electrostatic measurements, respectively. For both experiments, topographic data were acquired using a JPK NanoWizard 3 AFM equipped with cantilevers: either NSG01 for bulge experiments or ACTA-50 for actuator experiments. Freestanding membranes were obtained as described in section 7.5.

Microbulge Tests on TNR/GO/SF and TNR/(GO/rGO)/SF Membranes

Freestanding membranes on substrates with a circular aperture were glued onto custom-built sample holders using double-sided tape (Tesa 05338). By mounting the sample holder in the AFM, the membrane was connected to the pressure sensors and the rotary vane pump (S 1.5 Leybold). The pressure was controlled using three pressure gauges (Sensortechnics, HDIB001DBF8P5 -100–100 kPa, HDIM100DUF8P5 0–10 kPa, HDIM010-DUF8P5 0–1 kPa). Within the total scan area of 100×100 μm^2, ten evenly spaced line scans of 512 pixels were recorded in intermittent contact mode. The scan area covered major

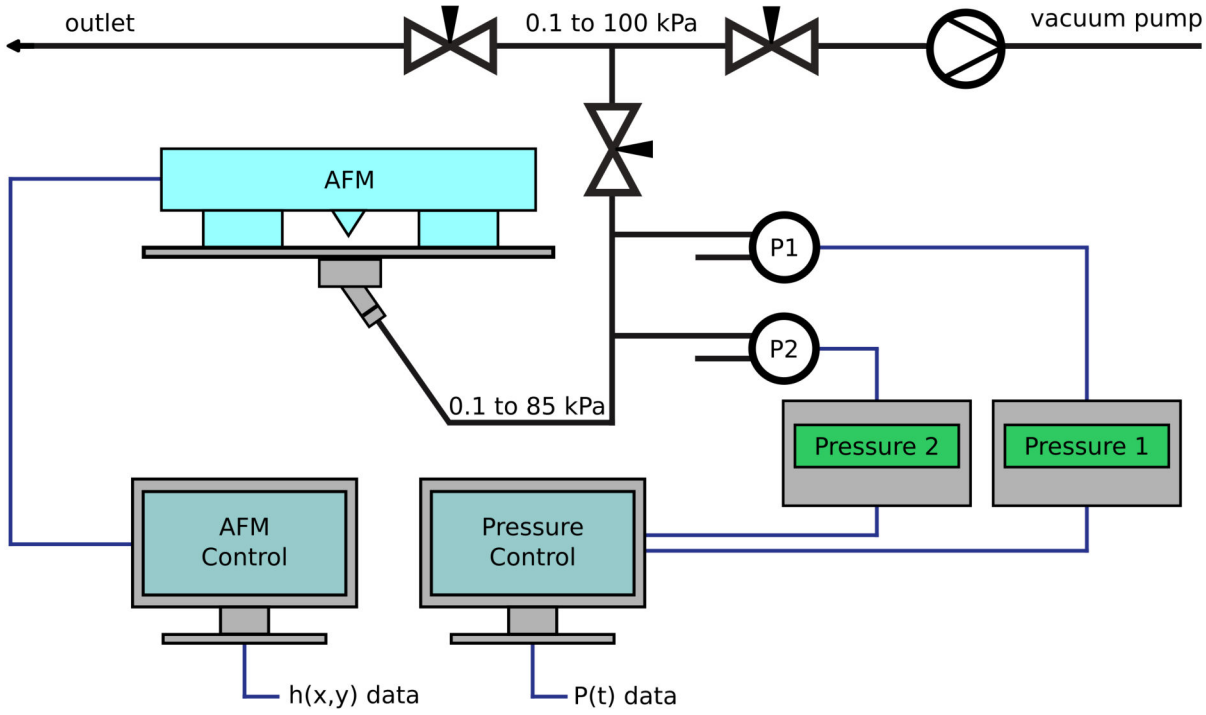

Figure 7.6: Schematic depiction of the experimental setup used for microbulge measurements. Reduced pressures down to 100 kPa were generated using a vacuum pump. Pressures were applied underneath the substrate and controlled using pressure gauges. The latter were read out to obtain time-dependent pressure (P) data. Simultaneously, the spatially resolved deflection (h) data were collected using an AFM.

parts of the freestanding membrane section, including the apex of the bulged membrane as well as sections of the substrate. For bulge experiments, negative differential pressures in the range between 0.1–6 kPa were applied in ascending and descending arrangement using distinct increments. Increments were 0.1 kPa below 1 kPa, 0.2 kPa between 1–3 kPa, and 0.3 kPa between 3–6 kPa, with the same increments applied for descending pressure. For burst experiments, the pressure was increased up to 85 kPa. The increments to 6 kPa were kept the same and then increased to 1 kPa between 6–10 kPa, 2 kPa between 10–40 kPa, and reduced to 1 kPa between 40–85 kPa. Data were processed using the spherical cap model of a thin-walled spherical pressure vessel. The custom-scripted python program was kindly provided by Clemens Jasper Schröter, former research associate at University of Hamburg.

TNR/(GO/rGO)/SF Actuators

The cavity substrates were glued onto custom-designed PCBs and connected via wire-bonding and conductive silver paint, to enable electrostatic actuation of the DUV-treated TNR/(GO/rGO)/SF freestanding membranes. Voltages in increments of 2 V, up to ±40 V were applied to the membrane using a Keithley 2601A sourcemeter unit. Each voltage was maintained for 2 s, followed by 4 s at 0 V. The membrane's deflection was monitored as a function of time at fixed x,y-coordinates by operating the AFM in intermittent contact mode. The measurements were repeated at different positions on the freestanding membrane and the substrate-supported sections.

8 Bibliography

[1] F. Dobschall, H. Hartmann, S. C. Bittinger, N. Schulz, H. Schlicke, H. K. Trieu, T. Vossmeyer, *Adv. Electron. Mater.* **2025**, *11*, 2400602.

[2] S. C. Bittinger, J. Struck, F. Dobschall, S. Benthien, H. Hartmann, H. Schlicke, M. Kohantorabi, H. Noei, T. Vossmeyer, *ACS Appl. Nano Mater.* **2025**, *8*, 7428–7439.

[3] F. Dobschall, S. C. Bittinger, C. T. Tioka, J. Struck, E. Pariente, M.-H. Delville, H. Schlicke, T. Vossmeyer, *ACS Appl. Nano Mater.* **2025**, *8*, 22955–22964.

[4] M. Javaid, A. Haleem, S. Rab, R. Pratap Singh, R. Suman, *Sens. Int.* **2021**, *2*, 100121.

[5] K. Ekinci, *Small* **2005**, *1*, 786–797.

[6] H. G. Craighead, *Science* **2000**, *290*, 1532–1535.

[7] R. A. Potyrailo, *Chem. Rev.* **2016**, *116*, 11877–11923.

[8] P. T. Moseley, *Meas. Sci. Technol.* **2017**, *28*, 082001.

[9] O. S. Wolfbeis, *Fresenius' J. Anal. Chem.* **1990**, *337*, 522–527.

[10] M. Khatib, H. Haick, *ACS Nano* **2022**, *16*, 7080–7115.

[11] S. Fanget, S. Hentz, P. Puget, J. Arcamone, M. Matheron, E. Colinet, P. Andreucci, L. Duraffourg, E. Myers, M. Roukes, *Sens. Actuator B Chem.* **2011**, *160*, 804–821.

[12] J. Dai, O. Ogbeide, N. Macadam, Q. Sun, W. Yu, Y. Li, B.-L. Su, T. Hasan, X. Huang, W. Huang, *Chem. Soc. Rev.* **2020**, *49*, 1756–1789.

[13] S. Hong, M. Wu, Y. Hong, Y. Jeong, G. Jung, W. Shin, J. Park, D. Kim, D. Jang, J.-H. Lee, *Sens. Actuator B Chem.* **2021**, *330*, 129240.

[14] V. Montes-García, M. A. Squillaci, M. Diez-Castellnou, Q. K. Ong, F. Stellacci, P. Samorì, *Chem. Soc. Rev.* **2021**, *50*, 1269–1304.

[15] T. Zhou, T. Zhang, *Small Methods* **2021**, *5*, 2100515.

[16] Z. Meng, R. M. Stolz, L. Mendecki, K. A. Mirica, *Chem. Rev.* **2019**, *119*, 478–598.

[17] G. Jiménez-Cadena, J. Riu, F. X. Rius, *Analyst* **2007**, *132*, 1083.

[18] K. Chikkadi, M. Muoth, C. Roman, M. Haluska, C. Hierold, *Beilstein J. Nanotechnol.* **2014**, *5*, 2179–2191.

[19] J. Schneider, M. Matsuoka, M. Takeuchi, J. Zhang, Y. Horiuchi, M. Anpo, D. W. Bahnemann, *Chem. Rev.* **2014**, *114*, 9919–9986.

[20] A. Fujishima, K. Honda, *Nature* **1972**, *238*, 37–38.

[21] L. Hu, D. S. Hecht, G. Grüner, *Chem. Rev.* **2010**, *110*, 5790–5844.

[22] L. Petti, N. Münzenrieder, C. Vogt, H. Faber, L. Büthe, G. Cantarella, F. Bottacchi, T. D. Anthopoulos, G. Tröster, *Appl. Phys. Rev.* **2016**, *3*, 021303.

[23] A. Bétard, R. A. Fischer, *Chem. Rev.* **2012**, *112*, 1055–1083.

[24] T. Druffel, N. Mandzy, M. Sunkara, E. Grulke, *Small* **2008**, *4*, 459–461.
[25] E. Fortunato, P. Barquinha, R. Martins, *Adv. Mater.* **2012**, *24*, 2945–2986.
[26] T. D. Lee, A. U. Ebong, *Renew. Sust. Energ. Rev.* **2017**, *70*, 1286–1297.
[27] J. Li, J. A. Hutchison, D. Smith, H. Wu, P. Mulvaney, *Nano Lett.* **2024**, *24*, 4362–4368.
[28] H. Schlicke, M. Behrens, C. J. Schröter, G. T. Dahl, H. Hartmann, T. Vossmeyer, *ACS Sens.* **2017**, *2*, 540–546.
[29] M. Cargnello, T. R. Gordon, C. B. Murray, *Chem. Rev.* **2014**, *114*, 9319–9345.
[30] H. Zhang, J. F. Banfield, *Chem. Rev.* **2014**, *114*, 9613–9644.
[31] T. Rajh, N. M. Dimitrijevic, M. Bissonnette, T. Koritarov, V. Konda, *Chem. Rev.* **2014**, *114*, 10177–10216.
[32] M. Ismael, *Sol. Energy* **2020**, *211*, 522–546.
[33] E. Matijevi , M. Budnik, L. Meites, *J. Colloid Interface Sci.* **1977**, *61*, 302–311.
[34] C. Deiana, M. Minella, G. Tabacchi, V. Maurino, E. Fois, G. Martra, *Phys. Chem. Chem. Phys.* **2013**, *15*, 307–315.
[35] M. Zhao, L. Li, H. Lin, L. Yang, G. Li, *Chem. Commun.* **2013**, *49*, 7046.
[36] F. Pellegrino, E. Ortel, J. Mielke, R. Schmidt, V. Maurino, V.-D. Hodoroaba, *Adv. Eng. Mater.* **2022**, *24*, 2101347.
[37] A. Vioux, *Chem. Mater.* **1997**, *9*, 2292–2299.
[38] M. Niederberger, M. H. Bartl, G. D. Stucky, *Chem. Mater.* **2002**, *14*, 4364–4370.
[39] M. Niederberger, M. H. Bartl, G. D. Stucky, *J. Am. Chem. Soc.* **2002**, *124*, 13642–13643.
[40] T. R. Gordon, M. Cargnello, T. Paik, F. Mangolini, R. T. Weber, P. Fornasiero, C. B. Murray, *J. Am. Chem. Soc.* **2012**, *134*, 6751–6761.
[41] R. I. Bickley, T. Gonzalez-Carreno, J. S. Lees, L. Palmisano, R. J. Tilley, *J. Solid State Chem.* **1991**, *92*, 178–190.
[42] A. L. Linsebigler, G. Lu, J. T. Yates, *Chem. Rev.* **1995**, *95*, 735–758.
[43] D Reyes-Coronado, G Rodríguez-Gattorno, M. E. Espinosa-Pesqueira, C Cab, R De Coss, G Oskam, *Nanotechnology* **2008**, *19*, 145605.
[44] Q. Guo, C. Zhou, Z. Ma, X. Yang, *Adv. Mater.* **2019**, *31*, 1901997.
[45] P. J. D. Lindan, N. M. Harrison, M. J. Gillan, J. A. White, *Phys. Rev. B* **1997**, *55*, 15919–15927.
[46] S. Chrétien, H. Metiu, *J. Phys. Chem. C* **2011**, *115*, 4696–4705.
[47] Y. Lan, Y. Lu, Z. Ren, *Nano Energy* **2013**, *2*, 1031–1045.
[48] A. Di Paola, M. Bellardita, L. Palmisano, *Catalysts* **2013**, *3*, 36–73.
[49] Y. Ma, X. Wang, Y. Jia, X. Chen, H. Han, C. Li, *Chem. Rev.* **2014**, *114*, 9987–10043.
[50] J. Bai, B. Zhou, *Chem. Rev.* **2014**, *114*, 10131–10176.

[51] M. M. Mahlambi, C. J. Ngila, B. B. Mamba, *J. Nanomater.* **2015**, *2015*, 790173.
[52] J. Zhang, P. Zhou, J. Liu, J. Yu, *Phys. Chem. Chem. Phys.* **2014**, *16*, 20382–20386.
[53] T. A. Kandiel, L. Robben, A. Alkaima, D. Bahnemann, *Photochem. Photobiol. Sci.* **2013**, *12*, 602–609.
[54] Z. Li, S. Cong, Y. Xu, *ACS Catal.* **2014**, *4*, 3273–3280.
[55] B. Navinšek, P. Panjan, I. Milošev, *Surf. Coat. Technol.* **1999**, *116-119*, 476–487.
[56] Y. Zhang, L. Zhang, C. Zhou, *Acc. Chem. Res.* **2013**, *46*, 2329–2339.
[57] R. M. Pasquarelli, D. S. Ginley, R. O'Hayre, *Chem. Soc. Rev.* **2011**, *40*, 5406.
[58] L. E. Scriven, *Mater. Res. Soc. symp. proc.* **1988**, *121*, 717.
[59] F. Scarpelli, T. F. Mastropietro, T. Poerio, N. Godbert in *Titanium Dioxide - Material for a Sustainable Environment*, InTech, **2018**.
[60] C. Xu, D. Gao, *J. Phys. Chem. C* **2012**, *116*, 7236–7241.
[61] N. Tétreault, E. Arsenault, L.-P. Heiniger, N. Soheilnia, J. Brillet, T. Moehl, S. Zakeeruddin, G. A. Ozin, M. Grätzel, *Nano Lett.* **2011**, *11*, 4579–4584.
[62] M. Manera, A. Taurino, M. Catalano, R. Rella, A. Caricato, R. Buonsanti, P. Cozzoli, M. Martino, *Sens. Actuator B Chem.* **2012**, *161*, 869–879.
[63] J. Watté, P. Lommens, G. Pollefeyt, M. Meire, K. De Buysser, I. Van Driessche, *ACS Appl. Mater. Interfaces* **2016**, *8*, 13027–13036.
[64] S. Zhang, T. Lei, D. Li, G. Zhang, C. Xie, *Sens. Actuator B Chem.* **2014**, *202*, 964–970.
[65] N. D. Chinh, C. Kim, D. Kim, *J. Alloys Compd.* **2019**, *778*, 247–255.
[66] B. O'Regan, M. Gratzelt, *Nature* **1991**, *353*, 737–740.
[67] A. Hensel, C. J. Schröter, H. Schlicke, N. Schulz, S. Riekeberg, H. K. Trieu, A. Stierle, H. Noei, H. Weller, T. Vossmeyer, *Nanomaterials* **2019**, *9*, 1230.
[68] T. Ishihara, S. Matsubara, *J. Electroceramics* **1998**, *2*, 215–228.
[69] P. Pasierb, M. Rekas, *J. Solid State Electrochem.* **2009**, *13*, 3–25.
[70] Y. Jian, W. Hu, Z. Zhao, P. Cheng, H. Haick, M. Yao, W. Wu, *Nano-Micro Lett.* **2020**, *12*, 71.
[71] T. Seiyama, A. Kato, K. Fujiishi, M. Nagatani, *Anal. Chem.* **1962**, *34*, 1502–1503.
[72] Y. Masuda, *Sens. Actuator B Chem.* **2022**, *364*, 131876.
[73] M. A. Franco, P. P. Conti, R. S. Andre, D. S. Correa, *Sens. Actuator Rep.* **2022**, *4*, 100100.
[74] C. Dong, R. Zhao, L. Yao, Y. Ran, X. Zhang, Y. Wang, *J. Alloys Compd.* **2020**, *820*, 153194.
[75] M. C. Lonergan, E. J. Severin, B. J. Doleman, S. A. Beaber, R. H. Grubbs, N. S. Lewis, *Chem. Mater.* **1996**, *8*, 2298–2312.
[76] N. Krasteva, Y. Fogel, R. Bauer, K. Müllen, Y. Joseph, N. Matsuzawa, A. Yasuda, T. Vossmeyer, *Adv. Funct. Mater.* **2007**, *17*, 881–888.

[77] Y. Gönüllü, G. C. M. Rodríguez, B. Saruhan, M. Ürgen, *Sens. Actuator B Chem.* **2012**, *169*, 151–160.
[78] S. Mahajan, S. Jagtap, *Appl. Mater. Today* **2020**, *18*, 100483.
[79] M. Franke, T. Koplin, U. Simon, *Small* **2006**, *2*, 36–50.
[80] N. Barsan, U. Weimar, *J. Electroceramics* **2001**, *7*, 143–167.
[81] M. J. Madou, S. R. Morrison, *Chemical Sensing with Solid State Devices*, Academic Press, New York, **1989**.
[82] N. Yamazoe, G. Sakai, K. Shimanoe, *Catal. Surv. Asia* **2003**, *7*, 63–75.
[83] H. Ogawa, M. Nishikawa, A. Abe, *J. Appl. Phys.* **1982**, *53*, 4448–4455.
[84] J. Tamaki, Z. Zhang, K. Fujimori, M. Akiyama, T. Harada, N. Miura, N. Yamazoe, *J. Electrochem. Soc.* **1994**, *141*, 2207–2210.
[85] K. Schierbaum, U. Weimar, W. Göpel, R. Kowalkowski, *Sens. Actuator B Chem.* **1991**, *3*, 205–214.
[86] T. Sahm, L. Mädler, A. Gurlo, N. Barsan, S. Pratsinis, U. Weimar, *Sens. Actuator B Chem.* **2004**, *98*, 148–153.
[87] Z. Wang, L. Zhu, J. Wang, R. Zhuang, P. Mu, J. Wang, W. Yan, *RSC Adv.* **2022**, *12*, 24614–24632.
[88] D. Kohl, *Sens. Actuator B Chem.* **1990**, *1*, 158–165.
[89] N. Yamazoe, *Sens. Actuator B Chem.* **1991**, *5*, 7–19.
[90] S. Saito, M. Miyayama, K. Koumoto, H. Yanagida, *J. Am. Ceram. Soc.* **1985**, *68*, 40–43.
[91] S. Matsushima, Y. Teraoka, N. Miura, N. Yamazoe, *Jpn. J. Appl. Phys.* **1988**, *27*, 1798.
[92] L. Skubal, N. Meshkov, M. Vogt, *J. Photochem. Photobiol. A* **2002**, *148*, 103–108.
[93] S. X. Jin, J. Li, J. Y. Lin, H. X. Jiang, *Appl. Phys. Lett.* **2000**, *77*, 3236–3238.
[94] Figaro, Figaro Product Information, TGS2600, (18.08.2025), **2022**.
[95] E. Espid, F. Taghipour, *Crit. Rev. Solid State Mater. Sci.* **2017**, *42*, 416–432.
[96] B. Liu, Y. Luo, K. Li, H. Wang, L. Gao, G. Duan, *Adv. Mater. Interfaces* **2019**, *6*, 1900376.
[97] J. M. Suh, T. H. Eom, S. H. Cho, T. Kim, H. W. Jang, *Mater. Adv.* **2021**, *2*, 827–844.
[98] A. A. Haidry, W. Yucheng, Q. Fatima, A. Raza, L. Zhong, H. Chen, C. R. Mandebvu, F. Ghani, *Trends Anal. Chem.* **2024**, *170*, 117454.
[99] Z. Wu, M. Su, X. Song, D. Li, X. Li, J. Liu, J. Zhang, *ACS Appl. Electron. Mater.* **2024**, *6*, 4356–4368.
[100] A. Šutka, R. Eglitis, A. Kuzma, K. Smits, A. Zukuls, J. D. Prades, C. Fàbrega, *ACS Appl. Nano Mater.* **2021**, *4*, 2522–2527.
[101] H. Chen, Y. Liu, C. Xie, J. Wu, D. Zeng, Y. Liao, *Ceram. Int.* **2012**, *38*, 503–509.

[102] A. Hazra, B. Bhowmik, K. Dutta, P. Chattopadhyay, P. Bhattacharyya, *ACS Appl. Mater. Interfaces* **2015**, *7*, 9336–9348.
[103] L. Liu, X. Li, P. K. Dutta, J. Wang, *Sens. Actuator B Chem.* **2013**, *185*, 1–9.
[104] X. Tian, X. Yang, F. Yang, T. Qi, *Colloids Surf. A* **2019**, *578*, 123621.
[105] M. Egashira, M. Nakashima, S. Kawasumi, T. Selyama, *J. Phys. Chem.* **1981**, *85*, 4125–4130.
[106] S. Das, S. Mojumder, D. Saha, M. Pal, *Sens. Actuator B Chem.* **2022**, *352*, 131066.
[107] P. K. Kannan, R. Saraswathi, J. B. B. Rayappan, *Sens. Actuator A Phys.* **2010**, *164*, 8–14.
[108] P. Faia, C. Furtado, A. Ferreira, *Sens. Actuator B Chem.* **2004**, *101*, 183–190.
[109] J. Gong, Q. Chen, M.-R. Lian, N.-C. Liu, R. G. Stevenson, F. Adami, *Sens. Actuator B Chem.* **2006**, *114*, 32–39.
[110] B. Yadav, R. Srivastava, C. Dwivedi, *Phil. Mag.* **2008**, *88*, 1113–1124.
[111] T. Yildirim, L. Zhang, G. P. Neupane, S. Chen, J. Zhang, H. Yan, M. M. Hasan, G. Yoshikawa, Y. Lu, *Nanoscale* **2020**, *12*, 22366–22385.
[112] S. Markutsya, C. Jiang, Y. Pikus, V. V. Tsukruk, *Adv. Funct. Mater.* **2005**, *15*, 771–780.
[113] C. Jiang, M. E. McConney, S. Singamaneni, E. Merrick, Y. Chen, J. Zhao, L. Zhang, V. V. Tsukruk, *Chem. Mater.* **2006**, *18*, 2632–2634.
[114] R. J. Nicholl, H. J. Conley, N. V. Lavrik, I. Vlassiouk, Y. S. Puzyrev, V. P. Sreenivas, S. T. Pantelides, K. I. Bolotin, *Nat. Commun.* **2015**, *6*, 8789.
[115] X. Fan, F. Forsberg, A. D. Smith, S. Schröder, S. Wagner, M. Östling, M. C. Lemme, F. Niklaus, *Nano Lett.* **2019**, *19*, 6788–6799.
[116] B. Mondal, P. K. Gogoi, *ACS Appl. Electron. Mater.* **2022**, *4*, 59–86.
[117] T. Liu, W. Chen, T. Huang, G. Duan, X. Yang, X. Liu, *J. Mater. Sci.* **2016**, *51*, 6987–6997.
[118] R. Sellappan, J. Zhu, H. Fredriksson, R. S. Martins, M. Zäch, D. Chakarov, *J. Mol. Catal. A Chem.* **2011**, *335*, 136–144.
[119] M. El-Kemary, Y. Abdel-Moneam, M. Madkour, I. El-Mehasseb, *J. Lumin.* **2011**, *131*, 570–576.
[120] Y. Wang, S. Wang, H. Zhang, X. Gao, J. Yang, L. Wang, *J. Mater. Chem. A* **2014**, *2*, 7935.
[121] K. S. Novoselov, A. K. Geim, S. V. Morozov, D. Jiang, Y. Zhang, S. V. Dubonos, I. V. Grigorieva, A. A. Firsov, *Science* **2004**, *306*, 666–669.
[122] C. Cheng, S. Li, A. Thomas, N. A. Kotov, R. Haag, *Chem. Rev.* **2017**, *117*, 1826–1914.
[123] O. C. Compton, S. T. Nguyen, *Small* **2010**, *6*, 711–723.
[124] W. S. Hummers, R. E. Offeman, *J. Am. Chem. Soc.* **1958**, *80*, 1339–1339.

[125] P. P. Brisebois, M. Siaj, *J. Mater. Chem. C* **2020**, *8*, 1517–1547.
[126] A. Lerf, H. He, M. Forster, J. Klinowski, *J. Phys. Chem. B* **1998**, *102*, 4477–4482.
[127] K. Erickson, R. Erni, Z. Lee, N. Alem, W. Gannett, A. Zettl, *Adv. Mater.* **2010**, *22*, 4467–4472.
[128] J. Shao, W. Lv, Q. Yang, *Adv. Mater.* **2014**, *26*, 5586–5612.
[129] T. Lee, S. H. Min, M. Gu, Y. K. Jung, W. Lee, J. U. Lee, D. G. Seong, B.-S. Kim, *Chem. Mater.* **2015**, *27*, 3785–3796.
[130] I. Jung, D. A. Dikin, R. D. Piner, R. S. Ruoff, *Nano Lett.* **2008**, *8*, 4283–4287.
[131] S. Pei, J. Zhao, J. Du, W. Ren, H.-M. Cheng, *Carbon* **2010**, *48*, 4466–4474.
[132] H. Li, C. Bubeck, *Macromol. Res.* **2013**, *21*, 290–297.
[133] R. Larciprete, S. Fabris, T. Sun, P. Lacovig, A. Baraldi, S. Lizzit, *J. Am. Chem. Soc.* **2011**, *133*, 17315–17321.
[134] M. Koinuma, C. Ogata, Y. Kamei, K. Hatakeyama, H. Tateishi, Y. Watanabe, T. Taniguchi, K. Gezuhara, S. Hayami, A. Funatsu, M. Sakata, Y. Kuwahara, S. Kurihara, Y. Matsumoto, *J. Phys. Chem. C* **2012**, *116*, 19822–19827.
[135] K. Sellschopp, W. Heckel, J. Gäding, C. J. Schröter, A. Hensel, T. Vossmeyer, H. Weller, S. Müller, G. B. Vonbun-Feldbauer, *J. Chem. Phys.* **2020**, *152*, 064702.
[136] S. Ayissi, P. A. Charpentier, N. Farhangi, J. A. Wood, K. Palotás, W. A. Hofer, *J. Phys. Chem. C* **2013**, *117*, 25424–25432.
[137] G. Williams, B. Seger, P. V. Kamat, *ACS Nano* **2008**, *2*, 1487–1491.
[138] N. J. Bell, Y. H. Ng, A. Du, H. Coster, S. C. Smith, R. Amal, *J. Phys. Chem. C* **2011**, *115*, 6004–6009.
[139] B. Li, X. Zhang, X. Li, L. Wang, R. Han, B. Liu, W. Zheng, X. Li, Y. Liu, *Chem. Commun.* **2010**, *46*, 3499.
[140] X. Zhao, Z. Wang, Y. Xie, H. Xu, J. Zhu, X. Zhang, W. Liu, G. Yang, J. Ma, Y. Liu, *Small* **2018**, *14*, 1801325.
[141] S. Park, D. A. Dikin, S. T. Nguyen, R. S. Ruoff, *J. Phys. Chem. C* **2009**, *113*, 15801–15804.
[142] K. Hu, M. K. Gupta, D. D. Kulkarni, V. V. Tsukruk, *Adv. Mater.* **2013**, *25*, 2301–2307.
[143] R. Xiong, K. Hu, A. M. Grant, R. Ma, W. Xu, C. Lu, X. Zhang, V. V. Tsukruk, *Adv. Mater.* **2016**, *28*, 1501–1509.
[144] M. I. Dafinone, G. Feng, T. Brugarolas, K. E. Tettey, D. Lee, *ACS Nano* **2011**, *5*, 5078–5087.
[145] W. Oliver, G. Pharr, *J. Mater. Res.* **1992**, *7*, 1564–1583.
[146] H. Cho, J. Lee, H. Hwang, W. Hwang, J.-G. Kim, S. Kim, *Friction* **2022**, *10*, 282–295.
[147] M. K. Small, W. Nix, *J. Mater. Res.* **1992**, *7*, 1553–1563.

[148] J. S. Bunch, A. M. Van Der Zande, S. S. Verbridge, I. W. Frank, D. M. Tanenbaum, J. M. Parpia, H. G. Craighead, P. L. McEuen, *Science* **2007**, *315*, 490–493.

[149] A. M. V. D. Zande, R. A. Barton, J. S. Alden, C. S. Ruiz-Vargas, W. S. Whitney, P. H. Q. Pham, J. Park, J. M. Parpia, H. G. Craighead, P. L. McEuen, *Nano Lett.* **2010**, *10*, 4869–4873.

[150] A. Castellanos Gomez, M. Poot, G. A. Steele, H. S. J. Van Der Zant, N. Agraït, G. Rubio Bollinger, *Adv. Mater.* **2012**, *24*, 772–775.

[151] A. Reserbat-Plantey, K. G. Schädler, L. Gaudreau, G. Navickaite, J. Güttinger, D. Chang, C. Toninelli, A. Bachtold, F. H. L. Koppens, *Nat. Commun.* **2016**, *7*, 10218.

[152] H. Hartmann, J.-N. Beyer, J. Hansen, S. C. Bittinger, M. Yesilmen, H. Schlicke, T. Vossmeyer, *ACS Appl. Mater. Interfaces* **2021**, *13*, 40932–40941.

[153] M Suter, O Ergeneman, B. J. Nelson, C Hierold, *J. Micromech. Microeng.* **2011**.

[154] X. Zhang, R. Waitz, F. Yang, C. Lutz, P. Angelova, A. Gölzhäuser, E. Scheer, *Appl. Phys. Lett.* **2015**, *106*, 063107.

[155] A. Castellanos Gomez, V. Singh, H. S. J. Van Der Zant, G. A. Steele, *Ann. Phys. (Berlin)* **2015**, *527*, 27–44.

[156] J. T. M. Van Beek, R Puers, *J. Micromech. Microeng.* **2012**, *22*, 013001.

[157] C. Chen, S. Rosenblatt, K. I. Bolotin, W. Kalb, P. Kim, I. Kymissis, H. L. Stormer, T. F. Heinz, J. Hone, *Nat. Nanotechnol.* **2009**, *4*, 861–867.

[158] H. Schlicke, D. Battista, S. Kunze, C. J. Schröter, M. Eich, T. Vossmeyer, *ACS Appl. Mater. Interfaces* **2015**, *7*, 15123–15128.

[159] H. Schlicke, M. Rebber, S. Kunze, T. Vossmeyer, *Nanoscale* **2016**, *8*, 183–186.

[160] A. B. Kaul, E. W. Wong, L. Epp, B. D. Hunt, *Nano Lett.* **2006**, *6*, 942–947.

[161] A. Subramanian, A. R. Alt, L. Dong, B. E. Kratochvil, C. R. Bolognesi, B. J. Nelson, *ACS Nano* **2009**, *3*, 2953–2964.

[162] J. Svensson, N. Lindahl, H. Yun, M. Seo, D. Midtvedt, Y. Tarakanov, N. Lindvall, O. Nerushev, J. Kinaret, S. Lee, E. E. B. Campbell, *Nano Lett.* **2011**, *11*, 3569–3575.

[163] C. T. Tioka, MA thesis, University of Hamburg, Hamburg, **2023**.

[164] G. Sauerbrey, *Z. Phys.* **1959**, *155*, 206–222.

[165] C.-Y. Liu, PhD thesis, University of Hamburg, Hamburg, **2024**.

[166] R. Buonsanti, V. Grillo, E. Carlino, C. Giannini, T. Kipp, R. Cingolani, P. D. Cozzoli, *J. Am. Chem. Soc.* **2008**, *130*, 11223–11233.

[167] ICSD, ICSD Database Entry 9852, Anatase. Zeitschrift für Kristallographie - Crystalline Materials, 1972; Vol. 136 pp 273-281.

[168] ICSD, ICSD Database Entry 36408, Brookite. Canadian Mineralogist, 1979; Vol. 17, pp 77-85.

[169] A. Mills, S.-K. Lee, A. Lepre, I. P. Parkin, S. A. O'Neill, *Photochem. Photobiol. Sci.* **2002**, *1*, 865–868.
[170] L. Mino, F. Pellegrino, S. Rades, J. Radnik, V.-D. Hodoroaba, G. Spoto, V. Maurino, G. Martra, *ACS Appl. Nano Mater.* **2018**, *1*, 5355–5365.
[171] T. Sugimoto, X. Zhou, A. Muramatsu, *J. Colloid Interface Sci.* **2003**, *259*, 53–61.
[172] ICSD, ICSD Database Entry 9161, Rutile. Acta Crystallographica, 1971; Vol. 27, pp 2133-2139.
[173] H. Hahn, J. Logas, R. S. Averback, *J. Mater. Res.* **1990**, *5*, 609–614.
[174] K. Chang, C. Podder, H. Pan, *ACS Appl. Nano Mater.* **2023**, *6*, 23418–23429.
[175] H. Zhang, J. F. Banfield, *J. Phys. Chem. B* **2000**, *104*, 3481–3487.
[176] Y. Pellegrin, F. Odobel, *C. r. Chim.* **2016**, *20*, 283–295.
[177] H. Yang, H. Amari, L. Liu, C. Zhao, H. Gao, A. He, N. D. Browning, M. A. Little, R. S. Sprick, A. I. Cooper, *Nanoscale* **2020**, *12*, 24488–24494.
[178] B. Gehl, A. Frömsdorf, V. Aleksandrovic, T. Schmidt, A. Pretorius, J. Flege, S. Bernstorff, A. Rosenauer, J. Falta, H. Weller, M. Bäumer, *Adv. Funct. Mater.* **2008**, *18*, 2398–2410.
[179] S. Shaw, B. Yuan, X. Tian, K. J. Miller, B. M. Cote, J. L. Colaux, A. Migliori, M. G. Panthani, L. Cademartiri, *Adv. Mater.* **2016**, *28*, 8892–8899.
[180] X. Feng, J. Liang, Y. Yang, C. Xiao, *J. Nanopart. Res.* **2021**, *23*, 118.
[181] C. Aliaga, J. Y. Park, Y. Yamada, H. S. Lee, C.-K. Tsung, P. Yang, G. A. Somorjai, *J. Phys. Chem. C* **2009**, *113*, 6150–6155.
[182] N. Korner, E. Beck, A. Dommann, N. Onda, J. Ramm, *Surf. Coat. Technol.* **1995**, *76-77*, 731–737.
[183] P. Cools, N. De Geyter, E. Vanderleyden, P. Dubruel, R. Morent, *Plasma Chem. Plasma Process.* **2014**, *34*, 917–932.
[184] K. Raiber, A. Terfort, C. Benndorf, N. Krings, H.-H. Strehblow, *Surf. Sci.* **2005**, *595*, 56–63.
[185] Y. Muraoka, N. Takubo, Z. Hiroi, *J. Appl. Phys.* **2009**, *105*, 103702.
[186] H. Schlicke, S. C. Bittinger, H. Noei, T. Vossmeyer, *ACS Appl. Nano Mater.* **2021**, *4*, 10399–10408.
[187] Institut für Arbeitsschutz der Deutschen Gesetzlichen Unfallversicherung, GESTIS-Stoffdatenbank, (02.07.2025), **2025**.
[188] A. Bondi, *J. Phys. Chem.* **1964**, *68*, 441–451.
[189] V. Schomaker, D. P. Stevenson, *J. Am. Chem. Soc.* **1941**, *63*, 37–40.
[190] D. Zhao, X. Zhang, L. Sui, W. Wang, X. Zhou, X. Cheng, S. Gao, Y. Xu, L. Huo, *Sens. Actuator B Chem.* **2020**, *312*, 127942.
[191] H. Park, W. Choi, *J. Phys. Chem. B* **2004**, *108*, 4086–4093.
[192] M. Mrowetz, E. Selli, *New J. Chem.* **2006**, *30*, 108–114.

[193] S. Liu, J. Yu, M. Jaroniec, *J. Am. Chem. Soc.* **2010**, *132*, 11914–11916.
[194] L. Mohrhusen, K. Al-Shamery, *Catal. Lett.* **2023**, *153*, 321–337.
[195] L. Mohrhusen, J. Kräuter, K. Al-Shamery, *Phys. Chem. Chem. Phys.* **2021**, *23*, 12148–12157.
[196] J. Kräuter, L. Mohrhusen, F. Waidhas, O. Brummel, J. Libuda, K. Al-Shamery, *J. Phys. Chem. C* **2021**, *125*, 3355–3367.
[197] J. Kräuter, E. Franz, F. Waidhas, O. Brummel, Jörg Libuda, K. Al-Shamery, *J. Catal.* **2022**, *406*, 134–144.
[198] C. A. Walenta, S. L. Kollmannsberger, J. Kiermaier, A. Winbauer, M. Tschurl, U. Heiz, *Phys. Chem. Chem. Phys.* **2015**, *17*, 22809–22814.
[199] Y. K. Kim, B. D. Kay, J. M. White, Z. Dohnálek, *Catal. Lett.* **2007**, *119*, 1–4.
[200] Z. Li, R. S. Smith, B. D. Kay, Z. Dohnálek, *J. Phys. Chem. C* **2011**, *115*, 22534–22539.
[201] B. Karunagaran, P. Uthirakumar, S. Chung, S. Velumani, E.-K. Suh, *Mater. Charact.* **2007**, *58*, 680–684.
[202] K. S. Kim, M. A. Barteau, W. E. Farneth, *Langmuir* **1988**, *4*, 533–543.
[203] A. Tischner, T. Maier, C. Stepper, A. Köck, *Sens. Actuator B Chem.* **2008**, *134*, 796–802.
[204] Q. Qi, T. Zhang, X. Zheng, H. Fan, L. Liu, R. Wang, Y. Zeng, *Sens. Actuator B Chem.* **2008**, *134*, 36–42.
[205] H. Tada, Q. Jin, H. Nishijima, H. Yamamoto, M. Fujishima, S. Okuoka, T. Hattori, Y. Sumida, H. Kobayashi, *Angew. Chem. Int. Ed.* **2011**, *50*, 3501–3505.
[206] M. Nolan, *Phys. Chem. Chem. Phys.* **2011**, *13*, 18194.
[207] J. Kappler, N. Bârsan, U. Weimar, A. Dièguez, J. L. Alay, A. Romano-Rodriguez, J. R. Morante, W. Göpel, *Fresenius' J. Anal. Chem.* **1998**, *361*, 110–114.
[208] B. Kim, S. H. Choi, X.-Y. Zhu, C. D. Frisbie, *J. Am. Chem. Soc.* **2011**, *133*, 19864–19877.
[209] D. O. Scanlon, C. W. Dunnill, J. Buckeridge, S. A. Shevlin, A. J. Logsdail, S. M. Woodley, C. R. A. Catlow, M. J. Powell, R. G. Palgrave, I. P. Parkin, G. W. Watson, T. W. Keal, P. Sherwood, A. Walsh, A. A. Sokol, *Nat. Mater.* **2013**, *12*, 798–801.
[210] G. Menagen, J. E. Macdonald, Y. Shemesh, I. Popov, U. Banin, *J. Am. Chem. Soc.* **2009**, *131*, 17406–17411.
[211] C. Pacholski, A. Kornowski, H. Weller, *Angew. Chem.* **2004**, *116*, 4878–4881.
[212] F. Dobschall, MA thesis, University of Hamburg, Hamburg, **2021**.
[213] J. Chen, Y. Li, L. Huang, C. Li, G. Shi, *Carbon* **2015**, *81*, 826–834.
[214] D. C. Marcano, D. V. Kosynkin, J. M. Berlin, A. Sinitskii, Z. Sun, A. Slesarev, L. B. Alemany, W. Lu, J. M. Tour, *ACS Nano* **2010**, *4*, 4806–4814.
[215] S. C. Bittinger, PhD thesis, University of Hamburg, Hamburg, **2023**.

[216] D. N. Rockwood, R. C. Preda, T. Yücel, X. Wang, M. L. Lovett, D. L. Kaplan, *Nat. Protoc.* **2011**, *6*, 1612–1631.

[217] A. R. Murphy, D. L. Kaplan, *J. Mater. Chem.* **2009**, *19*, 6443.

[218] T. P. Nguyen, Q. V. Nguyen, V.-H. Nguyen, T.-H. Le, V. Q. N. Huynh, D.-V. N. Vo, Q. T. Trinh, S. Y. Kim, Q. V. Le, *Polymers* **2019**, *11*, 1933.

[219] Z. Sun, H. Li, J. Tian, A. Wu, J. Wang, C. Ge, *Int. J. Nanomed.* **2016**, *11*, 4373–4380.

[220] M. K. Choi, I. Park, D. C. Kim, E. Joh, O. K. Park, J. Kim, M. Kim, C. Choi, J. Yang, K. W. Cho, J. Hwang, J. Nam, T. Hyeon, J. H. Kim, D. Kim, *Adv. Funct. Mater.* **2015**, *25*, 7109–7118.

[221] Y.-M. Chen, S.-M. He, C.-H. Huang, C.-C. Huang, W.-P. Shih, C.-L. Chu, J. Kong, J. Li, C.-Y. Su, *Nanoscale* **2016**, *8*, 3555–3564.

[222] O. Akhavan, E. Ghaderi, *J. Phys. Chem. C* **2009**, *113*, 20214–20220.

[223] K. Spilarewicz-Stanek, A. Jakiminska, A. Kisielewska, M. Dudek, I. Piwonski, *Mater. Sci. Semicond. Process.* **2021**, *123*, 105525.

[224] J. Soria, M. López-Muñoz, V. Augugliaro, J. Conesa, *Colloids Surf. A* **1993**, *78*, 73–83.

[225] V. Bellotti, C. Daldossi, D. Perilli, M. D'Arienzo, M. Stredansky, C. Di Valentin, R. Simonutti, *J. Catal.* **2023**, *428*, 115074.

[226] T. Tanaka, S. Nishimura, K. Nishiyama, Y. Aso, H. Nishida, S. Cho, T. Sekino, *Asian J. Org. Chem.* **2024**, e202400270.

[227] X. Wang, Q. Lu, X. Wang, J. Joo, M. Dahl, B. Liu, C. Gao, Y. Yin, *ACS Appl. Mater. Interfaces* **2016**, *8*, 538–546.

[228] K. Hu, L. S. Tolentino, D. D. Kulkarni, C. Ye, S. Kumar, V. V. Tsukruk, *Angew. Chem.* **2013**, *125*, 14029–14033.

[229] H. Schlicke, S. Kunze, M. Finsel, E. W. Leib, C. J. Schröter, M. Blankenburg, H. Noei, T. Vossmeyer, *J. Phys. Chem. C* **2019**, *123*, 19165–19174.

[230] H. Schlicke, E. W. Leib, A. Petrov, J. H. Schröder, T. Vossmeyer, *J. Phys. Chem. C* **2014**, *118*, 4386–4395.

[231] J. S. Bunch, S. S. Verbridge, J. S. Alden, A. M. Van Der Zande, J. M. Parpia, H. G. Craighead, P. L. McEuen, *Nano Lett.* **2008**, *8*, 2458–2462.

[232] X. Zhang, A. Beyer, A. Gölzhäuser, *Beilstein J. Nanotechnol.* **2011**, *2*, 826–833.

[233] P. Podsiadlo, G. Krylova, B. Lee, K. Critchley, D. J. Gosztola, D. V. Talapin, P. D. Ashby, E. V. Shevchenko, *J. Am. Chem. Soc.* **2010**, *132*, 8953–8960.

[234] J. He, P. Kanjanaboos, N. L. Frazer, A. Weis, X.-M. Lin, H. M. Jaeger, *Small* **2010**, *6*, 1449–1456.

[235] J. W. Suk, R. D. Piner, J. An, R. S. Ruoff, *ACS Nano* **2010**, *4*, 6557–6564.

[236] C. Jiang, X. Wang, R. Gunawidjaja, Y.-H. Lin, M. Gupta, D. Kaplan, R. Naik, V. Tsukruk, *Adv. Funct. Mater.* **2007**, *17*, 2229–2237.

[237] S. Keten, Z. Xu, B. Ihle, M. J. Buehler, *Nat. Mater.* **2010**, *9*, 359–367.

[238] A. Turchanin, A. Beyer, C. T. Nottbohm, X. Zhang, R. Stosch, A. Sologubenko, J. Mayer, P. Hinze, T. Weimann, A. Gölzhäuser, *Adv. Mater.* **2009**, *21*, 1233–1237.

[239] J. Vlassak, W. Nix, *J. Mater. Res.* **1992**, *7*, 3242–3249.

[240] F. Schedin, A. K. Geim, S. V. Morozov, E. W. Hill, P. Blake, M. I. Katsnelson, K. S. Novoselov, *Nat. Mater.* **2007**, *6*, 652–655.

[241] M. K. Rabchinskii, V. V. Sysoev, O. E. Glukhova, M. Brzhezinskaya, D. Y. Stolyarova, A. S. Varezhnikov, M. A. Solomatin, P. V. Barkov, D. A. Kirilenko, S. I. Pavlov, M. V. Baidakova, V. V. Shnitov, N. S. Struchkov, D. Y. Nefedov, A. O. Antonenko, P. Cai, Z. Liu, P. N. Brunkov, *Adv. Mater. Technol.* **2022**, *7*.

[242] A. A. Haidry, Z. Wang, Q. Fatima, A. Zavabeti, L. Xie, H. Zhu, Z. Li, *Appl. Surf. Sci.* **2020**, *531*, 147285.

[243] J. A. Voss, BA thesis, University of Hamburg, Hamburg, **2020**.

[244] D. V. Leff, L. Brandt, J. R. Heath, *Langmuir* **1996**, *12*, 4723–4730.

[245] S. Willruth, PhD thesis, University of Hamburg, Hamburg, **2023**.

[246] J. I. Langford, A. J. C. Wilson, *J. Appl. Crystallogr.* **1978**, *11*, 102–113.

[247] Merck, Microchemicals Safety Data Sheet, AZ 326 MIF, Product No. 697332, (02.07.2025), **2023**.

[248] Merck, Microchemicals Safety Data Sheet, AZ 726 MIF, Product No. 697333, (02.07.2025), **2023**.

[249] Merck, Microchemicals Safety Data Sheet, AZ 3012 ECI, Product No. 211724, (02.07.2025), **2022**.

[250] Merck, Microchemicals Safety Data Sheet, AZ nLOF 2020, Product No. 583503, (02.07.2025), **2023**.

[251] Technic, Safety Data Sheet, TechniEtch Cr01, Product No. STD0473, (02.07.2025), **2024**.

[252] Technic, Safety Data Sheet, TechniStrip NI555, Product No. STD5028, (02.07.2025), **2024**.

A Appendix

A.1 Supplementary Data

A.1.1 DUV Radiation Source

For both projects presented in the framework of this thesis, a crucial step was the post deposition tuning of the material composition governed by the photocatalytic activity of the TNCs. To trigger the photocatalytic activity, the TNCs were illuminated using a custom-built DUV light source. Figure A.1 shows a photograph of the light source, the latter consisting of four commercial low-pressure mercury vapor UVC fluorescent lamps (OSRAM HNS-L 18 W 2G11 FS1) arranged with a tilt angle of 60°. The photograph was kindly provided by Dr. Sophia Caroline Bittinger, research associate at the CIC biomaGUNE. The main emission was detected at a wavelength of 254 nm using an Ocean Insights Flame-T Spectrometer. The distance between the lamps and the substrates during irradiation was ~4 cm. The irradiance at 254 nm was measured using a Thorlabs PM100 powermeter equipped with a Thorlabs S120UV sensor and averaged as ~520 mW/cm^2 over a 5 min period.

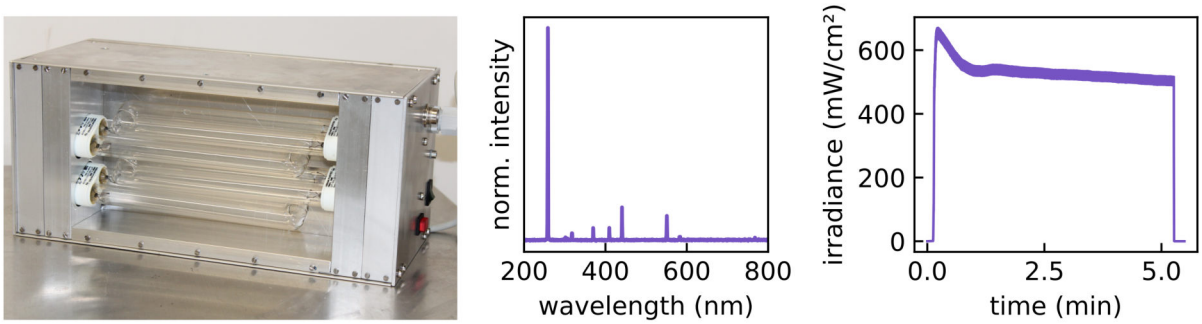

Figure A.1: Photograph (left) and normalized emission spectrum (center) of the DUV light source. The irradiance at the main emission peak wavelength of 254 nm was measured and averaged over a 5 min period (right).

A.1.2 Characterization of LEDs for Photoactivation

For photoactivation of TNC-based sensors, LEDs with different emission wavelengths (UV: CUD7MN1A Sensor Electronic Technology Inc., blue: TCN0MF1A Sensor Electronic Technology Inc., NIR: LST1-G01-IR03-00 NewEnergy LLC.) were used. The LEDs were mounted in the test cell (cf. the Experimental section 7.6) and the spectra were recorded using an Ocean Insights Flame-T Spectrometer or a Thorlabs CCS200/M spectrometer. Figure A.2 shows the characterization with main emission wavelengths of 278 nm, 401 nm, and 947 nm for the UV, vis blue, and NIR LED, respectively. Further, the irradiances were measured through the quartz glass using a Thorlabs PM100 powermeter equipped with a Thorlabs S120 UV sensor. To obtain the irradiance acting on the TNC thin films during the photoactivation, the S120 UV sensor was kept at a distance of approx. 15 mm comparable to the distance between LED and thin film. Average irradiances at the corresponding peak emission wavelengths were determined as ~23 mW/cm^2 for the UV LED, ~195 mW/cm^2 for the vis blue LED, and ~710 mW/cm^2 for the NIR LED. The data with corresponding LED driving currents are shown in figure A.2 over a period of 90 s.

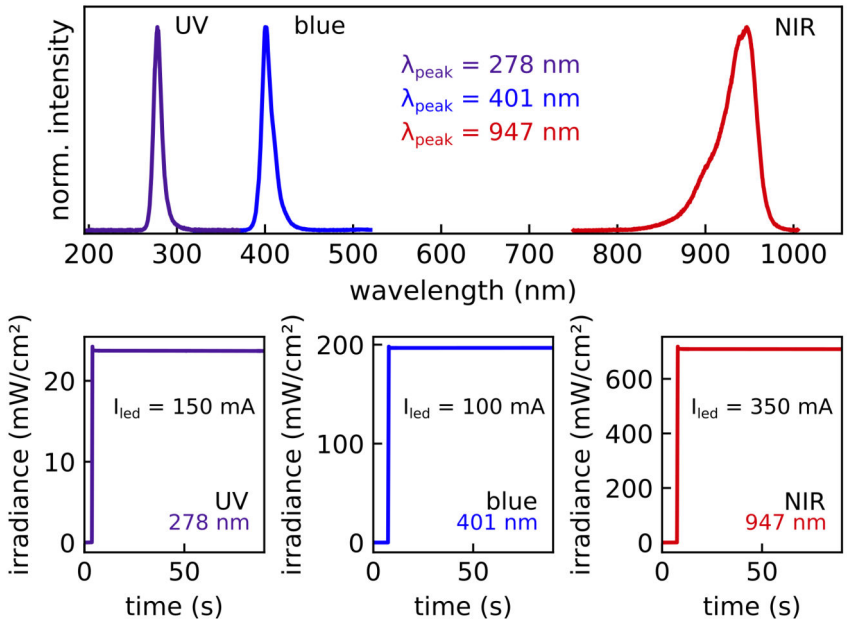

Figure A.2: Characterization of the LEDs of the test cell used for photoactivation of the TNC-based sensors. Normalized emission spectra (top) and optical power output recorded over 90 s (bottom).

Since the photoactivation of TNC thin films was only achieved using the UV LEDs, these were further characterized to investigate the influence of the irradiance on the vapor sensing properties. To constantly assess the irradiance during the measurement, a calibration between the irradiance and the LED's operating voltage was obtained. To achieve this, the LEDs were driven with distinct currents of 20 mA, 40 mA, 80 mA, and 160 mA and

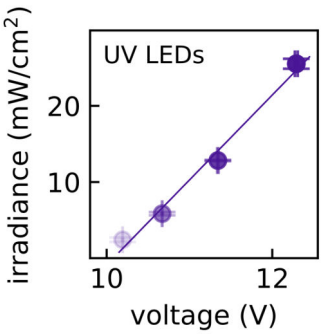

Figure A.3: Irradiance vs. operating voltage of the UV LEDs for distinct LED driving currents with the linear fit representing the calibration curve. Reprinted from Dobschall el al., Ref. [3], *Creative Commons CC-BY 4.0* license ©2025 The Authors. ACS Appl. Nano Mater. published by American Chemical Society. (DOI: 10.1021/acsanm.5c03648)

the corresponding voltage as well as the irradiance was recorded. Figure A.3 shows the calibration for both UV LEDs. In the current range used for driving the LEDs, the irradiance scales linearly with the operating voltage. For a typical chemiresistive measurement, the LEDs were driven with a constant current of 150 mA, which resulted in an operating voltage of ~12.3 V and an irradiance of ~23 mW/cm^2

A.1.3 Size Determination of TNDs

The size of the TNDs was calculated using the Scherrer (cf. equation 11) by estimating the diameter of the particles based on the crystallite size L.[246]

$$L = \frac{K\lambda}{(\mathrm{FWHM} - b)\cos\theta_0}\frac{180°}{\pi} \tag{11}$$

Here, K is the shape factor (1.0747 for spherical particles[246]), λ is the x-ray wavelength (0.154 nm for Cu K_α), b is the instrument broadening factor (0.06°), and $2\theta_0$ and FWHM are the reflection angle and full width at half maximum of the reflection, respectively. The center position and FWHM were obtained by fitting the reflections of the lattice planes (101) and (200) with a Lorentzian. Figure A.4 shows the x-ray diffractogram of the TNDs with anatase reference reflections as well as the zoom-in to the angular range of the (101) and (200) reflections with the Lorentz fit. Fit parameters are shown in table A.1, resulting in calculated particle sizes of approx. 7 nm.

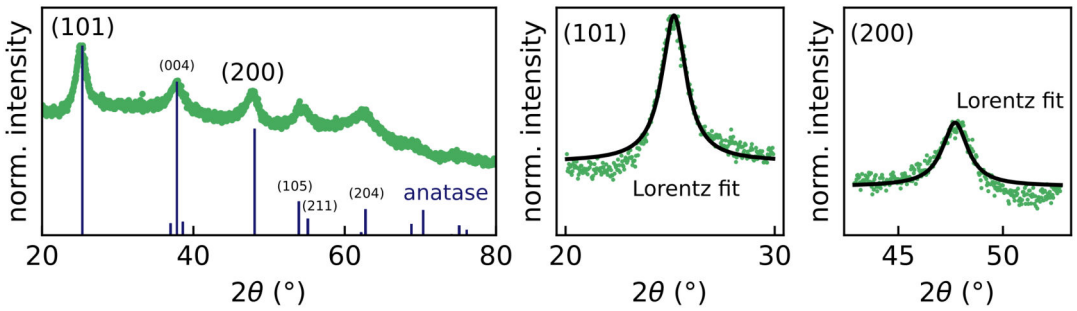

Figure A.4: Calculation of the crystallite using the Scherrer equation. Normalized x-ray diffractogram of the TNDs with anatase reference reflections and facet indication (left). The XRD reference data were taken from Ref. [172]. Zoom-in to the angular range of the (101) and (200) lattice plane reflections (center and right). Each cutout was fitted with Lorentzian curve (black line) for size calculation.

Table A.1: Calculation of the crystallite sizes using the Scherrer equation on the parameters obtained by fitting the reflections of the lattice planes (101) and (200) with a Lorentzian function.

lattice plane	FWHM (°)	$2\theta_0$ (°)	L (nm)
(101)	1.40	25.2	7.23
(200)	1.48	47.7	7.29

A.1.4 Thermogravimetric Analysis

TNCs used for the sensor fabrication were characterized by themrogravimetric analysis (TGA) to determine the organic content (OC) of differently shaped crystals. Further, this method was used to determine the mass concentration of the stock solutions. Figure A.5 shows the change in mass vs. temperature for the TNR, TNP, TND, and TNB stock solutions as well as the P25 powder. TGA of OLAM-stabilized TNRs, TNPs, and TNDs show the distinct decrease in mass between 340–400 °C corresponding to the decomposition of OLAM (boiling point: 348–350 °C[187]). For TNDs the pronounced decrease in mass at temperatures below 340 °C corresponds to the decomposition of DEG (boiling point: 245 °C[187]), which was used for their synthesis (cf. Experimental section 7.1). The OC was 39.3%, 28.5%, and 42.5% for TNRs, TNPs, and TNDs respectively. For hydrothermally synthesized TNBs and for commercial P25 TNCs the OC was 2.5% and 0.9%, respectively. These results confirmed the bare nature of these TNBs and P25 TNCs.

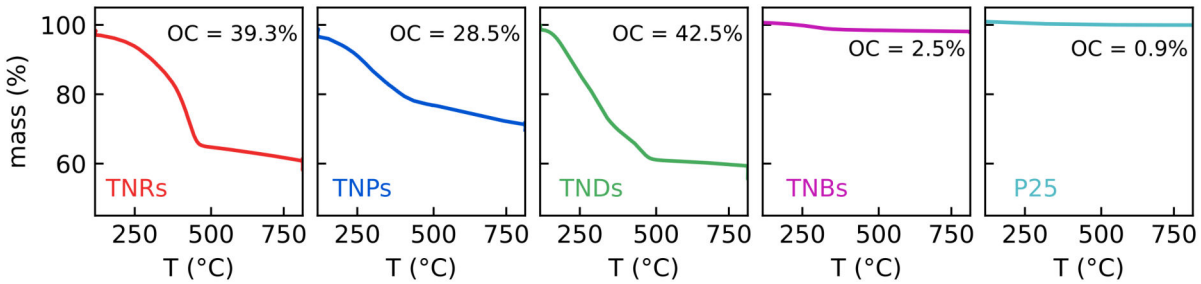

Figure A.5: TGA of TNC stock solutions (TNR, TNP, TND, and TNBs) or powder (P25 TNC). OLAM-stabilized TNRs, TNPs, and TNDs in chloroform are shown in red, blue, and green, respectively. Bare TNBs are shown in purple. The commercial P25 powder is shown in turquoise. These TNCs were used for the fabrication of TiO_2-based chemiresistors. Adapted and reprinted from Dobschall el al., Ref. [3], *Creative Commons CC-BY 4.0* license ©2025 The Authors. ACS Appl. Nano Mater. published by American Chemical Society. (DOI: 10.1021/acsanm.5c03648)

Figure A.6 shows the change in the mass against the temperature for the TNR stock solution used for the fabrication of hybrid membranes of GO, TNR, and SF. The OC was 34.9%.

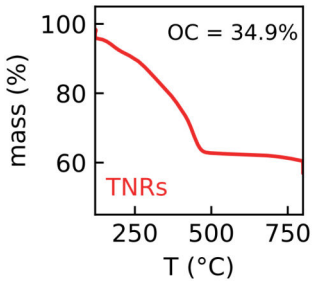

Figure A.6: TGA of the oleylamie-stabilized TNR stock solution in chloroform used for hybrid film fabrication.

A.1.5 TNC Thin Film Deposition via Layer-by-Layer Spin-Coating

As an alternative approach, TNC thin films were fabricated using a LbL SC method while the layer deposition was traced using UV-vis spectroscopy after every deposition step. Figure A.7 shows the absorbance evolution of the TNR, TNP, and TND thin films. Here, the facile method to fabricate thin films of desired thickness without the usage of organic linker molecules was indicated by the increased absorbance with increasing number of layers. Thus, it was possible to reduce the amount of organic molecules in the fabrication of TNC thin films, as reported in a previous study.[67]

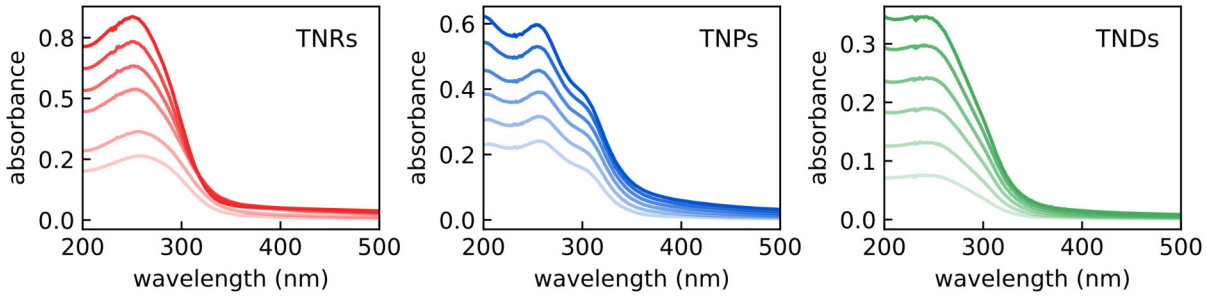

Figure A.7: Evolution of the UV-vis absorbance spectra of TNR (left), TNP (center), and TND (right) thin films deposited via spin-coating from chloroform dispersions of 1–6 layers. The colors intensify with the number of layers, showing highest absorbance for 6 layers. The concentrations of the dispersions were 2 mg/mL, the volume for each layer was 25 µL, and the deposition steps were spaced by 25 s delay time.

To obtain TNC thin films with comparable amounts of titania, the concentrations of the dispersions were adjusted to achieve an absorbance at the maximum of ~0.4 for all thin films. Next, the influence of the DUV treatment on the absorbance was investigated. Figure A.8 shows the UV-vis absorbance spectra for exposure times of 0 min, 30 min, 60 min, 120 min, 180 min, and 240 min. These results indicate that the absorbance slightly decreased after the first exposure to UV illumination of 30 min but remained constant for the following exposure times.

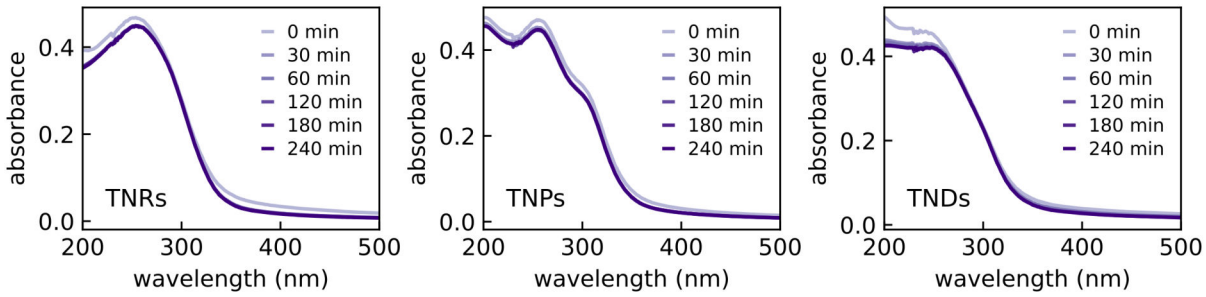

Figure A.8: Evolution of the UV-vis absorbance spectra of 3 layer TNR (left), TNP (center), and TND (right) thin films with increasing exposure times of UV illumination. The concentrations of the dispersions were 1.25 mg/mL, 2 mg/mL, and 4 mg/mL for TNRs, TNPs, and TNDs, respectively. The volume for each layer was 25 µL and the deposition steps were spaced by 25 s delay time.

A.1.6 Surface Treatments of TNC Thin Films

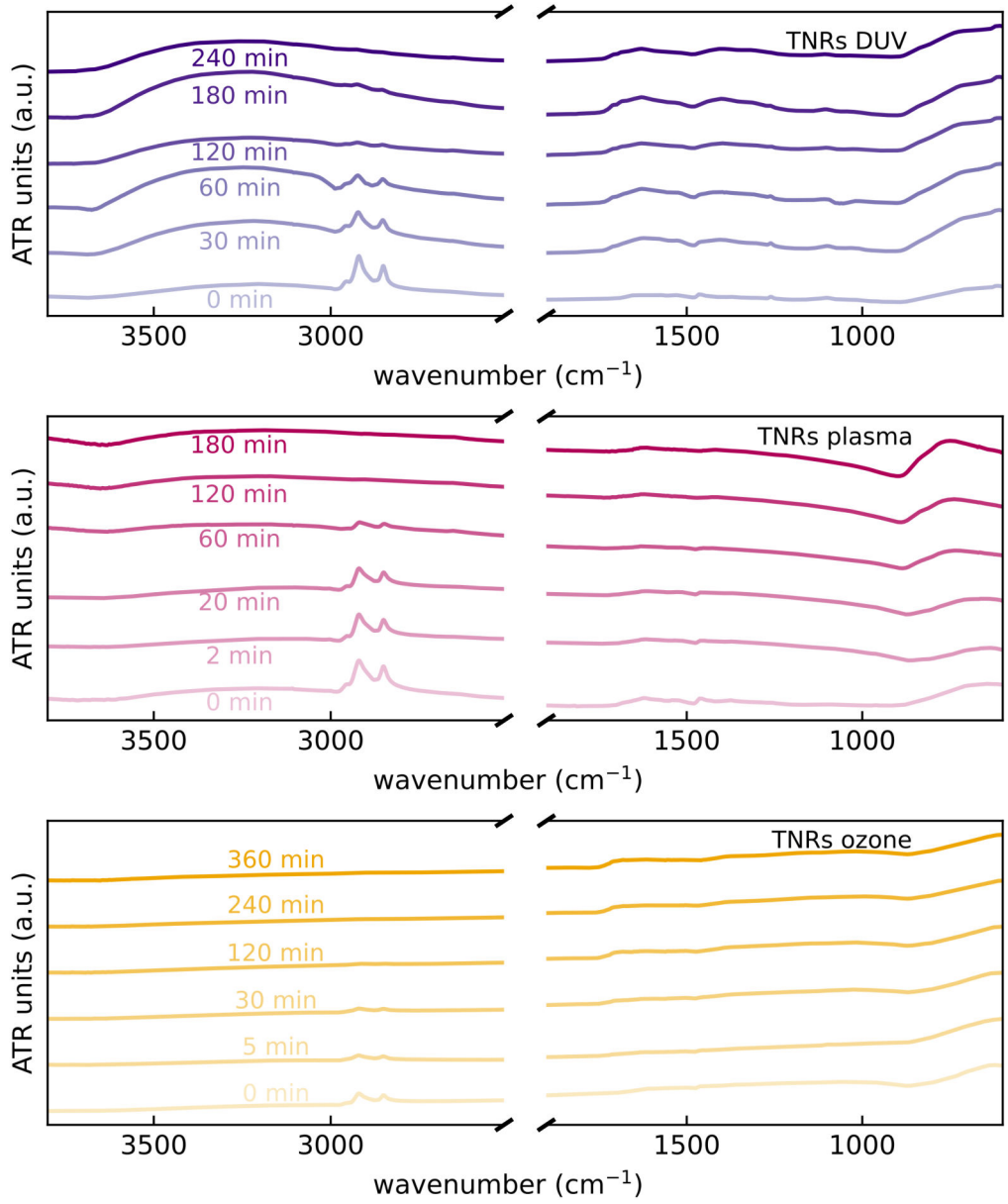

Figure A.9: Stacked plots of normalized ATR-FTIR spectra of drop-casted TNR films treated with DUV (top), plasma (center), and ozone (bottom) for increasing exposure times.

Figures A.9 and A.10 show all ATR-FTIR spectra of differently shaped TNCs for the surface treatments (DUV, plasma, and ozone) for varying exposure times between 0–360 min.

The impact of the surface treatment on the crystal structures of the TNCs was evaluated by XRD. Figure A.11 shows the diffractograms of the TNRs, TNPs, and P25 TNCs before and after the DUV treatment. Further, the diffractograms of TNRs before and after the plasma treatment are displayed.

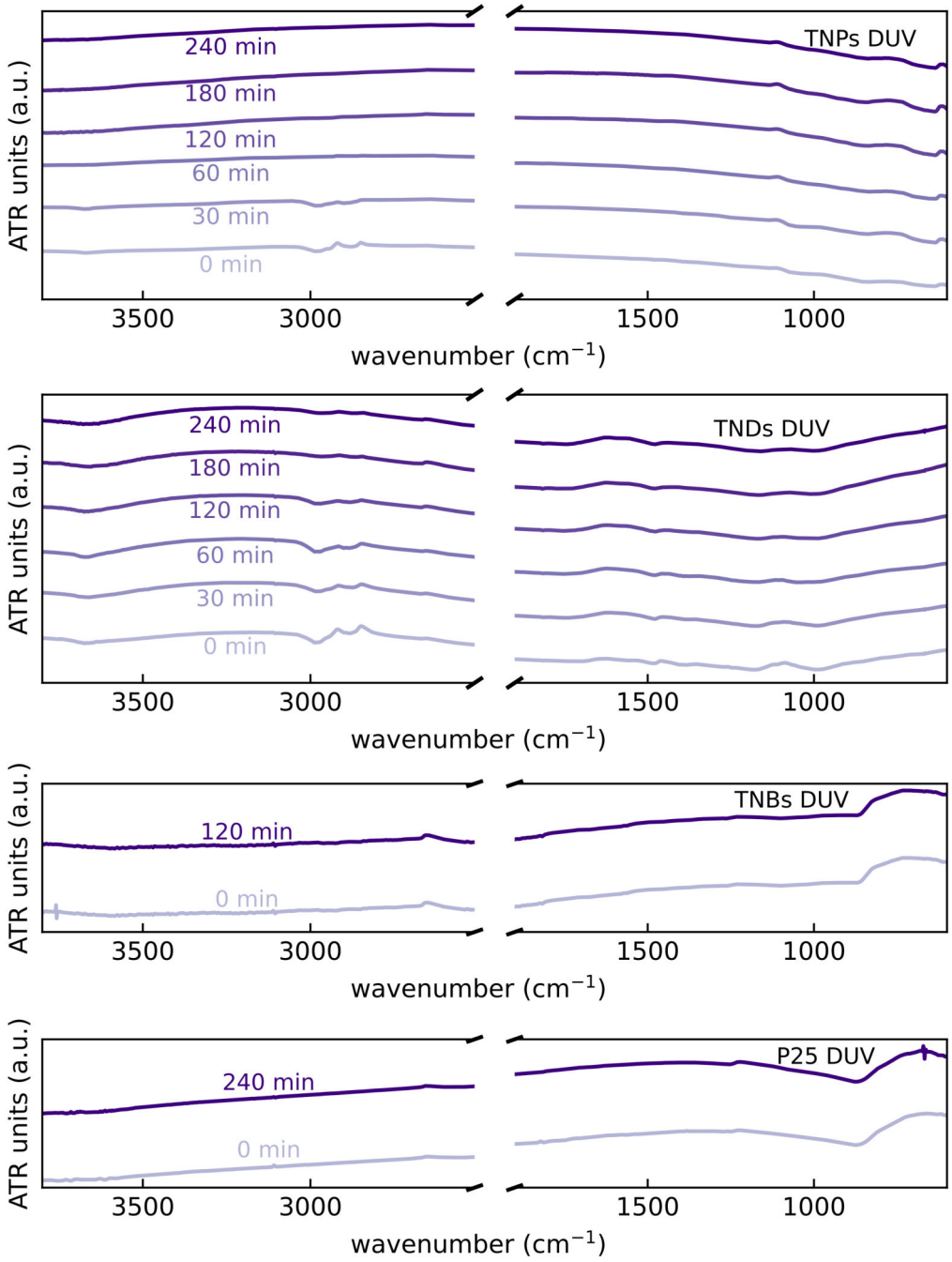

Figure A.10: Stacked plots of normalized ATR-FTIR spectra of drop-casted TNP (first), TND (second), TNB (third), and P25 (fourth) films treated with DUV for increasing exposure times.

SEM analysis of thin films deposited on silicon substrates was used to study the thin film morphology before (0 min) and after (120 min) the DUV treatment. Figure A.12 shows the images of thin films fabricated using OLAM-stabilized TNPs and TNDs as well as bare TNBs and P25 TNCs. All images reveal deposits, where individual particles can clearly be distinguished. The increased contrast in images of TNPs and TNDs after the DUV exposure indicated the removal of OLAM, while the contrast for the TNBs and P25 TNCs was already high before the DUV treatment due to the bare nature of the particles.

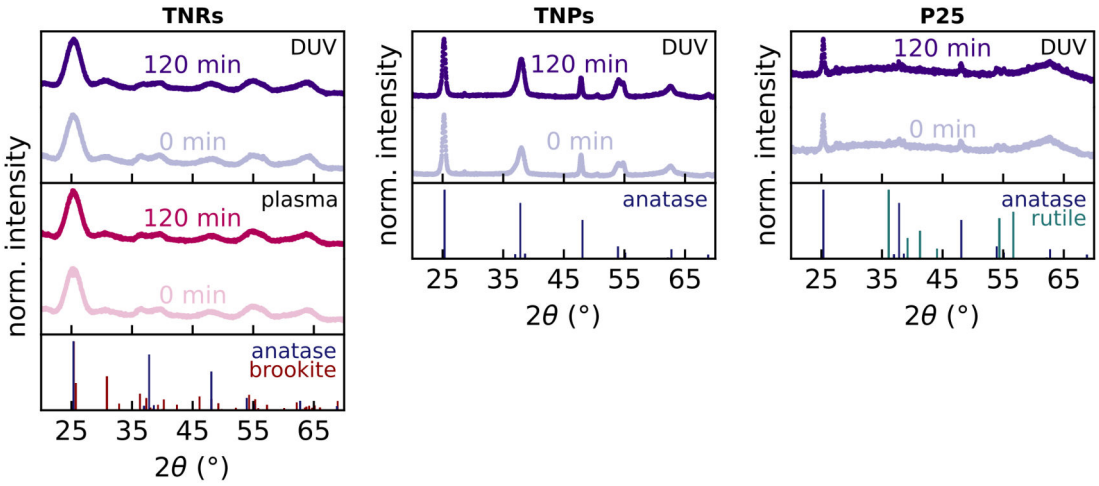

Figure A.11: Stacked plots of normalized x-ray diffractograms of TNR (left), TNP (center), and P25 (right) films before and after the treatments with corresponding reference reflections of anatase/brookite, anatase, and anatase/rutile, respectively. The XRD reference data were taken from Refs. [167, 168, 172]. DUV and plasma treatment are shown in purple and red, respectively. Adapted and reprinted from Dobschall el al., Ref. [3], *Creative Commons CC-BY 4.0* license ©2025 The Authors. ACS Appl. Nano Mater. published by American Chemical Society. (DOI: 10.1021/acsanm.5c03648)

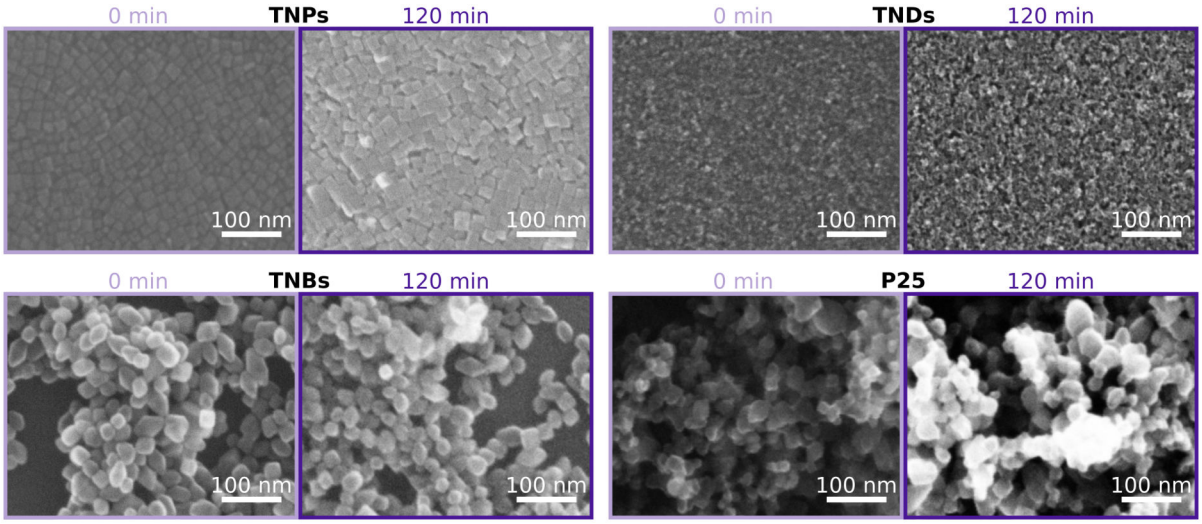

Figure A.12: SEM images of TNP (top left), TND (top right), TNB (bottom left), and P25 (bottom right) thin films before (light purple) and after 120 min DUV treatment (dark purple).

While, the TNPs and TNDs formed homogeneous films with disordered particles, the TNB and P25 deposits were dominated by aggregates and cracks.

Figures A.13 and A.14 show representative AFM scans of the thin films fabricated from differently shaped TNCs after the respective treatment. The thin films were deposited on SiO_2/Si substrates and the thickness of the TNR films were 178 ± 15 nm, 134 ± 13 nm, and 196 ± 20 nm after the DUV, plasma, and ozone treatment, respectively. After the DUV treatment, the thicknesses were 124 ± 13 nm, 158 ± 11 nm, 99 ± 31 nm, and 148 ± 42 nm for TNPs, TNDs, TNBs, and P25 TNCs, respectively. Large standard deviations of the TNB and P25 thin films resulted from the inhomogeneous morphology.

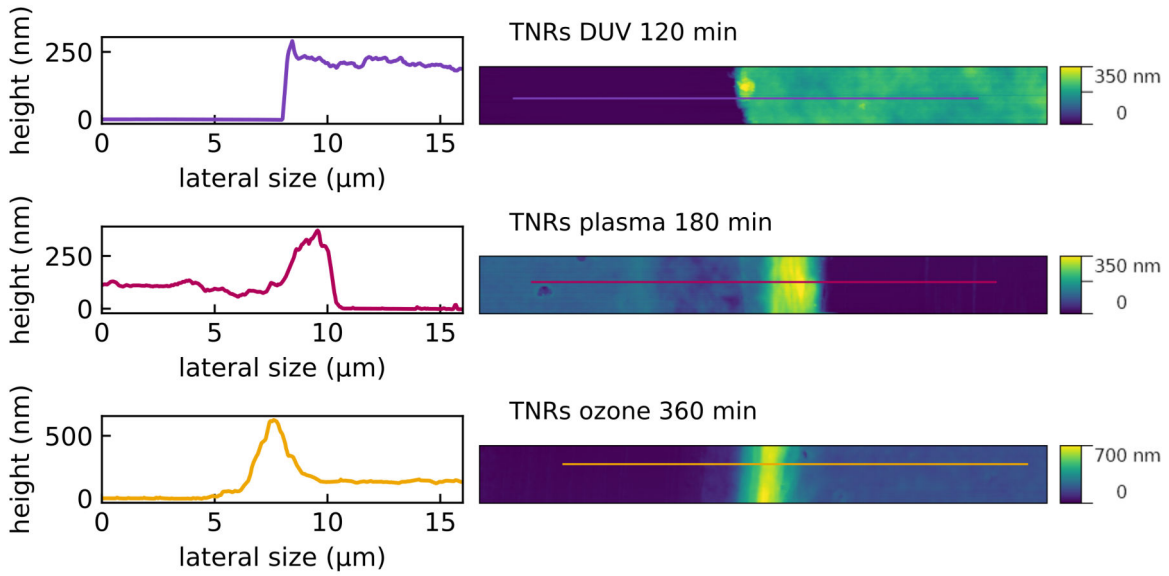

Figure A.13: Representative topographic AFM scans (20×2 µm^2) and extracted line profiles for TNR thin films after the respective treatment measured at intentionally created step edges. Adapted and reprinted from Dobschall el al., Ref. [3], *Creative Commons CC-BY 4.0* license ©2025 The Authors. ACS Appl. Nano Mater. published by American Chemical Society. (DOI: 10.1021/acsanm.5c03648)

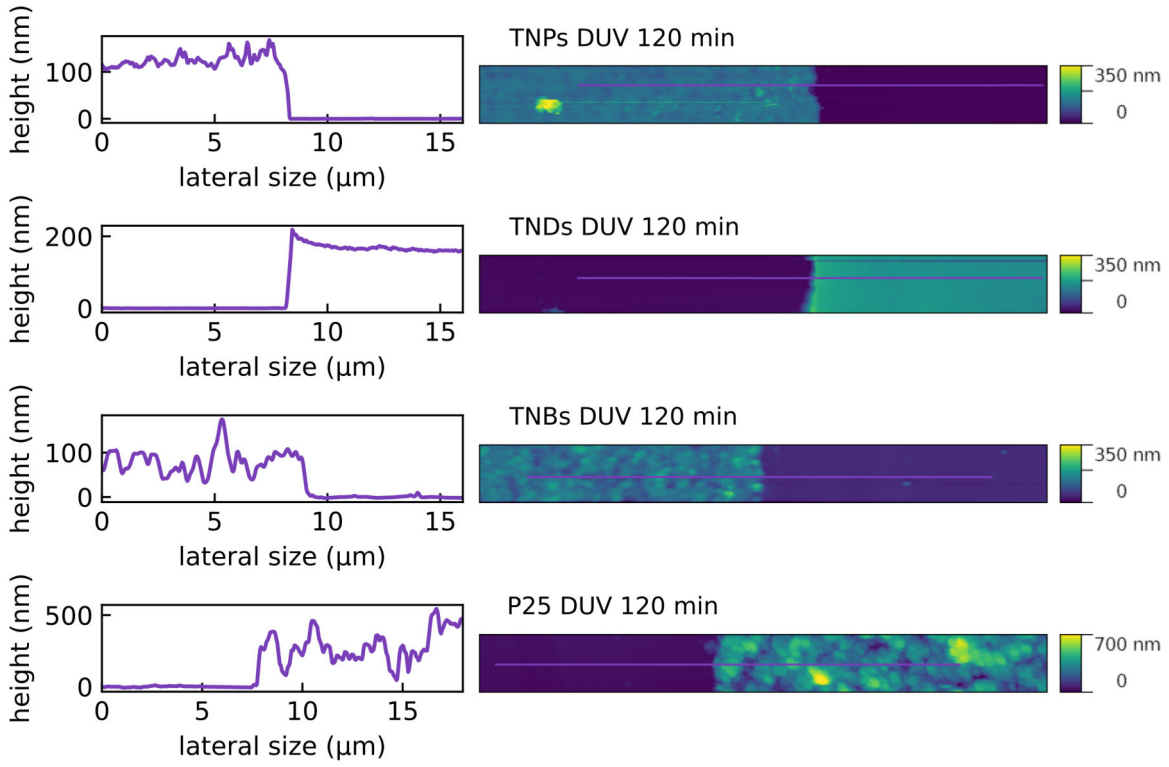

Figure A.14: Representative topographic AFM scans (20×2 µm^2) and extracted line profiles for thin films fabricated from differently shaped TNCs (TNPs, TNDs, TNBs, and P25 TNCs) after the DUV treatment for 120 min measured at intentionally created step edges. Adapted and reprinted from Dobschall el al., Ref. [3], *Creative Commons CC-BY 4.0* license ©2025 The Authors. ACS Appl. Nano Mater. published by American Chemical Society. (DOI: 10.1021/acsanm.5c03648)

A.1.7 OLAM Degradation via UV LEDs

In addition to the DUV treatment, that was carried out using the custom-built DUV radiation source (cf. the Appendix, section A.1.1), the degradation of OLAM was monitored inside the test cell using the UV LEDs (cf. the Appendix, section A.1.2). For this purpose, two TNR thin films were drop-casted onto QCM substrates and the deposited film mass was determined from the change of their resonance frequencies. From there, one thin film was DUV-treated for 2 h while the other remained untreated. Figure A.15 shows the timetraces of the relative resonant frequency of the DUV-treated and untreated TNR thin films during illumination using the UV LEDs at an irradiance of ~23 mW/cm^2 over a period of 14 h and 24 h, respectively. The samples were continuously purged with purified, dry air with a flow of 0.5 L/min. The relative mass reduction - calculated by normalizing the mass change using the respective initial film mass - for the untreated film was 17.12% after 24 h (and 10.86% after 12 h) of UV LED exposure which indicated a slow degradation of OLAM. For the DUV-treated film, the relative mass reduction after total treatment time of 16 h (DUV 2 h and UV LED 14 h) was 34.7%. However, the major mass reduction of 33.3% and thus the decomposition of most of the OLAM was obtained after the DUV treatment using the custom-built DUV radiation source at an irradiance of ~520 mW/cm^2. Considering the results of TGA (cf. the Appendix, section A.1.4) that showed an OC of 39.3% for TNRs, the microgravimetric results indicate that the DUV treatment is necessary to thoroughly remove the OLAM from the TNR surface. However, small amounts of OC remained in the thin films after DUV treatment. As the UV LED also excites the TNCs, a continuous decomposition of organic material was observed inside the test cell using the UV LEDs, also during the chemiresistive and microgravimetric measurements.

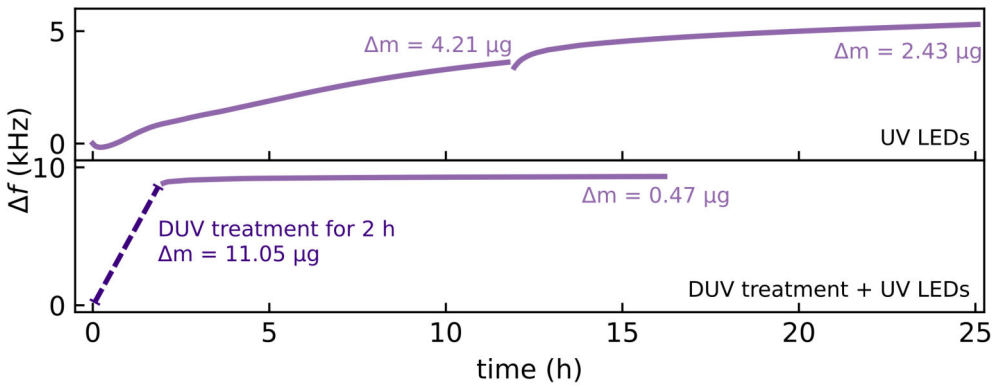

Figure A.15: Resonant frequency shifts of TNR thin films deposited onto QCM substrates under UV illumination using UV LEDs (emission wavelength: 278 nm) at an irradiance of ~23 mW/cm^2. Relative resonant frequency timetrace of a TNR thin film without any surface treatment (top). TNR thin film exposed to DUV illumination (emission wavelength: 254 nm, irradiance: ~520 mW/cm^2) for 2 h before monitoring the frequency shifts inside the test cell (bottom).

A.1.8 NaOH Treatment of TNP Thin Films

The adsorption of fluoride ions on the TNP surface is known from literature.[40,67] In the present project the fluoride ions originated from the TiF_4 precursor that was used for the synthesis of TNPs. However, the removal of fluoride ions is not trivial and is typically done either by using NaOH washing or calcination.[40,193] As calcination leads to particle deformation and fusion often accompanied by phase transition,[173–175] the NaOH washing was chosen to preserve the plate shape. To examine the effect of fluoride ions on the chemiresistive properties, TNP thin films were submerged in NaOH solution (0.1 M) for varying treatment times. Next, the thin films were rinsed with DI water and 2-propanol and dried in a stream of nitrogen. Figure A.16 shows the SEM images of two TNP thin films before and after the NaOH treatment. The thin film treated for 20 min was fragmented into small parts, while the film treated for 40 min revealed larger areas that are still intact. However, for the treatment time of 40 min, the silicon wafer was etched. The chemiresistive data of the initial and NaOH-treated TNP-based chemiresistors are

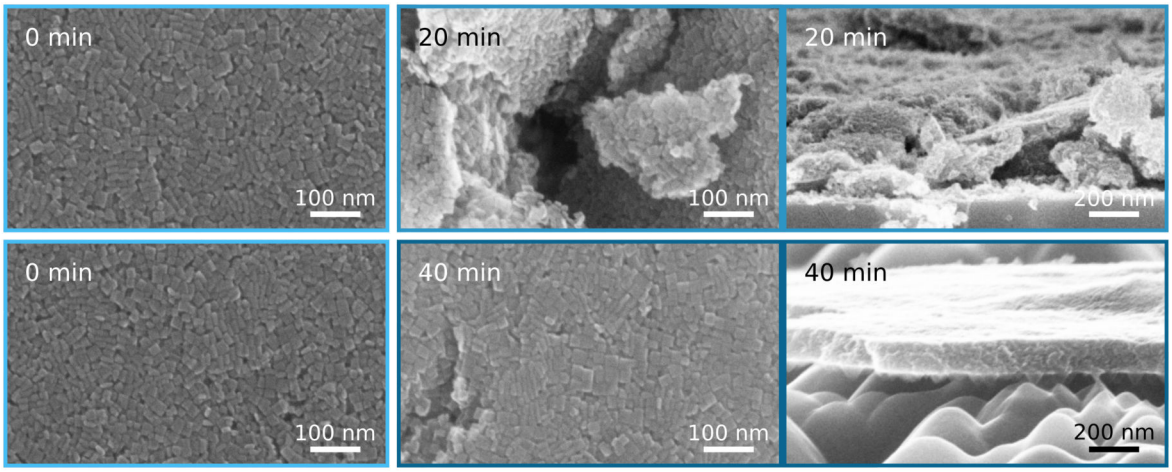

Figure A.16: SEM images of TNP thin films before (left) and after the NaOH treatment (right). Images on the right were obtained after a treatment time of 20 min (top) and 40 min (bottom).

displayed in figure A.17, showing altered transient shapes with slower response dynamics and reduced maximum response currents after the NaOH treatment compared to those of the untreated sensor. Due to the surface passivation by fluoride ions, their removal is anticipated to lead to an increase in the response currents when exposed to 1-propanol vapor. This assumption is based on the amount of ionosorbed oxygen species on the surface of the TNPs, which is expected to increase for the removal of fluoride ions. Further, the evolution of the film mass was monitored by drop-casting the TNP thin film on a QCM substrate. Comparing the resonance frequency before and after the respective duration of the NaOH treatment, shows the increase in the film mass after 20 min NaOH exposure. This is could result from the incorporation of sodium ions into the thin film. After total

treatment time of 40 min, the film mass decreased and almost reached the initial value. From these results it is concluded, that the NaOH treatment of the TNP thin films was not suitable for the removal of fluoride ions and caused rupture of the films and altered response currents.

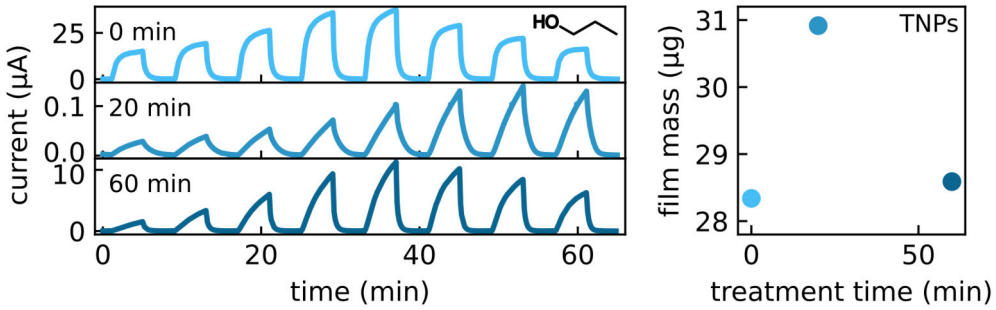

Figure A.17: Current timetraces of TNP-based sensors after increasing exposure times of NaOH treatment from top to bottom (left). All timetraces are shown without baseline correction. The chemiresistors were excited with UV LEDs at an irradiance of ~23 mW/cm^2 and exposed to 1-propanol with concentrations of 25, 50, 100, 200, 200, 100, 50, and 25 ppm. Evolution of the mass of a TNP thin film deposited on a QCM substrate for increasing NaOH treatment times (right).

A.1.9 Operating Environment: Commercial Sensor Timetraces

The influence of oxygen in the operating environment was additionally monitored by a commercial sensor (BME680, Bosch SensorTec) featuring a capacitive type humidity sensor and a resistive type gas sensor. The commercial sensor was read out using a Raspberry Pi and was operated in a separate test cell which was connected behind the test cell containing the TNR thin films on IDE and QCM substrates. In this setup, the commercial sensor was not exposed to any illumination by the UV LEDs. Figure A.18 shows the humidity (blue) and resistive (purple) timetrace obtained by the commercial sensor which was measured in parallel to the relative resonant frequency and current timetraces of the TNR thin films shown in figure 6.10. The timetraces in the left plot were recorded in parallel to the measurement in the dark, while the timetraces in the right plot were recorded in parallel to the measurement under UV illumination. The humidity timetrace shows that the presence of water can be excluded for interpreting the chemiresistive and microgravimetric data of the TNR thin films. Further, the resistive timetraces of the commercial sensor support the assumption, that the sorption of oxygen causes the distinct changes in the resonant frequency and the current shown in figure 6.10. As the commercial sensor features a thermally activated MOX-based chemiresistor, the increase in resistance suggests the sorption of oxygen molecules when switching the atmosphere to the nitrogen/oxygen mixture (green background). For thermally activated MOX-based gas sensors, the formation of dissociated, ionosorbed oxygen species results in an electron-depleted space-charge-layer, that causes band bending and impedes the charge transport,[79,80] as described in detail in section 4.2.1.

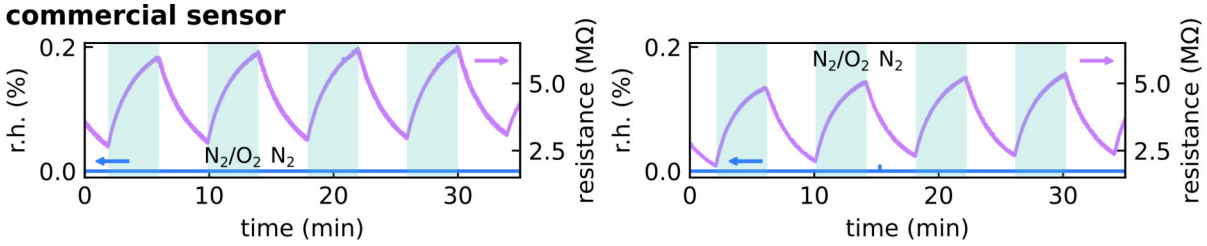

Figure A.18: Timetraces of the humidity (blue) and the resistance (purple) measured using a commercial sensor that was transiently exposed to nitrogen and a nitrogen/air mixture (1/1, v/v) the latter are indicated in the timetrace plot as white and green background, respectively. Timetraces shown in the left plot were recorded in parallel to the chemiresistive and microgravimetric measurements of the TNR thin films in the dark. Timetraces shown in the right plot were recorded in parallel to the chemiresistive and microgravimetric measurements of the TNR thin films under UV illumination. All timetraces are shown without baseline correction.

A.1.10 Surface Treatments: Timetraces

Figure A.19 shows the photoactivated current timetraces of the TNR-based chemiresistors after different surface treatments to 1-propanol vapor with concentrations of 25, 50, 100, 200, 200, 100, 50, and 25 ppm (cf. figure 6.4). Chemiresistors were photoactivated using the UV LEDs at an irradiance of ~23 mW/cm^2.

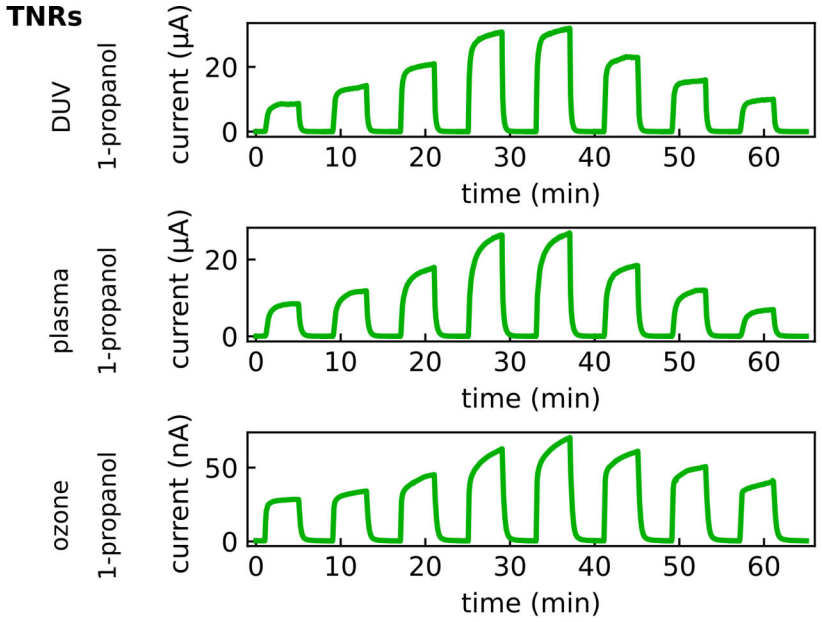

Figure A.19: Current timetraces of photoactivated TNR-based chemiresistors treated with DUV, plasma, and ozone for 120 min, 120 min, and 360 min, respectively. All timetraces are shown without baseline correction.

A.1.11 Excitation Wavelength: Timetraces

Figures A.21 and A.20 show the current timetraces of the TNR- and TNP-based chemiresistors exposed to 1-propanol vapor with concentrations of 25, 50, 100, 200, 200, 100,

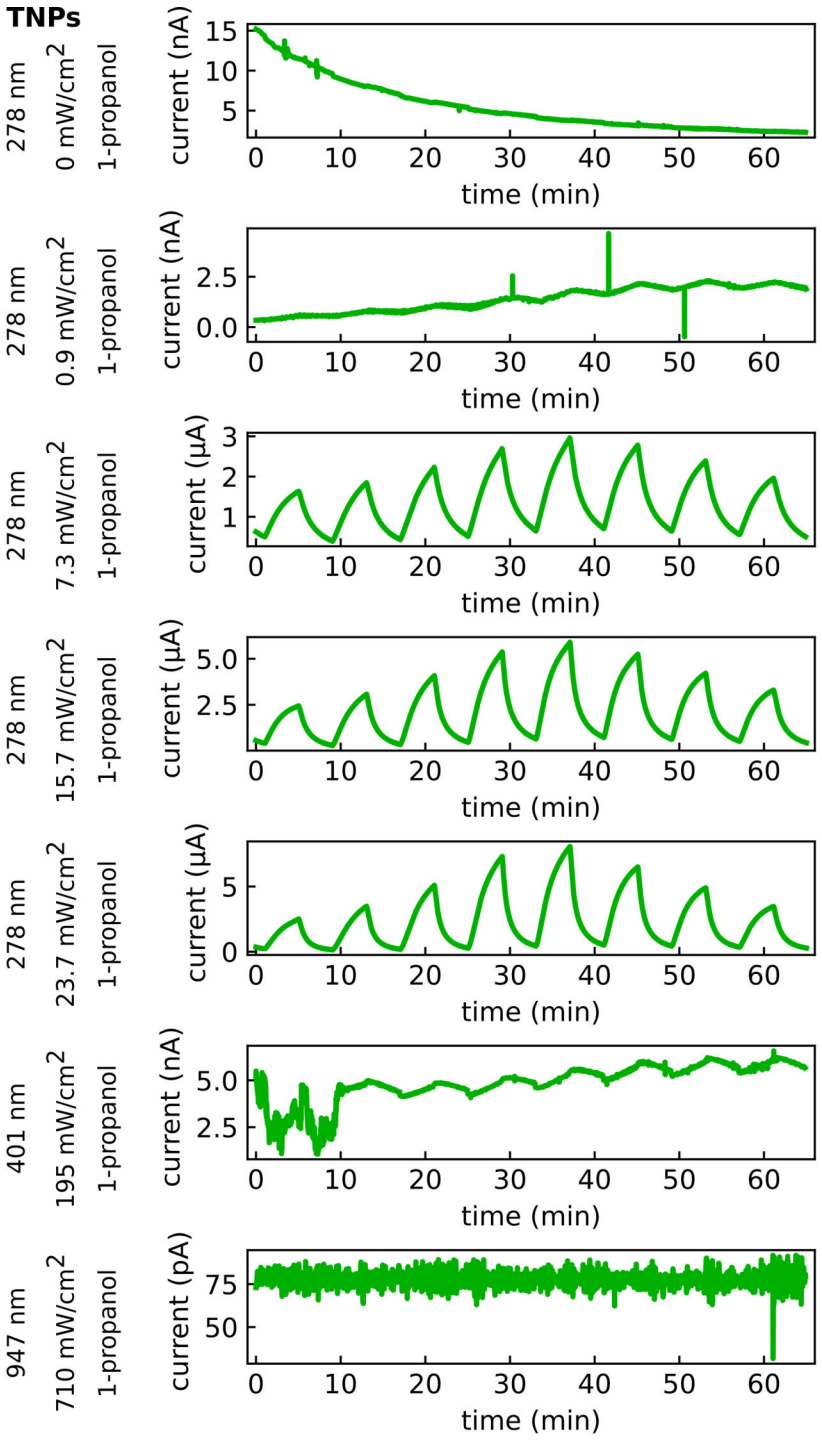

Figure A.20: Current timetraces of a TNP-based chemiresistor under various wavelengths and irradiances. All timetraces are shown without baseline correction. Adapted and reprinted from Dobschall el al., Ref. [3], *Creative Commons CC-BY 4.0* license ©2025 The Authors. ACS Appl. Nano Mater. published by American Chemical Society. (DOI: 10.1021/acsanm.5c03648)

50, and 25 ppm under photoactivation using different LEDs (cf. figures 6.8 and 6.9).

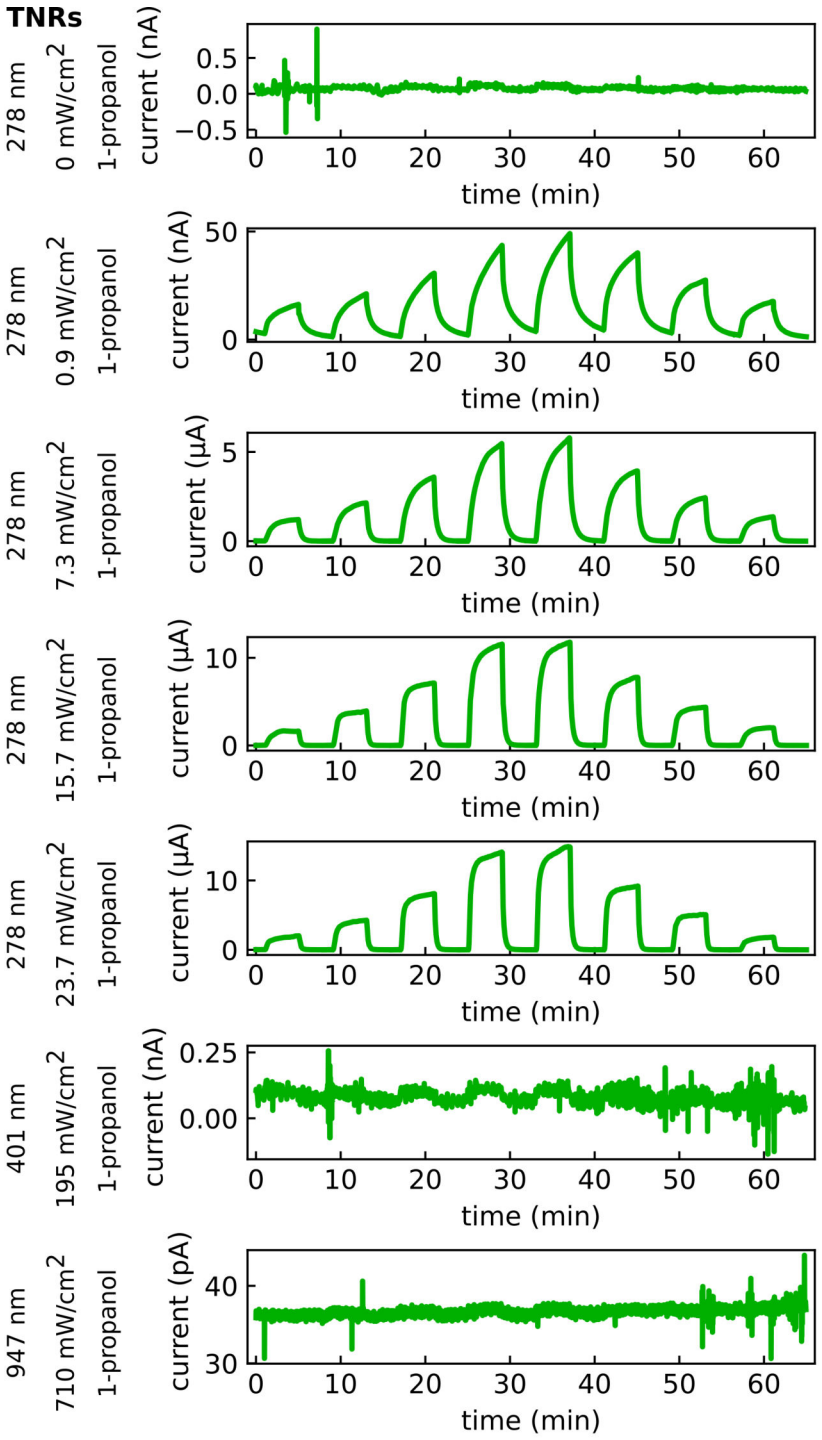

Figure A.21: Current timetraces of a TNR-based chemiresistor under various wavelengths and irradiances. All timetraces are shown without baseline correction. Adapted and reprinted from Dobschall el al., Ref. [3], *Creative Commons CC-BY 4.0* license ©2025 The Authors. ACS Appl. Nano Mater. published by American Chemical Society. (DOI: 10.1021/acsanm.5c03648)

A.1.12 Film Morphology and Particle Shape: Timetraces

The following figures show the photoactivated current timetraces of all TNC-based chemiresistors exposed to the VOCs tested in this study using UV LEDs at an irradiance of ~23 mW/cm^2 (cf. figures 6.11 and 6.12). VOC concentrations were 25, 50, 100, 200, 200, 100, 50, and 25 ppm for ethanol, 1-propanol, 2-propanol, 1-butanol, toluene, MIBK, and ethyl acetate and 50, 100, 200, 200, 100, and 50 ppm for 1-butylamine.

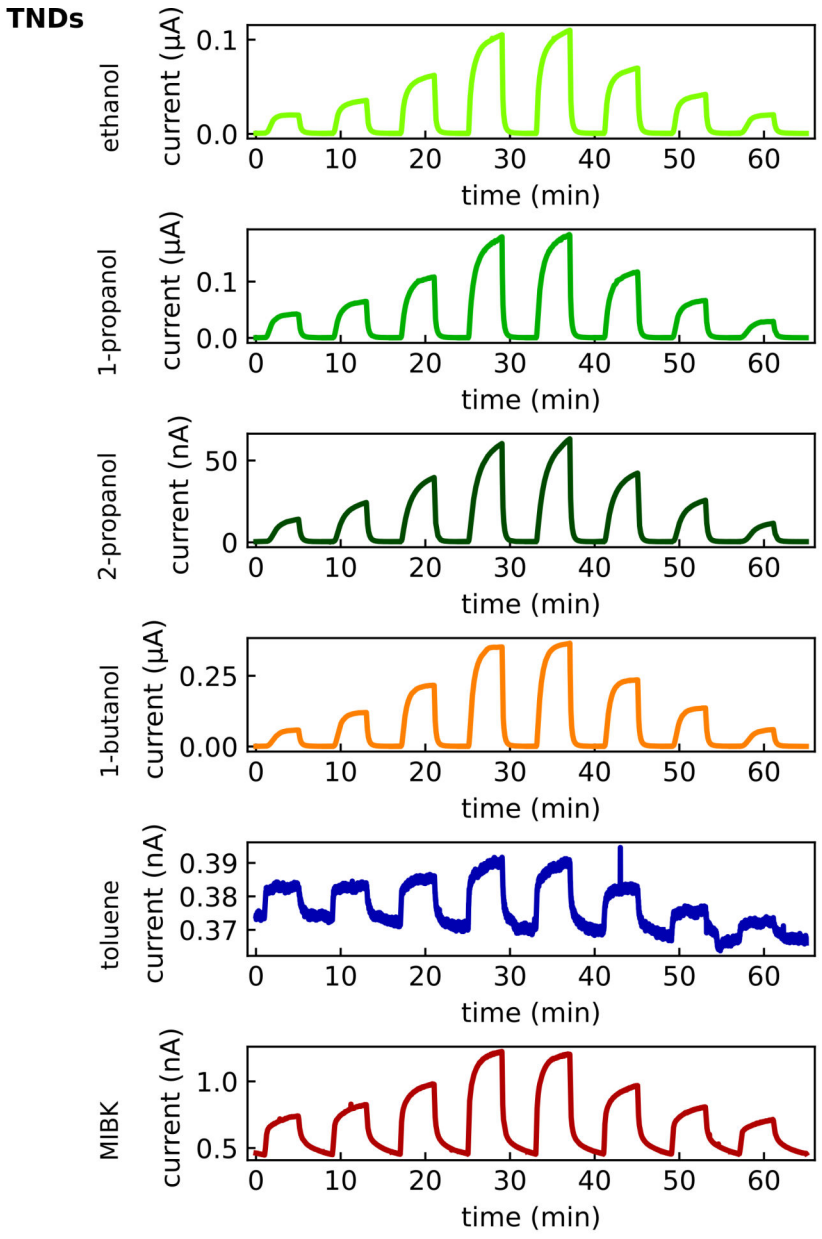

Figure A.22: Current timetraces of a photoactivated TND-based chemiresistor exposed to six analyte vapors. All timetraces are shown without baseline correction.

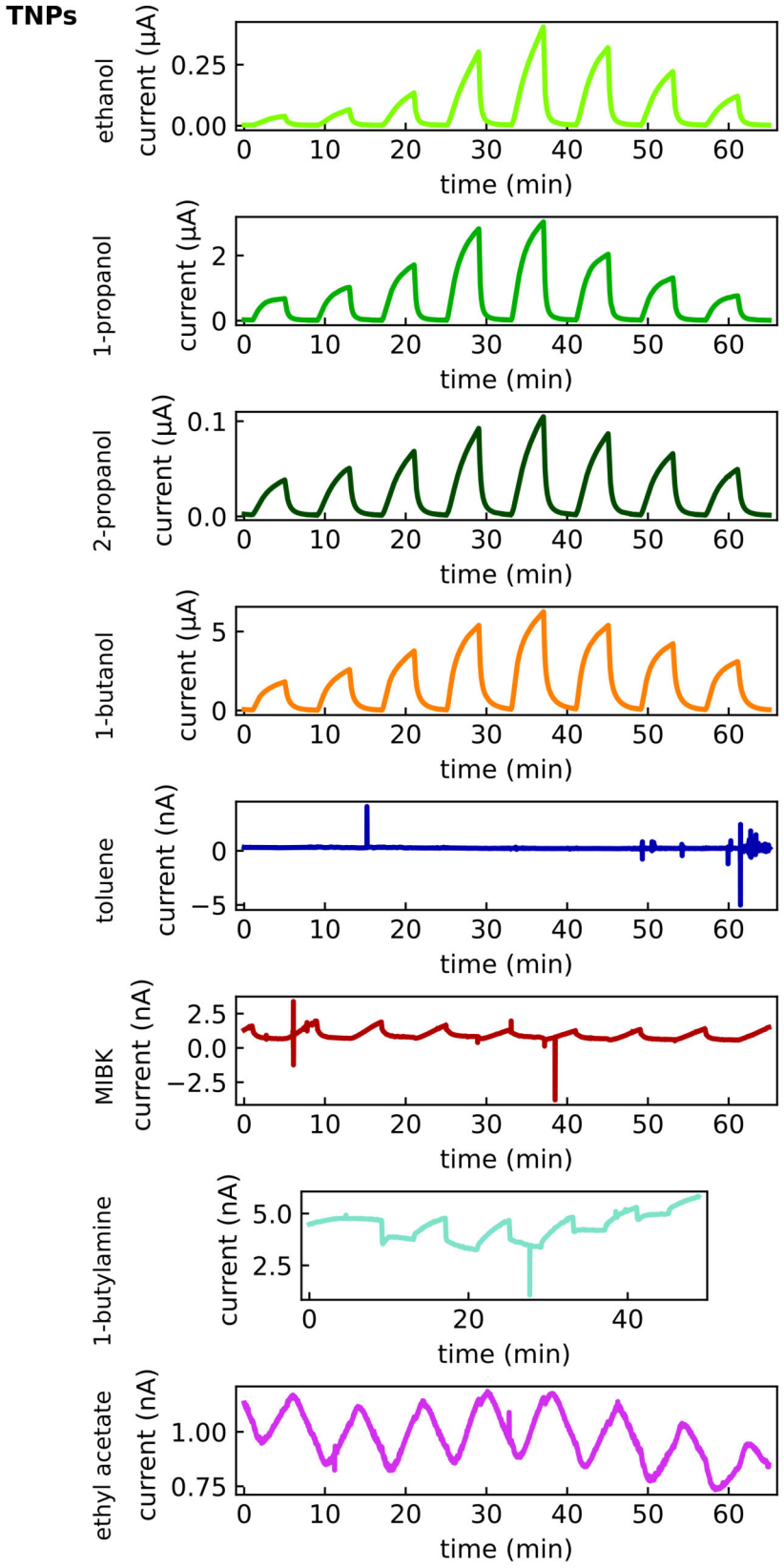

Figure A.23: Current timetraces of a photoactivated TNP-based chemiresistor exposed to eight analyte vapors. All timetraces are shown without baseline correction. Adapted and reprinted from Dobschall el al., Ref. [3], *Creative Commons CC-BY 4.0* license ©2025 The Authors. ACS Appl. Nano Mater. published by American Chemical Society. (DOI: 10.1021/acsanm.5c03648)

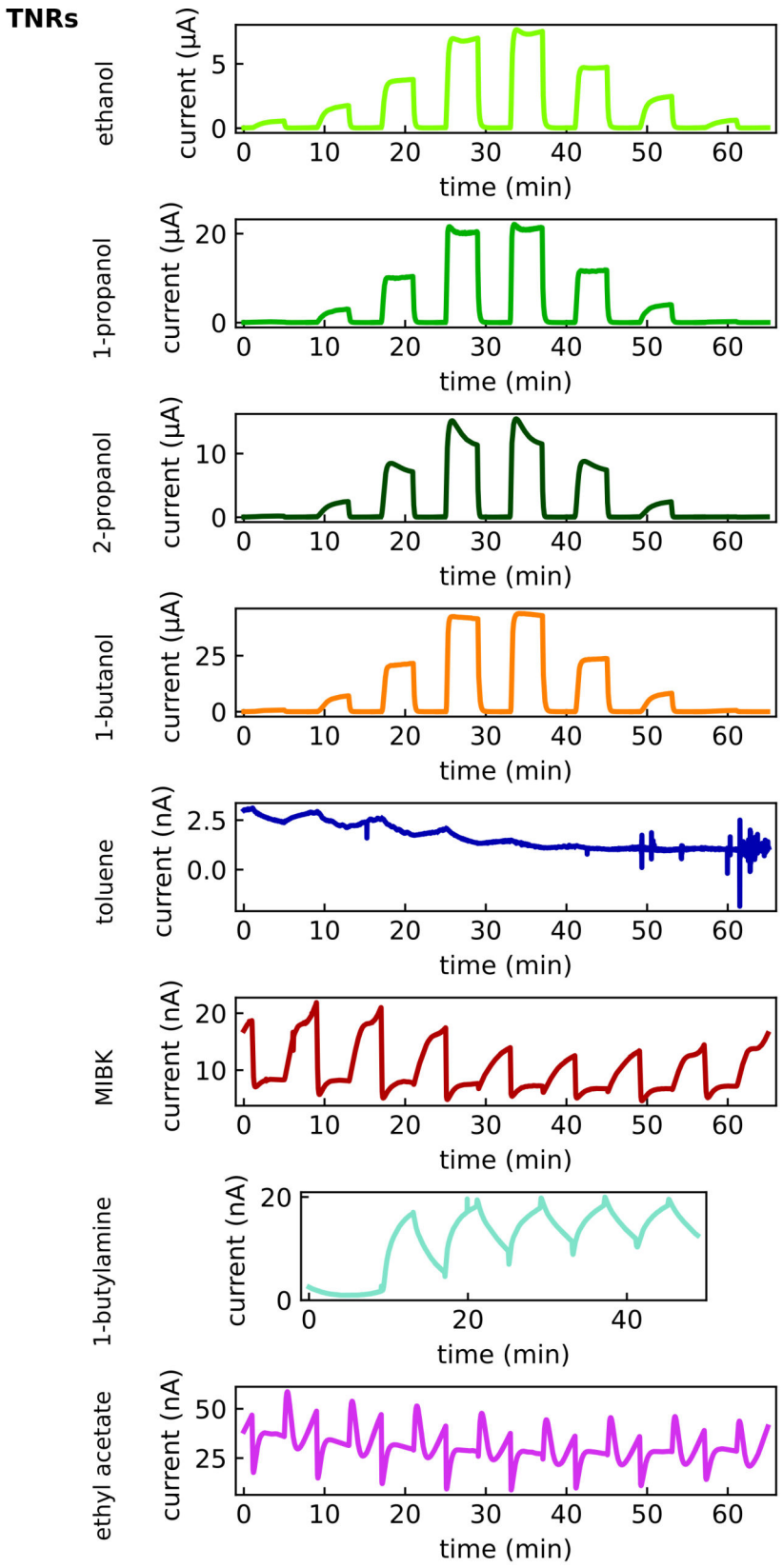

Figure A.24: Current timetraces of a photoactivated TNR-based chemiresistor exposed to eight analyte vapors. All timetraces are shown without baseline correction. Adapted and reprinted from Dobschall el al., Ref. [3], *Creative Commons CC-BY 4.0* license ©2025 The Authors. ACS Appl. Nano Mater. published by American Chemical Society. (DOI: 10.1021/acsanm.5c03648)

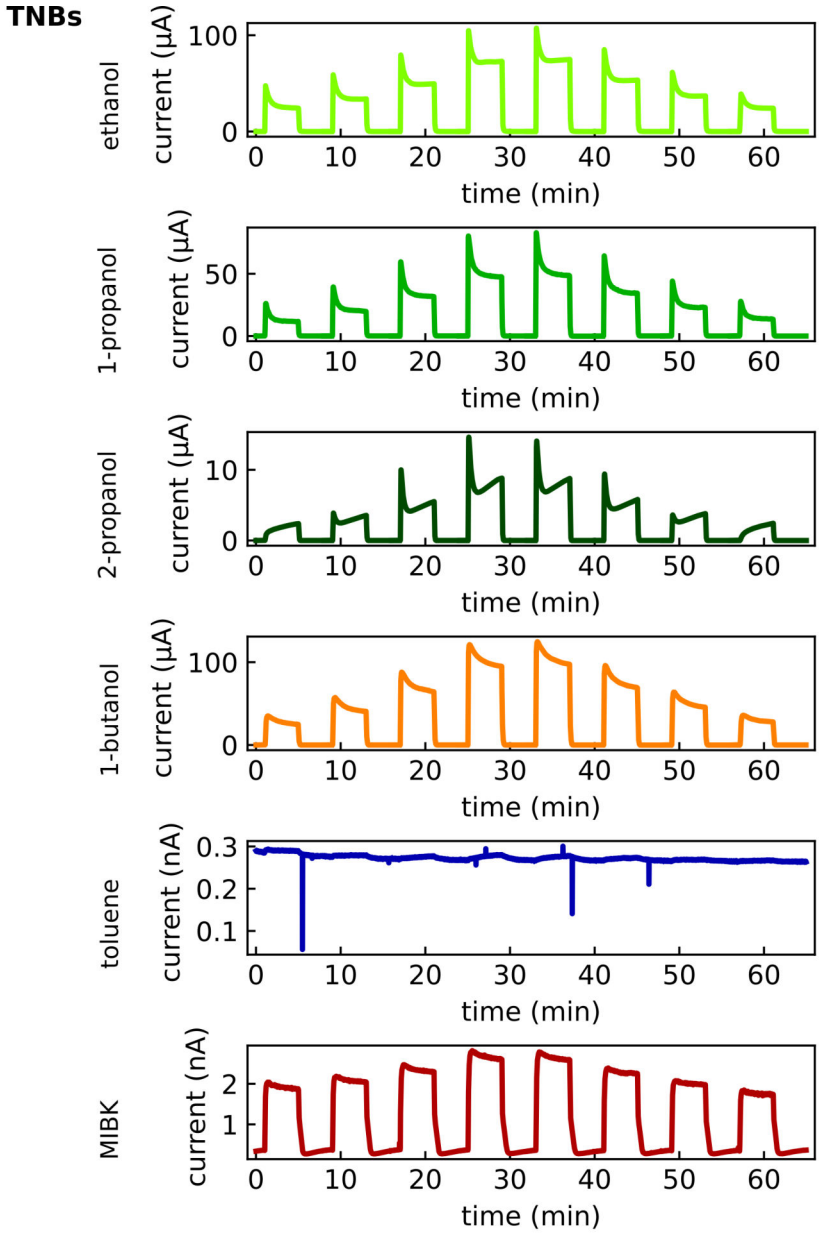

Figure A.25: Current timetraces of a photoactivated TNB-based chemiresistor exposed to six analyte vapors. All timetraces are shown without baseline correction.

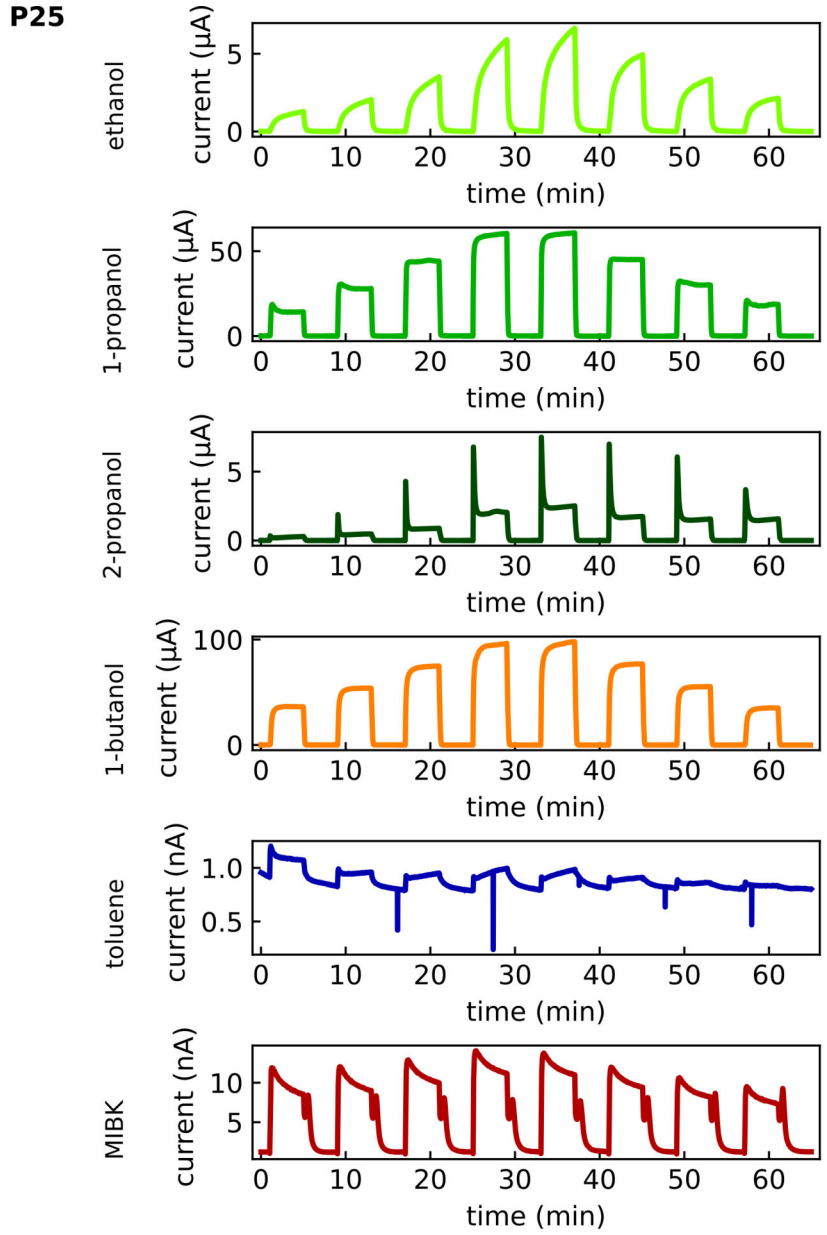

Figure A.26: Current timetraces of a photoactivated P25-based chemiresistor exposed to six analyte vapors. All timetraces are shown without baseline correction.

The following figures show the baseline-corrected relative resonant frequency timetraces of photoactivated TNR, TNP, and P25 thin films deposited on QCM substrates exposed to various VOCs (cf. figure 6.13). For photoactivation, UV LEDs were used at an irradiance of ~23 mW/cm^2. VOC concentrations were 25, 50, 100, 200, 200, 100, 50, and 25 ppm for ethanol, 1-propanol, 2-propanol, 1-butanol, toluene, and MIBK and 100, 200, 200, and 100 ppm for 1-butylamine.

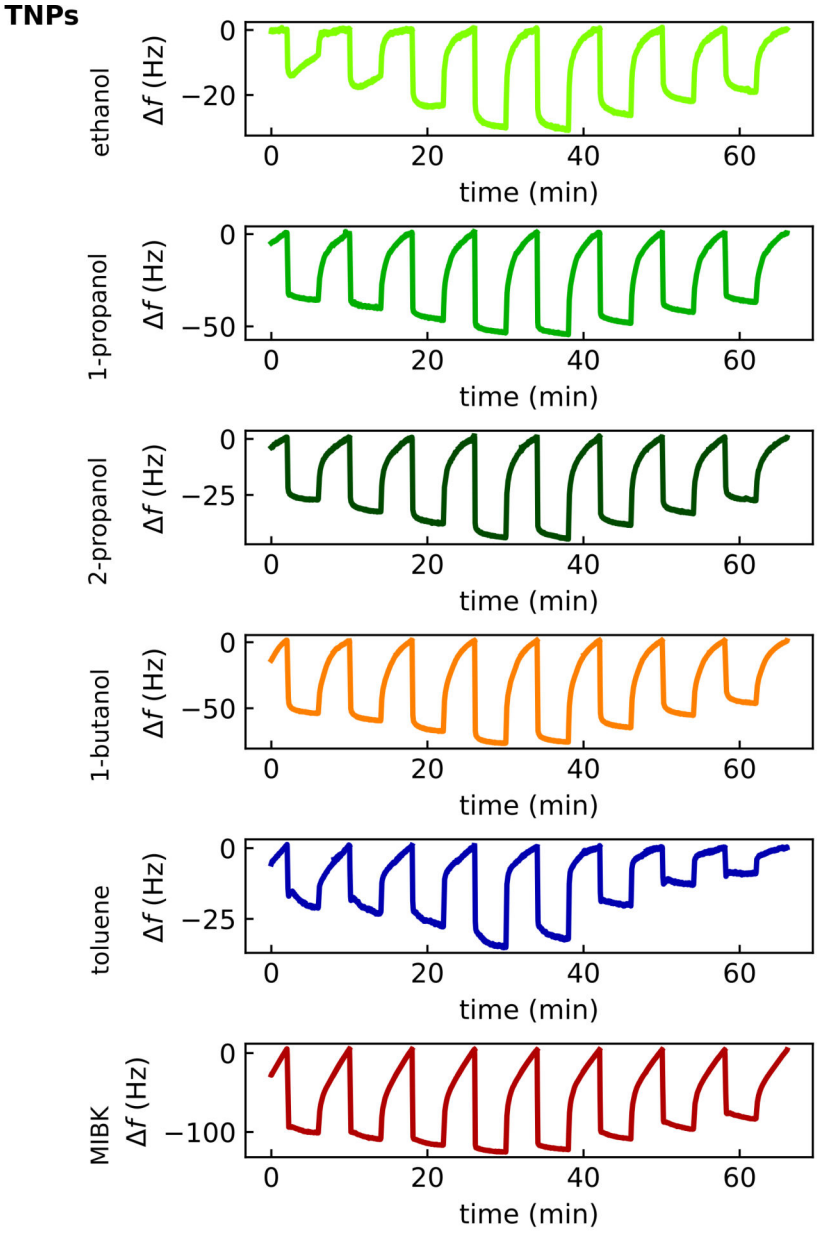

Figure A.27: Baseline-corrected relative resonant frequency timetraces of a QCM coated with a TNP thin film and exposed to six analyte vapors under UV illumination.

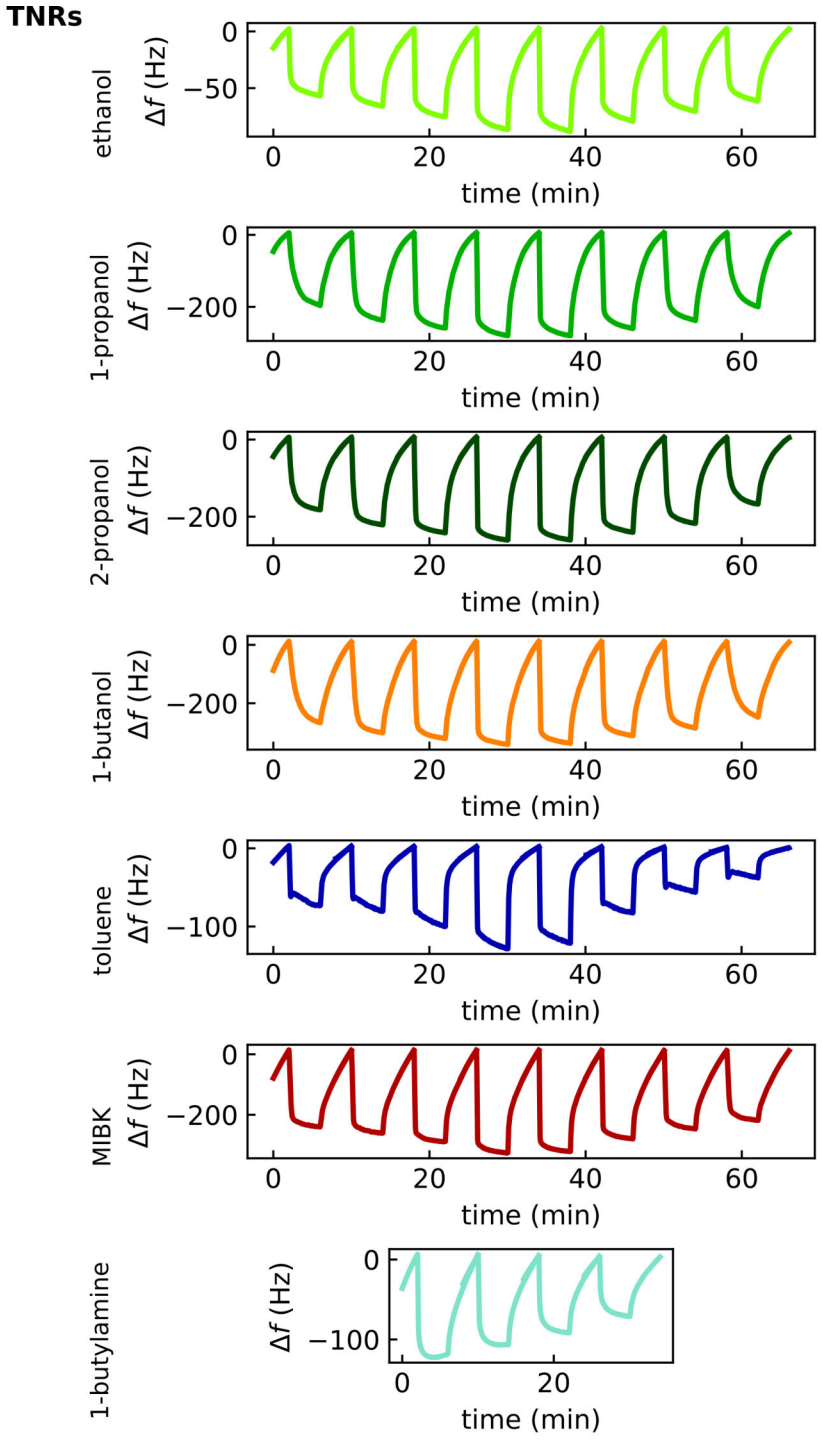

Figure A.28: Baseline-corrected relative resonant frequency timetraces of a QCM coated with a TNR thin film and exposed to seven analyte vapors under UV illumination.

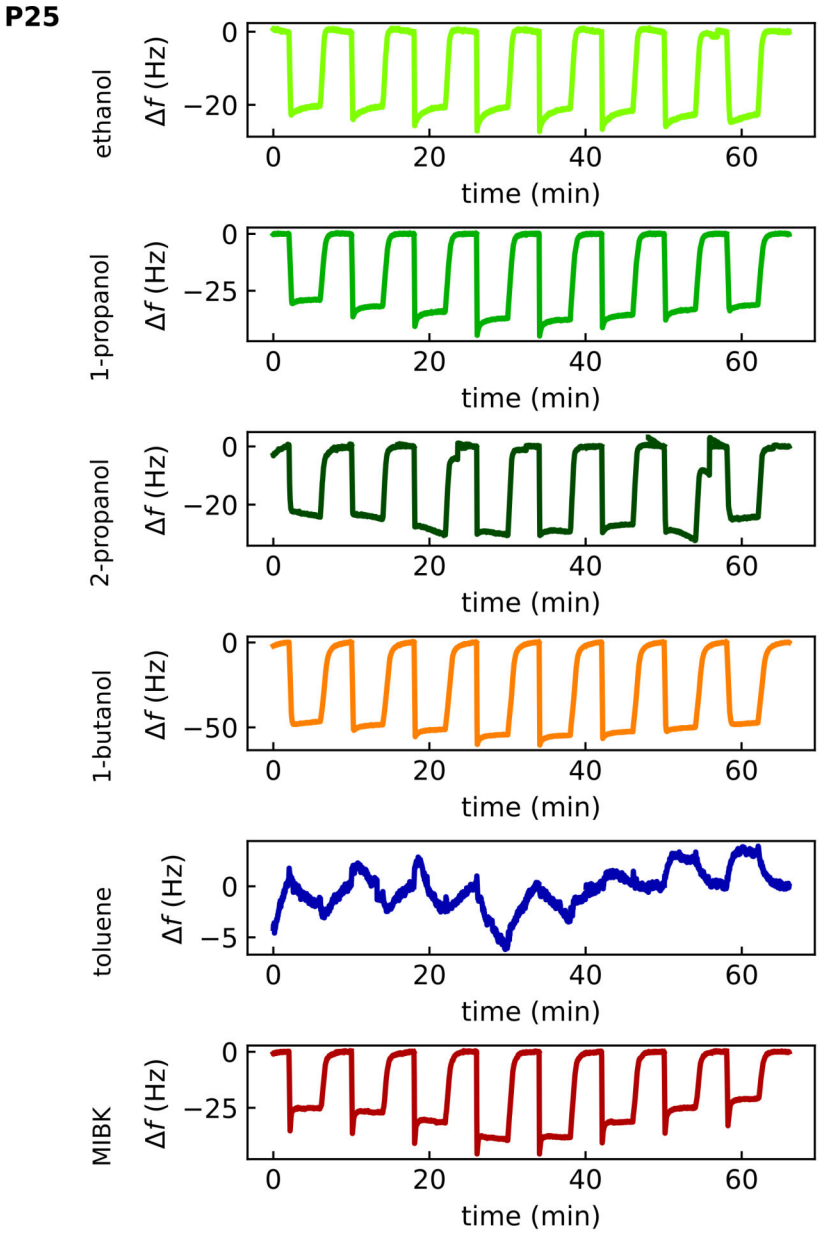

Figure A.29: Baseline-corrected relative resonant frequency timetraces of a QCM coated with a of a P25 thin film and exposed to six analyte vapors under UV illumination.

Current timetraces and baseline-corrected relative resonant frequency timetraces of the TNR thin films are shown in figure A.30 and in figure A.31, respectively (cf. figure 6.14). The current timetraces are recorded in the dark and under UV illumination (UV LEDs, irradiance: ~23 mW/cm^2) for 1-propanol and 2-propanol with concentrations of 25, 50, 100, 200, 200, 100, 50, and 25 ppm. Baseline-corrected relative resonant frequency timetraces were recorded in the dark for 1-propanol, 2-propanol, toluene, and MIBK with concentrations of 25, 50, 100, 200, 200, 100, 50, and 25 ppm.

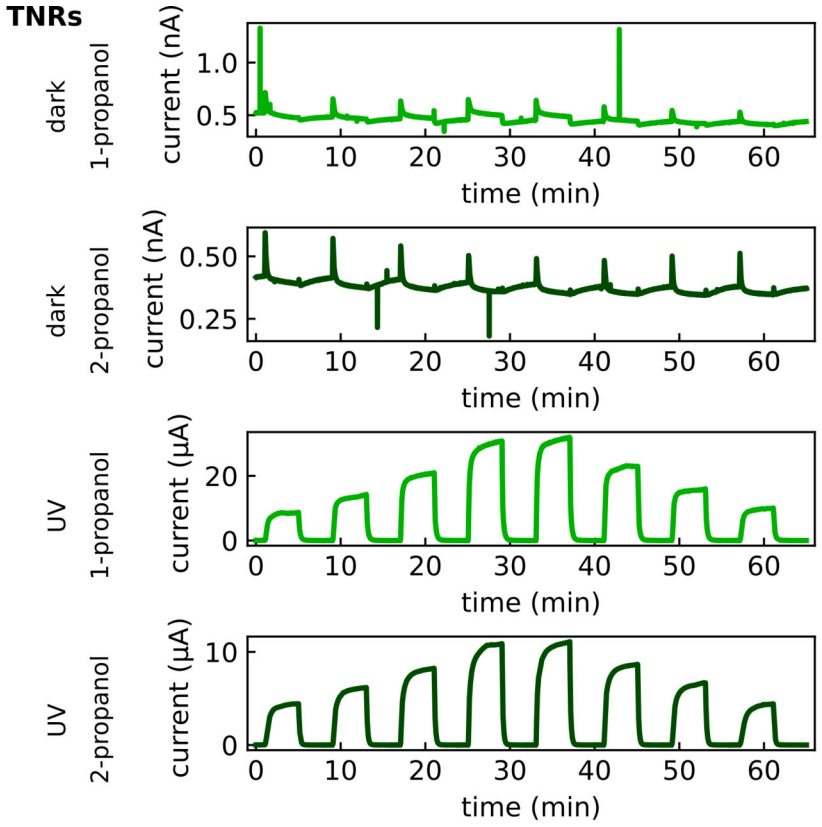

Figure A.30: Current timetraces of a TNR-based chemiresistor exposed to 1-propanol and 2-propanol in the dark (upper two) and under UV illumination (lower two). All timetraces are shown without baseline correction.

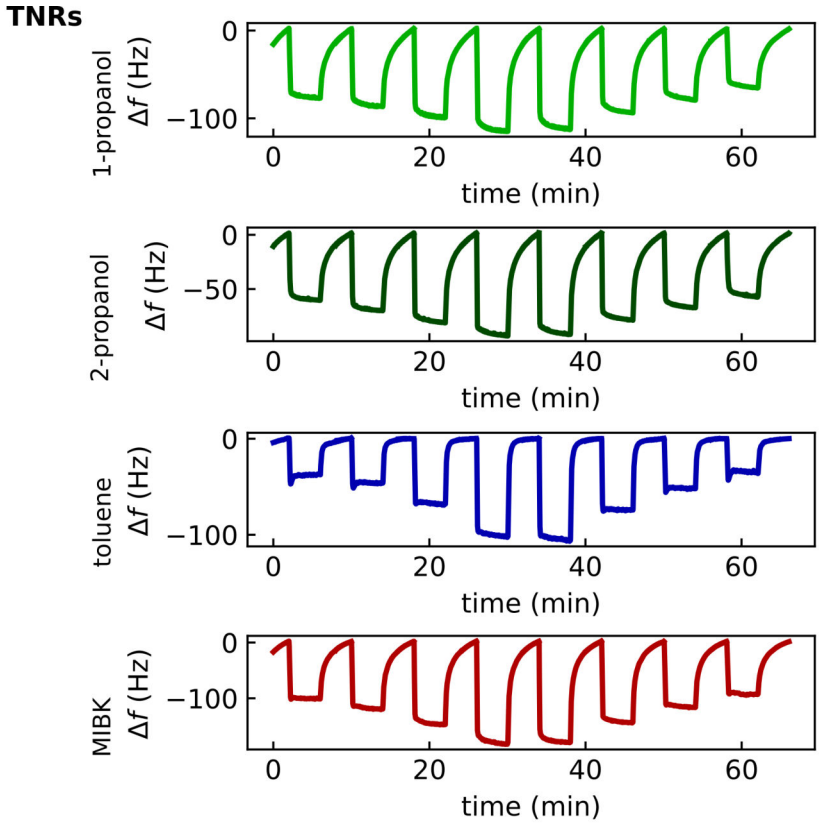

Figure A.31: Baseline-corrected relative resonant frequency timetraces of a QCM coated with a TNR thin film exposed to four analyte vapors in the dark.

A.1.13 Extended Concentration Range of 1-Propanol

The chemiresistive measurements presented to examine the photoactivated sensing mechanism focused on the analyte selectivity and the influence of the particle shape of the TNCs only using a rather narrow concentration range between 25–200 ppm. In this range, the TNR-based chemiresistors exhibited a nearly linear increase in the response current with increasing analyte concentration (cf. figure 6.11a) part iii)). In order to examine possible influences of the analyte concentration on the sensor responses, the concentration range was extended. Since the TNC-based chemiresistors are highly selective to alcohol vapors, 1-propanol in the concentration range between 0.5–5000 ppm was used as target analyte for this study. TNR thin films were deposited on IDE and QCM substrates to combine chemiresistive measurements and microgravimetric analysis. The current timetraces are provided in figure A.33 and the baseline-corrected relative resonant frequency timetraces are provided in figure A.34. Figure A.32 shows the current response isotherm in the extended concentration range (left plot) that clearly deviates from the linear shape and follows a saturation function for increasing concentration. The inset shows that the detection of 1-propanol was possible in the sub-ppm range with rather low response currents in the range of a few nA. The center plot in figure A.32 displays the current response isotherm on a double logarithmic scale, that is often used for thermally activated MOX-based chemiresistors. Usually, a linear function is obtained in the lower concentration range, from which the slope is considered as the sensitivity of the sensor. However, due to the lack of data points for small concentrations, it was not reasonable to fit a linear function to this range. Further, figure A.32 displays the isotherm of the relative substance uptake (right plot), showing a strong increase in the substance uptake for low concentrations that levels off for higher concentrations. When comparing the current response isotherm (cf. figure A.32, left) with the isotherm of the relative substance uptake (cf. figure A.32, right), the different curvatures indicate, that the response current for 1-propanol

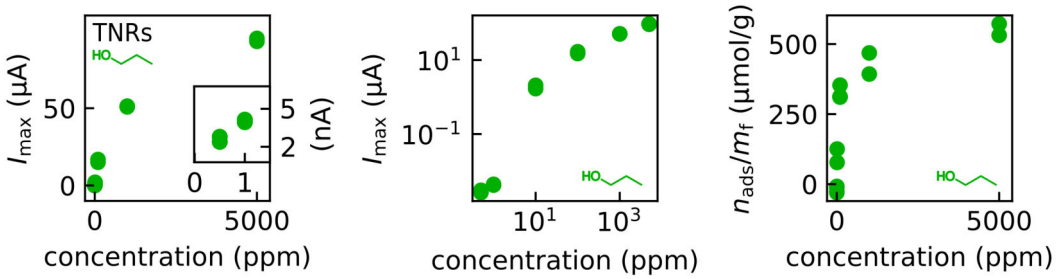

Figure A.32: Photoactivated current response isotherm of the TNR-based chemiresistor on an IDE substrate exposed to 1-propanol vapor in the concentration range between 0.5–5000 ppm (left). The inset shows a zoom-in to the current range for 1-propanol concentrations of 0.5 and 1 ppm. Current response isotherm on a double logarithmic scale (center). Isotherm of the relative substance uptake of a photoactivated TNR thin film deposited on a QCM substrate during 1-propanol exposure (right).

is not directly related to the number of analyte molecules sorbed on the TNR thin film in this extended concentration range. Nevertheless, these experiments demonstrate the detection of 1-propanol over a large concentration range including the sub-ppm level. Current and baseline-corrected relative resonant frequency timetraces of photoactivated TNR thin films to 1-propanol in an extended concentration range between 0.5, 1, 10, 100, 100, 10, 1, and 0.5 ppm as well as 100, 1000, 5000, 5000, 1000, and 100 ppm are shown in figures A.33 and A.34, respectively. The TNR thin films were photoactivated using UV LEDs (emission wavelength: 278 nm) at an irradiance of ~23 mW/cm^2. The insets provide a zoom-in to the range of the response current and the relative resonant frequency at concentrations of 0.5 and 1 ppm.

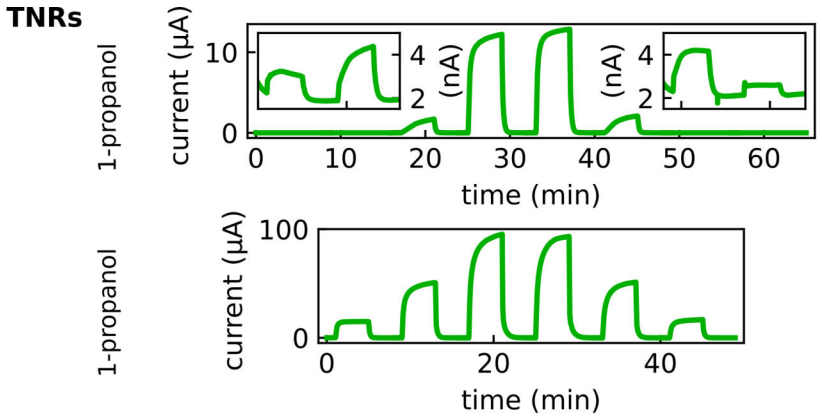

Figure A.33: Current timetraces of a photoactivated TNR-based chemiresistor exposed to 1-propanol with concentrations ranging from 0.5–5000 ppm. Insets: zoom-in to the range of the response current at low 1-propanol concentrations of 0.5 and 1 ppm. All timetraces are shown without baseline correction.

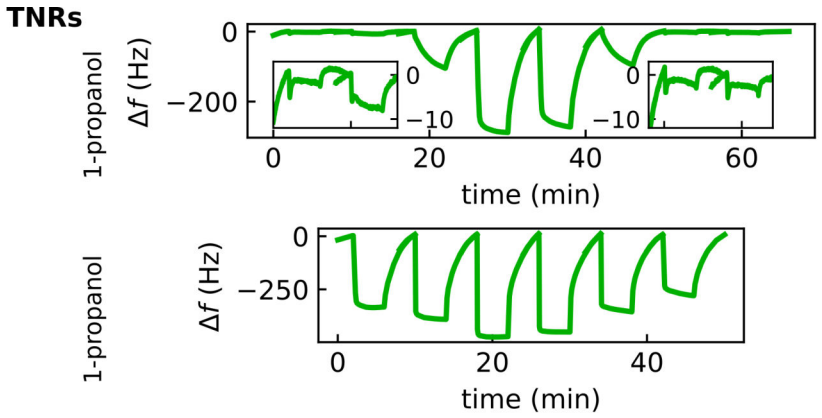

Figure A.34: Baseline-corrected relative resonant frequency timetraces of a QCM coated with a TNR thin film exposed to 1-propanol with concentrations ranging from 0.5–5000 ppm under photoactivation. Insets: zoom-in to the range of the relative resonant frequency at low 1-propanol concentrations of 0.5 and 1 ppm.

A.1.14 Humidity Influence: Timetraces

The following figures show the photoactivated current timetraces of TNR-, TNP-, and P25-based chemiresistors exposed to 1-propanol (25, 50, 100, 200, 200, 100, 50, and 25 ppm) at increasing r.h. levels of 0%, 10%, and 46% (cf. figure 6.15). For photoactivation, UV LEDs were used at an irradiance of ~23 mW/cm^2.

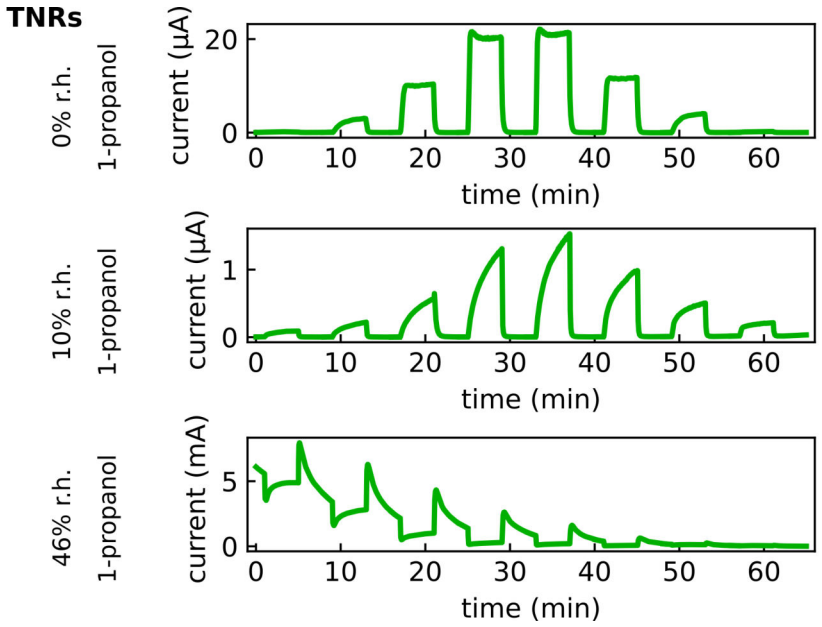

Figure A.35: Current timetraces of a photoactivated TNR-based chemiresistor exposed to 1-propanol at increasing r.h. levels. All timetraces are shown without baseline correction. Adapted and reprinted from Dobschall el al., Ref. [3], *Creative Commons CC-BY 4.0* license ©2025 The Authors. ACS Appl. Nano Mater. published by American Chemical Society. (DOI: 10.1021/acsanm.5c03648)

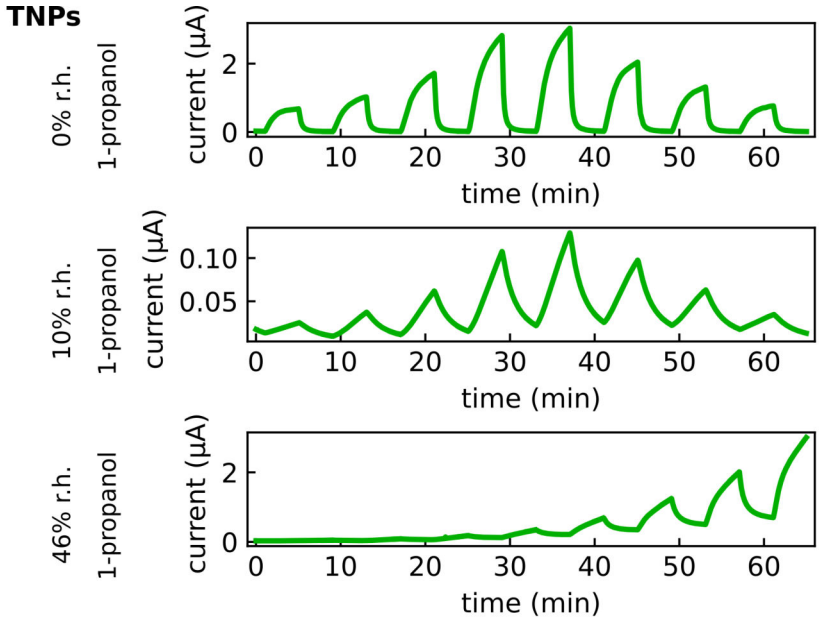

Figure A.36: Current timetraces of a photoactivated TNP chemiresistor exposed to 1-propanol at increasing r.h. levels. All timetraces are shown without baseline correction. Adapted and reprinted from Dobschall el al., Ref. [3], *Creative Commons CC-BY 4.0* license ©2025 The Authors. ACS Appl. Nano Mater. published by American Chemical Society. (DOI: 10.1021/acsanm.5c03648)

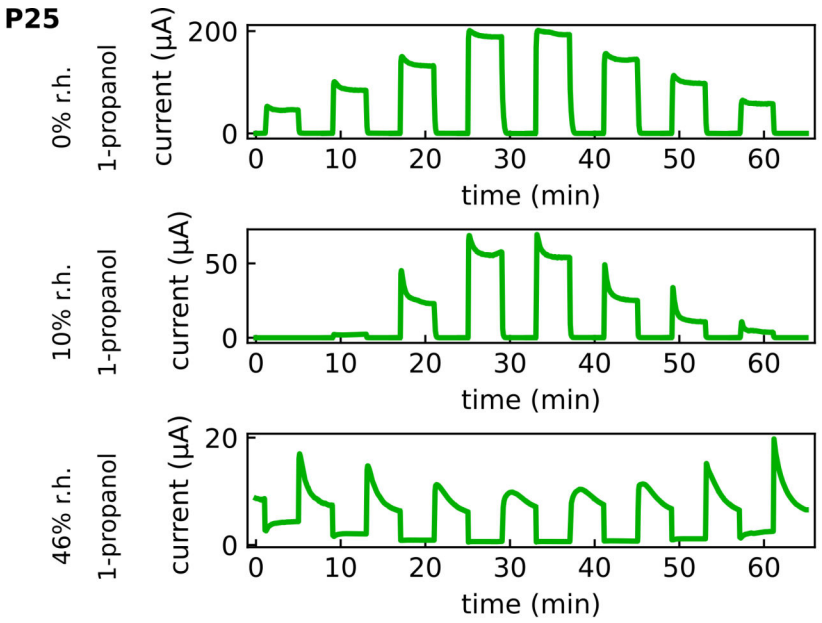

Figure A.37: Current timetraces of a photoactivated P25-based chemiresistor exposed to 1-propanol at increasing r.h. levels. All timetraces are shown without baseline correction. Adapted and reprinted from Dobschall el al., Ref. [3], *Creative Commons CC-BY 4.0* license ©2025 The Authors. ACS Appl. Nano Mater. published by American Chemical Society. (DOI: 10.1021/acsanm.5c03648)

The following figures show the photoactivated, baseline-corrected relative resonant frequency timetraces of QCMs coated with TNR, TNP, and P25 thin films and exposed to transient r.h. variations of 0%, 10%, 30%, and 50% (cf. figure 6.16). For photoactivation, UV LEDs were used at an irradiance of ~23 mW/cm^2. For the TNR thin film, the baseline-corrected relative resonant frequency timetrace without photoactivation is shown additionally.

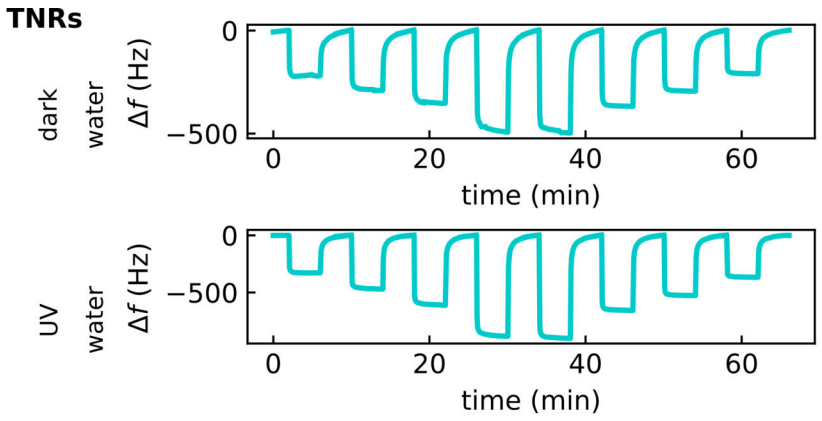

Figure A.38: Baseline-corrected relative resonant frequency timetraces of a QCM coated with a TNR thin film with and without photoactivation exposed to transient r.h. variations.

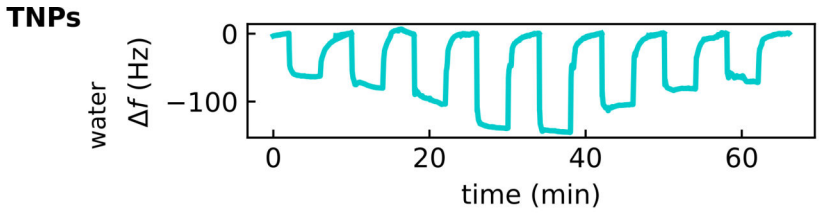

Figure A.39: Baseline-corrected relative resonant frequency timetrace of a QCM coated with a TNP thin film exposed to transient r.h. variations under photoactivation.

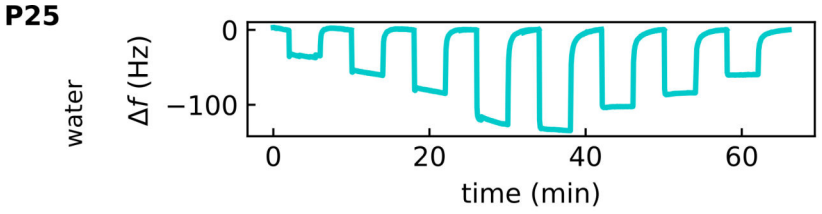

Figure A.40: Baseline-corrected relative resonant frequency timetrace of a QCM coated with a P25 thin film exposed to transient r.h. variations under photoactivation.

A.1.15 Influence of P25 Film Thickness on Chemiresistive Properties

To obtain thin films of bare P25 TNCs with a similar thickness compared to those of the OLAM-stabilized thin films, four P25 TNC dispersions in water/MeOH (1/1, v/v) with concentrations between 2–5 mg/mL were drop-casted (10 µL) on SiO_2/Si substrates featuring IDE structures. Figure A.41 (left) shows the increasing film thickness with increasing concentration of the P25 TNC dispersion. Representative AFM scans are displayed in figure A.42 showing a film thickness of ~128 nm, ~148 nm, ~201 nm, and ~210 nm for the

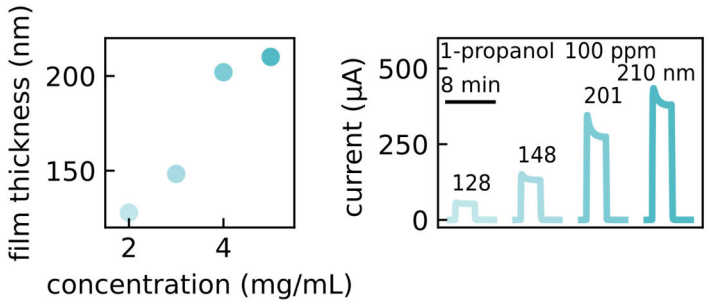

Figure A.41: Influence of the P25 film thickness on the structural and chemiresistive properties. Scatter plot of the film thickness as a function of the concentration of the dispersion used for film deposition (left). Current transients of the photoactivated P25-based chemiresistors to 100 ppm 1-propanol vapor (right).

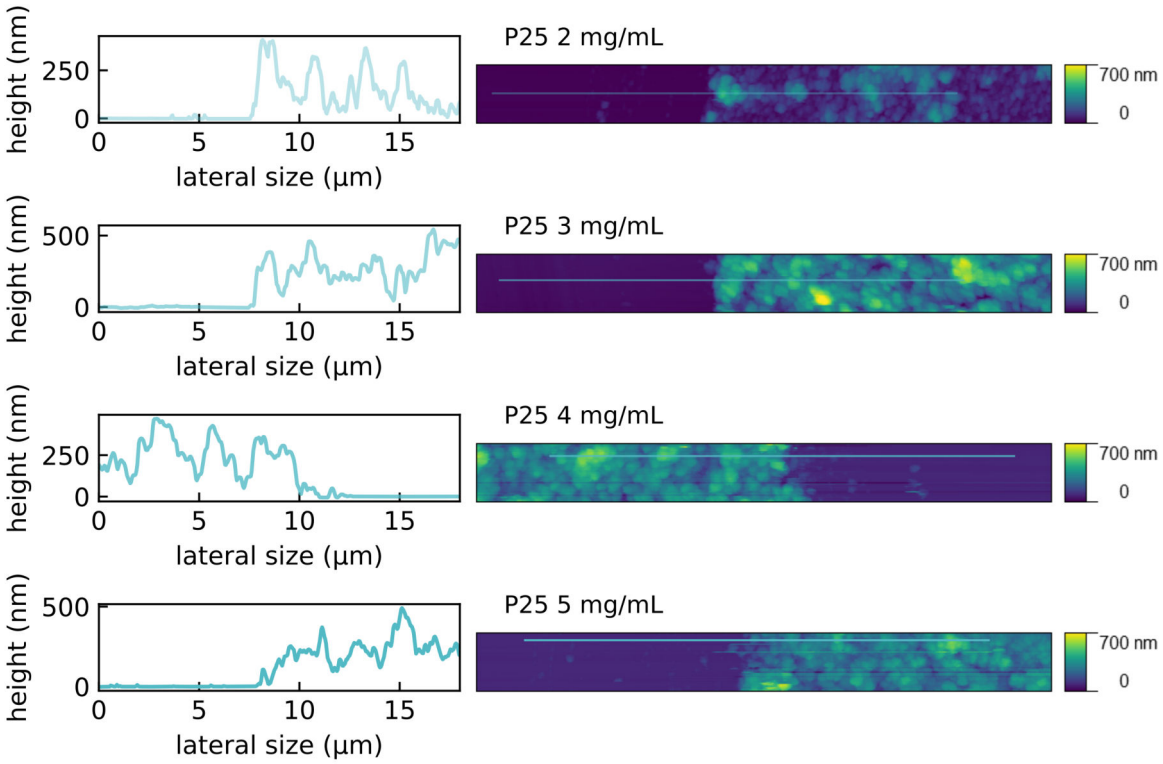

Figure A.42: Representative topographic AFM scans (20×2 µm^2) and extracted line profiles for P25 thin films fabricated from dispersions in water/MeOH (1/1, v/v) of different concentrations after 120 min DUV treatment.

concentration of 2 mg/mL, 3 mg/mL, 4 mg/mL, and 5 mg/mL, respectively. Further, the topographic data demonstrate the island-like structure of the P25 thin films. Figure A.41 (right) shows the current transients of the P25-based sensors to 100 ppm propanol vapor, in which the maximum response current increases with increasing film thickness. This trend is attributed to the extended amount of material deposited and thus the increased number of photoactivated reactions on the sensitive TiO_2 layer. Figure A.43 shows the photoactivated current timetraces of the P25-based chemiresistors prepared from dispersions in water/MeOH (1/1, v/v) with concentrations of 2 mg/mL, 3 mg/mL, 4 mg/mL, and 5 mg/mL and exposed to 1-propanol vapor (25, 50, 100, 200, 200, 100, 50, and 25 ppm). For photoactivation, UV LEDs were used at an irradiance of ~23 mW/cm^2.

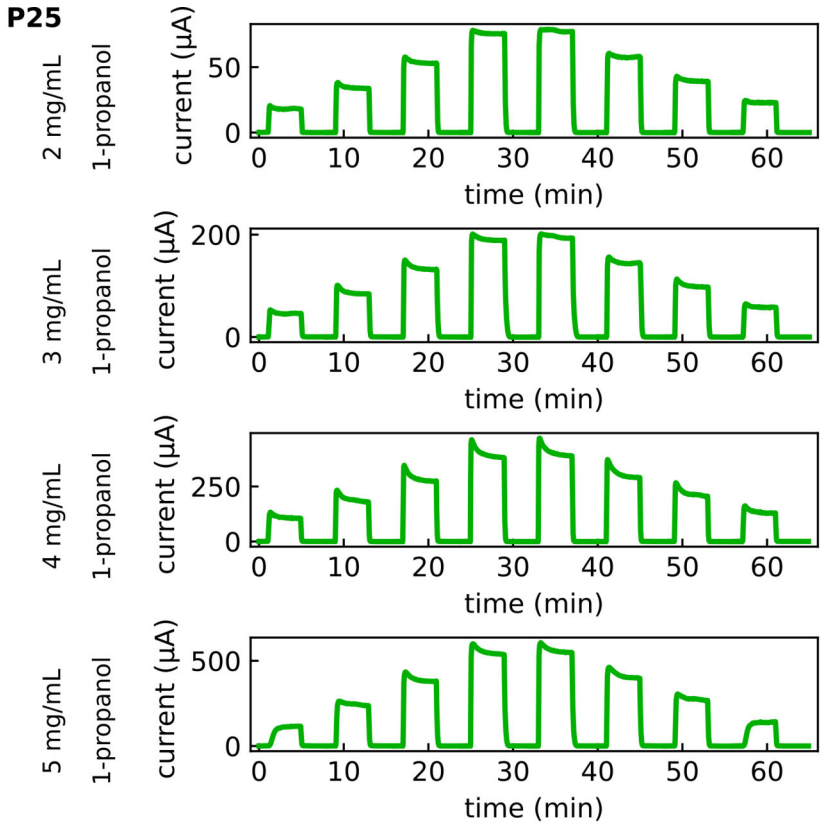

Figure A.43: Current timetraces of the photoactivated P25-based chemiresistors exposed to 1-propanol vapor. The chemiresistors were fabricated from dispersions with concentrations between 2–5 mg/mL. All timetraces are shown without baseline correction.

A.1.16 TNR-Based Chemiresistors on Alumina Substrates

Operating Temperature Calibration. For conducting photoactivated chemiresistor measurements at elevated operating temperatures, a TNR thin film was drop-casted on an alumina substrate. The latter contained an IDE structure, a heating meander, and a resistance temperature detector (RTD), all made of platinum. First, temperatures measured at the chemiresistor surface using an IR-thermometer (Fluke-62 Max) were correlated to the resistance change of the RTD. Figure A.44 shows the data that were obtained outside the test cell in purple with the corresponding calibration curve as the linear fit. The fit was used to calculate the temperatures inside the test cell and the temperature was controlled via the resistance value of the RTD. The influence of the operating temperature on the electrical and chemiresistive properties was investigated for a TNR-based sensor at 23 °C, 50 °C, and 72 °C.

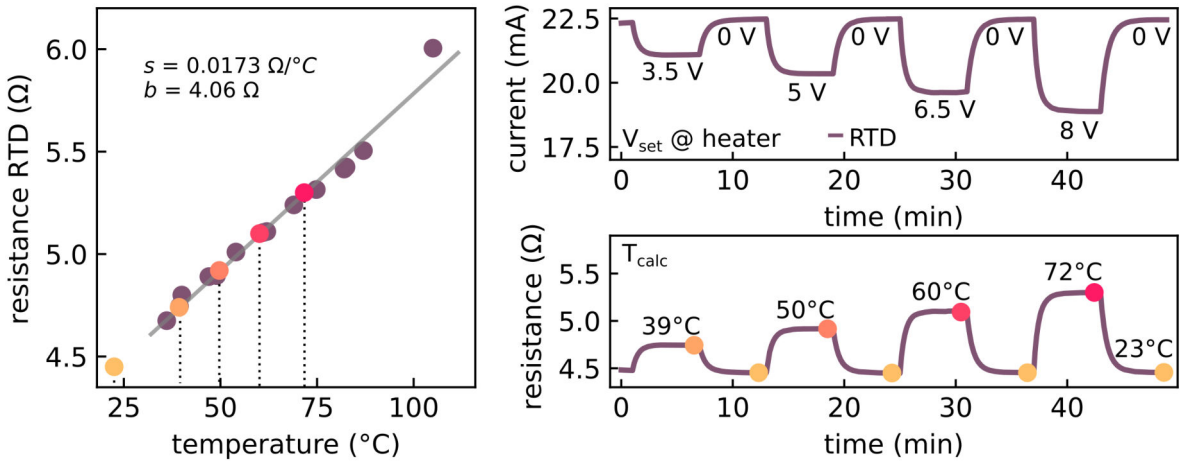

Figure A.44: Operating temperature calibration of the TNR thin film LSH1 deposited on an alumina substrate. Scatter plot of the RTD resistance vs. temperature of the sensor surface (left). The grey curve represents the linear fit to the data and was used to calculate the chemiresistor temperature inside the test cell. Yellow to red dots indicate the values of increased operating temperatures used in this study. Current timetrace of the RTD unit with increasing heater voltages (top right). Resistance timetrace of the RTD with calculated temperatures, indicated as colored dots.

Thin Film Morphology on Alumina Substrates. The film morphology of the TNR thin film on the alumina substrate was investigated using AFM analysis and SEM (cf. figure A.45). The AFM analysis of the bare substrate revealed a rather rough surface compared to SiO_2/Si substrates. Upon film deposition, this roughness was translated to the TNR thin film, as indicated by the line profiles recorded on the TNR-covered alumina substrate. Further, the SEM images on the TNR-covered alumina substrate showed comparable features with corresponding lateral dimensions. For the lowest magnification, the electrodes of the alumina substrate are shown (lower right corner). For higher magnification, the morphology of the TNR thin film is indicated, which featured a comparable surface structure like the underlying substrate. Finally, for the highest magnification, the

SEM image shows the homogeneous distribution of disordered particles, where individual rods can be distinguished. On the scale of individual rods, the morphologies of the TNR thin films on the alumina and the SiO_2/Si substrates are comparable (cf. figure 6.6). However, the alumina substrate influenced the morphology of the thin film on the micrometer scale.

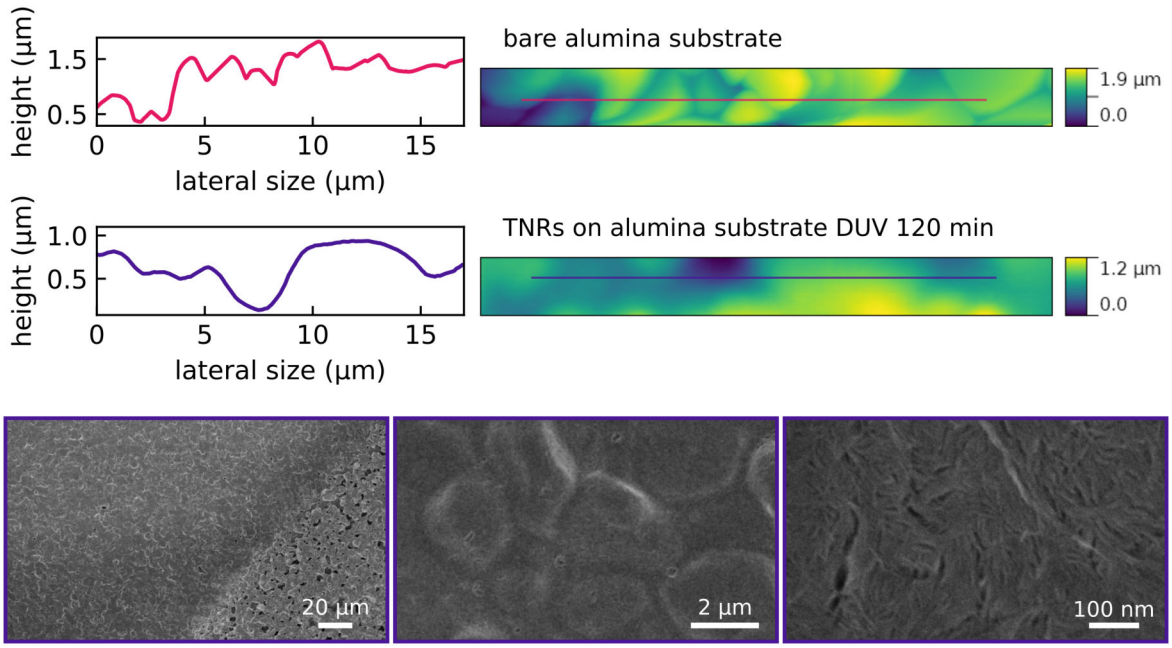

Figure A.45: Representative topographic AFM scans (20×2 μm^2) and extracted line profiles for the bare alumina substrate and the TNR-covered alumina substrate (top). The TNR thin film was DUV-treated for 120 min. SEM images of the TNR thin film deposited on the alumina substrate with different magnifications (bottom).

Electrical Properties. Figure A.46 shows the results of current-voltage (*IV*) measurements of the TNR-based chemiresistor on the alumina substrate purged with the desired atmosphere. The temperature was set to distinct values of 23 °C, 50 °C, and 72 °C, while the r.h. level was varied between 0%, 10%, 30%, and 50%. For photoactivated measurements, the samples were illuminated by UV LEDs (emission wavelength: 278 nm) at an irradiance of ~23 mW/cm^2. The latter was switched off for measurements in the dark. Linear *IV* curves were obtained by sweeping the voltage between ±10 V and the conductance was extracted as the slope of the respective curve. These conductance values are depicted in the scatter plots of figure 6.17.

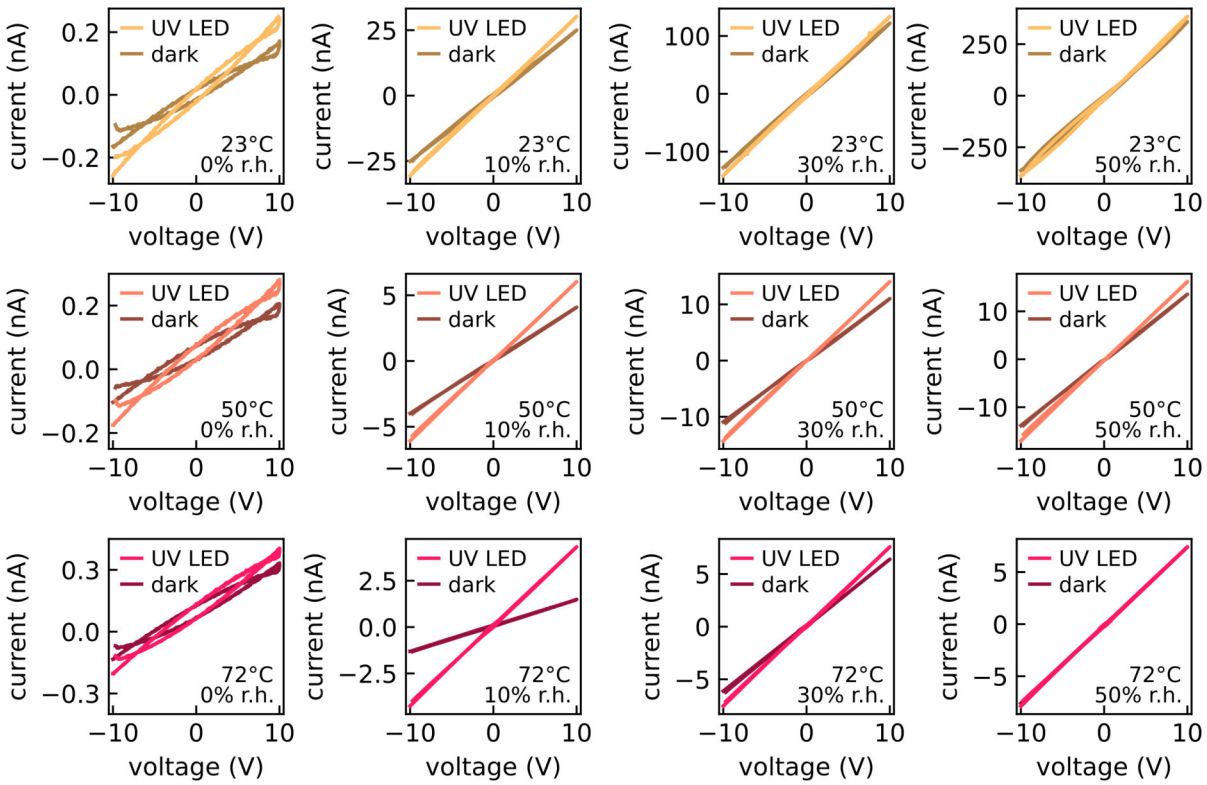

Figure A.46: *IV* curves of the TNR-based sensor deposited on the alumina substrate with and without photoactivation by UV LEDs, measured at varying operating temperatures and r.h. levels. The top, center, and bottom rows correspond to operating temperatures of 23 °C, 50 °C, and 75 °C, respectively. The r.h. level increases from left to right: 0%, 10%, 30%, and 50%.

A.1.17 Increased Operating Temperature: Dark Conditions

In addition to the transients obtained under UV illumination (cf. figure 6.20), this section focuses on the chemiresistive responses of the TNR-based sensor to 1-propanol at varying operating temperatures and various r.h. levels in the dark. Figure A.47 shows the current and relative conductance change transients of each operating temperature at r.h. levels of 0%, 10%, 30%, and 50% using the same scale as for the photoactivated plots in figure 6.20. As expected, no responses to 1-propanol were detected without photoactivation and the baseline conductance increased with increasing r.h. level (cf. figure 6.17). However, decreased response currents were observed to 1-propanol transients at higher r.h. levels, which were more pronounced at lower operating temperatures. We assume that this is due to the adsorption of 1-propanol onto the surface of the TNRs, interrupting the charge transport directed by the Grotthuss mechanism and therefore reducing the conductance. For the relative conductance change ($\frac{\Delta G}{G_0}$) only small variations between the temperatures were detected. Based on these minor differences, it is assumed that the ratio of adsorbed water to 1-propanol was not affected by the operating temperature.

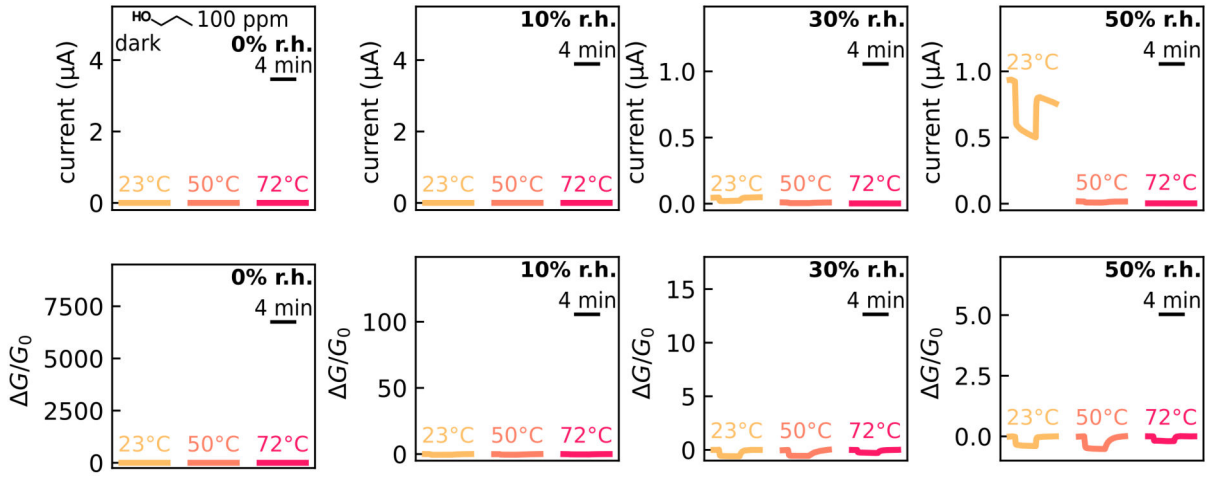

Figure A.47: Transients of the current (top row) and the baseline-corrected relative conductance change (bottom row) of the TNR-based chemiresistor exposed to 1-propanol at operating temperatures of 23 °C, 50 °C, and 72 °C without UV illumination. The data were obtained for r.h. levels of 0%, 10%, 30%, and 50% with the latter increasing from left to right.

A.1.18 Increased Operating Temperature: Timetraces

The following figures show the current and baseline-corrected relative conductance change timetraces of the TNR-based chemiresistor exposed to 1-propanol vapor with concentrations of 50, 100, 200, 200, 100, and 50 ppm at r.h. levels of 0%, 10%, 30%, and 50% and operating temperatures of 23 °C, 50 °C, and 72 °C with and without photoactivation (cf. figures 6.18, 6.19, 6.20, 6.21, and A.47). For photoactivation, UV LEDs were used at an irradiance of ~23 mW/cm^2.

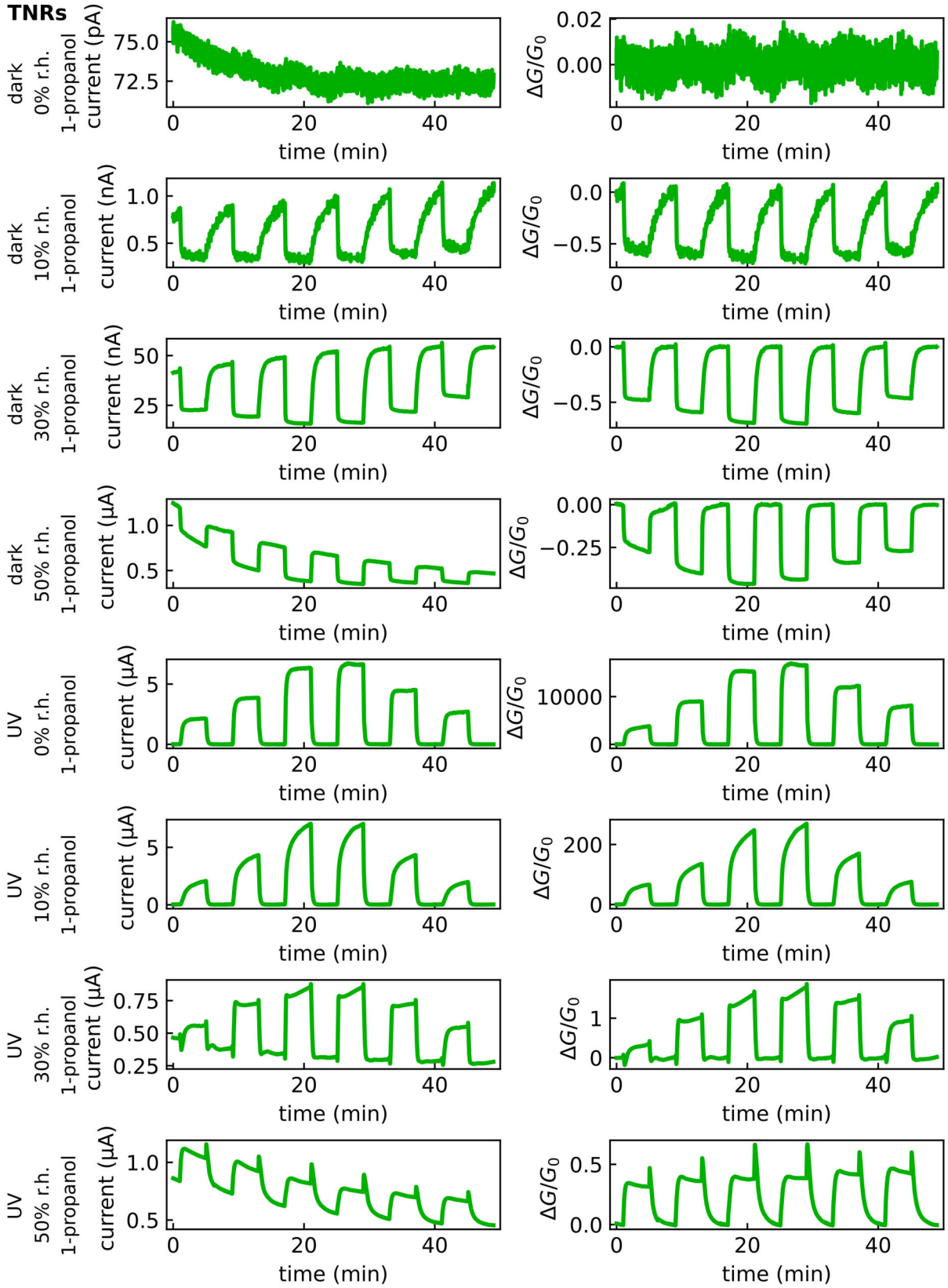

Figure A.48: Timetraces of the current (left column, without baseline correction) and the relative conductance change (right column, baseline-corrected) of the TNR-based chemiresistor exposed to 1-propanol vapor at increasing r.h. levels and at 23 °C with and without photoactivation.

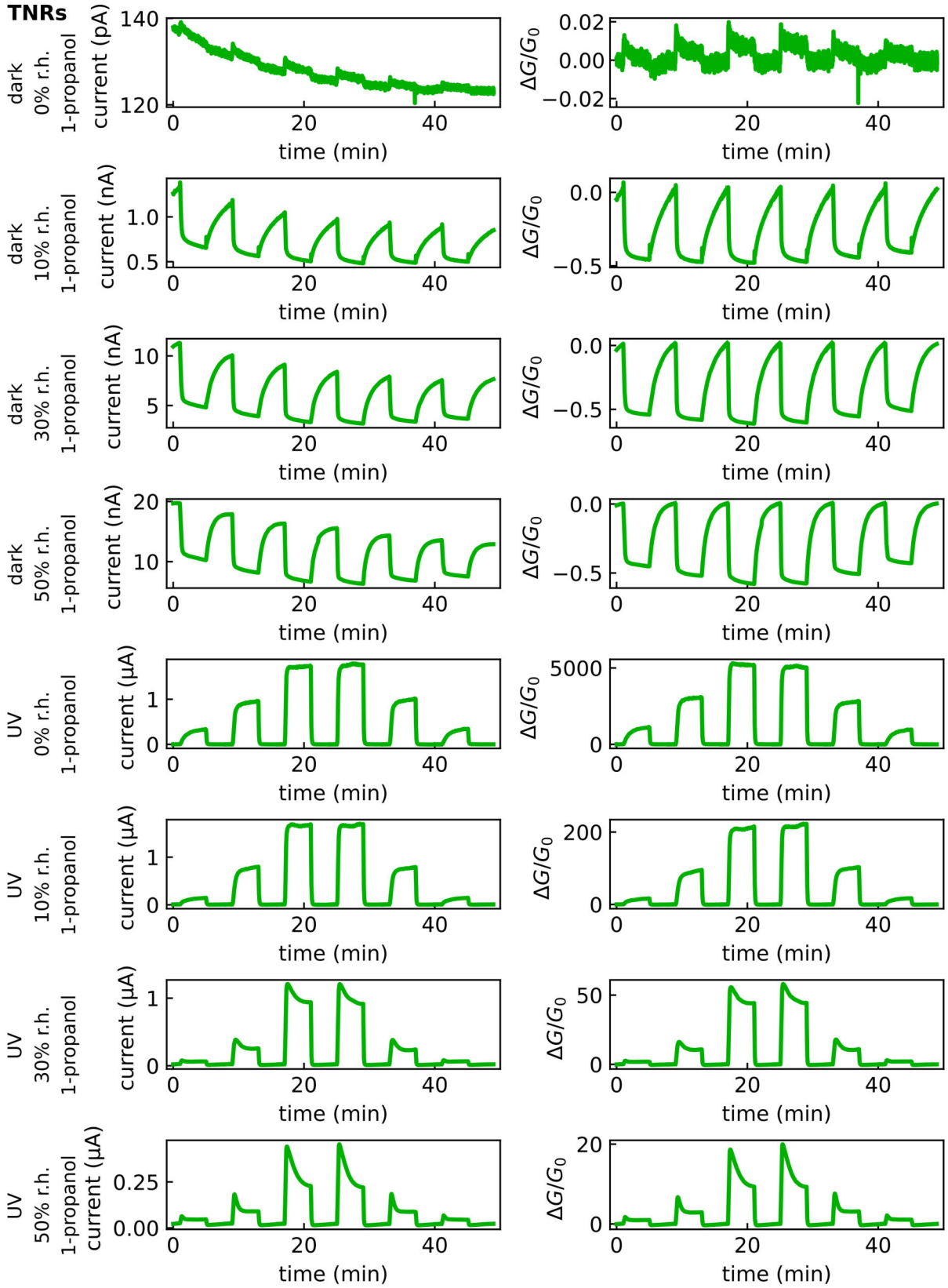

Figure A.49: Timetraces of the current (left column, without baseline correction) and the relative conductance change (right column, baseline-corrected) of the TNR-based chemiresistor exposed to 1-propanol vapor at increasing r.h. levels and at 50 °C with and without photoactivation.

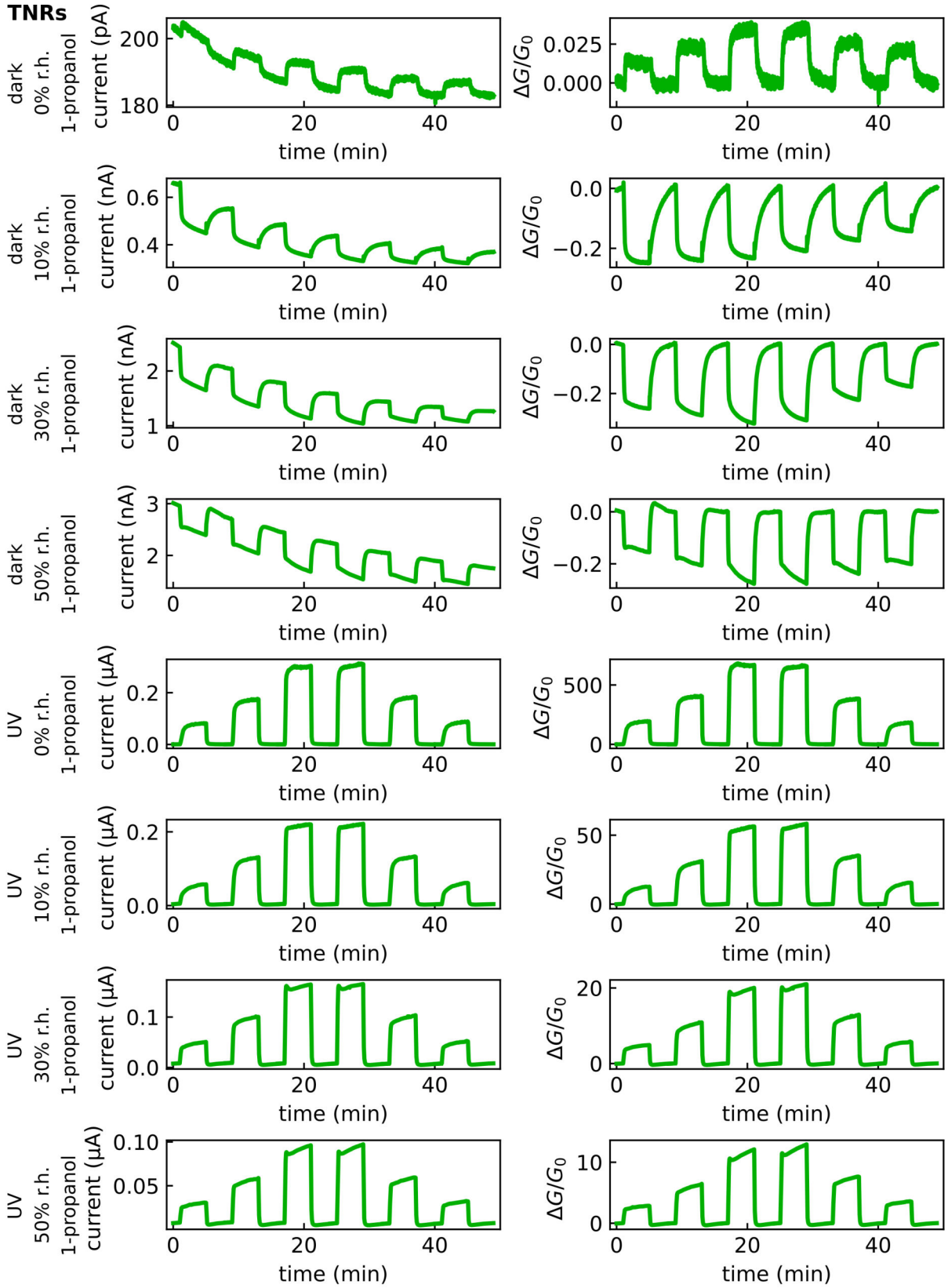

Figure A.50: Timetraces of the current (left column, without baseline correction) and the relative conductance change (right column, baseline-corrected) of the TNR-based chemiresistor exposed to 1-propanol vapor at increasing r.h. levels and at 72 °C with and without photoactivation.

A.1.19 Surface Modification: Nanocrystal Characterization

SPIONs. Superparamagnetic iron oxide nanoparticles (SPIONs) were synthesized in a flow reactor[245] and kindly provided by Dr. Sebastian Willruth, former research associate at University of Hamburg. Figure A.51 shows a representative TEM image of the spherical nanocrystals with a diameter of ~3 nm and the corresponding TGA displaying an organic content of 65.4%.

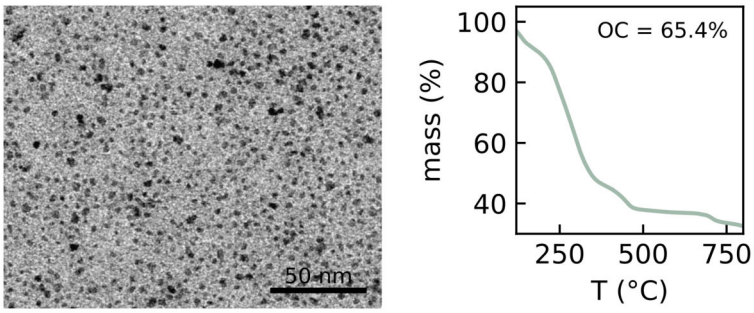

Figure A.51: Characterization of SPIONs used for the surface modification of TNR-based chemiresistors. TEM image (left) and TGA (right) of the oleyl phosphate-stabilized SPIONs.

GNPs. Gold nanoparticles GNPs were synthesized following the Leff procedure[244] and kindly provided by Ahir Bose, research associate and PhD student at University of Hamburg. Figure A.52 shows a representative TEM image of the spherical nanocrystals with a diameter of ~4 nm and the UV-vis spectrum of a GNP solution in n-heptane with the characteristic localized surface plasmon resonance at ~520 nm.

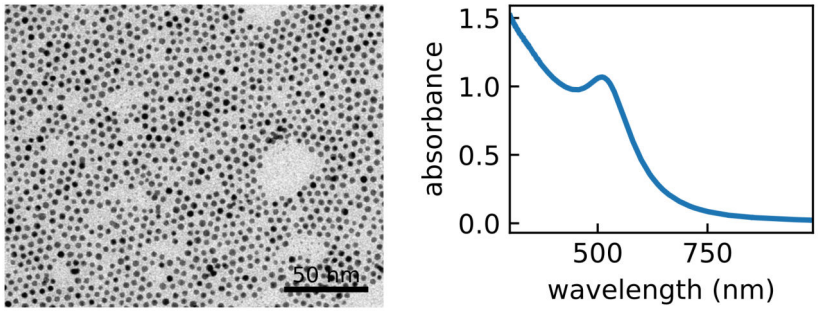

Figure A.52: Characterization of GNPs used for the surface modification of TNR-based chemiresistors. TEM image (left) and UV-vis spectrum (right) of dodecylamine-stabilized GNPs. UV-vis data were kindly provided by Ahir Bose, research associate and PhD student at University of Hamburg.

A.1.20 Surface Modification: Timetraces

The following figures show the photoactivated current timetraces of surface-modified TNR-based chemiresistors with iron oxide, Pt, and Au exposed to 1-propanol, MIBK, and 1-butylamine with concentrations of 100, 200, 200, and 100 ppm (cf. figures 6.22, 6.23, 6.24, and 6.25). The iron oxide modification was achieved by spin-coating of SPIONs, the modification with Pt was achieved by sputtering, and Au modification was done either by spin-coating of GNPs or by photocatalytic reduction of an Au precursor. For photoactivation, UV LEDs were used at an irradiance of ~23 mW/cm^2.

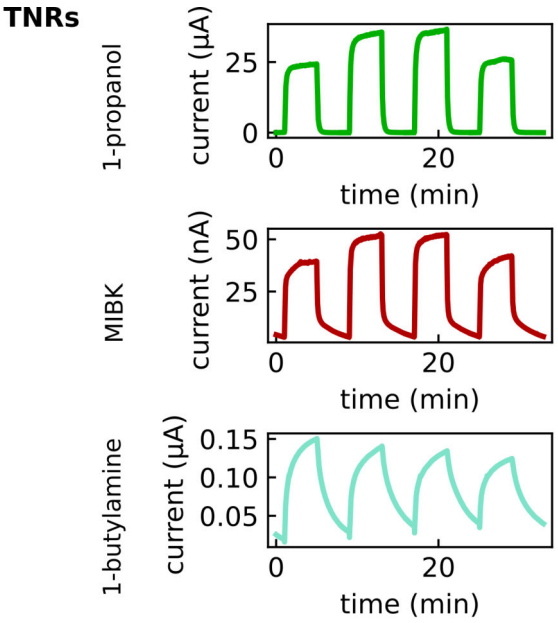

Figure A.53: Current timetraces of a photoactivated TNR-based chemiresistor exposed to three analyte vapors. All timetraces are shown without baseline correction.

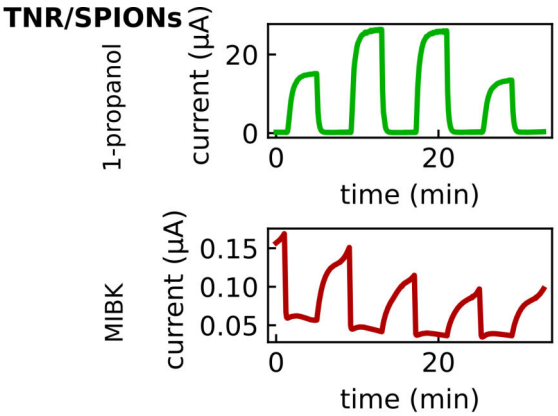

Figure A.54: Current timetraces of a photoactivated TNR-based chemiresistor modified by spin-coating SPIONs exposed to 1-propanol and MIBK. All timetraces are shown without baseline correction.

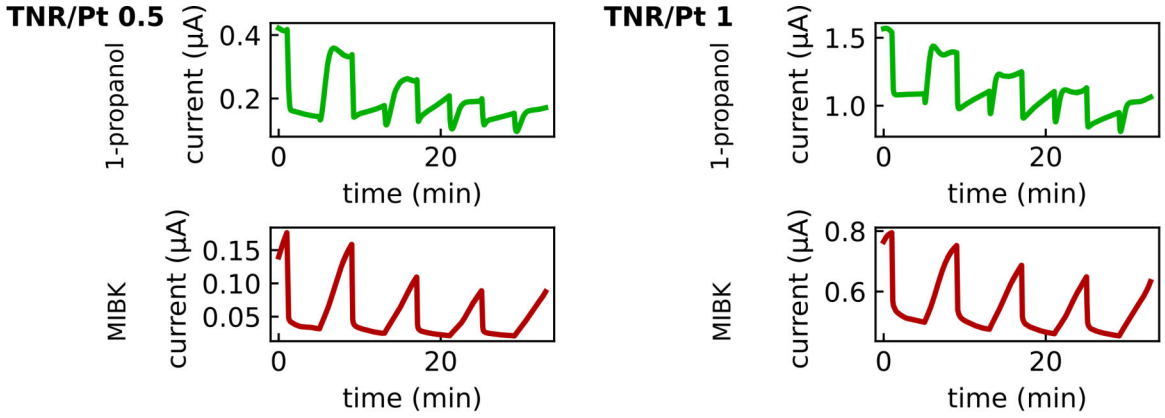

Figure A.55: Current timetraces of photoactivated TNR-based chemiresistors modified by sputtering different amounts of platinum exposed to 1-propanol and MIBK. All timetraces are shown without baseline correction.

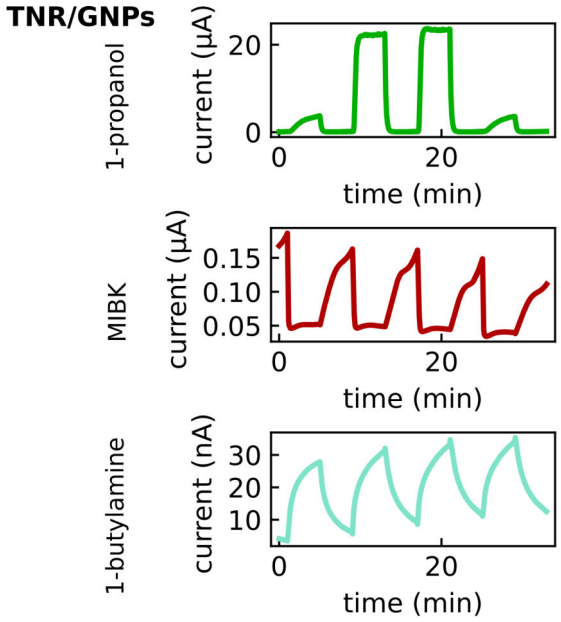

Figure A.56: Current timetraces of a photoactivated TNR-based chemiresistor modified by spin-coating GNPs exposed to 1-propanol, MIBK, and 1-butylamine. All timetraces are shown without baseline correction.

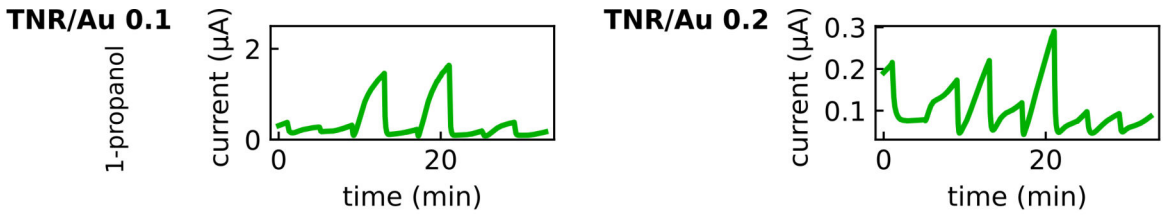

Figure A.57: Current timetraces of a photoactivated TNR-based chemiresistor modified by photocatalytic reduction of different amounts of Au precursor exposed to 1-propanol. All timetraces are shown without baseline correction.

A.1.21 Tuning of the Hybrid Thin Film Composition

As a reference experiment, figure A.58 shows the influence of DUV illumination on the UV-vis absorbance spectra of the individual components (GO, TNRs, and SF) used for the hybrid thin film fabrication. The absorbance spectra of GO indicate the formation of rGO also in the absence of a photocatalyst, as reported in literature.[132] Further, the spectra of SF show a slight decomposition after being exposed to DUV illumination, indicated by the decrease in absorbance of the peptide bonds below ~230 nm. For the TNRs, only a small decrease in absorbance was recorded after the DUV illumination.

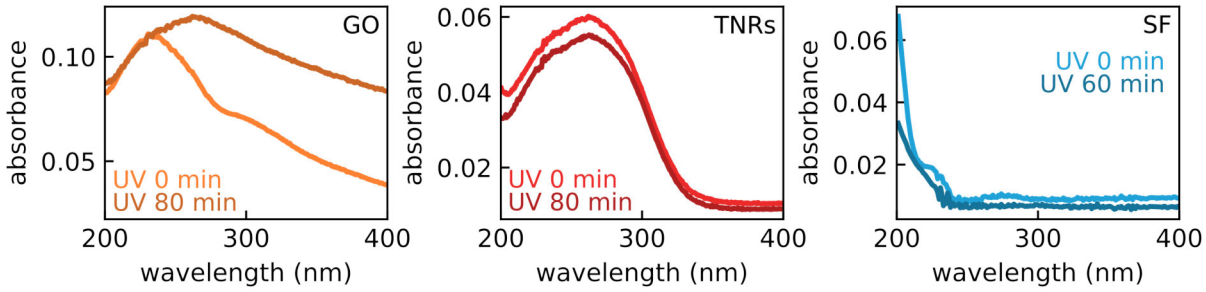

Figure A.58: UV-vis spectra of the individual materials used for hybrid thin film fabrication after 0 min and 60 min or 80 min DUV exposure times. Eight, two, and five layers of GO (left), TNRs (center), and SF (right), respectively, were spin-coated onto quartz slides.

Figure A.59 shows exemplary AFM scans of the freestanding hybrid TNR/GO/SF membranes before the DUV exposure and TNR/(GO/rGO)/SF membranes after DUV exposure. Membranes M1 and M2 were transferred onto substrates with a circular aperture and exposed to DUV illumination for 80 min, while membrane M3 was transferred to a substrate with square cavities and exposed to DUV illumination for 120 min. All scans

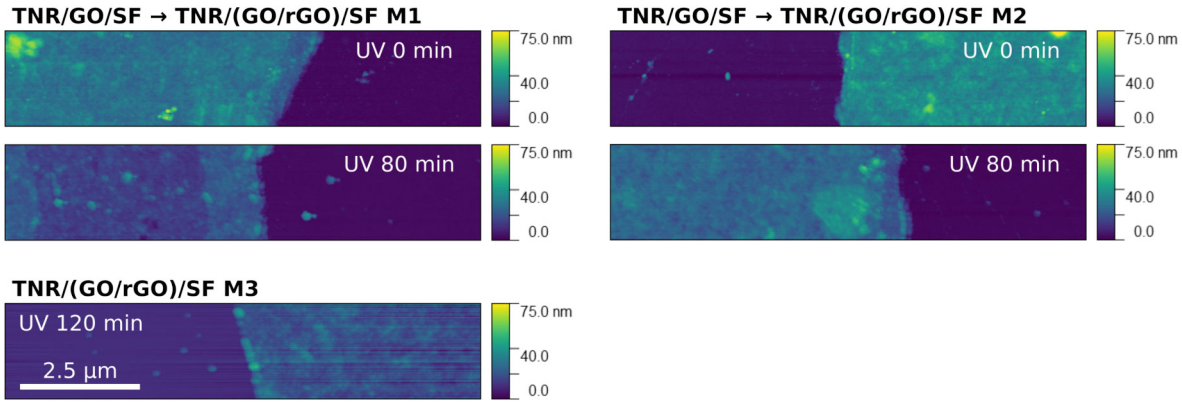

Figure A.59: Exemplary AFM scans of hybrid TNR/GO/SF membranes M1 and M2 used for microbulge tests recorded for DUV exposure times of 0 min and 80 min (top), and membrane M3 used for electrostatic actuation after DUV exposure time of 120 min (bottom). Adapted and reprinted from Dobschall el al., Ref. [1] *Creative Commons CC-BY 4.0* license ©2025 The Authors. Adv. Electron. Mater. published by Wiley-VCH GmbH. (DOI: 10.1002/aelm.202400602)

were recorded at the edges of the substrate-supported section of hybrid thin films, showing a reduction in thickness caused by the TNR-mediated photocatalytic tuning of the membrane composition.

Optical micrographs of the hybrid membranes M1 and M2 deposited on substrates with a circular aperture before the bulge tests and after burst test are shown in figure A.60 and reveal a rather homogeneous morphology. However, bright spots correspond to aggregates of TNRs. The membrane composition was photocatalytically tuned which is seen by a slight change in color of the substrate-supported thin film sections resulting from the formation of rGO and the compaction. After burst tests, only few freestanding membrane sections remain close to the aperture rim.

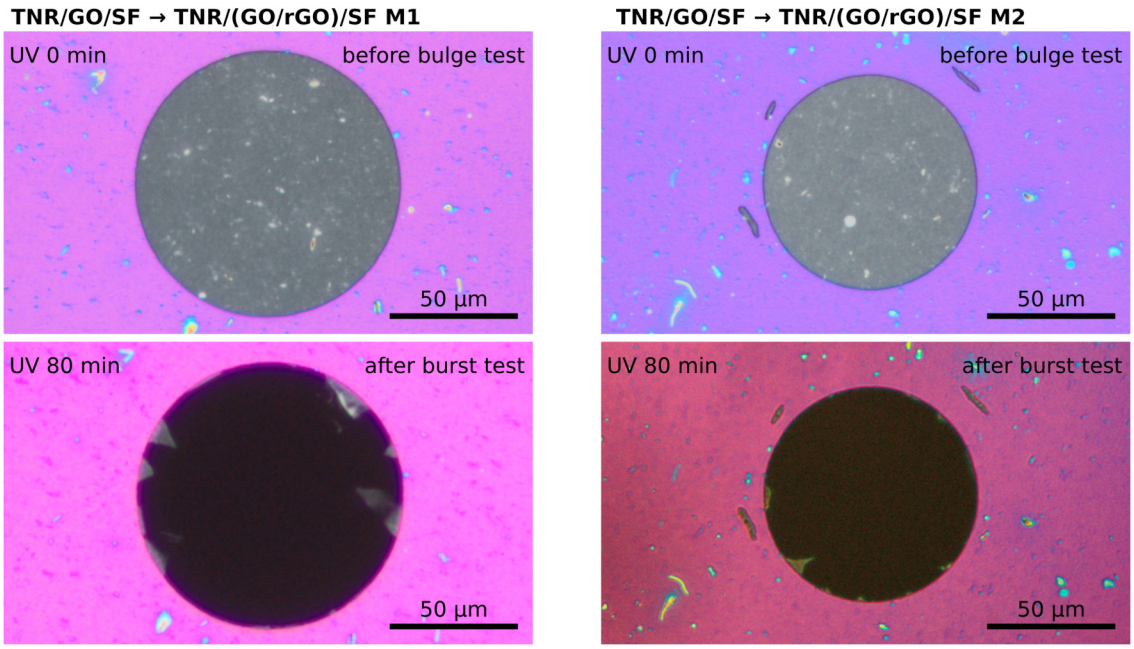

Figure A.60: Optical micrographs of freestanding membranes M1 and M2 before DUV treatment and bulge tests (top) and after 80 min DUV treatment and burst tests (bottom). The membranes span circular apertures with diameters of ~105 µm and ~84 µm for M1 and M2, respectively. Adapted and reprinted from Dobschall el al., Ref. [1], *Creative Commons CC-BY 4.0* license ©2025 The Authors. Adv. Electron. Mater. published by Wiley-VCH GmbH. (DOI: 10.1002/aelm.202400602)

A.1.22 Mechanical Properties: Microbulge Tests

Figure A.61 shows a cross-sectional schematic of a bulged membrane and includes the quantities that are relevant for data analysis. The membrane thickness t_m and the aperture radius a_r were determined prior to microbulge tests by AFM and optical microscopy, respectively. The radius of the bulged membrane was obtained by fitting the bulged membrane with a spherical cap,[147] and was used to geometrically determine the full arc length s. Ultimately, stress-strain curves were obtained by approximating the bulged membrane as part of a thin-walled spherical pressure vessel. Additionally, the membrane peak deflection h with respect to the surrounding substrate-supported film sections was extracted at the central point of the bulged, spherical freestanding membrane section.

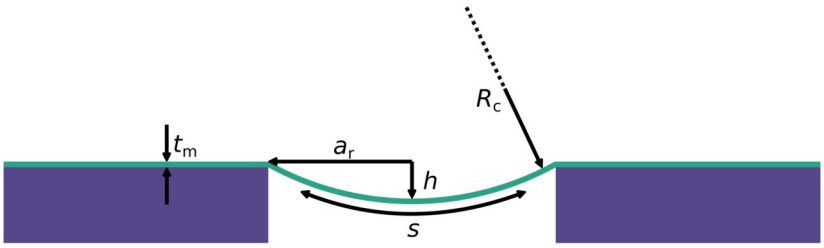

Figure A.61: Cross-sectional schematic of the bulged membrane. Important quantities are the membrane thickness (t_m), aperture radius (a_r), membrane deflection (h), arc length (s), and radius of the spherical cap (R_C).

A.1.23 Electrostatically Driven TNR/(GO/rGO)/SF Actuators

Figure A.62 shows an SEM image of the substrates featuring square cavities (right) used for the electrostatic actuation and a schematic of the measurement setup (left) used for obtaining the voltage-dependent deflection data. For fitting the voltage-dependent de-

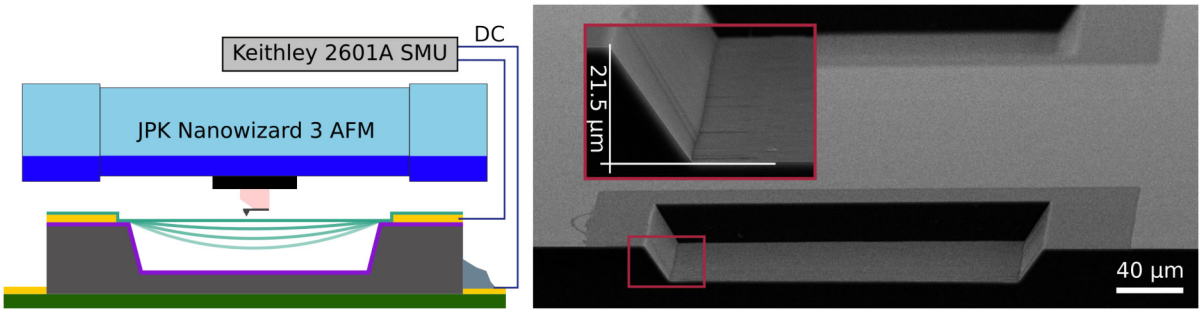

Figure A.62: Schematic of the DUV-treated TNR/(GO/rGO)/SF membrane actuator using the AFM to measure the deflection (left). Cross-sectional SEM image of the SiO_2/Si substrate with square cavities, that were used for electrostatic actuation (right). The inset displays a higher magnification of the red framed section, showing the cavity depth of ~21.5 µm. Adapted and reprinted from Dobschall el al., Ref. [1], *Creative Commons CC-BY 4.0* license ©2025 The Authors. Adv. Electron. Mater. published by Wiley-VCH GmbH. (DOI: 10.1002/aelm.202400602)

flection data, the simple model of a parallel arrangement of the membrane and the silicon substrate was assumed, as descried in a previous study of our group.[158] Thus, the two electrodes formed a parallel-plate capacitor with the capacitance C of the freestanding membrane section. The latter was calculated according to equation 12,

$$C = \frac{A\epsilon}{d} \tag{12}$$

in which A is the area of the freestanding membrane section, d is the distance between the plates, and ϵ is the permittivity of the dielectric between the electrodes. By applying a bias voltage V, both electrodes were charged, according to equation 13.[158]

$$|\pm Q| = CV \tag{13}$$

Here, the capacitance is the constant of proportionality between the charge Q and the applied bias voltage. Next, a homogeneous electric field E_f was assumed that can be described using equation 14,

$$E_f = \frac{Q}{2A\epsilon} \tag{14}$$

in which changes due to membrane deformation were neglected. The force F per unit area acting on the freestanding membrane section was approximated according to equation 15.

$$\frac{F}{A} = \frac{Q}{A}E_f = \frac{Q^2}{2A^2\epsilon} = \frac{C^2V^2}{2A^2\epsilon} = \frac{\epsilon V^2}{2d^2} \tag{15}$$

Here, the electric field is screened by the charge density Q/A of the opposing electrode, and the force is acting along the electric field and thus orthogonal to the membrane's surface. By applying the model, shown in equation 16, that is commonly used to approximate bulge data,[147,239] the relation of the center point deflection h and the applied pressure P can be described.

$$P(h) = c_1 \frac{\sigma_0 t_m}{{a_e}^2} h + c_2 \frac{Y t_m}{3{a_e}^4} h^3 \tag{16}$$

Here, t_m is the membrane thickness, a_e is half the edge length of the square cavity, Y is the biaxial modulus, σ_0 is the prestress, and $c_{1,2}$ are constants. For square membranes these constants are $c_1 = 3.393$[239] and $c_2 = 8/6(1+\nu)$[239] with ν being the Poisson ratio of the membrane. For small deflections ($h << a_e$) and low membrane thicknesses ($t_m << h$), this model can be used to accordingly describe the pressure-dependent deflection, as described in a previous study.[230] In the case of the actuator however, the deflection was not caused by the actual change in pressure but due to the electrostatic force per unit area. Since the maximum deflection of ~1.7 µm at ±40 V still implied a low curvature of the membrane, the deviation from the assumed homogeneous electric field was small. This allowed for replacing the pressure of the microbulge tests with the electrostatic force per unit area and resulted in equation 10. The latter was then fitted to the deflection data of the electrostatically driven actuator.

A.2 Safety

A.2.1 Chemicals and CMR Substances

All chemicals used in this work are listed in table A.2 with their respective GHS symbols (depicted in figure A.63) and hazardous and precautionary statements. The data are taken from the GESTIS Substance Database[187] if not indicated otherwise.

Table A.2: Used chemicals with respective GHS symbols, hazardous and precautionary statements.

Substance	GHS symbol	Hazardous statements	Precautionary statements
Acetone	02, 07	225, 319, 336	210, 233, 305+351+338
AZ 326 MIF[247]	05, 06, 08	290, 302, 311, 314, 371, 373	280, 302+352, 305+351+338, 308+310
AZ 726 MIF[248]	05, 06, 08	290, 302, 311, 314, 371, 373	260, 280, 301+330+331, 303+361+353, 304+340+310, 305+351+338
AZ ECI 3012[249]	02, 05, 07	226, 318, 335	210, 280, 305+351+338, 313
AZ nLOF 2020[250]	02, 07	226, 336	210
1-Butanol	02, 05, 07	226, 302, 315, 318, 335, 336	210, 280, 302+352, 305+351+338, 313
1-Butylamine	02, 05, 06	225, 302, 311+331, 314, 335	210, 280, 301+330+331, 303+361+353, 304+340, 305+351+338+310
Chlorobenzene	02, 07, 09	226, 315, 332, 411	210, 273, 302+352, 304+340+312
Chloroform	06, 07	302, 315, 319, 331, 336, 351, 361d, 373	202, 301+312, 302+352, 304+340+311, 305+351+338 308+313
Diethylene glycol	07	302	264, 270, 301+312, 501

Table A.2: Used chemicals with respective GHS symbols, hazardous and precautionary statements.

Substance	GHS symbol	Hazardous statements	Precautionary statements
Ethanol	02, 07	225, 319	210, 280, 310
Ethyl acetate	02, 07	225, 319, 336	210, 233, 240, 305+351+338, 403+235
n-Heptane	02, 07, 08, 09	225, 304, 315, 336, 410	210, 261, 273, 310+301, 331, 501
Hydrogen peroxide	03, 05, 07	302+332, 315, 318, 335	280, 305+351+338, 310
Iodine	07, 08, 09	312+332, 315, 319, 335, 372, 400	261, 273, 280, 305+351+338, 314
Methanol	02, 06, 08	225, 317	210, 260, 280, 301+310, 311
Methoxyper-fluorobutane	-	-	-
4-Methylpentan-2-one	02, 07	225, 332, 335, 319	210, 305+351+338, 304+340
1-Octadecene	08	304	301+310, 331
Oleic acid	-	-	-
Oleylamine	05, 07, 08, 09	302, 304, 314, 335, 373, 410	260, 280, 301+310, 303+361+353, 304+310+340, 305+351+338
Oxygen	03, 04	270, 280	220, 244, 370+376+403
PDMS	-	-	-
Potassium iodide	-	-	-
PMMA	-	-	-

Table A.2: Used chemicals with respective GHS symbols, hazardous and precautionary statements.

Substance	GHS symbol	Hazardous statements	Precautionary statements
PVA	-	-	-
1-Propanol	02, 05, 07	225, 318, 336	210, 233, 240, 280, 303+361+353, 310, 305+351+338, 370+378, 501
2-Propanol	02, 07	225, 319, 336	201, 261, 305+351+338
Silk Fibroin	-	-	-
Sodium hydroxide	05	290, 314	280, 301+330+331, 305+351+338, 308+310
TechniEtch Cr01[251]	05	314	264, 280, 303+361+353 305+351+338, 310, 321, 405, 501
TechniStrip NI555[252]	07	302, 312	-
Tetrachloro-auric(III) acid trihydrate	05, 07, 08, 09	290, 302, 314, 373, 411	260, 273, 280, 303+361+353, 305+351+338, 314
Titanium(IV)-oxide Aeroxide™ P25	05, 06	314, 330, 335	260, 271, 280, 303+361+353, 304+340+310, 305+351+338
Titanium(IV) chloride	05, 06	314, 330, 335	260, 271, 280, 303+361+353, 304+340+310, 305+351+338
Titanium(IV) fluoride	05, 07	302, 312, 332, 314	360, 280, 301+312, 303+361+353, 304+340+310, 305+351+338 305+351+338

Table A.2: Used chemicals with respective GHS symbols, hazardous and precautionary statements.

Substance	**GHS symbol**	**Hazardous statements**	**Precautionary statements**
Toluene	02, 07, 08	225, 361D, 304, 373, 315, 336	210, 240, 301+330+310, 302+352, 308+313, 314, 403+233
Triammonium citrate	07	315, 319, 335	361, 305+351+338

Table A.3 lists all substances classified as carcinogenic, mutagenic, or toxic to reproduction (CMR) on basis of the GESTIS Substance Database,[187] that were used within the framework of this thesis.

Table A.3: List of CMR classified substances used in the framework of this thesis.

Substance	CMR classification	Usage and amount
Chloroform	C category 1B, M category 2, R_D category 2	solvent, 2 L
Toluene	R_D category 2	solvent, 4 L

A.2.2 GHS Symbols

Figure A.63: GHS hazard pictograms 01 - 09.

B Danksagung

Herrn Prof. Dr. Horst Weller und später Frau Prof. Dr. Nadja C. Bigall möchte ich für die freundliche Aufnahme in den jeweiligen Arbeitskreis danken.
Ganz besonders danke ich PD Dr. Tobias Vossmeyer für die exzellente Betreuung, wertvollen Diskussionen und hilfreichen Anregungen während meiner Promotion und Deine Unterstützung. Prof. Dr. Tobias Beck danke ich für die Übernahme des Zweitgutachtens dieser Arbeit.
Mein besonderer Dank gilt auch Dr. Sophia C. Bittinger, die für einen Teil der Projekte wichtige Vorarbeit geleistet hat und mir im Laufe der Promotion immer wieder hilfsbereit zur Seite stand. Die Begeisterung für diverse Projekte auch außerhalb Deiner eigenen Forschung hat mich motiviert und die Zusammenarbeit mit Dir hat mir immer sehr viel Spaß gemacht.
Außerdem möchte ich mich bei allen aktuellen und ehemaligen Mitglider:innen der Sensorgurppe: Dr. Hendrik Schlicke, Dr. Sophia C. Bittinger, Dr. Bendix Ketelsen, Dr. Chi-Yin Liu, Hauke Hartmann, Clemens J. Schröter, Jana Struck, Ahir Bose und Jan-Niklas Beyer für die gute Zusammenarbeit und schönen Stunden im Labor bedanken. Besonders danken möchte ich Hauke für die hervorragende Betreuung während meiner Masterarbeit, Clemens für das Einarbeiten am Bulge Setup inklusive der Auswertungsskripte, Sophia für das Einarbeiten in diverse Setups, Jana für die Unterstützung bei Synthesen sowie Hendrik für die Einführung in Python und die Unterstützung bei diversen experimentellen Aufbauten. Meinen Masterstudierenden Christoph T. Tioka und Tzu-Ying Yu danke ich für die tatkräftige Unterstützung und den damit verbundenen Beitrag zu dieser Arbeit.
Auch bei allen Mitglieder:innen des Graduiertenkollegs Nanohybrid bedanke ich mich für die interessanten Gespräche und Diskussionen bei unseren zahlreichen Workshops, Meetings und Konferenzen. In diesem Zuge möchte ich auch Prof. Dr. Alf Mews und Prof. Dr. Volker Abetz danken, die als Co-Betreuer viele Anregungen für meine Projekte gegeben haben.
Bei Marion Manin und Dr. Corinna Flügge möchte ich mich für die Hilfe bei allen organisatorischen Fragen bedanken.
Für das Bereitstellen der bipyramidalen Partikel sowie das Initiieren der Kollaboration danke ich Dr. Marie-Hélène Delville und Eugénie Pariente sowie Prof. Dr. Mona Tréguer-Delapierre, die am Institut de Chimie de la Matière Condensée de Bordeaux, CNRS tätig sind.
Für die Produktion und das Bereitstellen der Lochsubstrate danke ich Prof. Dr.-Ing. Hoc Khiem Trieu und Dr. Norbert Schulz, die an der Technischen Universität Hamburg tätig sind/waren.

Den zahlreichen Personen in verschiedenen Serviceabteilungen der Universität Hamburg: Dr. Charlotte Ruhmlieb, Stefan Werner und Robert Schön sowie Stefan Werner, Charis Rabea Schlundt und Nina Schöber möchte ich für die Durchführung der SEM-, TEM- sowie XRD-Messungen danken. Dr. Sebstian Willruth danke ich für das Bereitstellen der Eisenoxidnanopartikel und Ahir Bose danke ich für das Bereitstellen der Goldnanopartikel.
Der Forschungswerkstatt des Instituts für Physikalische Chemie danke ich für die Anfertigung verschiedener Messzellen, die Anpassung weiterer Aufbauten und die Hilfsbereitschaft bei vielen weiteren Kleinigkeiten. Hier möchte ich auch Jan Flügge für die Unterstützung bei Fragen im Bereich der Elektronik danken.
Für die unterhaltsamen Zeiten aber auch fachlich wertvollen Gespräche danke ich meinen Bürokolleg:innen in 253, 347 und 016.4: Hauke Hartmann, Dr. Bendix Ketelsen, Dr. Sophia C. Bittinger, Dr. Lea R. Klauke, Dr. Sönke Wengler-Rust, Dr. Elena Felgenhauer, Ahir Bose, Jana Struck, Christoph T. Tioka, und Jan-Niklas Beyer. Weiterhin danke ich allen ehemaligen AK-Weller und aktuellen AK-Bigall Mitglieder:innen für die schöne Zeit.
Für die Durchsicht dieser Arbeit danke ich Dr. Karen Schäfer, Linda S. Joseph und Kai-Fu Wong, letzterem auch für die Unterstützung und Zusammenarbeit im Laufe unseres gemeinsamen Studiums.
Ein großes Dankeschön möchte ich auch an alle Freund:innen aussprechen, die mich immer bekräftigt und wenn es mal nötig war gut vom Uni-Alltag abgelenkt haben.
Schließlich möchte ich von ganzem Herzen meiner Familie für ihre bedingungslose Unterstützung in allen Belangen danken: Linda, meiner Mutter Christina, meinem Vater Uwe und meiner Schwester Alina für Euren Zuspruch, Eure Liebe und Eure Geduld!

C Eidesstattliche Erklärung

Hiermit versichere ich an Eides statt, die vorliegende Dissertationsschrift selbst verfasst und keine anderen als die angegebenen Quellen und Hilfsmittel benutzt zu haben. Sofern im Zuge der Erstellung der vorliegenden Dissertationsschrift generative Künstliche Intelligenz (gKI) basierte elektronische Hilfsmittel verwendet wurden, versichere ich, dass meine eigene Leistung im Vordergrund stand und dass eine vollständige Dokumentation aller verwendeten Hilfsmittel gemäß der Guten wissenschaftlichen Praxis vorliegt. Ich trage die Verantwortung für eventuell durch die gKI generierte fehlerhafte oder verzerrte Inhalte, fehlerhafte Referenzen, Verstöße gegen das Datenschutz- und Urheberrecht oder Plagiate.

December 12, 2025

Finn Dobschall